EPFL

Thèse n° 10 644

Magnetism of Single Surface Adsorbed Atoms Studied with Radio-Frequency STM

Présentée le 16 février 2024

Faculté des sciences de base
Laboratoire de nanostructures superficielles
Programme doctoral en physique

pour l'obtention du grade de Docteur ès Sciences

par

Clément Marie SOULARD

Acceptée sur proposition du jury

Prof. F. Mila, président du jury
Prof. H. Brune, directeur de thèse
Prof. S. Loth, rapporteur
Prof. F. Natterer, rapporteur
Prof. H. Dil, rapporteur

École polytechnique fédérale de Lausanne

2024

" [...] Supra idolum age primum et septimum de quatuor"
The Name of the Rose, Umberto Eco

À mes parents.

Acknowledgments

I would like to express my sincere gratitude to Prof. Harald Brune for offering me the opportunity to work in his research group for the last four years.

On the night of September 8, 2022 at 2:38 am, I was sitting in front of the controller screen when I observed a small increase of a few femtoamperes in the tunneling current, measured over a TiH molecule. Unsure if this peak originated from the molecule itself or if it was caused by some other undesired sources, I repeated the measurement. The peak showed up again and shifted linearly with the RF frequency. I realized, at that moment, that we had finally measured ESR signals on a single molecule. Achieving this challenge took us three years of hard work, improving the machine, overcoming technical issues, facing Helium shortages, and going through the challenges of the pandemic. I am grateful to have experienced such a moment that day, which could not have happened without the trust of Harald and the invaluable expertise of Dr. Johannes Schwenk. I extend my sincere thanks to Johannes for dedicating his time to explain the technical and physical aspects of a low-temperature STM. His knowledge and patience were crucial, and I could not have done it without his help.

I would also like to thank all the lab and administrative members who supported me throughout this journey: Aistis, Alberto, Alexis, Anh, Boris, Dante, Darius, Francesco, François, Jean-Guillaume, Jiří, Maria, Marina, Nataly, Nathalie, Pardis, Sébastien, Serni, Shixuan, and Stefano. My thanks also go to Gilles Grandjean, Claude Amendola, and François Patthey for their help, their technical expertise, and the various discussions we had together.

Doing a Ph.D. in experimental physics could be summarized by working a lot, sometimes overnight and on weekends. This has prevented me from being as available for my friends. I want, therefore, to express my sincere gratitude to them for their patience and support during these four years. In particular, I want to thank Rémi, FG, Emilien, Alicia, Paul, Alice, Yara, Benoit, and last but not least, my wonderful friends of *La Meute*.

J'aimerais dédier ce travail de thèse à mes parents, qui m'ont tant inspiré et à qui je dois tellement. Ils ont été suffisamment fous pour croire en moi, sans totalement comprendre ce que je faisais. Je vous remercie pour votre aide et votre amour pendant ces années qui, comme vous le savez, ont été difficiles. J'aimerais aussi dire merci à Louis et Jeanne pour leur soutien et leur bonne humeur permanente. Merci à mes grands-parents Francine, Suzanne, Jacques, et Raymond de m'avoir fait vivre ces moments de bonheur que je n'oublierai jamais.

Enfin, merci à toi Ann-Rivière, pour ta confiance, ta patience, et tes conseils. Tu sais véritablement à quel point ce fut difficile, et je n'y serai jamais arrivé sans ton aide et ton amour. Merci du fond du cœur.

Paris, December 21, 2023

Abstract

This thesis investigates the magnetic properties of single atoms and molecules adsorbed on thin magnesium oxide decoupling layers, grown on a silver single crystal. To address these systems experimentally, we use a low temperature scanning tunneling microscope capable of applying radio-frequency bias modulations in the tunneling junction. The main motivation is to investigate and control the spin dynamics of single surface adsorbed atoms and molecules using spin-polarized scanning tunneling microscopy within and beyond the I/V converter bandwidth.

We first present the technical upgrades implemented on the system that enable a high radio-frequency bias transmission up to 40 GHz in the tunneling junction. The presentation of the corresponding transfer function is followed by electron spin resonance results on adsorbed hydrogenated titanium molecules at 0.4 K and 4.2 K. We determine the magnetic moment and the g-factor of the molecules and achieve measuring narrow signal linewidths, below 40 MHz at 0.4 K, further motivating the use of this technique to address new systems.

The magnetism of single dysprosium and terbium atoms adsorbed on the top-Oxygen site of magnesium oxide thin films is investigated. The magnetic bi-stability of these systems, with an out-of-plane easy axis of the magnetization, allows us to record two-state noise at low temperatures and in an externally applied magnetic field. An analysis of the magnetization switching rate is presented and shows consistent results for dysprosium with the existing literature. We report a first energy threshold of the system at 140 meV. A similar analysis is done for terbium, from which magnetization reversal pathways are identified from quantum chemical calculations and estimated experimentally for the first time. We find three energy onsets at 72 meV, 123 meV and 164 meV. Terbium and dysprosium atoms adsorbed on the bridge-Oxygen site, however, do not show two-state noise within the real-time limit of our instrument. On this site, terbium atoms show spectroscopic spin excitation features at $\pm$23 meV. A comparison with a spectroscopy database in the gas phase allows to speculate on their complete electronic configuration, including the valence electrons. We find two possible configurations based on this comparison: $4f^{8}5d^{1}6s^{2}$ and $4f^{8}5d^{1}6s^{1}$.

Finally, quantum stochastic resonance applied to the magnetism of single iron atoms on thin magnesium oxide films is presented. This technique also benefits from the high radio-frequency transmission, as a bias modulation is employed to drive the spin dynamics of the adatom, at frequencies beyond the I/V converter bandwidth and at 0.4 K. We introduce the time $\tau^{*}/2$ that should correspond to the first excited state lifetime, assuming that the radio-frequency modulation is sufficiently synchronized with the magnetic bi-stable system. We show that this time scales linearly with the relaxation time of the system, in current- and magnetic field-dependent measurements of the relative magnetic ground state population.

Keywords: Magnetism, rare-earth, transition metal, single atom, magneto crystalline anisotropy energy, scanning tunneling microscopy, spin polarized scanning tunneling microscopy, radio-frequency, electron spin resonance, quantum stochastic resonance, spin dynamics, two-state noise, relaxation time, coherence time, decoupling layer, thin films, magnesium oxide.

Résumé

Cette thèse étudie les propriétés magnétiques d'atomes et de molécules individuels, adsorbés sur des couches minces d'oxyde de magnésium, préparées sur un monocristal d'argent. Pour étudier ces systèmes expérimentalement, nous utilisons un microscope à effet tunnel, opérationnel à basse température et capable d'appliquer des modulations radio-fréquences en tension dans la jonction tunnel. L'objectif est de mesurer et contrôler la dynamique de spins atomiques et moléculaires en utilisant la microscopie à effet tunnel polarisée en spin au sein et au-delà de la bande passante de notre amplificateur électronique.

Nous commençons par présenter les améliorations techniques apportées à notre microscope, qui permettent une haute transmission de la tension radio-fréquence jusqu'à 40 GHz dans la jonction tunnel. La présentation de notre fonction de transfert est suivie par des résultats de résonance paramagnétique électronique sur des molécules de titane hydrogénées à 0.4 K et 4.2 K. Nous déterminons le moment magnétique et le facteur de Landé de ces molécules et mesurons des largeurs à mi-hauteur étroites, inférieures à 40 MHz à 0.4 K. Ces résultats motivent l'utilisation de cette technique afin d'explorer de nouveaux systèmes.

Nous présentons ensuite le magnétisme des atomes individuels de dysprosium et de terbium, adsorbés sur le site d'oxygène des couches minces d'oxyde de magnésium. La bistabilité magnétique de ces systèmes, avec un axe privilégié de l'aimantation hors du plan, nous permet d'enregistrer un bruit à deux états à basse température, dans un champ magnétique externe. Une analyse du taux de renversement de l'aimantation est présentée et montre des résultats cohérents avec la littérature pour le dysprosium. Nous observons un premier seuil en énergie à 140 meV pour ce système. Une analyse similaire est réalisée pour le terbium, et nous rapportons pour la première fois les trajectoires de renversement de l'aimantation, identifiées à partir de calculs chimiques quantiques. Nous trouvons trois seuils d'énergie à 72 meV, 123 meV et 164 meV. Cependant, les atomes de terbium et de dysprosium adsorbés sur le site oxygène-pont ne montrent pas de bruit à deux états dans la limite temporelle de notre instrument. Sur ce site, les atomes de terbium montrent des signatures spectroscopiques, correspondant à des excitations du spin, à ± 23 meV. Une comparaison avec une base de données spectroscopique en phase gazeuse permet de spéculer sur leur configuration électronique complète, comprenant les électrons de valence. Nous trouvons deux configurations possibles basées sur cette comparaison : $4f^{8}5d^{1}6s^{2}$ et $4f^{8}5d^{1}6s^{1}$.

Enfin, nous présentons la résonance stochastique quantique appliquée au magnétisme des atomes individuels de fer. Cette technique bénéficie également de la haute transmission en radio-fréquence, car une modulation de la tension est utilisée pour contrôler la dynamique du spin de l'adatome, à des fréquences au-delà de la bande passante du convertisseur I/V et à 0.4 K. Nous introduisons le temps $\tau^{*}/2$ qui devrait correspondre au temps de vie du premier état excité, sous l'hypothèse d'une modulation radio-fréquence suffisam-

ment synchronisée avec le système magnétique bi-stable. Nous montrons que ce temps est proportionnel au temps de relaxation du système, dans des mesures en courant tunnel et en champ magnétique.

Mots clés: Magnétisme, terre-rare, lanthanide, métal de transition, atome individuel, énergie magnéto-cristalline, microscopie à effet tunnel, microscopie à effet tunnel à polarisation de spin, radio-fréquence, résonance paramagnétique électronique, résonance stochastique quantique, dynamique de spin, bruit à deux états, temps de relaxation, temps de cohérence, couche isolante, films fins, oxyde de magnésium.

EPFL

Contents

EPFL

List of Figures

EPFL

List of Tables

EPFL

Frequently Used Abbreviations, Molecules and Atoms

Ag Silver.

CF crystal field.

Co Cobalt.

Cr Chromium.

Cu Copper.

Cu_2N Copper-Nitride.

DFT Density Functional Theory.

Dy Dysprosium.

ESR Electron Spin Resonance.

ESR-STM Electron Spin Resonance - Scanning Tunneling Microscopy.

Eu Europium.

Fe Iron.

FER Field-Emission Resonance.

FWHM Full-Width at Half Maximum.

Ho Holmium.

HWHM Half-Width at Half Maximum.

IETS Inelastic Electron Tunneling Spectroscopy.

LDOS Local Density of States.

MAE Magneto-crystalline Anisotropy Energy.

Mg Magnesium.

MgO Magnesium Oxide.

ML monolayer.

Mn Manganese.

QSR Quantum Stochastic Resonance.

QTM Quantum Tunneling of the Magnetization.

RF Radio-Frequency.

SES Spin Excitation Spectroscopy.

Sm Samarium.

SP Spin-Polarized.

SP-IETS Spin-Polarized - Inelastic Electron Tunneling Spectroscopy.

SP-SES Spin-Polarized Spin Excitation Spectroscopy.

SP-STM Spin-Polarized - Scanning Tunneling Microscopy.

SP-STS Spin-Polarized - Scanning Tunneling Spectroscopy.

STM Scanning Tunneling Microscopy.

STS Scanning Tunneling Spectroscopy.

Tb Terbium.

TF Transfer Function.

Ti Titanium.

TiH hydrogenated Titanium.

TMR Tunneling Magnetoresistance.

UHV Ultra-High Vacuum.

XAS X-ray Absorption Spectroscopy.

XMCD X-ray Magnetic Circular Dichroism.

ZFS Zero-Field Splitting.

1 Introduction

Quantum mechanics has revolutionized the twentieth century by its relentless theoretical development that we owe to a remarkable synergy of researchers. The main contributors posed for what is often referred to as the most intelligent photograph ever taken at the fifth International Solvay Congress in 1927, shown in figure 1.1. The same year, the concept of quantum tunneling is introduced by Friedrich Hund and then developped by Jacov Frenkel who described that "electrons [...] can pass even with insufficient kinetic energy" a potential hill [1–4].

Following these theoretical breakthroughs leading to the first quantum revolution, technologies relying on quantum mechanics were not yet conceivable. The invention of the transistor in 1947 marks however the start of a new development era converging towards quantum-based technologies, known as the second quantum revolution. If the number of transistors on a chip doubled every year following Moore's law of 1965, it becomes now difficult to continue scaling transistor size and density with classical semiconductor technology [5]. With the ever-increasing miniaturization of these components, transistors have reached the nanometer scale where dissipation and quantum tunneling can occur as dominant contributions and induce a drop in their performance. Alternative fields aiming to overcome Moore's law limitation emerged, including spintronics in the 1980s. This field is based on using the electron's magnetic moment as an additional degree of freedom to process information in solid-state devices. From the discovery of giant magnetoresistance by Fert and Grünberg in 1988 on Iron (Fe) and Chromium (Cr) multi-layers [6], spintronics has rapidly enabled the engineering of many modern technologies including hard-drive disks or magnetic random-access memory. This field provides attractive solutions for the ever-increasing data storage demand as *IBM* estimates that 175 zettabytes of new data will be created in 2025 [7]. One might wonder: what can be the spatial limit for storing information? In an incredibly farsighted paper, written in 1961, Richard Feynman argued that "the law of physics present no barrier to reducing the size of computers until bits are the size of atoms, and quantum behavior holds dominant way" [8]. Following this remarkable statement, single-atom magnets are nowadays considered as the ultimate miniaturization limit since they can store information by their spin being stable in absence of external magnetic field and either pointing "up" or "down". Even if such system is far from being commercialized, it shows promising results that would overcome by orders of magnitude the current areal density record of 317 gigabytes per square inch held by *IBM* and *Fujifilm* (2020) [9].

To address these systems on the atomic scale, experimental techniques have emerged such as Scanning Tunneling Microscopy (STM), invented in 1981 by Binning and Rohrer. STM consists of a conductive sharp tip and a conductive sample separated by a distance on the order of 1 ångström (Å) such that the electron wave functions of tip and sample partially overlap. When a bias voltage is applied over the junction, tunneling electrons lead to a net tunneling current that can be measured. After the first reconstructed image of the 7x7

unit cells of Silicon Si(111) in 1982 [10], this technique underwent multiples developments to become an efficient tool to image the surface of conductive samples but also to probe electronic and magnetic properties on the atomic scale. In 1990, R. Wiesendanger *et. al.* were the first to describe and investigate the vacuum tunneling of spin-polarized electrons with STM, using a spin-polarized tip (SP-STM) on the Cr(001) terraces [11]. The same year, D. M. Eigler *et. al.* published the well known image of *IBM*'s initials written with 35 Xenon (Xe) atoms moved laterally on a Nickel Ni(110) surface [12]. From there, a huge interest grew in probing and controlling the magnetic states of single surface adsorbed atoms with the first Spin-Polarized - Inelastic Electron Tunneling Spectroscopy (SP-IETS) showing spin excitations of Manganese (Mn) and Fe atoms on thin Copper-Nitride Cu_2N decoupling layers in 2010 [13]. Five years later, the first Electron Spin Resonance (ESR) experiment was performed with STM, at 0.6 K, on single Fe atoms adsorbed on thin Magnesium Oxide (MgO) films, leading to the first quantum coherent spin manipulation with STM [14]. ESR transitions are driven by an Radio-Frequency (RF) bias modulation, applied from the STM tip or coupled into the tunneling junction via an antenna in the tunneling junction [15]. While more and more sample systems are characterized with this technique [16–20], the working principle of ESR-STM is not yet fully understood but shows promising ways of generating coherent spin states that could be used as quantum bits of information in quantum computing devices.

In this context, this thesis conducts experimental investigations into the magnetism of single surface adsorbed atoms and molecules. We use SP-STM to find and study single-atomic systems that can retain their magnetic moment for a long time, at low temperatures, and in a given direction with respect to the sample's surface. To perform ESR-STM and to identify single atom spin systems that have not yet been characterized and that could reveal long coherence times, we use a home-built STM, equipped with an RF bias line that can apply modulations in the tunneling junction. The application of RF modulations in an STM is not only restricted to ESR-STM. We want to understand how the spin dynamics of a single atom on a surface can be driven by an RF bias modulation. For this reason, we conduct Quantum Stochastic Resonance (QSR) experiments, applied to magnetic bi-stable single atoms on a surface. All experiments, shown in this thesis, are conducted on few monolayers (ML)-thick MgO films, grown on a silver single crystal Ag(100).

The thesis is organized as follows. In chapter 2 we introduce the theory of magnetism applied to single surface adsorbed atoms on thin decoupling layers. We focus particularly on 3d transition metal and rare-earth atoms, as they are investigated in this thesis. In chapter 3 follows the presentation of our STM and the technical upgrades that we have implemented on the entire system and in particular concerning the RF cabling. As a benchmark for our microscope, we present ESR results on adsorbed hydrogenated Titanium (TiH) molecules at different temperatures in chapter 4. Chapters 5 and 6 are dedicated to the study of Dysprosium (Dy) and Terbium (Tb) single atoms with SP-STM and, in particular, to the measurement of two-state noise. We show how the magnetic switching rate gives information about the magnetic system and the possible magnetization reversal pathways. In chapter 6, we demonstrate

that the complete electronic configuration of Tb atoms, adsorbed on the Oxygen-bridge site of MgO, can be estimated from spectroscopy data. In chapter 7 we discuss the spin dynamics of single Fe atoms, probed by the QSR technique.

Figure 1.1: Colorized version of the photograph taken at the 1927 Solvay Conference. 17 of the 29 attendees were or became Nobel prize winners.

2 Theory and Methods

In order to study their magnetic properties, single atoms of a material can be deposited onto a suitable sample surface. If a fraction of a monolayer of the material is adsorbed on the surface at sufficiently low temperature, the surface diffusion of the atoms is inhibited, avoiding the formation of clusters. This allows the experimentalist to probe individual surface adsorbed atoms, referred to as adatoms. In the following, an introduction to the magnetism of surface adatoms and the differences from the simple free atomic case are discussed. The main interactions described in the Hamiltonian are defined to understand how magnetism is generated in these structures. An introduction to STM is then provided with an emphasis on Spin-Polarized (SP) tunneling and SP-STM. Combining this technique with the magnetism of adatoms enables the measurement of single atomic spin lifetimes, observing the two-state noise resulting from magnetization switching of the adatom, both, within as well as beyond the bandwidth of the I/V converter that is used to measure the tunneling current. The last part of the chapter is dedicated to ESR-STM, with theoretical and technical descriptions and the various theories proposed to explain the driving mechanism of ESR-STM are discussed.

2.1 An introduction to Spin Angular Momentum

The concept of quantum electronic spin originated from Niels Bohr's postulate in 1913, assigning a quantized magnetic moment to electrons. As shown in figure 2.1, Stern and Gerlach observed a deviation of a Silver (Ag) particle beam in an inhomogeneous magnetic field, contradicting classical theories [21, 22]. Since the concept of spin remained a hypothesis without theoretical description, the result of this experiment was incorrectly interpreted by Stern and Gerlach as caused by the orbital angular momentum [23]. Only after Pauli's exclusion principle in 1925 and the work of Uhlenbeck and Goudsmit [24], the electronic spin was described by the quantum number S with $S = \frac{1}{2}$ for Ag, which explained a quantized angular momentum for individual Ag atoms and the spatial deviation observed for small Ag clusters in the Stern-Gerlach experiment.

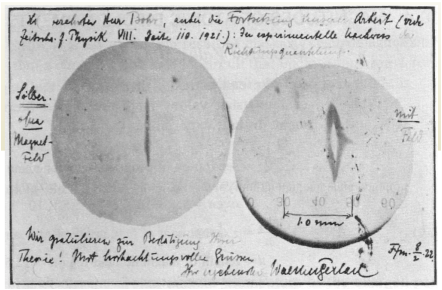

Figure 2.1: Walther Gerlach's postcard to Niels Bohr. The image shows the recorded pattern of Ag particles without (left) and with (right) an inhomogeneous magnetic field, where a deviation is visible.

Other Stern-Gerlach experiments were performed more recently on different cluster sizes of Fe, Ni and Cobalt (Co) to understand the transition of magnetic properties from bulk to

single atoms [25–27]. By starting with a description of the free atom, we present in the next section how a crystal surface can provide an environment in which an adatom shows magnetism.

2.2 From the Free Atom to an Atom Adsorbed on a Surface

Shortly after the first Stern-Gerlach experiment, Friedrich Hund formulated a set of rules for calculating the quantum numbers L, S and J of a multi-electron system in its ground state configuration. The simplest example is a single isolated atom for which the magnetic moment is defined by:

$$\mathbf{m}_{\text{at}} = \mathbf{m}_{\text{orbital}} + \mathbf{m}_{\text{spin}} = -\mu_B(g_L\mathbf{L} + g_S\mathbf{S}) = -\mu_B g_J\mathbf{J} \tag{2.1}$$

where μ_B is the Bohr magneton, g_L the orbital g-factor, g_S the spin g-factor and g_J the Landé factor [28]. From equation 2.1, the quantum number $m_J \in \{-J, -J+1, ..., +J\}$ can be introduced, associated to the operator $\hat{J}_z$, as well as m_L and m_S for $\hat{L}_z$ and $\hat{S}_z$, respectively. We choose $\hat{z}$ as the quantization axis.

When applying Hund's rules to elements of the periodic table, most of them have a non-zero spin quantum number J. Nevertheless, none of them shows magnetism in the absence of an external magnetic field since all the states in a given multiplet J are $(2J+1)$-fold degenerated. The example of a free Ti atom is given, based on the isolated Hamiltonian H_{at}:

$$H_{\text{at}} = \underbrace{\sum_{i=1}^{Z}\left(\frac{p_i^2}{2m} - \frac{Ze^2}{r_i}\right)}_{H_{\text{intra}}} + \underbrace{\left(\sum_{i<j}^{Z}\frac{e^2}{|r_i - r_j|}\right)}_{H_{\text{e-e}}} + \underbrace{\lambda\ \mathbf{L}\cdot\mathbf{S}}_{H_{\text{SO}}} \tag{2.2}$$

The first sum in equation 2.2 refers to the kinetic energy of a single electron as well as its attractive interaction to the nucleus. The electron is defined by its momentum p_i, its mass m and its distance r_i to the nucleus with atomic number Z. The second term is the electron-electron interaction known as the Coulomb repulsion and the last refers to the spin-orbit coupling defined as the interaction of the electron spin with the magnetic field generated by its own orbital motion. Figure 2.2 shows the energy spectrum of an isolated Ti atom with electronic configuration [Ar]$4s^2 3d^2$, where [Ar] is the electronic configuration of Argon. The first two energy splittings in figure 2.2 can be explained by the intra-atomic Coulomb repulsion, described in equation 2.2. The spin-orbit interaction is responsible for the last splitting, leading to a ground state written as ${}^3F_2$ with degeneracy $(2J+1) = 5$. Note that spectroscopic notations ${}^{2S+1}L_J$ are used here. When an external magnetic field $\mathbf{B}$ is applied along $\hat{z}$, the Zeeman interaction $\mu_B g_J\ \mathbf{J}\cdot\mathbf{B}$ is added to the Hamiltonian in equation 2.2 and lifts the 5-fold degeneracy of ${}^3F_2$. Although Ti has $J_z \neq 0$, its isotropic and degenerate behavior does not give a preferential orientation of the magnetization and does not generate stable magnetic order. However, some adatoms can preserve their orbital moment and the crystal field (CF) interaction with the substrate can induce strong directional bonding, leading to an anisotropic orbital and magnetic moment, along an energetically favorable easy axis.

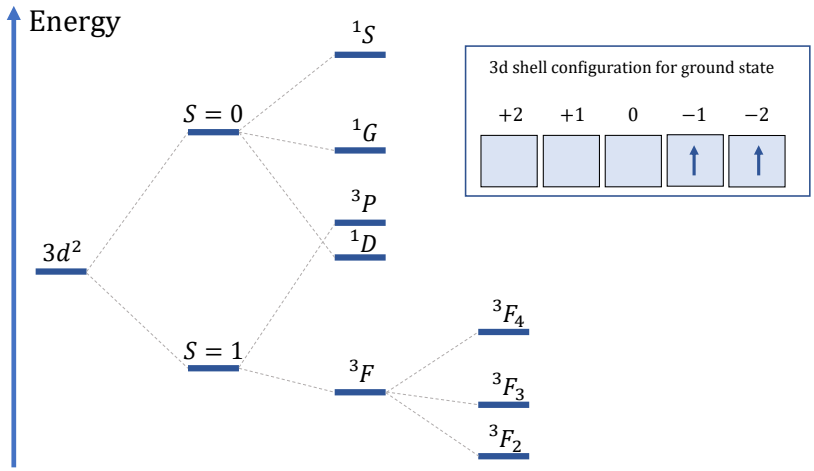

Figure 2.2: Qualitative energy spectrum of an isolated Ti atom. The inset shows the ground state configuration $^3F_2$ according to Hund's rules where J has to be minimized.

An example is a single Fe atom adsorbed on a top-Oxygen site of a thin MgO film where the unquenched out-of-plane L_z, restored by the spin-orbit interaction, leads to an out-of-plane magnetic moment in the ground state. It is important to note that the orbital moment and the magnetic moment do not always coincide [29]. The stability of the magnetization of these anisotropic systems is given by the Magneto-crystalline Anisotropy Energy (MAE) defined as the energy needed to reverse the magnetization in a classical reversal process. A qualitative energy scheme is shown in figure 2.3 for an adatom adsorbed on an ideal out-of-plane uni-axial environment with effective spin $J^* = 2$, projected along the surface normal $\hat{z}$. We will regularly use the notation J^* that accounts for an effective adatom spin. This number typically differs from the free atomic case since substrate interactions and hybridization effects occur on the surface.

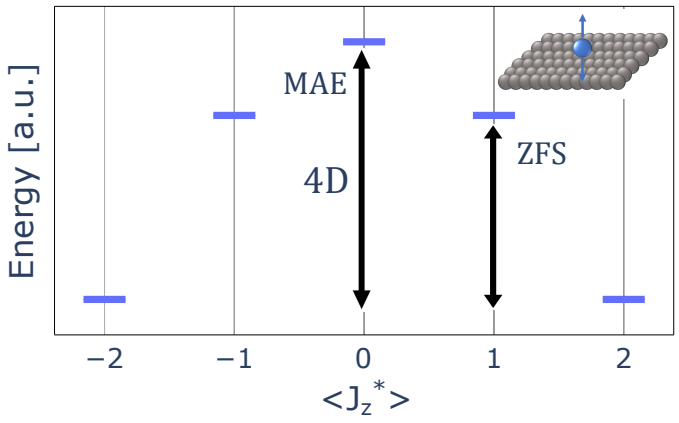

Figure 2.3: Energy level scheme of an adatom with $J^* = 2$ and a large MAE of $4D$, where D is the axial anisotropy term (see section 2.2.1). ZFS refers to the Zero-Field Splitting, i.e., the first accessible state in absence of external magnetic field.

2.2.1 Spin Hamiltonian Model

For an atom adsorbed on a surface, the Hamiltonian can be written as:

$$H = H_{\text{at}} + H_Z + H_{\text{CF}} \quad \text{with} \quad H_Z = \mu_B g_J \, \mathbf{J} \cdot \mathbf{B} \tag{2.3}$$

where the first term is defined in equation 2.2 and the second term is the Zeeman interaction, for a given external magnetic field **B**. The g-factor is best described by a 3x3 tensor that includes anisotropic effects in the three-dimensional space. H_{CF} in equation 2.3 is the crystal field that interacts with the adatom's orbital momentum and originates from the surrounding charges positioned at a distance $|\mathbf{R}_j - \mathbf{r}|$. The electrostatic potential experienced by the adatom is [30]:

$$V_{\text{CF}}(\mathbf{r}) = \sum_j = \frac{q_j}{|\mathbf{R}_j - \mathbf{r}|} \tag{2.4}$$

After expanding equation 2.4 into spherical harmonics, using the Laplace expansion [31], Stevens' operators $\mathbf{O}_n^m$ can be introduced as:

$$H_{\text{CF}} = \sum_n \sum_m B_n^m \mathbf{O}_n^m \tag{2.5}$$

where $|m| < n$. The Stevens operators are hermitian and reflect the crystal symmetry. This fact significantly reduces the number of non-zero terms in equation 2.5 [32–34]:

- n is positive and has an upper limit set by $n \leq 2l$, where l is the single-electron orbital momentum of the incomplete shell.
  - $n \leq 4$ for 3d transition metals.
  - $n \leq 6$ for rare-earths.
- For a single atom on a surface with crystal symmetry $C_{\chi v}$, the allowed Stevens' operators in the expansion are $\mathbf{O}_{2p}^{(-1)^{m\chi} m\chi}$ with $m, p \in \mathbb{N}$.

Stevens' operators can be written in the orbital momentum basis as shown in table 2.1. The contributions $\mathbf{O}_n^m|_{|m|=n}$ are expressed as a linear combination of the m-th power of ladder operators $\hat{L}_\pm$, defined as:

$$\begin{cases} \hat{L}_\pm = \hat{L}_x \pm i\hat{L}_y \\ \hat{L}_\pm |l, m_l\rangle = \hbar\sqrt{l(l+1) - m(m\pm 1)}\,|l, m\pm 1\rangle \end{cases} \tag{2.6}$$

The spin-Hamiltonian presented in equation 2.3 is generally complex to handle since it requires the knowledge of all quantum numbers, modified by the ligand-field and the external magnetic field.

A good approximation is to use an effective spin-Hamiltonian, where the individual contributions of orbital and spin moments are replaced by an effective spin J^* that possesses the crystal and spin symmetry properties. In this case, one obtains:

$$H_{\text{eff}} = H_{\text{CF}}(J^*) + H_{\text{Z}}(g^{\text{eff}}, J^*) \tag{2.7}$$

where g^{eff} is the effective g-factor that typically differs from the free electron case $g \approx 2$. Depending on the CF symmetry, Stevens' prefactors B_n^m can be expressed as a linear combination of parameters D_n and E_n, defined respectively as the axial and transverse anisotropy terms. Examples are shown in section 2.2.2.

n	**m**	$\mathbf{O_n^m}$
2	0	$3L_z^2 - l\mathbb{1}$
	±1	$\pm\frac{1}{2}\left[L_z, L_+ \pm L_-\right]_+$
	±2	$\pm\frac{1}{2}(L_+^2 \pm L_-^2)$
4	0	$35L_z^4 - \left(30l-25\right)L_z^2 + \left(3l^2 - 6l\mathbb{1}\right)$
	±1	$\pm\frac{1}{2}\left[7L_z^3 - (3l+1)L_z, L_+ \pm L_-\right]_+$
	±2	$\pm\frac{1}{2}\left[7L_z^2 - (l+5)\mathbb{1}, L_+^2 \pm L_-^2\right]_+$
	±3	$\pm\frac{1}{2}\left[L_z, L_+^3 \pm J_-^3\right]_+$
	±4	$\pm\frac{1}{2}(L_+^4 \pm L_-^4)$

Table 2.1: List of the first Stevens' operators with even n, written in terms of orbital operators ($\hat{L}_z$, $\hat{L}_+$, $\hat{L}_-$). $[\hat{A}, \hat{B}]_+$ indicates the symmetric product $(\hat{A}\hat{B} + \hat{B}\hat{A})/2$ and $l = L(L+1)$ [35].

When L is sufficiently quenched by the CF and when S takes the symmetry of the crystal via the spin-orbit coupling, Stevens' operators can be written in the S-basis similarly to the definition provided in table 2.1. In this case, S becomes a good quantum number for determining the magnetic states and thus $J^* \sim S$ [36]. Smaller contributions from L can still be incorporated in a modified g-factor g^{eff} [37]. This effective Hamiltonian is particularly accurate for describing Fe on MgO [38]. Another approximation $J^* \sim J$ is used for rare-earth adatoms, where an atomic value of L is preserved for the 4f shell and the spin-orbit interaction is dominant over the CF that acts as a perturbation on the $|J, m_J\rangle$ basis.

2.2.2 Crystal-Field and Magnetic Stability

In this section, we show how the interaction with the substrate can lead to a stable magnetic ground state for a given adatom. The quantum number J^* is used in the spin-Hamiltonian, written as a function of D and E instead of the complete Steven's operators. Figure 2.4 shows how the CF distributes the magnetic states of an atom on adsorption sites with different crystal field symmetries $C_{\chi\nu}$ with respect to the rotation around the out-of-plane direction.

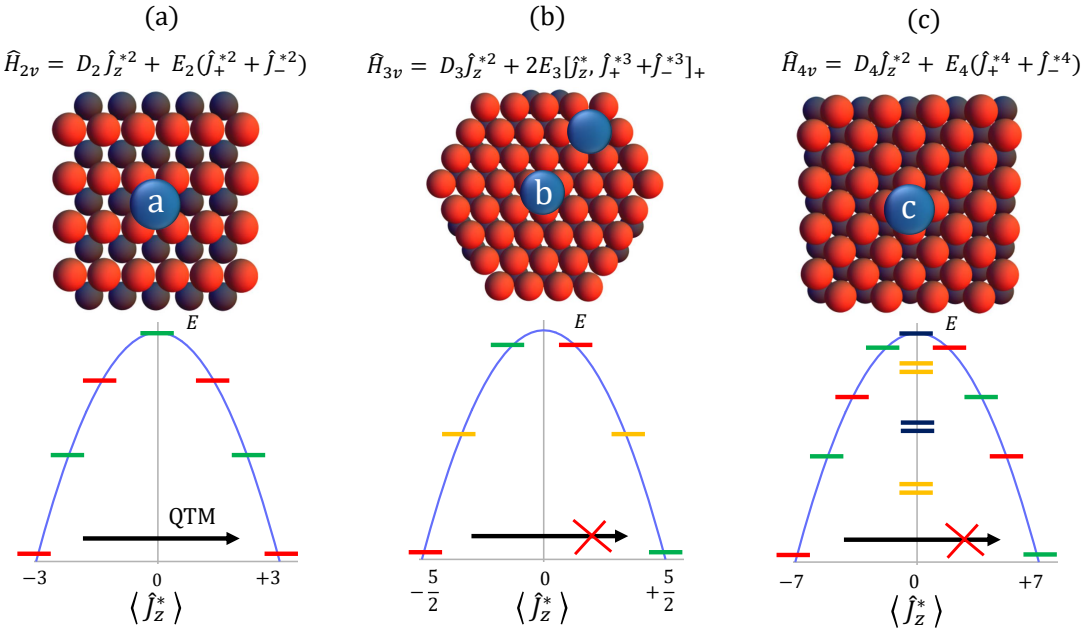

Figure 2.4: Spin-Hamiltonian, adsorption-site geometries and corresponding energy level schemes of adatoms with different effective spin configurations and environments: (a) C_{2v}, $J^* = 3$, (b) C_{3v}, $J^* = 5/2$, (c) C_{4v}, $J^* = 7$. The figure is adapted from [33, 39].

The three cases in figure 2.4 all show an out-of-plane MAE induced by the CF. This suggests a negative uni-axial anisotropy term $D_{\chi v}$ in the Hamiltonians. As shown in figure 2.3, the MAE barrier height is $-|D_{\chi v}|J^{*^2}$ for integer spins and $-|D_{\chi v}|(J^{*^2} - \frac{1}{4})$ for half-integer spins [40, 41]. States drawn with the same color belong to the same eigenstate of $H_{\chi v}$ and are mixed by the ladder operators, with a strength $E_{\chi v}$. This transverse anisotropic term enables spin reversal paths at reduced energies compared to the MAE and compromises the magnetic ground state stability. When a spin travels through the MAE barrier via mixed states, Quantum Tunneling of the Magnetization (QTM) occurs and leads to a reversal of the magnetic moment. This mechanism typically shortens the lifetime of the initial magnetic state and is present for integer spins, that can form split doublet states at $J_z^* = 0$, as illustrated in figure 2.4(c). Half-integer spins however, as shown in figure 2.4(b), are protected against direct QTM following Kramer's theorem[42]. The best way to build a long-lived magnetic ground state is therefore to provide a large MAE, with large negative D and small transverse anisotropy E. Moreover, high coordination environments are preferred since they space the mixed levels further apart, preventing direct QTM between degenerate ground states at zero magnetic field. Other spin reversal mechanisms have to be considered and are illustrated in figure 2.5.

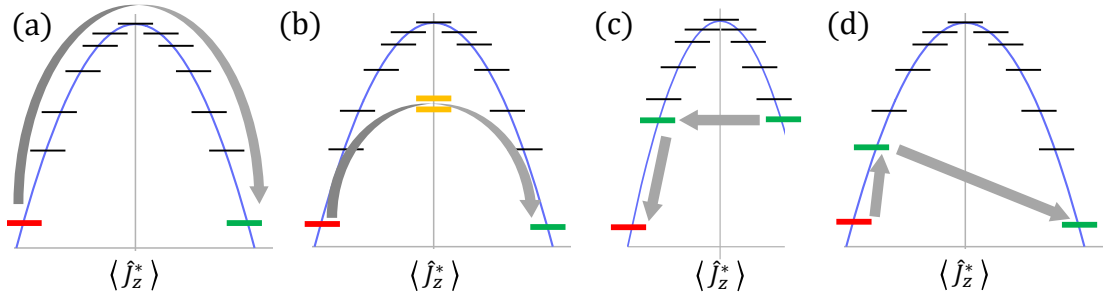

Figure 2.5: Reversal path mechanisms of the adatom's magnetic moment [33].

Figure 2.5 (a) shows the reversal of the magnetic moment with an energy equal or larger than the MAE. This can be induced by an inelastically scattered electron, phonon or both. As indicated in figure 2.5(b), shortcut tunneling can occur for integer spins traveling to opposite magnetization via the $J_z^* = 0$ states. This reversal mechanism is generated by the symmetric or anti-symmetric mixing of two states induced by the crystal-field. As shown in figure 2.5(c), an external magnetic field lifts the degeneracy of the two magnetic ground states and leads to a resonant magnetization tunneling when mixed states are energetically aligned [43]. The arrows in figure 2.5(d) indicate transitions for a change in the adatom's effective spin $\Delta m_{J^*} = \pm 1$ induced by inelastic scattering events. In this case, when the system is excited, the spin can tunnel and relax to the other side of the barrier via mixed states. In an STM experiment, the magnetic moment stability in the ground state can be weakened by scattering events from the tip and substrate electrons. To reduce the scattering probability with the tip electrons, the tunneling current can be lowered. Additionally, adatoms can be protected from substrate electrons by placing them on insulating layers grown on top of a conductive crystal. In this thesis, thin insulating films of MgO are grown on a Ag(100) single crystal for this purpose. This choice is strongly motivated by the existing successful studies with ESR-STM [14–16, 44–48] and with probing the magnetic ground state lifetime of adatoms [44, 49, 50]. With a simple cubic structure [51], MgO is attractive due to its high stiffness, translating into a low phonon density in the low energy regime [52], minimizing direct, Orbach and Raman scattering processes [53–55]. In conclusion, the combination of CF and spin-orbit interactions define how the magnetic energy levels are arranged along an easy axis as well as how they mix. The intrinsic magnetic ground state lifetime depends on the scattering cross-sections with substrate electrons and phonons. When addressing these systems with STM, an additional scattering contribution from the tip electrons reduces this lifetime.

2.2.3 3d Transition Metal Adatoms

For 3d elements adsorbed on a crystalline surface, the Hamiltonian is, in order of decreasing contribution:

$$H = H_{\text{e-e}} + H_{\text{CF}} + H_{\text{SO}} + H_{\text{Z}} \tag{2.8}$$

The terms $H_{\text{e-e}}$ and H_{SO} in equation 2.8 are introduced in equation 2.2 as H_{CF} and H_{Z} are

defined in equation 2.3. The unpaired electrons are located in the outermost 3d shell, leading to a larger interaction with the field created by surrounding charges compared to intra-atomic spin-orbit perturbation. If the orbital moment is low and sufficiently quenched, S is a good quantum number for describing the energy level scheme of the adatom [56]. This is the case for Mn atoms adsorbed on top-Oxygen sites MgO that have $L = 0$ in the $3d^5$ configuration according to Hund's rules. Despite the crystal field adding small L contributions, the quantum numbers from the atomic case are almost preserved with $S_z \approx \frac{5}{2}$. In this case, the approximation $J^* \sim S$ is accurate and the spin-Hamiltonian can be written in terms of $\mathbf{S}$. However, the quenching of L is far from being a generality as Co and Fe on top-Oxygen sites MgO have non-negligible orbital moments. This is particularly true for Co that has an almost fully preserved L_z [57]. Figure 2.6 shows the projected expectation values of L_z and S_z in unit of $\hbar$ in a magnetic field for Mn, Co and Fe on MgO [58].

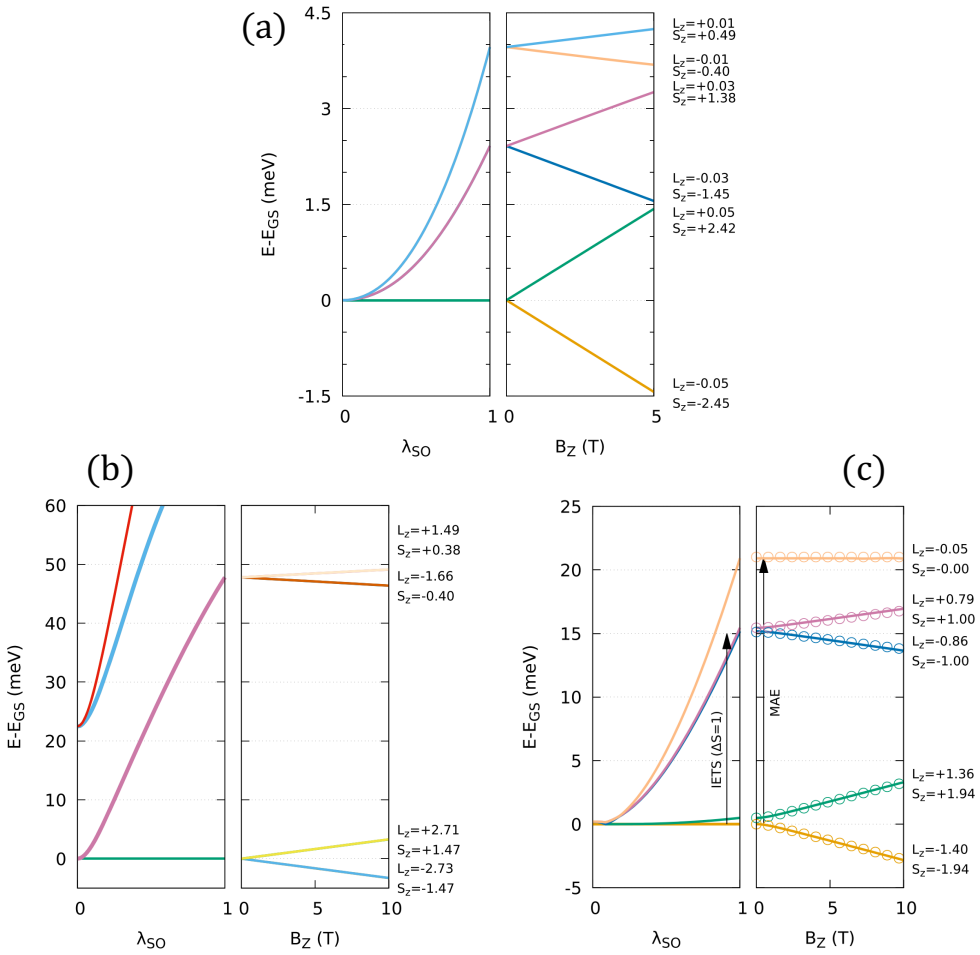

Figure 2.6: Low-energy spectra of Mn (a), Co (b) and Fe (c) adsorbed on MgO with energies given relative to the ground state [58]. The different colors indicate the distinct magnetic states of each system, defined by the quantum numbers L_z and S_z.

In figure 2.6, the solid lines are obtained by multiplet calculations combined with plane-

wave Density Functional Theory (DFT). The circles in figure 2.6 (c) correspond to the fitting to a spin Hamiltonian. The conservation of the atomic-like orbital momentum of Co, shown in figure 2.6, can be explained by an almost uni-axial CF C_∞ and a strong spin-orbit coupling $\Delta E = \lambda L\,\Delta S > 50$ meV. For Fe, the CF with symmetry C_{4v} completely quenches the orbital momentum which is then partially restored by the spin-orbit interaction on the order of 20 meV [38, 58].

2.2.4 Rare-earth Ions

Rare-earth or lanthanide atoms have an electronic ground state of the form [Xe]$4f^n5d^m6s^2$, with $n = 0$ for Lanthanum and $n = 14$ for Lutetium. For these two elements and for Cesium $m = 1$, otherwise $m = 0$. They are described on a surface with the following Hamiltonian, in order of decreasing contribution:

$$H = H_{\text{e-e}} + H_{\text{SO}} + H_{\text{CF}} + H_{\text{Z}} \tag{2.9}$$

Compared to 3d elements, the terms H_{CF} and H_{SO} in equation 2.9 are switched with $H_{\text{SO}} > H_{\text{CF}}$. The fact that the 4f electrons lie closer to the nucleus with a small spatial extension of their wavefunctions explains the lower contribution of H_{CF} with respect to H_{SO} for rare-earths compared to 3d adatoms [59]. The typically-large spin-orbit interaction mixes L and S quantum numbers so the CF can be treated as a perturbation that lifts the $(2J+1)$-fold degeneracy of the ground state. In this case, the effective spin J^* is approximated by J.

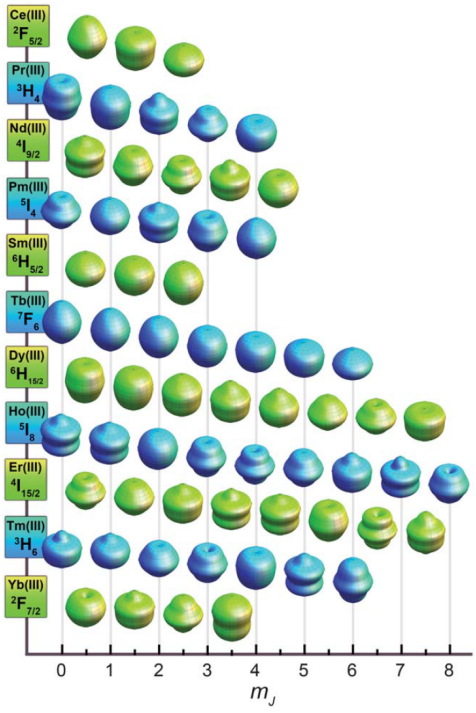

Figure 2.7: Approximations of the angular dependence of the 4f spatial charge density distribution as a function of m_J [60].

Figure 2.7 shows the different 4f spatial charge density distributions for rare-earths in the trivalent configuration $6s^2 5d^1 4f^{n-1}$, with the lowest spin-orbit state. The substrate-dependency on the adatom's charge density and the MAE is highlighted in figure 2.8 where the spin ground state orientation is shown for an Erbium (Er) atom deposited on Platinum Pt(111) and on Copper Cu(111). The CF determines the magnetic ground state m_J [61].

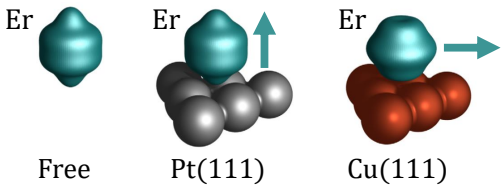

Figure 2.8: 4f charge density of an Erbium atom with $J = 15/2$ in the free case (left) and to the ground state on Pt(111) (middle) and on Cu(111) (right). The arrows indicate the ground state magnetization orientation on each substrate. The figure is adapted from reference [62].

2.3 Scanning Tunneling Microscopy (STM)

The magnetism of single adsorbed atoms deposited on thin insulating films can be investigated with STM and SP-STM. In this section, the working principle of STM is presented, followed by a theoretical description of electron tunneling, including the SP case. Similarly, STS and SP-STS are introduced with a focus on inelastic scattering that can generate magnetic transitions. A part is dedicated to the description of magnetic lifetime measurements, introducing the rate equations. Finally, the theoretical and technical aspects of ESR-STM are discussed.

2.3.1 Operational Principle

The working principle of an STM is presented in figure 2.9.

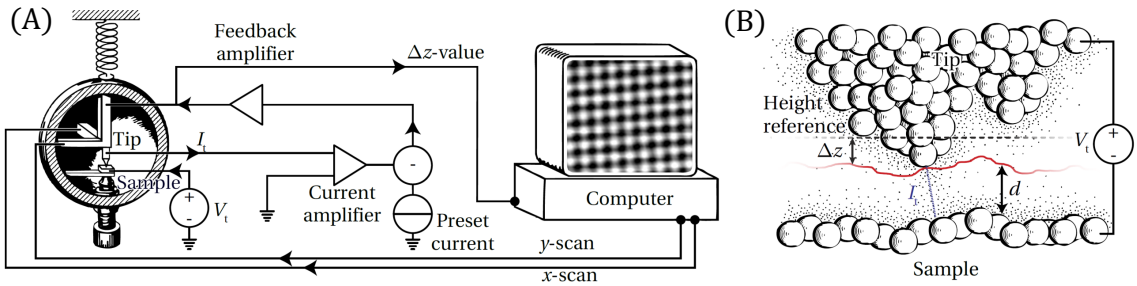

Figure 2.9: (a) Working principle of an STM where the microscope is placed in a Ultra-High Vacuum (UHV) chamber [63]. (b) Close up of a realistic tip-sample tunneling junction where a positive bias is applied on the tip [64].

The plane $\hat{x}\hat{y}$ is conventionally defined parallel to the sample surface and $\hat{z}$ is set along the tip-sample axis. Positive $\hat{z}$ signifies going away from the sample surface. Piezoelectric

transducers along $\hat{x}$, $\hat{y}$ and $\hat{z}$ allow the tip to move laterally and vertically in close vicinity to the conductive sample. During normal operation, a tunneling voltage V_t is applied and a tunneling current I_t is recorded. Typically, V_t is chosen between a few millivolts up to a few volts with I_t ranging from pA to nA. The latter is measured using a suitable current-to-voltage I/V amplifier. Samples can be scanned using the two following methods: (1) constant height mode where the tip is kept at an absolute tip-sample height z and the variation of the tunnel current is recorded; (2) constant current mode where an electronic feedback loop adjusts z in order to keep a constant I_t during the scan. In this thesis, only constant I_t STM images are shown as Δz maps in the sample plane $\hat{x}\hat{y}$.

2.3.2 Electron Tunneling

Although vacuum tunneling was predicted by theory in the 1930s [4, 65], the first experimental evidence of tunneling from an atomically sharp tip to a flat surface was realized by Young *et. al.* [66]. They showed a transition from field emission to tunneling regime using the topographiner, considered as the predecessor of STM [66, 67]. It was shortly after that Binnig and Rohrer published their first experimental results using their STM and showing tunneling current traces as a function of tip-sample distance [68].

A theoretical description of electron tunneling is provided here to understand the working principle of an STM. We start with a one-dimensional case where the time-independent Schrödinger equation of a single electron subject to a potential $U(z)$ is:

$$-\frac{\hbar^2}{2m}\nabla^2\Psi(z) + U(z)\Psi(z) = E\Psi(z) \tag{2.10}$$

where Ψ is the electron wave function, m its mass and E its energy approximated by the Fermi energy E_F. In a metal, the potential can be set to zero and the wave function Ψ_{free} is a plane-wave, giving the solution of equation 2.10 with momentum k:

$$\Psi_{\text{free}}(z) \;=\; Ae^{ikz} \text{ with } k \;=\; \sqrt{\frac{2m_eE_F}{\hbar^2}} \tag{2.11}$$

A is a normalization constant such that $|\Psi_{free}(z)|^2 = 1$. Adding the standing-wave travelling in opposite direction $A'e^{-ikx}$ is also possible and does not change the general solution. At a metal-vacuum interface, the particle at the Fermi level does not vanish outside the metal but rather follows an exponential decay [69]:

$$\Psi_{\text{vac}}(z) \;=\; Be^{-\kappa z} \text{ with } \kappa \approx \sqrt{\frac{2m}{\hbar^2}\cdot\Phi} \tag{2.12}$$

where B is a normalization constant satisfying the boundary conditions with equation 2.11 and Φ is the metal work function. Figure 2.10 sketches the behavior of $\mathfrak{Re}[\Psi(z)]$ in a metal-vacuum junction.

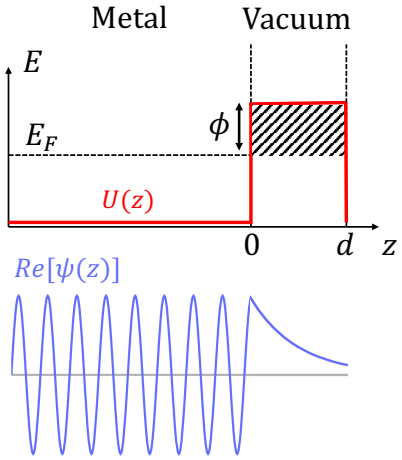

Figure 2.10: Potential scheme for a metal-vacuum junction (top). The shaded area corresponds to the classical forbidden region. The bottom graph shows the real part of the wave function traveling along positive $\hat{z}$. The figure is inspired from reference [70].

Since the wave function does not vanish across the vacuum barrier, a transmission coefficient can be estimated from the probability of the electron to be at $z = d$ with respect to $z = 0$ [70]:

$$T = \frac{|\Psi(d)|^2}{|\Psi(0)|^2} \approx e^{-2\kappa d} \tag{2.13}$$

Equation 2.13 reveals an exponentially decaying transmission with respect to the vacuum gap width. The factor of 2 in equation 2.13 accounts for two electrodes separated by a vacuum gap as in STM, where the two conductive regions are the STM tip and the sample. Applying a tunneling voltage V_t modifies the rectangular potential $U(z)$ of figure 2.10. In that case, the Fermi level of the tip shifts by $|e|V_t$ with respect to the one of the sample, as shown in figure 2.11.

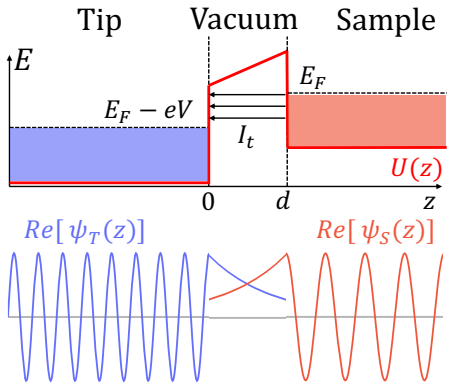

Figure 2.11: A positive bias applied to the STM tip has the effect of lowering its Fermi level with respect to the one of the sample by eV_t. Electrons tunnel between the two metals, close to the Fermi level, inducing a net tunneling current I_t in a direction set by the bias polarity.

Both metal wave functions are shown, with a spatial overlap in the tunneling gap leading to a tunneling current I_t. This one-dimensional model allows to understand the basic principle of STM but a three-dimensional geometry is required for a more accurate description.

2.3.3 Tersoff-Hamann (TH) Model

In 1983, Tersoff and Hamann provided a three-dimensional model describing electron tunneling in STM based on Bardeen's transfer Hamiltonian [71–73]. Initially, the Tersoff-Hamann (TH) model treats the tip and the sample as two separate sets of wave functions Ψ_T and Ψ_S subject to potentials U_T and U_S and evolving according to the time-dependent Schrödinger equation. The main idea lies in using perturbation theory as the two metals are brought closer to each other in an adiabatic process. Once the distance between the tip and the sample is reduced, the system can be described by the Schrödinger equation including both potentials U_T and U_S. The corresponding wave function of the complete system $\Psi(t)$ can be written as a linear combination of tip and sample wavefunctions:

$$\Psi(t) = \sum_{\mu} \Psi_{(S,\mu)}(t) + \sum_{\nu} c_\nu(t)\Psi_{(T,\nu)}(t) \tag{2.14}$$

where μ and ν describe the different states available in the sample and tip respectively. We consider, here, the case of a positive tip bias applied such that the system at $t = 0$ is initially described by the sum of sample wavefunctions with a time-dependent coefficient $c_\nu(t = 0) = 0$. From equation 2.14, we introduce the electron tunneling probability $P_{\mu\to\nu}$, defined as the probability of sample's state $\Psi_{S,\nu}$ evolving into a tip's state $\Psi_{T,\nu}$. A transition matrix $M_{\mu\nu}$ characterizes sample-tip electron transitions $\mu \to \nu$ [74]:

$$P_{\mu\to\nu} = |c_\nu(t)|^2 \propto |M_{\mu\nu}|^2 \tag{2.15}$$

The tunneling current is expressed as the time-varying probability $P_{\mu\to\nu}(t)$, incorporating the state occupancy at the Fermi level and a positive bias V_t applied to the sample [65]:

$$\begin{aligned} I_t(V_t, T) = &\frac{2\pi}{\hbar}\int_{-\infty}^{+\infty} |M|^2 \Big[f(E_F - eV_t + \epsilon) - f(E_F + \epsilon) \Big] \\ &\cdot 2e \cdot \rho_S(E_F - eV_t + \epsilon)\rho_T(E_F + \epsilon)\, d\epsilon \end{aligned} \tag{2.16}$$

The term $2e\cdot\rho_S(E_F - eV_t + \epsilon)$ corresponds to the number of available electrons (the factor of 2 arises from the spin) while the Fermi-Dirac distributions $f(E_F - eV_t + \epsilon) - f(E_F + \epsilon)$ describe the state occupations of both electrodes as a function of temperature and determine thereby which electrons can tunnel. At low temperatures and low voltages, the Fermi-Dirac distribution is sufficiently steep to evaluate the integral of equation 2.16 from 0 to eV_t. The tunneling current becomes then:

$$I_t = \frac{4\pi e}{\hbar}\int_0^{eV_t} \rho_S(E_F - eV_t + \epsilon)\rho_T(E_F + \epsilon)|M|^2 d\epsilon \tag{2.17}$$

The main assumption of the TH model is to treat the tip as a spherical *s*-orbital, leading to a flat Local Density of States (LDOS) at the center of the tip apex. This assumption gives the following expression for the tunneling current [64, 65]:

$$I_t \propto V\rho_S(E_F - eV_t)e^{-2dk} \tag{2.18}$$

where k is the electron momentum and d is the tip-sample distance. The exponential in equation 2.18 arises from the transition matrix $|M|$ in equation 2.17. This term is computed using Fermi's golden rule with the tip's and sample's wavefunctions that possess an exponential dependence in the tip-sample distance d (cf. equation 2.12). As k is typically on the order of 1 Å for a metal work function of 4 eV, an increase of d by 1 Å leads to a decay of the tunneling current by almost one order of magnitude [63]. Therefore, the atom positioned at the tip apex contributes mostly to the tunneling current measured.

As a conclusion, the TH model highlights the ability to access the sample's LDOS with the tunneling current in STM. STM images are therefore a convolution of the sample's surface topography with the sample LDOS and the tip geometry. Under some conditions, STM can also carry SP information about the sample and is known as SP-STM.

2.3.4 Spin-Polarized Scanning Tunneling Microscopy (SP-STM)

SP-STM is based on using a tip with a net magnetic moment, caused by the imbalance of spin "up" $\sigma = -\frac{1}{2}$ and spin "down" $\sigma = +\frac{1}{2}$ electron populations. The minority and majority states are split by the exchange interaction between electrons [75]. If the tip is positioned over a magnetic surface, the tunneling current is influenced by the Tunneling Magnetoresistance (TMR) effect, that depends on the relative orientation of the tip's and surface's magnetic moments. The tunneling processes of spin "up" and spin "down" electrons have to be considered independently [76]. In figure 2.12, the working principle of SP-STM is illustrated for an SP tip placed above a magnetic adatom adsorbed on a thin insulating film grown on the conductive sample. At low tunneling voltages, elastic tunneling of electrons contributes dominantly to the tunneling current, as we assume the absence of spin-flip scattering during the tunneling process. Under this assumption, high (low) tunneling conductance corresponds to a(n) (anti-)parallel orientation of the magnetic moments [77, 78].

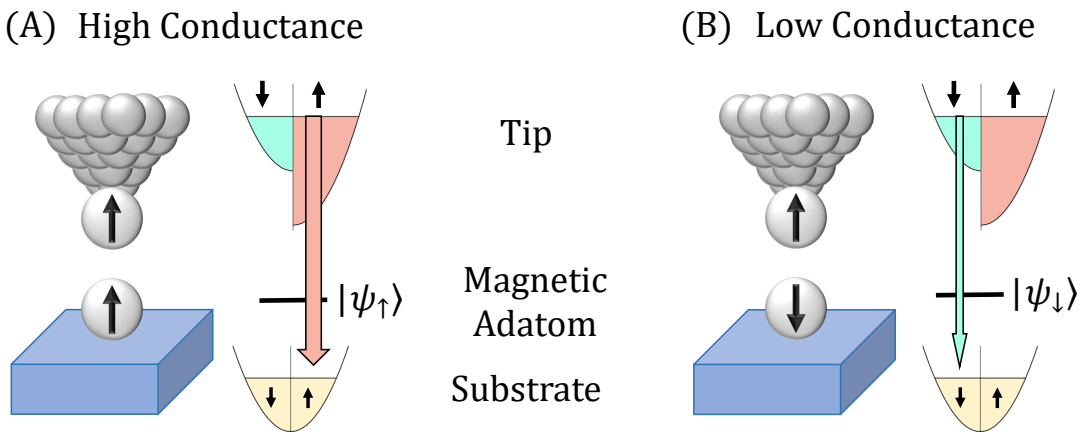

Figure 2.12: Working principle of SP-STM, in the context of single atom magnetism at low temperature. The tip is placed at the same height z with respect to the adatom in panels (A) and (B) and a constant negative tip bias is applied. The tunneling conductance depends on the relative orientation of the adatom's and tip's magnetic moments. We consider only elastic tunneling processes, and $|\Psi_\uparrow\rangle$ and $|\Psi_\downarrow\rangle$ denote the adatom magnetic states. A simplified band model shows the density of states of both electrodes close to the Fermi level.

Experimentally, an SP tip can be constructed from a bulk ferromagnetic or antiferromagnetic material, or by coating a non-magnetic tip with layers of magnetic material. In this thesis, we use another method consisting of picking up magnetic Fe atoms on the sample surface to spin-polarize an initially non-magnetic bulk tip.

2.3.5 Scanning Tunneling Spectroscopy (STS)

By taking equation 2.17 and using Leibniz's rule for calculating the derivative of I_t, one obtains:

$$\frac{dI_t}{dV}(V_t, x, y, z) \propto \rho_S(x, y, eV_t) \tag{2.19}$$

assuming a constant probability $|M|^2$ and a constant tip LDOS. STM has therefore the capability to measure the sample LDOS, which is only available via a tunnel junction. For these ideal assumptions, the tunneling conductance is directly proportional to the sample LDOS. The term spectroscopy used in this thesis refers to dI/dV measurements as a function of the tunneling bias and not to other types of spectroscopy like dz/dV. The typical operation of a spectroscopy experiment starts by positioning the tip over a specific point of interest on the sample's surface (adatom, thin insulating film, metal substrate) at given tunneling parameters (I_t, V_t). The feedback loop is then switched off to keep a constant tip-sample distance while the bias is swept over a given interval. The way dI/dV traces are recorded is not by a simple numerical derivative of $I(V)$ spectra since this would lead to a high level of noise [79]. Instead, a lock-in amplifier is used to measure the first derivative of I_t with respect to V_t.

Spin Excitation Spectroscopy (SES)

The tunneling of electrons from one electrode to another can occur elastically or inelastically depending on their energy and on the investigated system. Inelastic Electron Tunneling Spectroscopy (IETS) has been employed to study systems with vibrational, rotational or magnetic quantized levels [80–83]. In the context of single atom magnetism, we focus on Spin Excitation Spectroscopy (SES), which is a type of STS and IETS. Figure 2.13 illustrates the working principle of SES for an adatom, initially in the magnetic ground state $|\Psi_i\rangle$. In figure 2.13(A), a negative bias is applied to the tip. If the electron energy stays below $e|V_{\text{exc}}|$, tunneling through the barrier occurs elastically, without disturbing the magnetic moment of the atom. When $|V_t| \geq |V_{\text{exc}}|$, an additional conductance path opens for electrons that exchange energy and spin angular momentum with the adatom. In this case, the tunneling process is described by $\Delta\sigma = +1$ which imposes $\Delta m_{J^*} = -1$ on the magnetic adatom, excited in the state $|\Psi_f\rangle$. Figure 2.13(B) shows the corresponding dI/dV spectrum of the system where the tunneling bias is swept symmetrically around 0 V and beyond $|V_{\text{exc}}|$. Elastic tunneling contributes to the signal as a voltage-independent conductance (grey area E). The opening of a new inelastic conductance channel leads to a step-like increase of the signal at $|V_t| \geq |V_{\text{exc}}|$ (red areas I_- and I_+). For paramagnetic tip and substrate, the steps are symmetric around 0, leading to equal areas I_- and I_+.

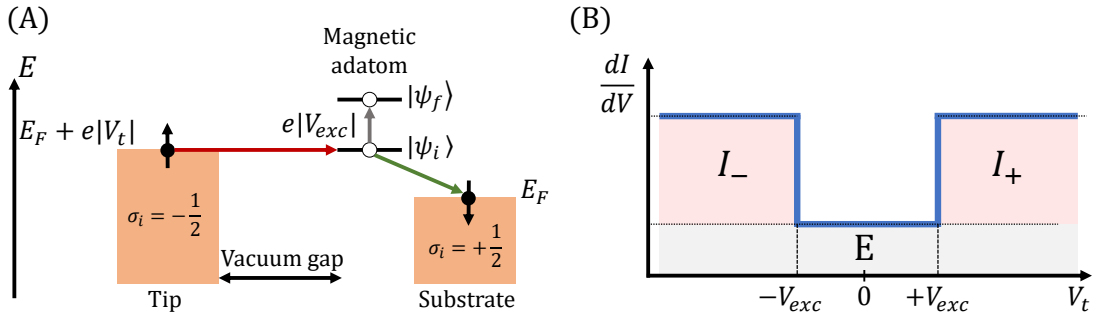

Figure 2.13: Working principle of SES. (a) Mechanism of inelastic tunneling via a magnetic atom sitting on the sample surface. The electron from the tip interacts with the adatom, changing its state from $|\Psi_i\rangle$ to $|\Psi_f\rangle$ [13]. (b) Idealized dI/dV measurement on the adatom with $|eV_{\text{exc}}|$ matching the energy difference between the states $|\Psi_i\rangle$ and $|\Psi_f\rangle$.

Figure 2.14 summarizes the different tunneling processes that can occur inelastically and elastically, with a magnetic adatom adsorbed on the sample surface at low temperature. The panels are drawn similarly to the one in figure 2.13 (A), with the vertical axis representing the energy carried by tunneling electrons and the adatom. Red and green arrows symbolize tunneling electrons with spin "up" ($\sigma = -\frac{1}{2}$) and "down" ($\sigma = +\frac{1}{2}$) respectively.

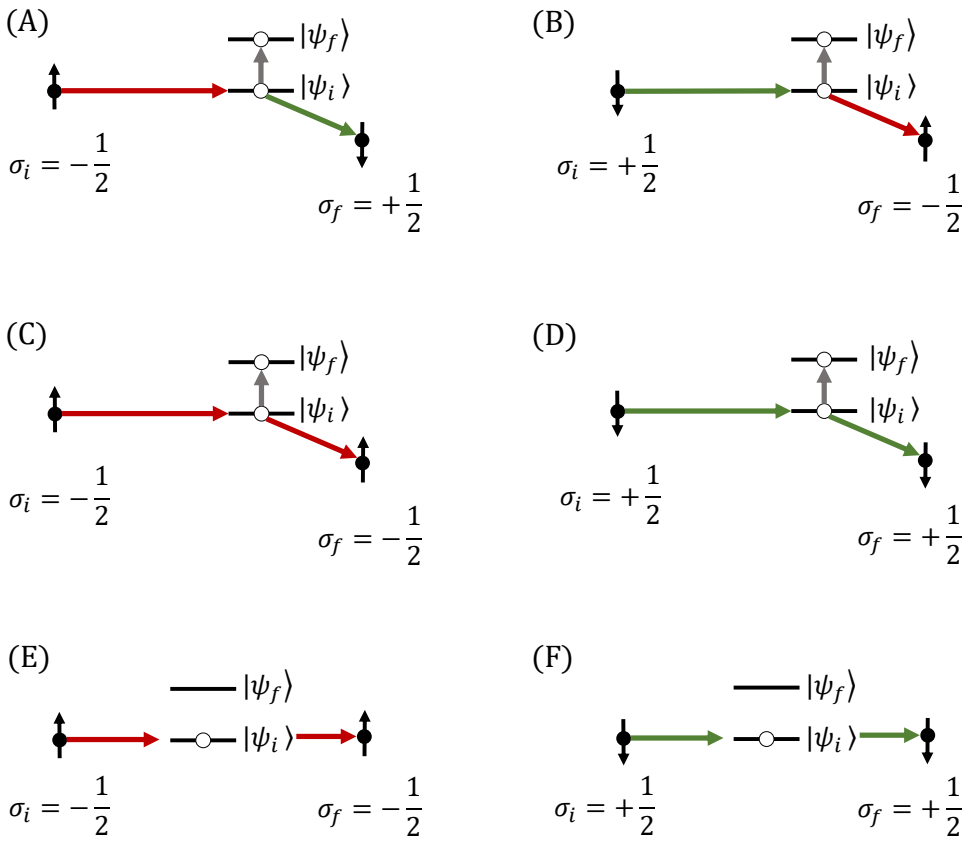

Figure 2.14: Inelastic and elastic electron tunneling processes, occurring when the tip is placed over a magnetic atom adsorbed on the sample surface. Panels (A) to (D) represent the inelastic processes, as (E) and (F) correspond to the elastic case where electrons do not exchange energy and spin with the adatom. The figure is inspired from reference [13].

For the inelastic processes, shown from panels (A) to (D), the electron has enough energy to induce transitions from $|\Psi_i\rangle$ to $|\Psi_f\rangle$ to the adatom. The elastic tunneling processes are shown in panels (E) and (F), where the adatom stays in the state $|\Psi_i\rangle$. In figure 2.14 (A) and (B), tunneling electrons exchange energy and spin with the adatom, imposing a change in the adatom's total angular momentum $\Delta m_{J^*} = \pm 1$ when transiting from $|\Psi_i\rangle$ to $|\Psi_f\rangle$. Panels (C) and (D) correspond to tunneling electrons transferring energy but not spin with the adatom. This imposes $\Delta m_{J^*} = 0$. Magnetic systems subject to transverse anisotropy can undergo such transitions, where the higher energy state $|\Psi_f\rangle$ is mixed with the initial one $|\Psi_i\rangle$. For panels (E) and (F), neither energy nor spin are exchanged and the adatom's magnetic state remains in $|\Psi_i\rangle$. In this case, we also have $\Delta m_{J^*} = 0$.

After the first spin-flip experiment on Mn adatoms on Aluminum Oxide Al_2O_3 [83], other 3d elements were studied, especially on Cu_2N [84–86] and later on MgO [38, 57]. Rare-earth adatoms were also addressed with STS and can reveal intra-atomic spin-excitation features, where the alignment of the 4f spin with respect to the valence spin is inverted [87, 88]. This enables the measurement of the intra-atomic exchange between 6s5d and 4f electrons [87].

Spin-Polarized Spin Excitation Spectroscopy (SP-SES)

Figure 2.15 shows the working principle of SP-SES in an idealized dI/dV spectrum measured on a magnetic adatom. We assume that the tip's and adatom's magnetic moments are aligned for $|V_t| < |V_{\text{exc}}|$. The elastic tunneling contributes in the signal as E_- and E_+ for negative and positive biases, respectively. As seen in section 2.3.4, the use of an SP tip discriminates tunneling probabilities of electrons with spin "up" and spin "down". As a consequence, an asymmetry in the dI/dV spectrum around $V_t = 0$ is observed as long as $\mathbf{m}_{\text{tip}} \cdot \mathbf{m}_{\text{adatom}} \neq 0$. Figure 2.15 introduces the dI/dV spectrum of a magnetic adatom, where a transition $\Delta m_{J^*} = -1$ occurs from the energy $e|V_{\text{exc}}|$. Given that the tunneling bias is applied to the tip, inelastic tunneling dominates at negative V_t with a signal I_- larger than I_+. Below the spectrum in figure 2.15, simplified band models are illustrated for negative (left) and positive (right) tip biases.

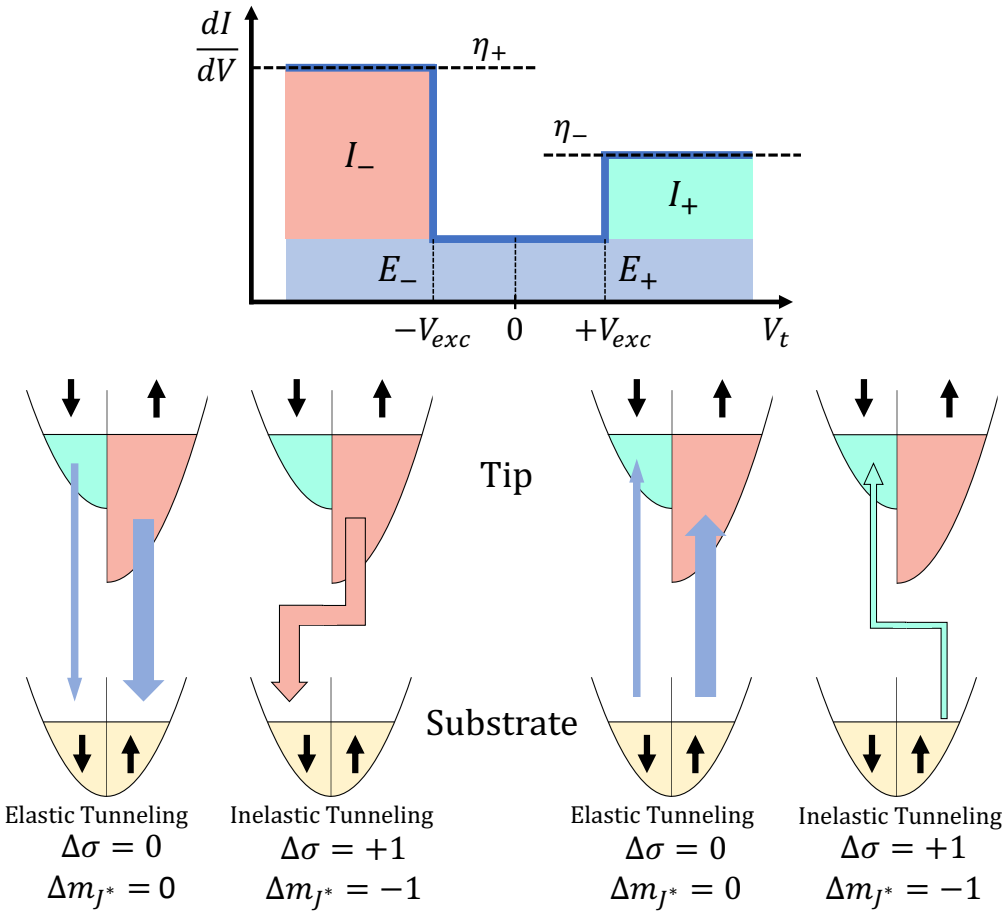

Figure 2.15: Working principle of SP-SES and idealized dI/dV spectrum. Spin-polarized tunneling processes are shown for a tip placed on a magnetic adatom adsorbed on the sample surface. A tunneling bias is applied to the tip and we consider only one possible magnetic transition for the adatom, such that $\Delta m_{J^*} = -1$ at $V_t = e|V_{\text{exc}}|$. The arrows indicate the tunneling path with thicknesses related to the strength of the process [13].

The spin-polarization of the inelastic tunnel conductance is obtained by estimating the height difference of the conductance steps at positive and negative voltages [13]:

$$P = \frac{\eta_+ - \eta_-}{\eta_+ + \eta_-} \propto \eta_S \tag{2.20}$$

where η_S is the spin polarization of the tip. In equation 2.20, η_+ and η_- are the conductance steps at negative and positive tip bias respectively, as shown in figure 2.15. From this description, quantifying the influence of tunneling electrons on the adatom's magnetic state is a fundamental step for determining and optimizing its magnetic stability with STM.

2.3.6 Magnetic State Lifetime: the Example of a Single Fe Adatom on MgO

To understand what limits the magnetic state lifetimes of single surface adsorbed atoms, we need to quantify the contribution of the different electronic scattering events when these systems are investigated with STM. We take the example of a Fe atom adsorbed on a few MLs-thick MgO/Ag(100), as this system will be studied with the QSR technique in chapter 7. We derive the ground and first excited state lifetimes of an Fe atom on MgO, based on the electronic rate equations. This system can be described by the following spin-Hamiltonian:

$$H_{\text{eff}} = D_2 \hat{S}_z^2 + E_4(\hat{S}_-^4 + \hat{S}_+^4) + g_z^{\text{eff}} \mu_B B_z \hat{S}_z \tag{2.21}$$

where $D_2 = -4.7$ meV and $|E_4| < 2\ \mu$eV [38, 49]. These parameters suggest an out-of-plane easy axis of the magnetization with an expectation value of $< S_z > \approx 2$ in the ground state. An effective g-factor of 2.57 is calculated and is significantly above the free-electron value [38]. At $B_z = 2$ T, the ground and first excited states, $|0\rangle$ and $|1\rangle$ respectively, are written as a superposition of $|S_z = -2\rangle$ and $|S_z = +2\rangle$, given the C_{4v} adsorption site symmetry for Fe [49]:

$$\begin{cases} |0\rangle = 0.9999 \cdot \left(|S_z = -2\rangle\right) - 0.0004 \cdot \left(|S_z = -2\rangle\right) \\ |1\rangle = -0.0004 \cdot \left(|S_z = -2\rangle\right) + 0.9999 \cdot \left(|S_z = +2\rangle\right) \end{cases} \tag{2.22}$$

Figure 2.16(a) illustrates the different electronic interactions with the adatom, sitting between the conductive tip and sample Ag(100). The calculations are based on reference [49] and we consider a positive tip bias $V_{t \to s} > 0$ where t = tip and s = sample. In figure 2.16 (b), the external magnetic field splits the energy of states $|0\rangle$ and $|1\rangle$. At 2 T, the energy separation is around $E_{01} \approx 1.19$ meV. QTM is induced by inelastic scattering and leads to the reversal of the magnetization along the easy axis. As the product $|\langle 0|\hat{S}_z|1\rangle|^2$ is non-zero, tunneling electrons exchange energy but not spin with the adatom during this process ($\Delta m_S = 0$).

Based on the notations introduced in figure 2.16, equation 2.23 provides the electronic relaxation rate $r_e^{1\to0}$ and the excitation rate $r_e^{0\to1}$:

$$\begin{cases} r_e^{1\to0} = r_{t\to t}^{1\to0} + r_{t\to s}^{1\to0} + r_{s\to t}^{1\to0} + r_{s\to s}^{1\to0} \\ \\ r_e^{0\to1} = r_{t\to t}^{0\to1} + r_{t\to s}^{0\to1} + r_{s\to t}^{0\to1} + r_{s\to s}^{0\to1} \end{cases} \tag{2.23}$$

where $1\to0$ and $0\to1$ indicate transitions from $|1\rangle$ to $|0\rangle$ and from $|0\rangle$ to $|1\rangle$ respectively.

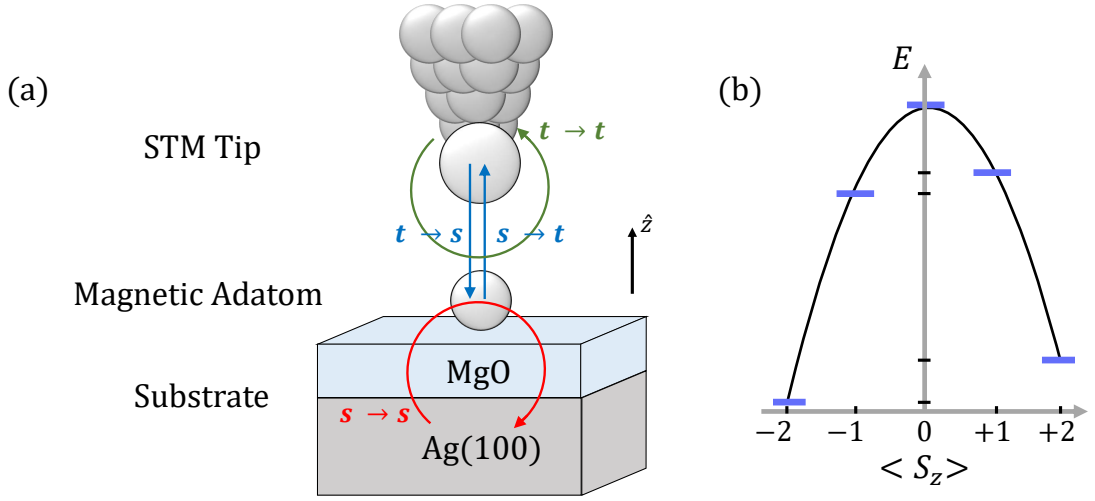

Figure 2.16: (a) Scheme of the different electronic scattering events for a magnetic Fe atom adsorbed on a few MLs-thick MgO/Ag(100) layers, and investigated with STM. $t\to s$ ($s\to t$) corresponds to the excitation or relaxation process from an electron tunneling from the tip (substrate) to the substrate (tip). $s\to s$ ($t\to t$) represents the spontaneous relaxation process from a substrate (tip) electron that return to the substrate (tip) after interacting with the adatom. (b) Qualitative energy level scheme of the Fe adatom with $J^*\sim S$ and $S_z=2$. An external magnetic field is applied along $\hat{z}$ and lifts the ground state degeneracy.

Following the calculations in reference [49], we express each transition rate from electrode m to electrode n using the Fermi-Dirac distribution $f(E)$:

$$\begin{cases} r_{m\to n}^{1\to0} = P\frac{G_{m\to n}}{|e|^2}\int_{-\infty}^{+\infty} f(E)\big[1-f(E+E_{01}-|e|V_{t\to s})\big]dE \\ \\ r_{m\to n}^{0\to1} = P\frac{G_{m\to n}}{|e|^2}\int_{-\infty}^{+\infty} f(E)\big[1-f(E-E_{01}-|e|V_{t\to s})\big]dE \end{cases} \tag{2.24}$$

where P is the inelastic scattering probability, $G_{m\to n}$ the conductance between electrodes m and n, E_{01} the energy difference between states $|0\rangle$ and $|1\rangle$, and $V_{t\to s}$ the positive tip bias applied.

For voltages $eV_{t\to s} >> k_B T$, one obtains the following approximation:

$$\begin{cases} r_e^{1\to 0} \approx \frac{P}{|e|^2}\Big(E_{01}\big(G_{s\to s}+G_{t\to t}\big)+(|e|V_{t\to s}+E_{01})G_{t\to s}\Big) \quad \text{with } G_{t\to t}=G_{t\to s}^2/G_{s\to s} \\ \\ r_e^{0\to 1} \approx \frac{P}{|e|^2}\big(|e|V_{t\to s}-E_{01}\big)G_{t\to s} \end{cases} \tag{2.25}$$

where E_{01} is the Zeeman splitting for a magnetic field B_z. Non-electronic processes r_{ne} can be added to the description leading to a total rate of $r_{\text{tot}} = r_e + r_{ne}$. The rate r_{ne} is attributed to spin-phonon coupling, defined at a given temperature, and considered independent of the MgO thickness. It is treated as a constant in reference [49] and an explicit form of r_{ne} is not discussed here. The associated magnetic lifetimes of $|0\rangle$ and $|1\rangle$ can be defined as:

$$\begin{cases} \tau_{|1\rangle} = \left(r_e^{1\to 0}+r_{ne}^{1\to 0}\right)^{-1} \approx T_1 \\ \\ \tau_{|0\rangle} = \left(r_e^{0\to 1}+r_{ne}^{0\to 1}\right)^{-1} \end{cases} \tag{2.26}$$

where T_1 is the relaxation time, defined as the time the adatom's magnetic moment relaxes from the excited state $|1\rangle$ to thermal equilibrium. At low temperature and high magnetic fields, the energy difference between $|0\rangle$ and $|1\rangle$ is large compared to $k_B T$. Under these conditions, we can approximate T_1 by the time the system takes to relax from $|1\rangle$ to $|0\rangle$, i.e. $\tau_{|1\rangle}$. In equation 2.25, the substrate-substrate conductance $G_{s\to s}$ strongly depends on the number of MLs of MgO on which the Fe atom is adsorbed. For 2 ML, $G_{s\to s} = 10^{-4}\cdot G_1$ and for 3 ML, $G_{s\to s} = 10^{-6}\cdot G_1$, where G_1 is the metallic conductance of the adatom. With these parameters, we show the relaxation time measured with pump-probe spectroscopy, with a SP tip, as a function of $G_{t\to s}$ in figure 2.17 [49].

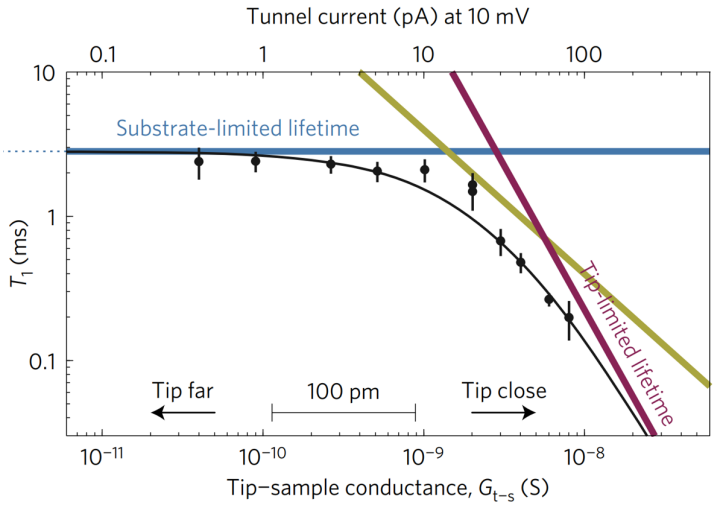

Figure 2.17: Pump-probe measurement of the relaxation time T_1 of Fe on 2 ML MgO versus tip-sample conductance at $B_z = 2$ T, $V_t = 10$ mV and $T_{\text{STM}} = 1.2$ K [49].

The solid black line in figure 2.17 fits the data using equation 2.25 with P, G_1 and r_{ne} as the fitting parameters. In this context, a pump-probe experiment consists of applying a voltage pulse across the tunneling junction to excite the adatom's spin (pump) followed by a weaker voltage pulse to measure the adatom's magnetic state at a time Δt after the excitation (probe). Many pump-probe cycles are performed at different times Δt and allow the measurement of a SP current as a function of Δt [85]. The relaxation time can be determined by fitting the exponentially decaying pump-probe signal and leads to the plot in figure 2.17. In figure 2.17, T_1 is limited by the substrate-substrate scattering rate $r_{s\to s} \propto G_{s\to s}$ (blue line) in the low conductance regime, where the influence of the tip is weak. At high conductance, T_1 is limited by tip-tip scattering rate (red line) $r_{t\to t} \propto G^2_{t\to s}/G_{s\to s}$, where the tip-adatom distance is short. Finally, the relaxation rates $r_{t\to s}$ and $r_{s\to t}$ represent the contribution from electrons tunneling from one electrode to another, and scattering with the adatom's spin (olive line).

In addition to pump-probe spectroscopy, other methods are available with SP-STM to address the spin dynamics of single atoms at different timescales. Some of them are presented in figure 2.18.

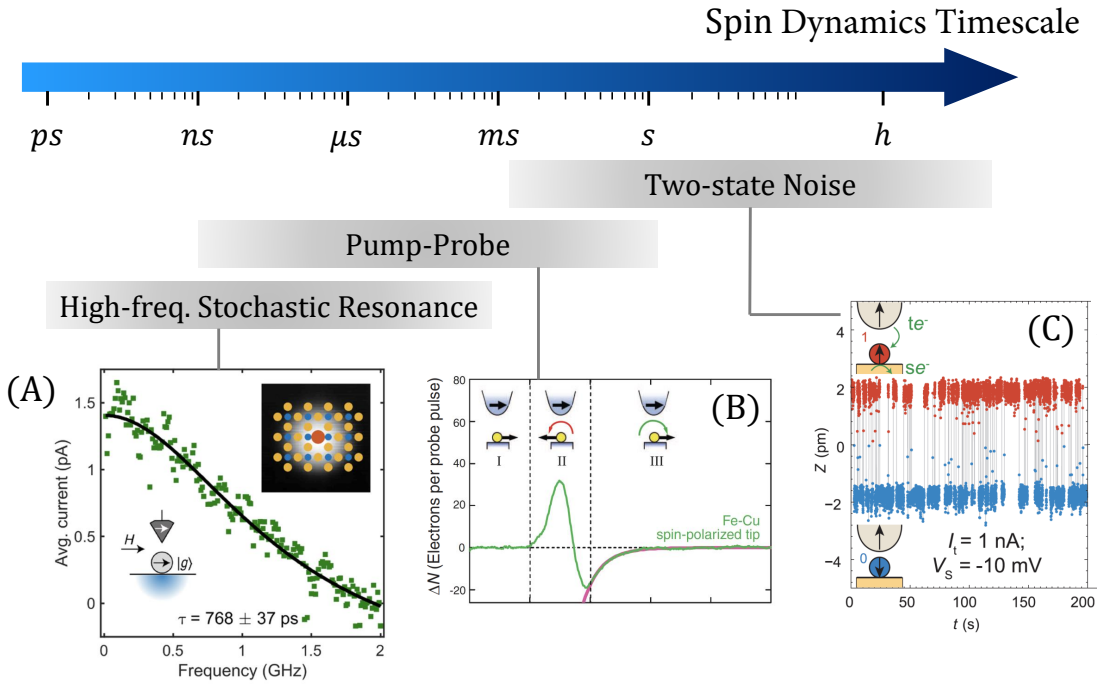

Figure 2.18: Non-exhaustive list of methods to address the spin dynamics of single atoms at different timescales with SP-STM. The techniques shown in (B) and (C) can measure T_1.

Panel (A) shows the high-frequency Quantum Stochastic Resonance (QSR) technique applied to Fe atoms adsorbed on Cu_2N [89]. On the same decoupling material, the first pump-probe experiment, carried on Fe-Cu dimers, is shown in panel (B) [85]. Panel (C) corresponds to the first experiment recording a two-state noise on a magnet made of five Fe atoms on Cu(111) [90]. Techniques shown in panels (B) and (C) are capable of measuring magnetic

state lifetimes directly and, consequently, T_1. QSR in panel (A) allows the measurement of a time τ^* that we introduce in section 2.3.8. Other methods, including lifetime broadening [91] or spin-pumping [92, 93], exist but are not discussed here. In this thesis, only the two-state noise and the high-frequency QSR are used and presented below.

2.3.7 Two-state Noise Experiment

When addressing the magnetism of single adsorbed atoms on surfaces with SP-STM, the reversal of the magnetization along the easy axis can be measured in real-time, either as a change in the tunneling current or in the tip-sample distance. This measurement, referred to as two-state noise, is accessible for systems showing a magnetic ground state lifetime within the current amplifier bandwidth, for a given temperature, magnetic field and tunneling voltage. The main motivation of conducting such experiment is to estimate the intrinsic magnetic lifetime of a system. In absence of tunneling electrons ($V_t = 0$), some magnetic adatoms can spontaneously switch and reveal two-state noise induced by substrate phonons and electrons from the crystal. Some other adatoms can retain a stable magnetic moment at $V_t = 0$ and no magnetization switching is observed. In this case, one needs to apply a tunneling voltage ($|V_t| > 0$) to induce QTM via tunneling electrons that can scatter, either elastically or inelastically, to the adatom. When the tunneling electron energy $|eV_t|$ equals or exceeds the energy of the first magnetization reversal path, QTM is induced by scattering processes, causing the system to switch between the two magnetization orientations along the easy axis. As long as the tip's magnetic moment has a non-zero projection with respect to the adatom's easy axis, the magnetization reversal can be probed as telegraph noise in the z or I_t signal, with the feedback loop closed or open, respectively.

Two-state noise experiments on MgO/Ag(100) have been conducted on different single atoms, such as Fe [49]. For a transition metal adatom, STM can directly access the 3d electrons at the Fermi level, and the telegraph noise is a direct measurement of the 3d magnetization reversal. Two-state noise have also been recorded on lanthanides in references [94–96] and [50, 87, 88], for Holmium (Ho) and Dy respectively. In this case, the STM cannot probe the confined 4f electrons and the telegraph noise corresponds to the magnetization reversal of spin-polarized outer shells, accessible with STM. We assume a strong intra-atomic exchange coupling such that the magnetic moment of the outer shell electrons follows the one of the 4f electrons, and vice versa. Under these assumptions, telegraph noise measured for rare-earth single atoms is an indirect measurement of the 4f magnetization reversal. We show in figure 2.19 (A) the two-state noise experiment on Dy adsorbed on the top-Oxygen site of MgO from reference [50].

In a two-state noise trace, the time occupations n_0 and n_1, of states $|0\rangle$ and $|1\rangle$ respectively, can be calculated over a long measurement period, such that lifetimes $\tau_{|0\rangle}$ and $\tau_{|1\rangle}$ can be determined accurately:

$$\begin{cases} \tau_{|0\rangle} = \frac{n_0}{n_0+n_1} \\ \tau_{|1\rangle} = \frac{n_1}{n_0+n_1} \approx T_1 \end{cases} \tag{2.27}$$

Intrinsic lifetimes can be estimated from equation 2.27 in a two-state noise experiment when performed at low tunneling current and low tunneling voltage. In these conditions, the influence of tunneling electrons on the magnetic system is minimized. For example, the magnetic moment of top-Oxygen Dy has been found stable in the ground state over days at low tunneling voltages and at $T_{\mathrm{STM}} = 1$ K [50], confirming the experimental results from XMCD studies [97].

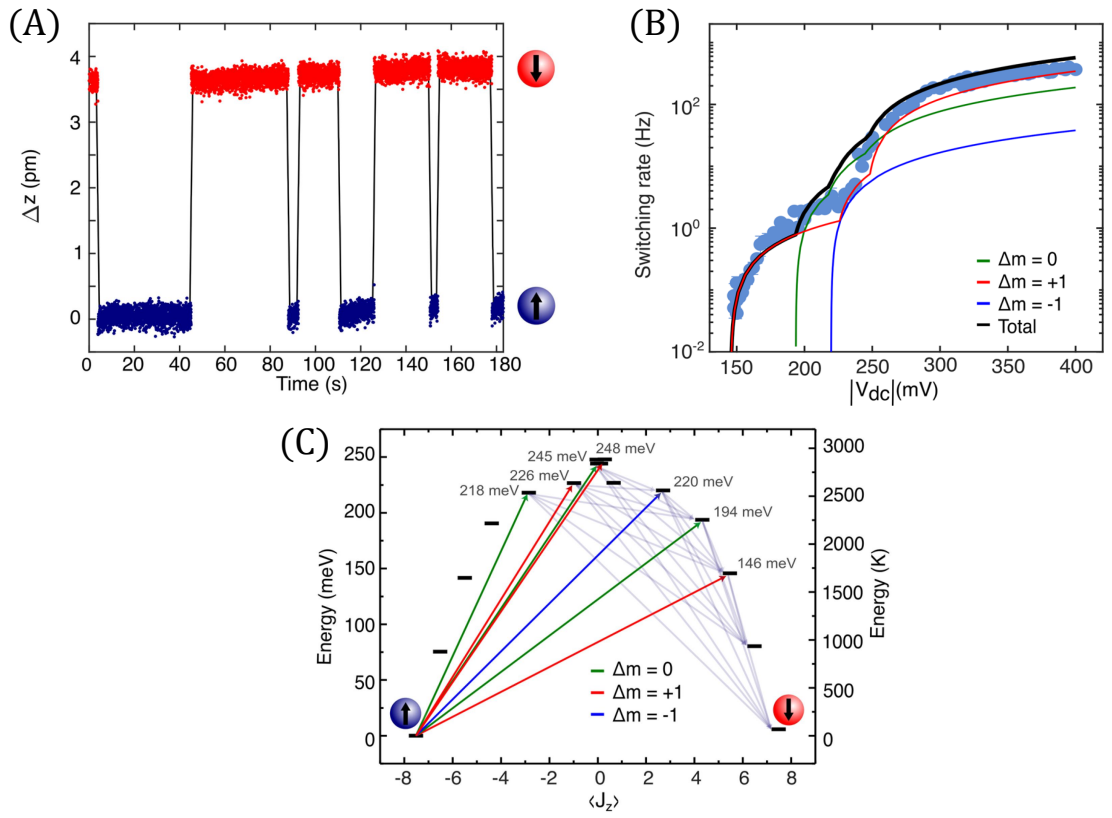

Figure 2.19: (A) Two-state noise experiment on a Dy adatom adsorbed on the top-Oxygen site of MgO at $V_t = 156$ mV, $T_{STM} = 1.8$ K and $B_z = 5$ T. (B) Switching Rate measured as a function of tunneling voltage. (C) 4f energy level scheme of top-Oxygen Dy, obtained from multiplet calculations for $B_z = 5$ T [50].

In figure 2.19 (B), the switching rate, defined as the total number of switchings divided by the corresponding measurement time, is shown as a function of the tunneling voltage V_t. Steep increases of the switching rate come from the opening of new scattering channels for

tunneling electrons. Each energy onset $e|V_t|$ can be assigned to a magnetization reversal path for the 4f electrons. The corresponding energy level scheme is shown in figure 2.19 (C). We will describe in more detail how this scheme is calculated in section 5.1. The first onset is identified around 146 meV and corresponds to a reversal induced by inelastic scattering $\Delta m_J = +1$. The switching rate, that we call Γ from now on, can also change with the tunneling current. As reported in references [90, 94, 98], Γ follows the power law $\Gamma \propto I^N$, where N is a fitting exponent. For Dy on MgO, an exponent $N \sim 1$ is reported experimentally and indicates that a single-electron process governs the magnetization switching.

2.3.8 Quantum Stochastic Resonance (QSR)

Stochastic resonance is a well-known phenomenon where the presence of noise can enhance the response of a non-linear system to a weak input signal. The auditory system provides an attractive example of how noise can augment the detection and processing of weak signals: the presence of background noise typically improves the detection of faint sounds by enhancing the system's sensitivity to low-intensity auditory stimuli [99]. An optimal amount of added noise improves the response of the system, whereas further noise increase only degrades the information content [100]. If stochastic resonance is at the core of many phenomena in nature such as the periodicity of ice ages [101, 102] or the charge carrier dynamics in micro-structure devices [103, 104], this mechanism has also been predicted at the quantum level [105, 106].

In the context of the magnetism of single atoms, QSR has been demonstrated for the magnetization reversal of Fe atoms adsorbed on Cu_2N [89]. Figure 2.20 illustrates the working principle of this technique. Figure 2.20 (A) shows the simultaneous application of DC and AC biases to the tip positioned over the adatom, where the ac component can be written as $V_{\mathrm{RF}}(t) = V_{0,\,\mathrm{RF}} \cos(\omega t)$. In absence of modulation, the adatom undergoes reversal of its magnetization at a given DC voltage and temperature. In the case of Fe on the Nitrogen site of Cu_2N, a small transverse anisotropy term allows a real-time SP read-out of the magnetization orientations, as a two-state noise trace shown in figure 2.20 (B) 1. An excited state lifetime on the order of milliseconds is reported for a tunneling bias V_t below the first inelastic excitation threshold. The corresponding histogram of τ_{ee}, representing the time intervals between consecutive excitations from the ground state $|0\rangle$ to the first excited state $|1\rangle$, is shown in green in figure 2.20 (C). In the absence of an AC voltage, the distribution of τ_{ee} follows a hypo-exponential function, as indicated by the black solid line fitting the data. This function corresponds to a Poisson distribution, describing well the waiting times between tunneling electrons scattering with the adatom's spin [89, 107]. The non-driven statistics exhibit a characteristic maximum at $\tau_{ee} \approx 0.5$ ms, which corresponds to the average round-trip time of the magnetic bi-stable system.

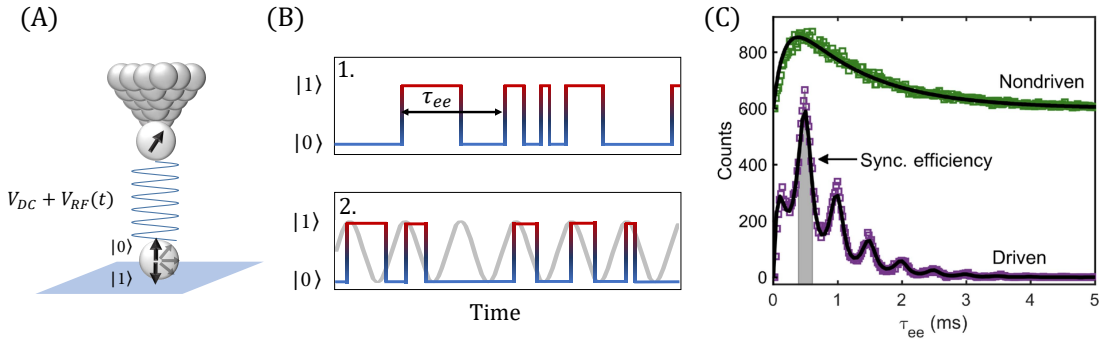

Figure 2.20: (A) Two-state noise experiment on a single Fe atom adsorbed on the top-Nitrogen site of 1 ML-thick $Cu_2N/Cu(100)$. An SP tip is used, and a DC bias and an RF modulation are applied. (B) Two-state noise without (1.) and with (2.) RF modulation applied with $f_{RF} = 2$ kHz. (C) Corresponding histograms for (B) 1. (green) and (B) 2. (purple) [89].

When an RF modulation is applied at a frequency of 2 kHz, corresponding to a characteristic time of 0.5 ms, the tunneling voltage $V_t + V_{RF}(t)$ becomes synchronized with the excitation rates of the adatom. Consequently, the counts of τ_{ee} undergo significant modifications, as shown by the purple trace in figure 2.20 (C). The counts for τ_{ee} now peak at integer multiples of the excitation period, $T_{RF} = 0.5$ ms. These observations indicate that QSR fundamentally alters the dynamics of the Fe atom and enhances the signal-to-noise ratio of the characteristic time τ_{ee} of the non-driven system.

As explained in reference [89], QSR is realized by modulating the excitation rates, mediated by voltage-dependent inelastic electrons tunneling from the tip. This synchronization makes the RF voltage acting as a drive for the magnetic excitations, efficient within a defined frequency range Δf_{RF}. In the case of Fe on the Nitrogen site of Cu_2N, the synchronization efficiency is $\Delta f_{RF} \in [0.2, 10]$ kHz, for $V_t = 15$ mV and $V_{RF} = 5$ mV. The relaxation rate is dominated by scattering with bath electrons and is found constant over a single drive period [89].

For Fe adsorbed on the copper-site of Cu_2N, the large transverse anisotropy generates a faster reversal of the magnetization, beyond the I/V converter bandwidth. To probe the dynamics of an adatom's spin under QSR with SP-STM, the lock-in amplifier is synchronized with the following RF chopping scheme: the driving voltage is turned "on" for the first half of the lock-in cycle and "off" for the second half. The demodulated current from the lock-in output is therefore directly related to the effect of the modulation and to the conductance difference between states $|0\rangle$ and $|1\rangle$ [89]. Figure 2.21 illustrates the working principle of high-frequency QSR. The term "high-frequency", introduced already in figure 2.18, refers to a timescale of the spin dynamics that exceeds the I/V converter bandwidth and the data sampling rate.

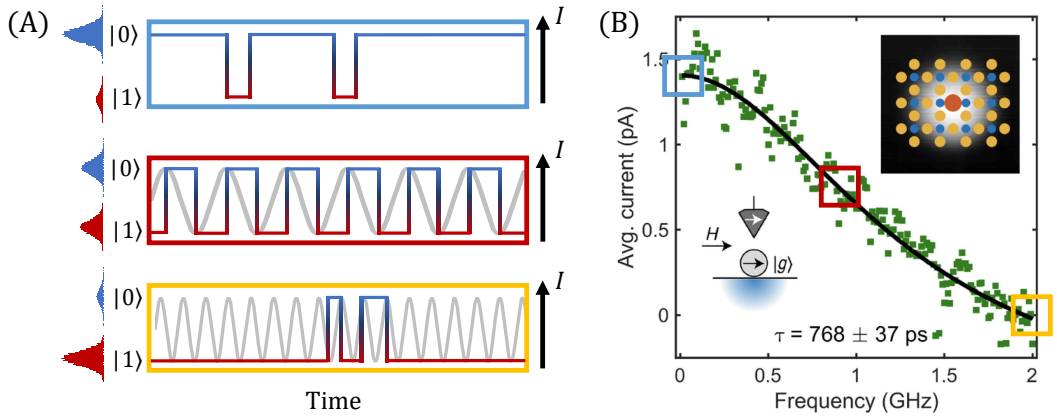

Figure 2.21: Working principle of high-frequency QSR, capable of probing fast spin dynamics in the context of single atom magnetism. Panel (B) is taken from reference [89] and shows the spin-polarized current measured on a single Fe atom adsorbed on the copper site of 1 ML-thick $Cu_2N/Cu(100)$.

Figure 2.21 (A) shows three subplots, each corresponding to a color-coded inset in panel (B). The average current shown in figure 2.21 (B) is the lock-in demodulated current, proportional to the integrated conductance difference between the ground and first excited states. This signal also provides a measurement of the relative magnetic population of the system, given the RF chopping scheme described above and assuming a sufficient synchronization between the drive and the adatom's excitation rate. We describe now the different assumptions that we make regarding this technique, represented by the three color-coded insets in figure 2.21. At 0 Hz (blue inset), we use a sufficiently low DC bias (10 mV) and a sufficiently large magnetic field along the adatom's easy-axis (1.5 T) to assume that the system is asymmetrically populated, mostly in the ground state. This leads to a high lock-in current at 0 Hz in figure 2.21 (B), since the tip's and adatom's magnetic moments are aligned here. As we apply an RF modulation and increase the frequency, excitation events occur more frequently leading to a Lorentzian-like decaying signal over the sweep. The minimum is reached when the drive frequency becomes larger than the relaxation rate, leaving the adatom mostly in the excited state (yellow inset). Based on these two assumptions, we define the characteristic time τ^* at the Lorentzian Half-Width at Half Maximum (HWHM) (red inset) as follow:

$$\tau^* = f_{\mathrm{HWHM}}^{-1} \tag{2.28}$$

At the HWHM, the synchronization of the RF drive with the adatom's excitation rate is maximum. Assuming identical ground and first excited state populations, as well as an ideal drive synchronization, τ^* corresponds to the characteristic round-trip time of the non-driven system, completing the transitions $|1\rangle \rightarrow |0\rangle \rightarrow |1\rangle$. Under these assumptions, $\tau^*/2$ represents an approximation of the first excited state lifetime and, therefore, of the relaxation time of the system at low temperature.

2.4 Electron Spin Resonance - Scanning Tunneling Microscopy (ESR-STM)

Electron Spin Resonance (ESR), also known as Electron Paramagnetic Resonance (EPR), is a spectroscopic technique invented in 1944 by Y. Zavoisky, who observed changes in the absorption of radio-frequencies by paramagnetic substances in a magnetic field [108]. Among its attractive features, this technique offers a high energy resolution for resolving spin excitations, whose main limitation comes from the intrinsic spin relaxation broadening [109]. However, standard continuous-wave ESR requires at least 10^7 spins for sufficient signal-to-noise ratio and has therefore a poor spatial resolution [110]. In contrast, STM offers subnanometer resolution but the energy resolution in STS is limited by $5.4 k_B T$ [111, 112]. Combining these two techniques, known as ESR-STM, is therefore a strong motivation for observing resonance signals on single adsorbed atoms.

Historically, the first ESR-STM experiment, in the sense of how we commonly understand it today, was reported by Baumann *et. al.* in 2015 [14]. In their work, they investigated ESR signals of Fe adatoms adsorbed on 2 ML MgO, at T_{STM} = 0.6 K. They measured a Rabi rate of $\Omega = (2.6 \pm 0.3)$ rad/μs and a coherence time of $T_2 = (210 \pm 50)$ ns , for V_{RF} = 8 mV. These parameters will be defined in section 2.4.3. Other systems have been investigated with ESR-STM and are listed in table 2.2.

Substrate	**Adsorbed Atoms or Molecules**	**References**
MgO/Ag(100)	Fe	[14], [44], [45], [46], [47], [113], [114], [115]
	TiH	[16], [47], [114], [45], [116], [117], [118], [119]
	Cu	[120]
	Eu	[20]
	Sm	
	FePc	[17]
	Li_2	[18]
	LiNa	
	Na_2	
NaCl/Au(111)	$TbPc_2$	[19]

Table 2.2: ESR-STM systems reported in literature so far.

Because the driving mechanism of ESR-STM is still unclear, it is difficult to predict if a magnetic system will reveal ESR signals. For this reason, most of the groups referenced in table 2.2 kept the ESR-compatible MgO substrate and tried other magnetic adsorbed systems, like TiH, which was the first molecule to reveal ESR signals. However, the study of Terbium phthalocyanine double-deckers ($TbPc_2$) on Sodium Chloride NaCl has proved that MgO is not the only decoupling medium to generate ESR contrast and opens the way for exploring new substrates.

In this section, we describe first the working principle of ESR-STM followed by a theoretical description using the Bloch formalism, employed also for standard ESR. Finally, the different proposed mechanisms, aiming to explain ESR-STM, are presented based on the theoretical review written by Delgado *et. al.* [121].

2.4.1 Working Principle

The working principle of ESR-STM is illustrated in figure 2.22. In panel (A), a magnetic adatom, with an out-of-plane easy axis, is placed in a vector magnetic field. An SP tip is employed and generates a magnetic field $\mathbf{B}_{\text{tip}}$, sensed by the adatom. The total field component $(B_{\text{ext, z}} + B_{\text{tip,z}})$, parallel to the easy axis of the magnetization, has the effect of splitting the energy levels, as shown in panel (B).

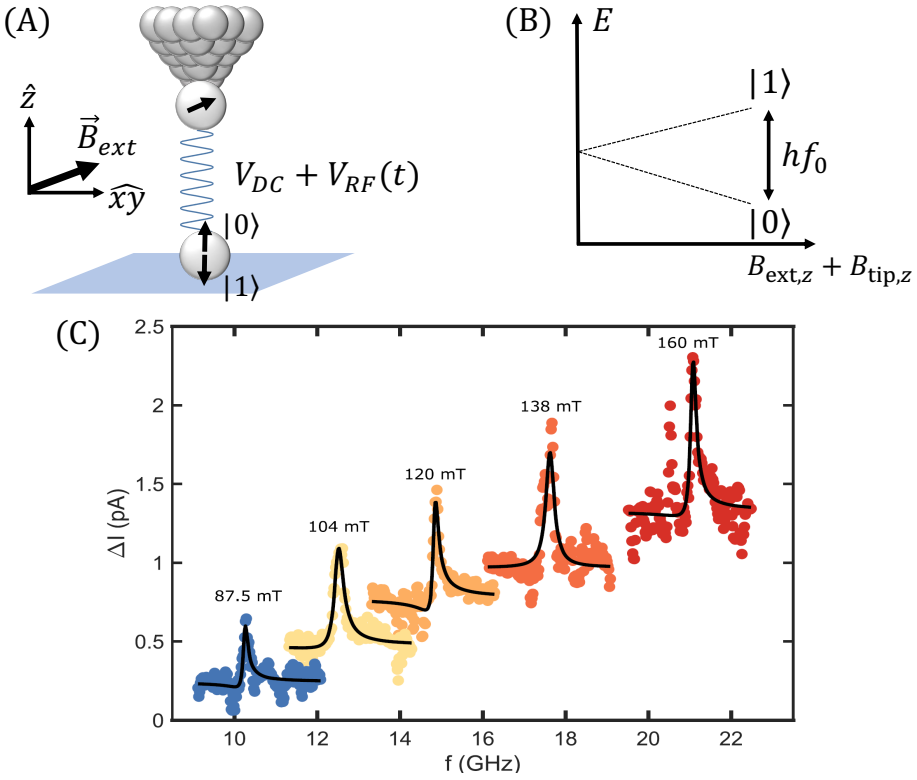

Figure 2.22: Working principle of ESR-STM. ESR signals on an Fe atom adsorbed on MgO are shown in (C) and are taken from reference [115]. The parameters are I_t = 60 pA, V_t = 60 mV, V_{RF} = 22 mV, B_{xy} = 1.5 T and T_{STM} = 0.8 K.

ESR is achieved when coherent transitions between $|0\rangle$ and $|1\rangle$ are driven by a continuous RF bias modulation whose frequency f_{RF} satisfies the resonance condition:

$$hf_{\text{RF}} = hf_0 = \mu_B g_z^{\text{eff}} \Delta J^* \cdot \left(B_{\text{ext, z}} + B_{\text{tip, z}}\right) \tag{2.29}$$

where hf_0 is the Zeeman splitting energy induced by the field component parallel to

the easy axis. The right term in equation 2.29 expresses this energy in term of an effective g-factor g_z^{eff}, where μ_B is the Bohr magneton. Equation 2.29 applies for systems with a strong out-of-plane magnetic anisotropy such as Fe/MgO/Ag(100). ESR signals measured on this system are shown in figure 2.22 (C), as an example. The magnetic field along $\hat{z}$ is indicated on top of each trace and shifts linearly with the RF frequency, as described in equation 2.29. The ESR lineshape will be discussed in section 2.4.3. For paramagnetic systems like TiH/MgO/Ag(100), the magnetic moment is aligned with the external magnetic field, if the corresponding Zeeman energy is strong enough compared to the tip magnetic field. In this case as well, a resonant RF electric field induces transitions between the Zeeman-split states $|0\rangle$ and $|1\rangle$ [122]. Experimentally, the RF modulation can be applied directly to the tip or to an antenna next to the tip in the tunneling junction [15]. ESR-STM signals translate into a change in the tunneling current ΔI, as the the two magnetic orientations $|0\rangle$ and $|1\rangle$ are differentiated with the SP tip through the TMR effect. This change in current is measured with the lock-in amplifier, synchronized with an RF chopping scheme, which will be presented in section 2.4.2.

The main requirements for conducting ESR-STM experiments are summarized below:

- A controllable vector magnetic field.
- An SP tip.
- A low STM temperature for sufficient spin polarization of the surface adatom at the desired energy level splitting.
- Sufficient RF transmission over a large frequency interval from the RF generator down to the tunneling junction.
- Low noise-level to prevent variations in the tip-sample distance leading to excessively broad linewidths.

In this thesis, two methods are used to measure ESR-STM signals. They are illustrated in figure 2.23 and described below.

- **Frequency sweep method**: the RF frequency is swept at a fixed external magnetic field and a constant tip-adatom distance. An ESR peak is recorded at the RF frequency f_{RF} satisfying equation 2.29. The effective g-factor can be estimated from the linear shift of ESR frequencies with the external magnetic field. However, the frequency-dependent losses of the RF cabling, from room temperature down to the tunneling junction, have to be compensated for applying a constant RF amplitude during the sweep.
- **Tip-field sweep method**: the tip-adatom distance is changed by sweeping the tunneling current linearly, at a fixed RF frequency and external magnetic field. We assume that the tunneling current is proportional to the tip magnetic field [16, 123]. This relation is expected for an exchange interaction field and for a dipolar field on a narrow

current range [47, 115]. Consequently, the tip-induced magnetic field B_{tip}, sensed by the adatom, is swept linearly and an ESR peak is recorded when the resonance condition in equation 2.29 is fulfilled. The main advantage of this method is that it does not require a compensation of the RF cabling losses, as we work at a constant f_{RF}. However, as the combined interactions contributing to B_{tip} are difficult to estimate, this method does not provide a precise and straightforward measurement of the magnetic moment nor of the g-factor.

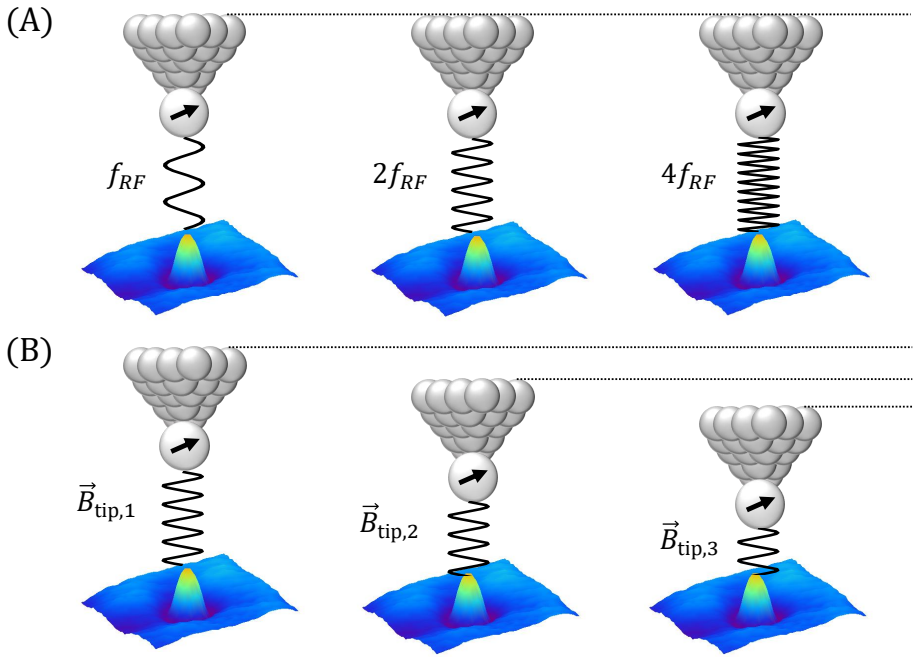

Figure 2.23: Working principle of the frequency sweep and tip-field sweep methods illustrated in (A) and (B) respectively. In (B), the field $B_{\text{tip},i}$ is defined as the tip magnetic field sensed by the adatom at three different tip-adatom distances. A 3.5 nm x 2.8 nm STM image of a single Fe adatom adsorbed on MgO is used for the illustration.

2.4.2 Lock-in Detection

For both methods described above, ESR signals are measured with a lock-in amplifier synchronized with an RF chopping scheme. Similarly to the high-frequency QSR technique, the RF modulation is chopped "on" and "off" at a period matching a lock-in cycle, as shown in figure 2.24 (A). We use in this thesis a chopping frequency of 323 Hz. The demodulated current ΔI is thus proportional to the rectified RF current induced by the RF modulation. Away from the resonance condition, in panel (B), the RF voltage is not capable of driving coherent transitions between $|0\rangle$ and $|1\rangle$, which results in no frequency-dependent changes in the SP tunneling current. In panel (C), when the RF modulation is chopped "on" and within the ESR peak linewidth, an SP current is observed at the lock-in frequency.

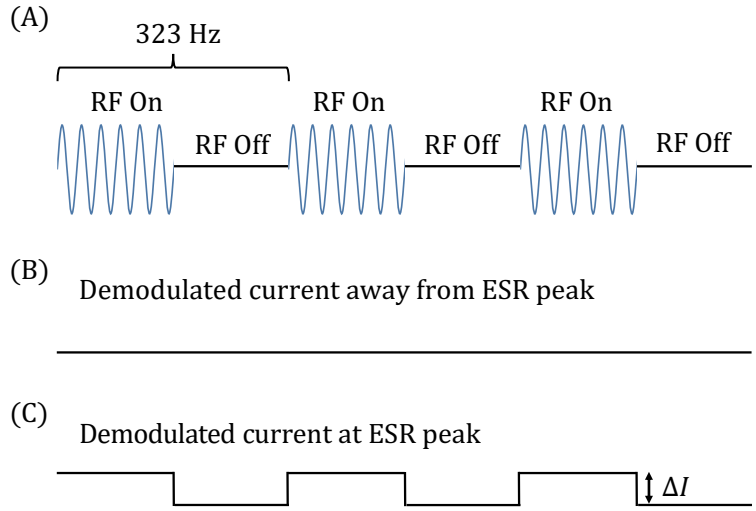

Figure 2.24: RF chopping scheme used for detecting ESR-STM signals [124].

The time-integrated lock-in signal leads to the measurement of the ESR peak, in a frequency or tip-field sweep. When the RF is chopped "off", the system relaxes at a rate T_1^{-1} typically much larger than 323 Hz.

2.4.3 Theoretical Description

The energy relaxation time T_1 and the coherence time T_2 are represented in the Bloch sphere in figure 2.25. Points on the sphere's surface correspond to pure states of the system (including superposed ones), whereas points on the inside of the sphere correspond to mixed states [125]. The axes $\hat{x}$ and $\hat{y}$ corresponds to pure states $\frac{|0\rangle+|1\rangle}{\sqrt{2}}$ and $\frac{|0\rangle+i|1\rangle}{\sqrt{2}}$, respectively.

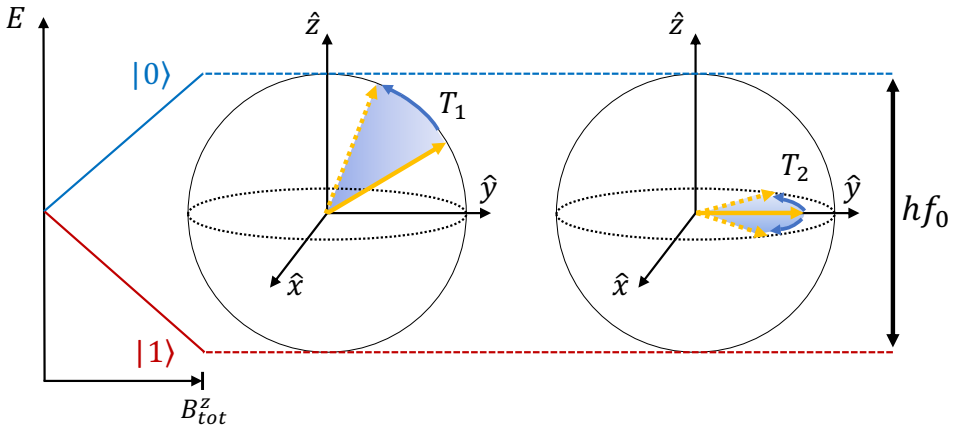

Figure 2.25: Bloch sphere representation of the relaxation and coherence times T_1 and T_2 at low temperature. The yellow arrow represents the wavefunction $|\Psi\rangle$ of the adatom in an ideal two-level system, such that $|\Psi\rangle = \alpha|0\rangle + \beta|1\rangle$ with $|\alpha|^2 + |\beta|^2 = 1$ [126].

Similarly to figure 2.22, we chose the $\hat{z}$ axis as the adatom's easy axis of the magnetization, along which the magnetic field B^z_{tot} splits the levels according to the Zeeman interaction. Once prepared in the first excited state $|1\rangle$, the system relaxes at a characteristic time T_1 toward thermal equilibrium, approximated by the pure ground-state $|0\rangle$ at low temperature. In the Bloch sphere, this is represented by the adatom's wavefunction moving away from $|1\rangle$ and relaxing towards $|0\rangle$ (cf. figure 2.25 left). When the system is prepared in a superposed state, in the $\hat{x}\hat{y}$ plane and along the sphere's surface, the interaction of the adatom's spin with the environment leads to a loss of coherence between states $|0\rangle$ and $|1\rangle$. This is described analytically by a exponential decrease of the off-diagonal elements $\alpha(t)\beta^*(t)$ and $\alpha^*(t)\beta(t)$ of the system's density matrix at a characteristic time T_2. In the Bloch sphere, this is represented by a decreasing projection of the adatom's wavefunction in the $\hat{x}\hat{y}$ plane (cf. figure 2.25 right). The coherence time T_2 is therefore defined as the time the system stays in a superposed state with a well-defined phase between $|0\rangle$ and $|1\rangle$, before mixing becomes too strong to distinguish each state. The upper limit of T_2 is given by $2T_1$; this relationship explains why adatoms with a long relaxation time are promising candidates for showing a long coherence time. We introduce the generalized Rabi rate $\tilde{\Omega} = \sqrt{\Omega^2 + 4\pi(f_{\text{RF}} - f_0)^2}$ defined as the rate at which the system precesses coherently between $|0\rangle$ and $|1\rangle$ under the applied RF electric field. The frequencies f_{RF} and f_0 are defined previously in equation 2.29.

We start our theoretical description by assuming that the magnetic system can be approximated by a pure two-level system; this assumption is justified in this context, as one deals generally with magnetic systems with a doubly degenerate ground state, such as half-integer spins, and/or systems where the two lowest states are well-protected by a uni-axial anisotropy term [127]. The Bloch equations of a two-level system can be applied to determine the time-dependent dynamics of the adatom's magnetic moment. In the steady-state limit $d < S_s > / dt = 0$, the expectation values of the adatom's magnetic moment $< S_s >$ and of the tip $< S_t >$ can be calculated, using the Bloch formalism [128] and the derivations from reference [118]. One has for the adatom:

$$< S_s^x > = < S_s^0 > \cdot \frac{\Delta\omega\Omega T_2^2}{1 + \Delta\omega^2 T_2^2 + \Omega^2 T_1 T_2} \tag{2.30}$$

$$< S_s^y > = < S_s^0 > \cdot \frac{\Omega T_2}{1 + \Delta\omega^2 T_2^2 + \Omega^2 T_1 T_2} \tag{2.31}$$

$$< S_s^z > = < S_s^0 > \cdot \frac{1 + \Delta\omega^2 T_2^2}{1 + \Delta\omega^2 T_2^2 + \Omega^2 T_1 T_2} \tag{2.32}$$

where $< S_s^0 >$ is the adatom spin in absence of $V_{\text{RF}}(t)$ and $\Delta\omega = \omega_0 - \omega_{\text{RF}}$ with $\omega_i = 2\pi f_i$. Note that these equations are valid in the frame rotating around $\hat{z}$ at a frequency f_{RF}. Similarly, the expectation values of the tip's magnetic moment $< S_t >$ can be estimated:

$$< S_t^x > = < S_t^{xy} > \cos(\omega_{\text{RF}} t) \tag{2.33}$$

$$< S_t^y > = < S_t^{xy} > \sin(\omega_{\mathrm{RF}} t) \tag{2.34}$$

$$< S_t^z > = S_t^z \tag{2.35}$$

These expressions suggest that the tip's magnetic moment is rotating at f_{RF} since it has in-plane components as shown in figure 2.22 (A). With the average spin components of the tip and of the adatom, one can estimate the time-average tunneling current that depends on the tunneling conductance G and on the angle between both moments:

$$\bar{I}(t) = G \cdot \big(V_{\mathrm{DC}} + V_{\mathrm{RF}}(t)\big) = G_j \big[1 + a < \mathbf{S_s} > \cdot < \mathbf{S_t} > \big] \cdot \big[V_t + V_{\mathrm{RF}}^0 \cos(\omega_{\mathrm{RF}} t + \phi)\big] \tag{2.36}$$

where G_j is the spin-average tunneling conductance in the junction, a a normalization factor and ϕ is the phase difference between the applied RF voltage and the precession of the adatom's magnetic moment in the lab frame. [45]. Moreover, we substract from equation 2.36 the contribution from $V_{\mathrm{RF}} = 0$ since the ESR signal ΔI is typically measured with the chopping scheme of figure 2.24. With $I(V_{\mathrm{RF}} = 0) = G_j V_{\mathrm{DC}}\big(1 + a S_t^z < S_s^0 >\big)$, one obtains the derived ESR signal ΔI from reference [118]:

$$\begin{aligned} \Delta I &= I(V_{\mathrm{RF}} \neq 0) - I(V_{\mathrm{RF}} = 0) \\ &= I_0 + I_{\mathrm{DC}}^{\mathrm{sat}} \cdot \frac{\Omega^2 T_1 T_2}{1 + \Omega^2 T_1 T_2} \cdot \big(1 + \beta \sin(\phi)\big) \cdot \frac{1 + \alpha\delta}{1 + \delta^2} \end{aligned} \tag{2.37}$$

where:

$$\begin{aligned} I_{\mathrm{DC}}^{\mathrm{sat}} &= a G_j V_{DC} < S_t^z >< S_s^0 > \\ \delta &= \frac{\Delta\omega}{\pi\Gamma} \\ \beta &= \frac{1}{2\Omega T_1} \cdot \frac{V_{\mathrm{RF}}}{V_{\mathrm{DC}}} \cdot \frac{< S_t^{xy} >}{< S_t^z >} \\ \alpha &= \frac{\beta \cos(\phi)}{1 + \beta \sin(\phi)} \cdot \sqrt{1 + \Omega^2 T_1 T_2} \end{aligned} \tag{2.38}$$

In equation 2.37, I_0 corresponds to the rectified current when the RF is on. In equation 2.38, $I_{\mathrm{DC}}^{\mathrm{sat}}$ is the saturation current under the applied DC voltage, β is the homodyne factor and α the asymmetric factor. From equation 2.37, the Full-Width at Half Maximum (FWHM) of the ESR peak can be defined as:

$$\Gamma = \frac{1}{\pi T_2} \sqrt{1 + \Omega^2 T_1 T_2} \tag{2.39}$$

In the first ESR-STM experiment by Baumann *et. al.*, they report an ESR linewidth of 3.6 MHz for $V_{\mathrm{RF}} = 1$ mV, $I_t = 560$ fA and $V_t = 5$ mV measured on Fe at $T_{\mathrm{STM}} = 1.2$ K [14]. The corresponding energy resolution of $1.5{\cdot}10^{-5}$ meV outperforms the IETS limit of $5.4 k_B T = 5.6{\cdot}10^{-1}$ meV at the same temperature, by four orders of magnitudes. In equation 2.37, terms

proportional to β account for the homodyne contribution to the ESR signal. It comes from the oscillating tunneling conductance, synchronized with the RF modulation frequency, that generates a DC tunneling current through mixing with the RF bias [45]. When the homodyne contribution is negligible ($\beta \approx 0$), the ESR lineshape can be described by a Lorentzian function [14]. When β is non-zero, the ESR lineshape is asymmetric and can be described by a Fano function, as it will be defined in section 4.2.

2.4.4 Proposed Mechanisms

In conventional ESR, a time-varying magnetic field can drive nuclear and electronic spins in resonance, when the modulation frequency matches the corresponding Zeeman splitting [129]. In contrast, ESR-STM uses an RF electric field in the tunneling junction and leads to ESR transitions. Despite the increasing number of groups succeeding in measuring ESR signals, the driving mechanism of this electrical-based technique is still unclear. Since 2015, different mechanisms have been suggested and we present some of them below, following the review [121]. Most of them are based on a piezoelectric response from the adatom or molecule.

Piezoelectric Response:

Under the application of a time-varying RF electric field, the adatom or molecule is subject to a vertical displacement $z(t)$ with respect to the substrate. The spin Hamiltonian of the system can be expanded in Taylor series around $z = 0$ and separated into two parts [109]:

$$H \approx H_0 + \delta H = H_0 + z(t) \frac{\partial H}{\partial z}\Big|_{z=0} \tag{2.40}$$

In equation 2.40, H_0 is the Hamiltonian describing the excitation spectrum of the system and δH describes the system's response to a displacement $z(t)$. In all piezoelectric-based mechanisms, the system enters in resonance when δH is modulated at a frequency matching the energy splitting hf_0 of states $|0\rangle$ and $|1\rangle$. Coherent transitions are provided by a non-zero Rabi force $F^{\text{Rabi}} = \langle 0| \frac{\partial H}{\partial z} |1\rangle$. The Rabi rate is defined as $\Omega = F^{\text{Rabi}} z_0$, where z_0 is the amplitude of the electric field-induced oscillations $z(t) = z_0 \cos(\omega t)$ [109]. All piezoelectric mechanisms are based on using a system's response δH that satisfies $F^{\text{Rabi}} \neq 0$. To assess the validity of a given mechanism, the experimental Rabi rate can be compared to the predicted term $z_0 F^{\text{Rabi}}$. This requires an estimation of the oscillation amplitude z_0 that can be done with DFT calculations [109]. Below, we describe two of the mechanisms based on a piezoelectric response $z(t)$ of the adatom to an RF electric field. The first one provides a description specific to the system Fe/MgO, which was the only ESR-active system at the time it was proposed. A more general mechanism based on a magnetic field modulation, similarly to conventional ESR, is then introduced.

1. **Modulation of the CF**: in the first ESR-STM experiment [14], Baumann *et. al.* proposed a time modulation of the transverse CF term F_4, defined using a ligand-field Hamiltonian $H_0(\mathbf{L}, \mathbf{S})$. In this case, the time-dependent mixing of $|0\rangle$ and $|1\rangle$ leads to a non-zero

Rabi force, expressed as $F_{\mathrm{CF}}^{\mathrm{Rabi}} = \frac{\partial F_4}{\partial z} \langle 0| L_x^4 + L_y^4 |1\rangle$. This model helps to understand the magnetic field dependency of ESR signals on Fe but restricts ESR-STM to this system. It also fails fitting the experimental Rabi rate as a function of the tip-adatom distance [45].

2. **Modulation of the exchange and dipolar interactions**: reference [109] proposes a more general mechanism, compatible with spin-1/2 systems. It is based on a time modulation of the tip-adatom exchange interaction $H_J(z(t)) = J(z(t)) < \mathbf{S}_{\mathrm{tip}} > \cdot \mathbf{S}$, where $< \mathbf{S}_{\mathrm{tip}} >$ is the statistical average of the tip's magnetization and $\mathbf{S}$ the adatom's magnetic moment. The corresponding Rabi force is $F_J^{\mathrm{Rabi}} = \frac{\partial J(z)}{\partial z} < \mathbf{S}_{\mathrm{tip}} > \cdot \langle 0|\mathbf{S}|1\rangle$. The modulation of the exchange interaction between the tip and the adatom can be understood as follows: due to the inhomogeneous magnetic field of the tip, the modulation of the adatom's position results in a time-varying exchange interaction field sensed by the adatom [118]. This oscillating field drives the ESR transitions in this model.

   By using an exchange coupling of 2 meV, found from experiments on $Fe/Cu_2N/Cu(100)$ [123], and using a tip-adatom distance of 0.6 nm, reference [109] calculates a driving strength of $\delta H/z_0 \approx 66.7$ meV/nm for Fe on MgO. This value is in good agreement with DFT calculations that find 65.9 meV/nm. However, this model fails explaining the exchange driving strength calculated for TiH molecules on MgO [116, 121]. This suggests other sources of piezoelectric displacements. For this reason, reference [45] added the long-range dipolar interaction to the exchange interaction to characterize the time-varying magnetic field sensed by the adatom. This model successfully explains the shifting of the resonance condition for a wide range of tip-adatom distances. However, they compute a piezoelectric displacement for the TiH molecule that is much smaller than other values [109, 116], showing the difficulty in giving a clear physical explanation for the excitation mechanism in ESR-STM [121].

Another mechanism has been proposed recently in reference [121]. It does not rely on a piezoelectric response. We present below the main ideas of this model.

Cotunneling Theory:

The work in reference [121] uses an effective cotunneling Hamiltonian to describe the quantum system, interacting with the two electrodes. This approach is based on the Anderson model [130] and has already described successfully SES spectra for a wide variety of systems adsorbed on surfaces [131]. In the context of ESR-STM, this theory models the change of the tunneling transmission induced by the RF electric field. This field induces time-oscillating hopping amplitudes described by the Anderson model. As a result, the off-diagonal elements of the renormalized Hamiltonian of the magnetic adatom possess finite oscillating terms directly proportional to the Rabi frequency [132]. A time-dependent magnetic field is therefore created by the tunneling barrier modulation from the RF electric field.

In this model, and in comparison to the previous mechanisms, a piezoelectric response is not required to explain the Rabi oscillations although it can enhance the barrier modulation and facilitate the resonance driving strength. However, the main limitation of this theory is that it requires a detailed description of the tip's and adatom's wave functions that are difficult to access experimentally [45].

3 ESR-STM Setup

Performing ESR-STM experiments requires a low-noise laboratory environment and an STM suited for RF modulations in the GHz range of the tunneling junction bias at low temperatures. This section is thus dedicated to the description of the ESR-STM used in this thesis, emphasizing on the upgrades brought to the system. The improvement of the Transfer Function (TF), defined as the frequency-dependent RF transmission through the tunneling junction, is presented in a second part. The last section is dedicated to the preparation and growth of the sample. For the experiments presented in this thesis, single Fe, Ti, Dy and Tb atoms are deposited on thin MgO films of various thicknesses, grown on Ag(100).

3.1 Overview of the ESR-STM and Repairs Made During the Thesis

The measurements presented in this thesis are acquired with a home-built low temperature UHV-STM, capable of holding a base temperature of 0.4 K for 21 hours. It is equipped with superconducting coils generating a vector magnetic field in the range $B_z \in [-8.0\,\mathrm{T}, +8.0\,\mathrm{T}]$ and $B_{xy} \in [-0.8\,\mathrm{T}, +0.8\,\mathrm{T}]$. The positive $\hat{z}$ axis is defined along the tip-sample direction and points from the sample toward the STM tip.

3.1.1 Laboratory Environment

The first task of this PhD thesis was to move the instrument from the first to the ground floor, in a more spacious lab whose concrete foundations are isolated from the rest of the building. This typically ensures a better decoupling from external mechanical vibrations. A sectional sketch of the lab environment is shown in figure 3.1. Our ESR-STM is placed on an active pneumatic damping system that minimizes vibrations induced by structure-borne noise, at frequencies typically below 200 Hz.

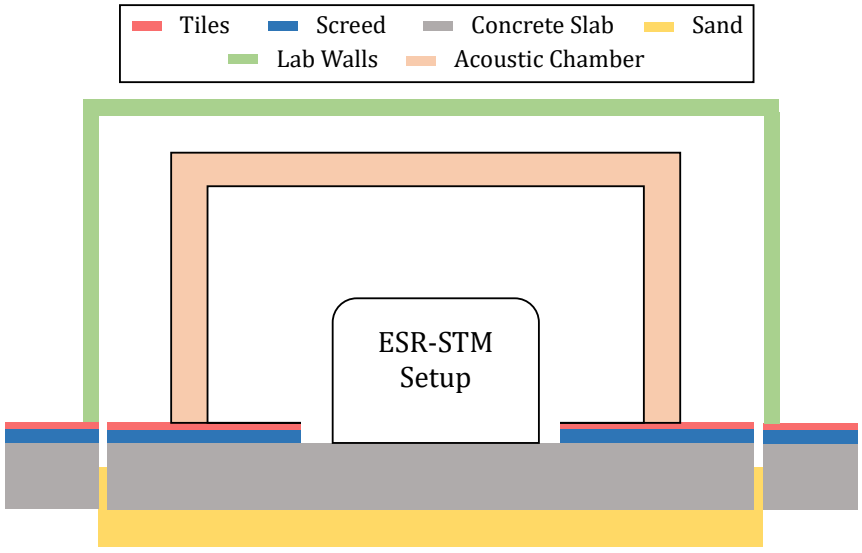

Figure 3.1: Section drawing of the laboratory where the ESR-STM was moved in 2020.

Tiles and screed have been removed, such that the active pneumatic damping system is in direct contact with the concrete slab. The latter provides a base which is rigid enough to absorb the dynamic forces generated by the active damping system. Due to the rigid connection to the cryostat and the vacuum system, required for sufficient thermal coupling and stable positioning in the magnetic field, our ESR-STM is susceptible to vibrations that limit the stability and resolution of atomic scale measurements. To improve the measurement conditions, a soundproof enclosure was constructed around the instrument in 2021 and is shown in more details in figure 3.2. It provides an acoustic noise reduction at frequencies from 20 Hz to 1 kHz.

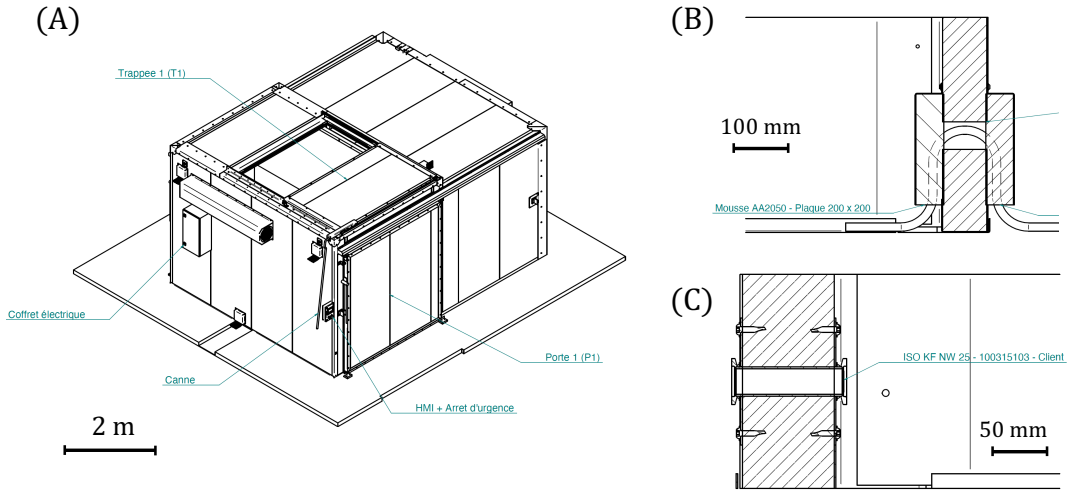

Figure 3.2: Drawings of the soundproof enclosure by the company *Spectra* in 2021 [133]. An overview is shown in (A) as (B) and (C) correspond to the types of constructions used for feedthroughs.

The acoustic panels are filled with rock wool with a thickness of 100 mm. Sliding doors allow to access the setup on both sides of the cabin and on the roof to operate the system during sample preparation, filing of liquid He and N_2 or maintenance. All doors of the chamber are closed during STM measurements. Cables and flanges, used for conducting the experiments, can still be passed through the cabin without compromising its insulation performance. In panel (B), a construction for soft and semi-rigid cables is shown with two parallel plates filled with dense foam on either side of the panel, minimizing the transmission of air-borne acoustic noise to the inside of the chamber. Similarly, in panel (C), KF nipple fittings, mounted inside the wall, are used for cryostat and primary vacuum operations.

3.1.2 The ESR-STM

As illustrated in figure 3.1, the ESR-STM sits in an environment protected from mechanical and acoustic vibrations. Figure 3.3 shows a photo (left) and a sketch of the instrument seen from above (right). The different parts of the instrument are indicated in red in figure 3.3 and can each be isolated from the others via VAT gate valves.

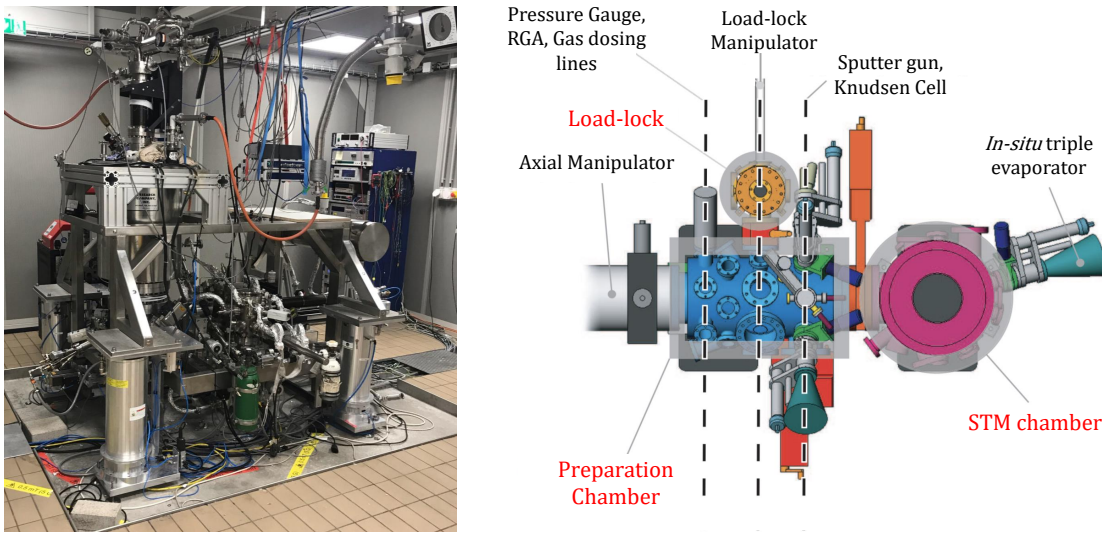

Figure 3.3: Photograph of the 0.4 K ESR-STM used in this thesis (left). A sketch shows the main components of the system in a top view (right) with the different UHV chambers labeled in red. The figure is adapted from reference [134].

- **The load-lock chamber** is used for transferring new samples from ambient conditions to the UHV preparation chamber with a linear manipulator. Unlike the other chambers, the vacuum is achieved only with a primary and turbo pumps.
- **The preparation chamber** is required in all UHV-STMs to prepare atomically clean single crystals *in-situ*. It can perform all the necessary operations: sputtering with an ion sputter gun, annealing by electron-bombardment and a direct measurement of the sample temperature with a K-type thermocouple [135]. It also includes a Knudsen cell containing Magnesium (Mg) for the MgO growth. Gas dosing lines (argon and oxygen) are also connected to the chamber via leak valves.
- **The STM chamber** contains the cryostat, the superconducting magnets and the STM. A triple evaporator is mounted to deposit single atoms onto the sample inside the STM at a sample temperature below 10 K.
- **The cryostat** is illustrated in figure 3.4. It is equipped with a closed-circuit single-shot ^{3}He stage reaching a temperature of 0.4 K for 21 hours at the STM. Measurements can also be performed at 4.2 K when filling the insert with liquid ^{4}He and leaving the ^{3}He in the gas phase. In this case, the STM can hold this temperature for a maximum of 22 hours. The main bath is filled with liquid ^{4}He and keeps the superconducting magnets at 4.2 K for up to 48 hours. The radiation heat load from the UHV chamber walls at room temperature is absorbed by an outer jacket cooled by liquid nitrogen to minimize heat losses in the inner volumes. The hold time of the jacket is approximately 20 hours. If any part of the cryostat warms up, adsorbed residual gas components, mostly hydrogen, desorb from the inner walls and generate a significant pressure increase in the STM chamber, which compromises the sample's cleanliness. The STM is rigidly

attached to the ^{3}He pot, where no internal vibration insulation is provided. This has a negative impact on the the measurement stability especially after filling the cryostat with helium or nitrogen. Bubbling of the liquid N_2 in the outer jacket causes vibrations in the cryostat, visible as excessive noise in the tip-sample distance. In order to make STM measurements feasible, the liquid N_2 has to be frozen. This is achieved by pumping the reservoir for approximately 5 hours. Additionally, strong spikes in the tunnel current are observed in the first 5-6 hours after filling the helium insert or the main bath. These "pinging events" are attributed to differential thermal expansion, caused by the increased temperature gradients due to the filling process. The frequency and intensity of these events decay over time, reducing the available measurement time to approximately 14 hours at T_{STM} = 0.4 K or T_{STM} = 4.2 K [136].

The measurements are carried out using the *Nanonis SPM control* software which is documented in reference [137]. The upgrades that improved the measurement and working conditions of this ESR-STM are presented below in section 3.1.3.

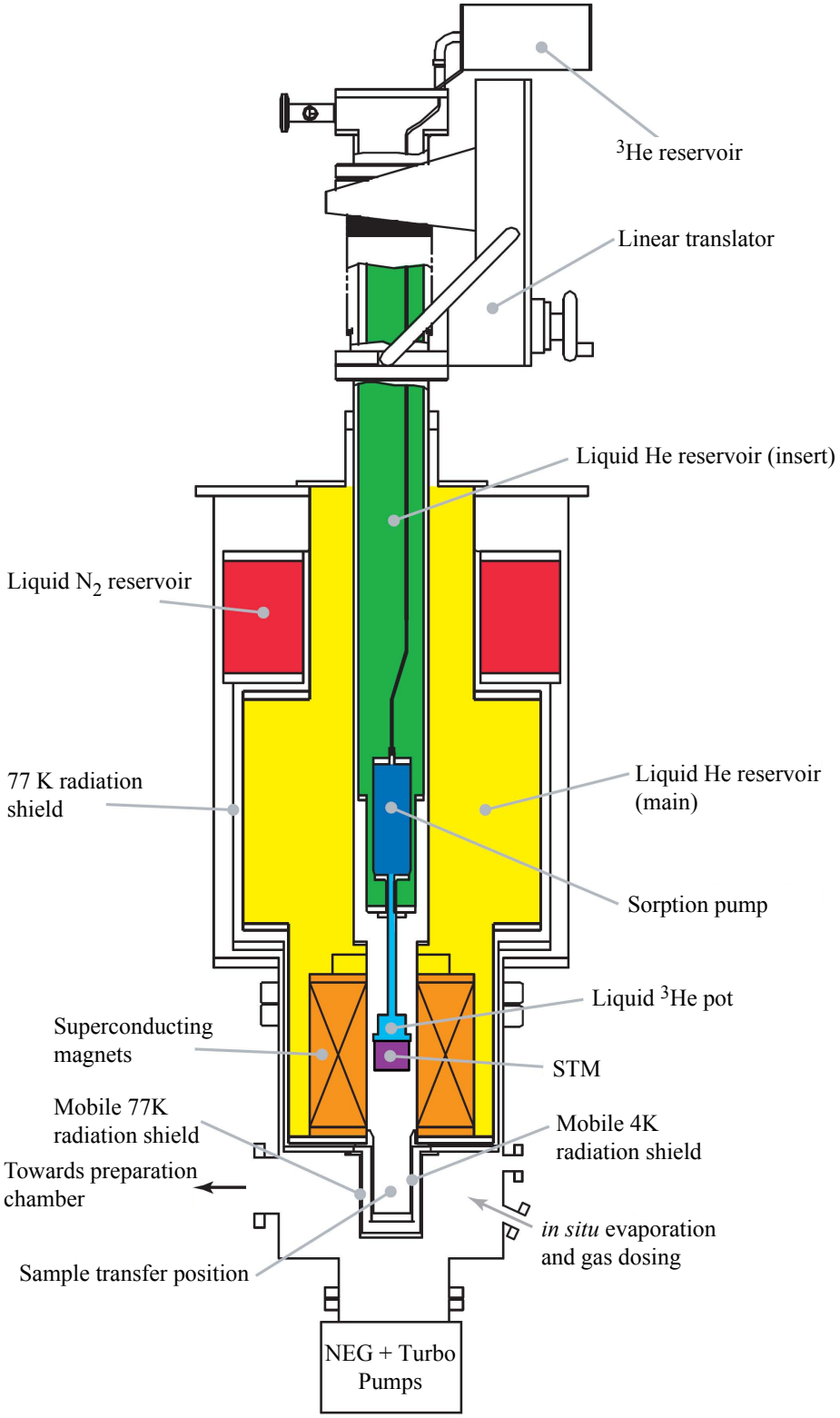

Figure 3.4: Schematic of the ^{3}He cryostat, adapted from reference [134]

3.1.3 Modification of the Vacuum Setup

The combination of Non-Evaporable Getter (NEG) pump with the preparation chamber ion pump led to a base pressure of $5.0 \cdot 10^{-10}$ mbar during the measurements, improving the vacuum by more than a factor of 2 compared to the previous setup. A small independent turbo pump has also been mounted to pump the STM chamber when the NEG gate valve and preparation chamber are closed for protection from higher pressures. The main limitation of the STM chamber base pressure comes from the fact that the superconducting magnets cannot be heated above 40°C, preventing a proper bake-out of the cryostat.

When preparing and growing the sample, the gate valve between the STM chamber and preparation chamber is closed leading to a base pressure that can go below $6.0 \cdot 10^{-11}$ mbar in the preparation chamber. This is a factor of 5 better than the value reported when starting this thesis. This improvement is due to multiple changes, including the installation of a gate valve to protect the ion pump from the argon partial pressure during sputtering, the replacement of an old leak valve for the sputter gun, the periodic use of a Titanium Sublimation Pump (TSP) over week-ends, and the installation of separate prevacuum pumps for the load-lock and preparation chambers.

3.1.4 Design of a New Sample Holder

Previously, the repeated cycles of sputtering and annealing led to the deposition of conductive material between the sample and sample holder. As the sample has to remain insulated from ground, this insulation was compromised after typically 20 sputter and annealing cycles. A new sample holder had to be designed to improve the durability of the electrical insulation of the sample with respect to ground. A scheme of the new setup is presented in figure 3.5.

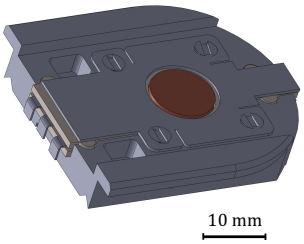

Figure 3.5: New sample holder. The sample is shown in brown and must remain electrically insulated from the sample holder during the measurements. A thin flexible tantalum plate is screwed on top of the construction to clamp the insulating alumina and sapphire parts visible in light grey.

During the sample preparation and growth, this design offers a larger contact area between the holder and the linear manipulator of the preparation chamber, leading to a more evenly distributed force holding the sample in place. As a result, insulating parts made of alumina and sapphire are less subject to crack. After this change, we observe an improved sample's insulation over time with respect to ground when placed in the STM.

3.1.5 STM Wiring

The wiring of the STM is concentrated in the insert that sits vertically centered in the cryostat. The insert contains the microscope on one end and the electrical feedthrough on the other. The wiring of the STM is organized as follows: the tunnel current, the tunnel bias, and the RF voltage are grouped in one feedthrough flange, and the coarse piezo and the piezo input lines are installed on an other flange. From room temperature, all the wires travel through two different stages down to their specific connection end around the microscope: i) a ^{4}He connection flange (4 K), ii) a ^{3}He pot flange. Wires are soldered to metallic pins that fit into conductive cylinder blocks with an input and an output pin; these blocks are meant for thermalizing the wires at the ^{4}He and ^{3}He stages. All connections between these two stages have been replaced by superconducting wires. This improved the ^{3}He hold time from 15 hours to 21 hours.

RF Line

The previous RF setup of our instrument offered a poor RF transmission to the tunnel junction, with a finite and low transmission only at discrete RF frequencies [48]. This limitation made the realization of continuous frequency sweeps impossible. Instead, external magnetic field sweeps were performed, leading to longer measurements and inducing piezo-actuator creep when changing the magnetic field. We present here the new ESR-STM setup leading to a smoother and much higher RF transmission up to 40 GHz. This allows to conduct ESR-STM and high-frequency QSR experiments using the frequency-sweep method, introduced in figure 2.23. The new electronic setup of our ESR-STM is shown in figure 3.6.

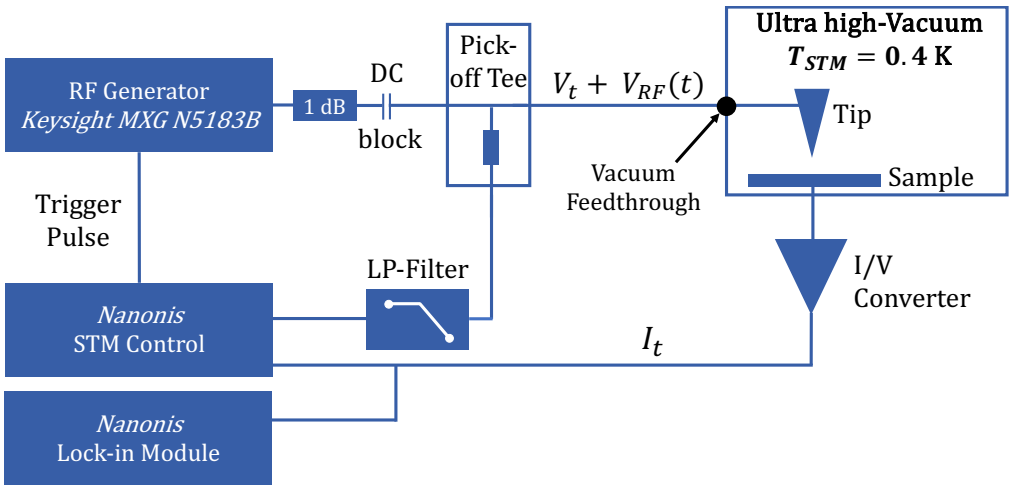

Figure 3.6: Electronic setup used for the 0.4 K ESR-STM at LNS-EPFL.

The RF output is inserted into a 1 dB attenuator, placed before the bias pick-off tee, and is made of a 450 Ω resistor to prevent charge build-up. We recall that −20 dB is equivalent to a signal attenuation by a factor of 10. The cable used in air is a 50 Ω flexible RF cable with a total length of 6 m, provided by the company *Teledyne Storm Microwave* [138]. The intrinsic cable losses for a 1 m cable are characterized by the company *elSpec* and are shown in figure 3.7.

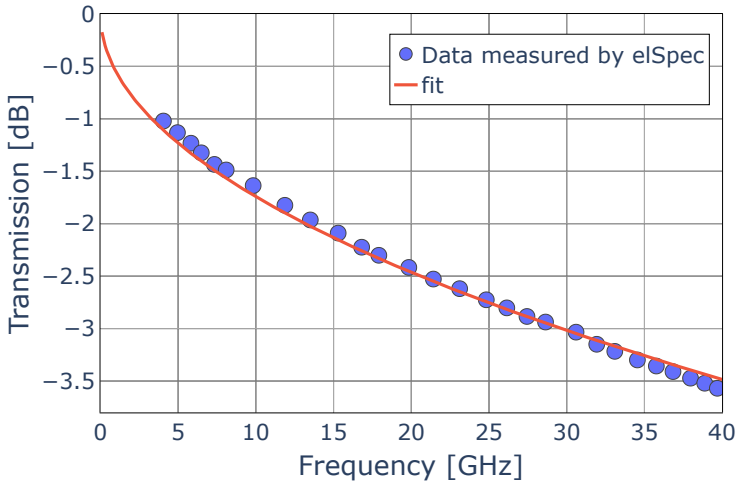

Figure 3.7: Losses for 1 m of the RF cable used in air. The data are provided by *elSpec*.

The following function is used for the fit:

$$y(f_{RF}) = -\sqrt{a \cdot f_{RF}} \quad \text{with} \quad a \approx 0.304 \tag{3.1}$$

where the square-root dependency comes from the resistive losses of a 50 Ω impedance cable. A linear term in f_{RF} is neglected and would account for the dielectric losses [15]. In-

tegrating the fit of figure 3.7 to 6 m and adding the 1 dB attenuator, a cable attenuation of approximately −11 dB is expected at 10 GHz before the vacuum feedthrough. We will use this fitting function to substract the 6 m cable losses in air and estimate the TF from the vacuum feedthrough down to the tunneling junction.

The RF cabling from the 300 K flange feedthrough down to the tunneling junction is presented in figure 3.8. SMK type 2.92 mm and SMPM connectors are used throughout the system to minimize reflections and losses over the entire frequency range. We use a silver-plated stainless steel coaxial cable of ~ 1.5 m from the 300 K feedthrough to the ^{4}He stage. From this stage, a semi-rigid NbTi cable of 0.3 m goes to the ^{3}He stage. Its superconducting state below 10 K provides attractive properties such as minimum heat transfer and RF power dissipation. From the ^{3}He stage, we use a flexible RF coaxial cable of ~ 0.1 m. We glued its center conductor with silver epoxy to contact the STM tip through a supporting PEEK cable guide. Cables data sheets are provided in references [139–141].

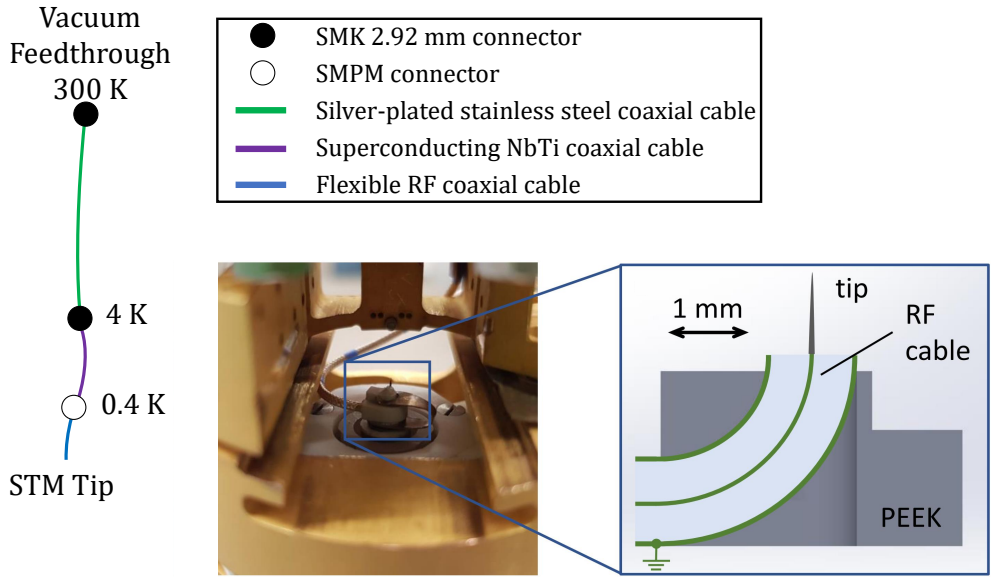

Figure 3.8: Sketch of the RF wiring used at the different temperature stages (left). A photo of the STM shows the flexible RF wire, the tip holder and the STM tip

3.2 Transfer Function (TF) Measurement

As mentioned in section 2.4.1, the determination of the frequency-dependent losses of the RF voltage from the generator down to the tunnel junction is crucial for conducting ESR-STM. The bias modulation amplitude V_{RF} in the junction, denoted $V_{\mathrm{RF}}^{\mathrm{jun}}$ from now on, has to be kept constant in frequency sweeps to control the amplitude and linewidth of ESR signals. Non-constant RF amplitude would lead to a variation of the background signal, making it unfeasible to identify the ESR peaks. Note that all RF bias amplitudes, in this thesis, are defined as zero-to-peak amplitudes.

The TF is measured using non-linear I(V) traces accessible with STS. The main idea is that the RF bias modulation, far beyond the current amplifier cutoff-frequency, induces a rectified current signal in a non-linear I(V) circuit. Therefore, the step, in the altered dI/dV trace, is broadened by the RF voltage transmitted in the tunnel junction. This broadening is determined by the convolution of the conductance trace in the absence of RF voltage with an arcsine distribution function, defined as:

$$w(V) = \frac{1}{\pi V_{\mathrm{RF}}^{\mathrm{jun}} \sqrt{1 - \left(\frac{(V - V_0)}{V_{\mathrm{RF}}^{\mathrm{jun}}}\right)^2}} \tag{3.2}$$

where V_0 is the applied DC bias.

In this thesis, the TF function was measured multiple times on different non-linear I(V) traces such as the surface-state of Ag(111) [142], the spin excitation of Fe around ±14 meV and the vibrational inelastic excitations of top-Oxygen site TiH around ±90 meV. We show here the typical steps for measuring the TF using the Ag(111) dI/dV spectrum in figure 3.9.

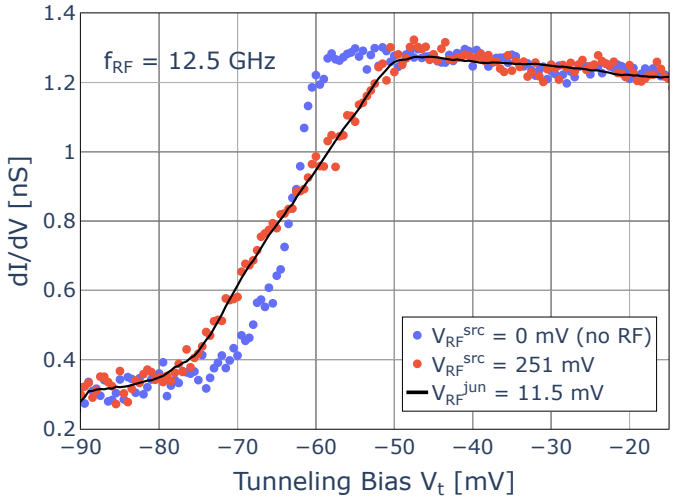

Figure 3.9: Effect of the RF modulation in a non-linear I(V) trace, as it appears in dI/dV. The step-like onset of the conductance corresponds to the surface state of Ag(111) without (blue) and with (red) the applied RF modulation. The black line corresponds to the convolution function defined in equation 3.2.

In absence of RF voltage, a steep onset, centered at −63 mV, is visible and corresponds to the expected energy of the Ag(111) surface state (blue trace in figure 3.9) [143]. A continuous RF bias modulation is then applied while the DC bias is swept at a given RF frequency and source amplitude (f_{RF} = 12.5 GHz , $V_{\mathrm{RF}}^{\mathrm{src}}$ = 251 meV). A broadening of 11.5 mV is induced by the RF modulation in the junction, according to the convolution function that reproduces well the broaden spectrum. This value is determined graphically by comparing the trace with applied RF with the convolution function. This method generally leads to a sufficiently

precise estimation of the broadening with respect to the more sophisticated least-squares method that finds, in this case, a broadening of (11.52 ± 0.02) meV. The RF transmission at $f_{\mathrm{RF}} = 12.5$ GHz can therefore be derived in equation 3.3. The voltages can be expressed in dBmV where 0 dBmV corresponds to an RF voltage of 1 mV RMS [124]. These units can be more convenient to use as they do not carry the logarithm function:

$$\begin{aligned} \mathrm{TF}(f_{\mathrm{RF}})[\mathrm{dB}] &= V_{\mathrm{RF}}^{\mathrm{jun}}(f_{\mathrm{RF}})[\mathrm{dBmV}] - V_{\mathrm{RF}}^{\mathrm{src}}[\mathrm{dBmV}] \\ &= 20\log_{10}\left(\frac{V_{\mathrm{RF}}^{\mathrm{jun}}(f_{\mathrm{RF}})[\mathrm{mV}]}{1\ \mathrm{mV}}\right) - 20\log_{10}\left(\frac{V_{\mathrm{RF}}^{\mathrm{src}}[\mathrm{mV}]}{1\ \mathrm{mV}}\right) \\ &= 20\log_{10}\left(\frac{V_{\mathrm{RF}}^{\mathrm{jun}}(f_{\mathrm{RF}})[\mathrm{mV}]}{V_{\mathrm{RF}}^{\mathrm{src}}[\mathrm{mV}]}\right) \\ &= -26.8\ \mathrm{dB} \quad \text{with} \quad \left(f_{\mathrm{RF}} = 12.5\ \mathrm{GHz}, V_{\mathrm{RF}}^{\mathrm{src}} = 251\ \mathrm{mV}\right) \end{aligned} \tag{3.3}$$

To extend the measurement of the RF transmission to other frequencies, we now modulate the RF signal according to the chopping scheme presented in figure 2.24 such that the lock-in signal ΔI is proportional to the rectified current. The tunneling voltage V_t is typically chosen at the center of the conductance step to maximize the rectified current induced by the RF modulation. The TF measurement is done in three steps. First, we record the lock-in signal ΔI while sweeping the source amplitude $V_{\mathrm{RF}}^{\mathrm{src}}$ at $f_{\mathrm{RF}} = 12.5$ GHz, as shown in figure 3.10 (left). Second, by swapping the axes of this graph, and using the transmission calculated in equation 3.3, we plot in figure 3.10 (right) the corresponding RF junction amplitude as a function of lock-in signal. A 3$^{\mathrm{rd}}$ order polynomial fit is performed and establishes the analytical relation $V_{\mathrm{RF}}^{\mathrm{jun}}(\Delta I)$ [15]. Third, we aim for a constant RF junction amplitude while sweeping

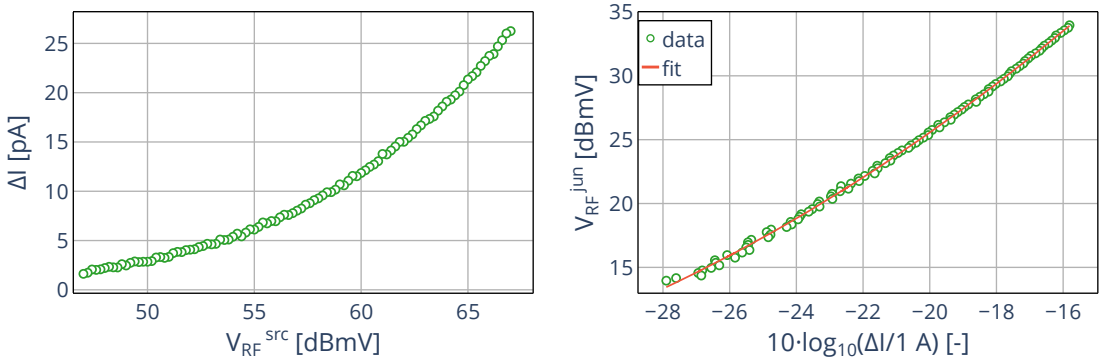

Figure 3.10: Experimental steps realized for the measurement of the TF. The demodulated current signal is calibrated to the source amplitude $V_{\mathrm{RF}}^{\mathrm{jun}}$ using the broadening of a non-linear I(V) trace (top panels).

the RF frequency. To do so, we provide an initial list of RF source amplitudes, applied at each frequency, and we record ΔI. After one iteration, the relation $V_{\mathrm{RF}}^{\mathrm{jun}}(\Delta I)$ allows to estimate the transmission $V_{\mathrm{RF}}^{\mathrm{jun}}[\mathrm{dBmV}] - V_{\mathrm{RF}}^{\mathrm{src}}[\mathrm{dBmV}]$. However, more than one iteration is generally required for a more precise measurement of the TF. We use three frequency sweep iterations

for measuring our TF, shown in figure 3.11 for $f_{RF} \in [10\ kHz, 40\ GHz]$. Using this TF, a constant junction amplitude of 20 dBmV (or 10 mV zero-to-peak) can be applied at frequencies between 10 GHz and 20 GHz and is shown in figure 3.12.

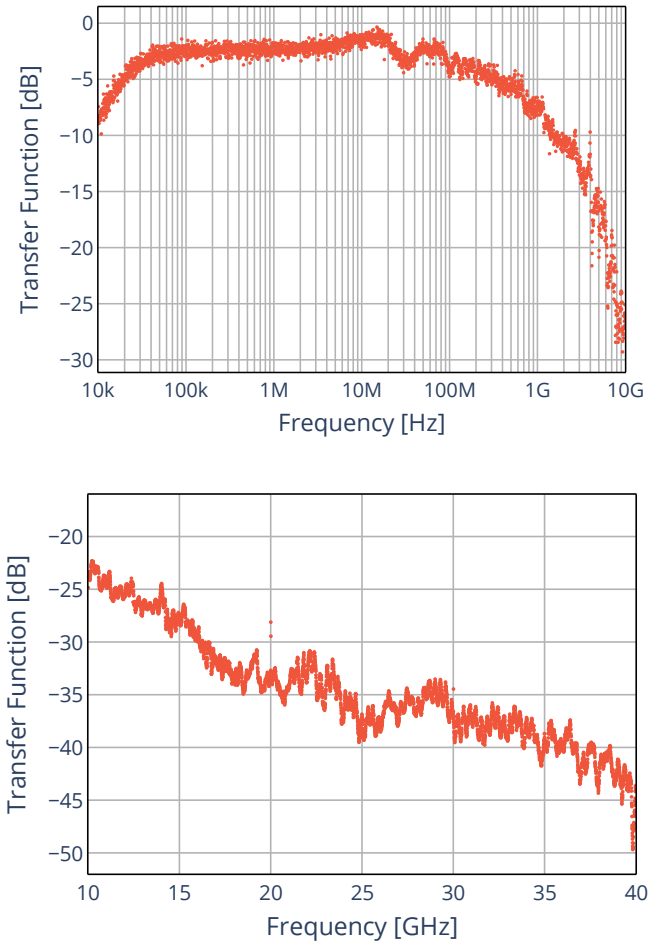

Figure 3.11: TF of our ESR-STM setup, split into two frequency intervals.

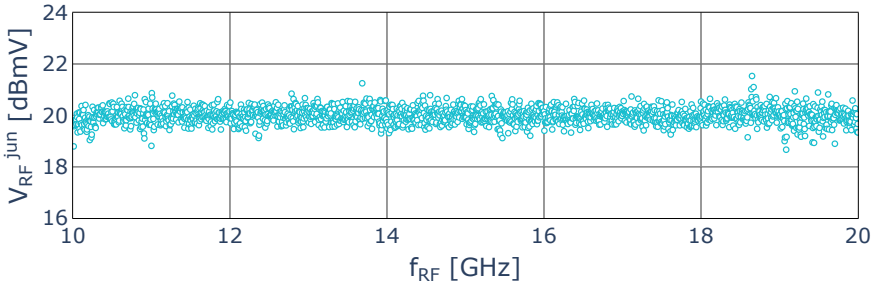

Figure 3.12: An RF junction amplitude of 20 dBmV is applied using the TF in figure 3.11.

Figure 3.11 shows the TF used for high-frequency QSR (top) and ESR-STM (bottom) experiments. Both TFs were measured at different times and their transmissions at 10 GHz do not exactly match. A change in the transmission can be explained by variations of the temperature profile of the stainless steel semi-rigid RF wire. We observe that our TF can change by nearly 2 dB at a given frequency on a period of measurement (~ 14 hours). That is why it has to be characterized before any frequency sweep experiments to ensure a constant junction amplitude. In figure 3.11, the RF transmission is excellent up to 300 MHz where it starts to drop to −25 dB. At higher frequency, it decreases down to −45 dB at $f_{\mathrm{RF}} = 40$ GHz. Transmitting RF voltages in the tunneling junction is still possible at high frequencies given the large power output available from the RF generator. A comparison can be made with the transfer functions published by Paul *et. al.* [124] and Seifert *et. al.* [15]: reference [124] uses a similar ESR setup with RF modulations applied from the STM tip as reference [15] uses an antenna in the tunneling junction. Note that they define their TF in a different way:

$$\begin{cases} \mathrm{TF}_{\mathrm{Paul}} = V_{\mathrm{RF}}^{\mathrm{jun}}[\mathrm{dBmV}] - P_{\mathrm{RF}}^{\mathrm{src}}[\mathrm{dBm}] = \mathrm{TF}_{\mathrm{EPFL}} + 50 \\ \mathrm{TF}_{\mathrm{Seifert}} = 10\log_{10}\left(\frac{V_{\mathrm{RF}}^{\mathrm{jun}}[\mathrm{mV}]}{V_{\mathrm{RF}}^{\mathrm{src}}[\mathrm{mV}]}\right) = \mathrm{TF}_{\mathrm{EPFL}}/2 \end{cases} \tag{3.4}$$

where $P_{\mathrm{RF}}^{\mathrm{src}}$ is the RF source power in dBm, $V_{\mathrm{RF}}^{\mathrm{jun,\,src}}$ are zero-to-peak voltages, and $\mathrm{TF}_{\mathrm{EPFL}}$ is our transfer function. The number 50 in equation 3.4 comes from the conversion of the RF source power in dBm to voltage amplitude in dBmV, for a cable impedance of 50 Ω. We show in figure 3.13 the two TF from references [15, 124].

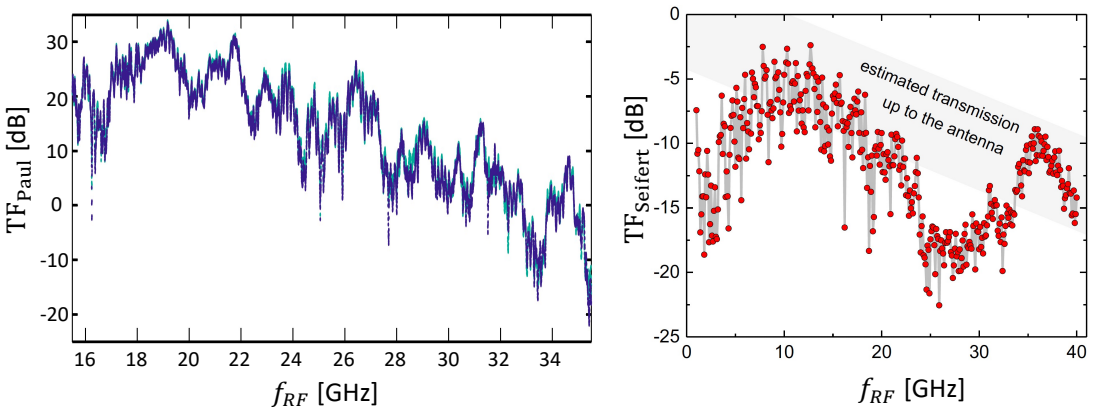

Figure 3.13: TFs taken from references [15, 124] and defined according to equation 3.4.

Our TF is on the same order of magnitude as the ones presented in references [15, 124] especially at frequencies below 32 GHz. $\mathrm{TF}_{\mathrm{Paul}}$ experiences a stronger decrease than $\mathrm{TF}_{\mathrm{EPFL}}$ after this frequency. However, $\mathrm{TF}_{\mathrm{Seifert}}$ is higher and more stable than our TF through the whole frequency range.

We can estimate the RF transmission from the 300 K flange feedthrough down to the tunneling junction by removing the cable loss contributions presented in figure 3.7. Figure 3.14 shows the TF from 10 GHz to 40 GHz after removing the contribution from the 6 m RF cable

and from the 1 dB attenuator.

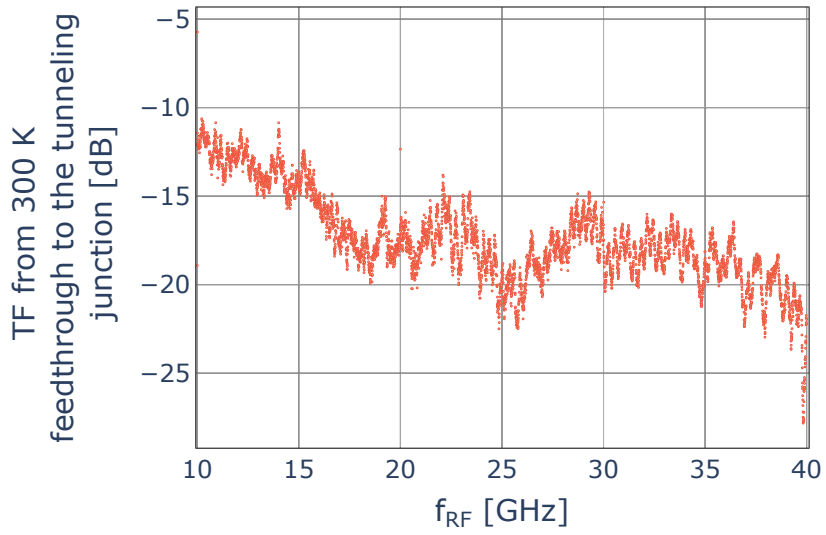

Figure 3.14: Estimate of the TF from the 300 K flange feedthrough down to the tunneling junction.

Comparing figures 3.11 and 3.14 shows that a major contribution of the attenuation comes from the long RF cables used in air. Our TF in figure 3.14 is now similar to $TF_{Seifert}$. However, the length of our 6 m cable cannot be reduced as the RF generator has to be placed outside of the acoustic chamber since it produces acoustic noise when running.

3.3 Sample Preparation and Growth

To achieve an atomically clean surface with a low density of defects, sputtering and annealing cycles are performed to the sample. The sputtering is done by the bombardment of Ar+ ions on the crystal surface using a high-voltage sputter gun. This process is followed by an annealing process that consists of heating the sample at a high temperature while staying below its melting point. In this thesis, only two single crystals are prepared, Ag(111), for the TF measurement, and Ag(100) on which MgO is grown. The preparation parameters for the two crystals are the same. The sputtering cycle is run over 30 minutes in an argon partial pressure of $1.0{\cdot}10^{-7}$ mbar. An annealing cycle is then started with a ramp from room temperature to 886 K at a rate of 100 K/min. The sample is kept at 886 K for 15 minutes before cooling it down at a rate of 20 K/min. The MgO growth takes place after the last annealing when the sample is cooling down from 886 K. The growth is controlled and optimized to obtain wide and regular MgO thin films. The growth of MgO is made by deposition of atomic Mg vapor from a Knudsen cell in an oxygen atmosphere. Table 3.1 summarizes the parameters used for the growth on the Ag(100) single crystal. Figure 3.15 shows an STM image of the MgO thin films grown on Ag(100), using the parameters listed in table 3.1.

Parameters	Value
Oxygen partial pressure [mbar]	$1.0 \cdot 10^{-7}$
Knudsen cell temperature [K]	613
Sample temperature [K]	756
Deposition time [min]	15

Table 3.1: Optimized parameters found for the growth of thin MgO films. The temperatures are the ones read in the lab, measured by different thermocouples.

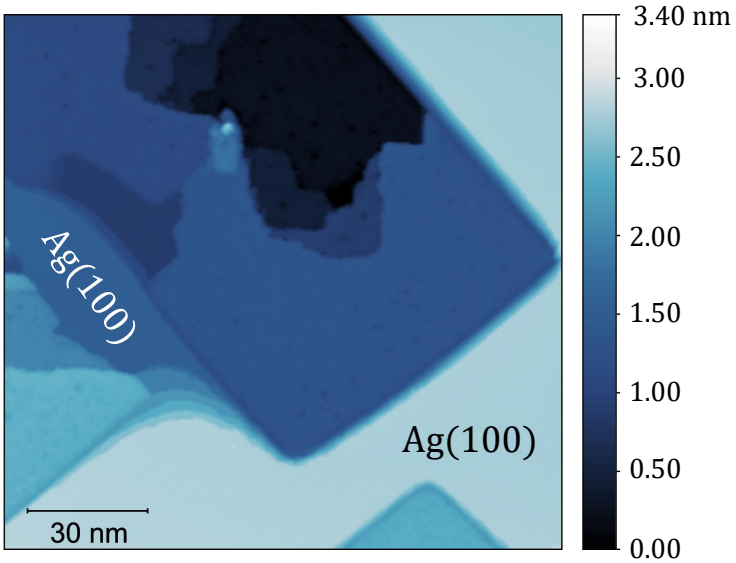

Figure 3.15: STM image of MgO thin films grown on Ag(100), measured at $T_{\mathrm{STM}} = 4.2$ K. The tunneling parameters are $I_t = 100$ pA and $V_t = 2.20$ V.

One sees that the MgO forms squared films of approximately 100 nm side, with different ML heights. For a tunneling bias below 2.5 V, it has been shown that the MgO reduces exponentially the probability of electron tunneling into the substrate [144]. Therefore, in a constant current STM image as in figure 3.15, a higher ML thickness of MgO corresponds to a lower apparent height with respect to a lower ML-thick MgO film. The determination of the absolute number of ML is however questionable: some groups start the MgO identification from 1 ML [51, 145, 146] as others start from 2 ML, assuming that 1 ML height of MgO occurs infrequently on the Ag(100) surface [124]. In this thesis, we assign the number of ML as in reference [49], assuming that the 1 ML MgO is unfavorable and only present at the edges of the more common 2 ML height patch. In addition to the apparent height measurement, another method is used to determine the ML height of MgO and is reported in reference [144]. It is known as Field-Emission Resonance (FER) spectroscopy and is operated with the feedback loop active. The tunneling bias is swept up to high values such that a strong electric field gradient induces electron emission between the tip and the sample. FER spectroscopy gives information about surface states and the sample's work function [144, 147]. Figure 3.16 shows the characteristic FER spectra measured on different surfaces.

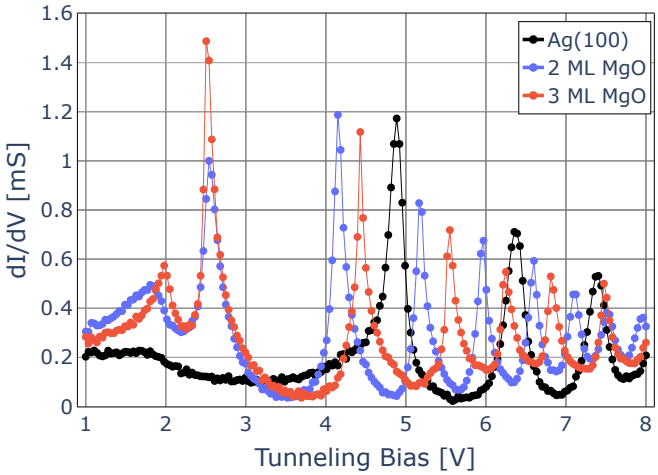

Figure 3.16: FER spectroscopies on Ag(100), 2 ML MgO and 3 ML MgO. All traces are normalized to the same tunneling conductance with I_t = 70 pA and V_t = 3.0 V.

As studied in reference [145], the energy separation between the first two MgO resonance peaks decreases with increasing MgO thickness. We, however, found that the position and spacing of these peaks depend strongly on the tip atomic termination. We therefore do not rely exclusively on this method and prefer to combine apparent height measurement with FER spectroscopy to assign the ML thickness of MgO films, for an underlying flat crystal surface.

The deposition of atoms on MgO is realized *in-situ* using a triple electron beam evaporator capable of depositing two species at the same time. Typical depositions are done over 40 s at a sample temperature below 10 K. Figure 3.17 shows an STM image after the deposition of Fe and Dy atoms on the sample surface.

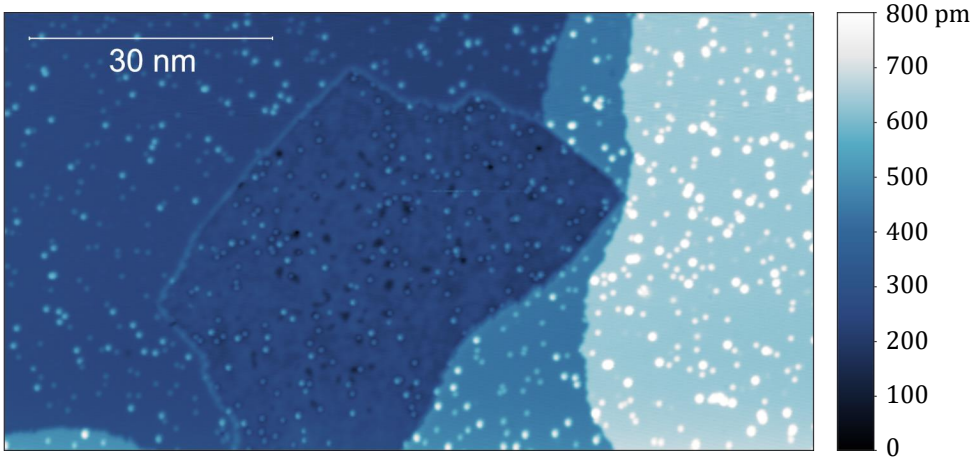

Figure 3.17: 105 nm x 90 nm STM image after the atom deposition on MgO/Ag(100). The tunneling parameters of the image are V_t = 100 mV, I_t = 10 pA.

The delimited patch appearing at the center of the image corresponds to a 2 ML-thick MgO film. The adatoms appear as protrusions in the STM image and their apparent height depends on their electronic affinity with the substrate, their adsorption site on the MgO lattice and on the tip apex.

3.3.1 Adatoms Adsorbed on Magnesium Oxide (MgO)

Figure 3.18 illustrates the three adsorption sites on the MgO lattice for the different adatoms deposited in this thesis. It is important to define and distinguish these sites as they provide different CF symmetries and therefore different magnetic properties for a given adatom. Table 3.2 introduces the adatom nomenclature and the corresponding adsorption sites.

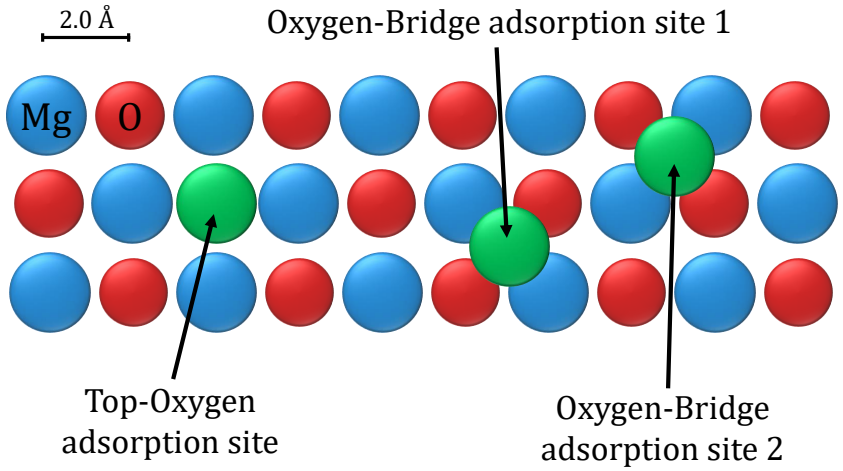

Figure 3.18: The different adsorption sites on MgO for TiH, Fe, Dy and Tb.

Adsorbed Atom or Molecule	Top-Oxygen site	Oxygen-Bridge site 1	Oxygen-Bridge site 2
Fe	X		
TiH_O	X		
TiH_B		X	X
Dy^{top}	X		
Dy^{br}		X	X
Tb^{top}	X		
Tb^{br}		X	X

Table 3.2: Notation used for the adsorbed atoms and molecules on their corresponding sites on MgO.

Fe is the only adatom in table 3.2 to be adsorbed exclusively on the top-Oxygen site of MgO. Other metals can each appear as top-Oxygen and Oxygen-bridge adatoms. The relative abundance of top-Oxygen and Oxygen-bridge sites depends on the deposition temperature and strongly on the thickness of the MgO film [97]. Since the main residual gas in UHV is hydrogen which has a high affinity with Ti, we assume that the evaporated Ti atoms dissociate the impinging H_2 molecules and bind one H atom [148]. Whereas Ti has a spin $S = 1$ in the gas phase, the TiH molecule adsorbed on the three sites of MgO has $S = 1/2$ [16]. Figures 3.19, 3.20 and 3.21 are STM images of the seven adatoms introduced in table 3.2. They are all adsorbed on a 2 ML-thick MgO film and we report their apparent heights that depend on the tunneling parameters, indicated for each image.

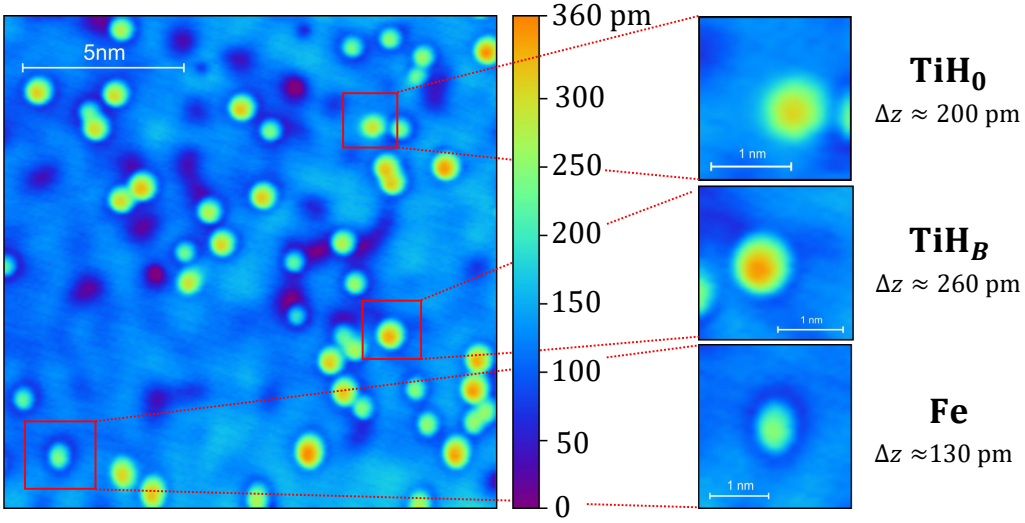

Figure 3.19: STM image of Fe adatoms and TiH molecules on 2 ML-thick MgO. The tunneling parameters are $V_t = 100$ mV, $I_t = 20$ pA.

In the three STM images, the MgO surface presents some small dark spots, appearing at a lower apparent height with respect to the MgO film. They are either attributed to defects or to a higher ML-thick MgO film starting to grow locally on top of the existing layer. In any case, we did not conduct experiments on adatoms adsorbed on these sites. In the three STM images, adatoms do not appear perfectly round as one should expect, especially in figure 3.21. This typically originates from the tip apex that is not always single-atomic and generates additional spatial features on the adatoms.

Finally, to address their distinct magnetic properties with SP-STM, it is necessary to identify the different adatoms on the surface. The best identification method is to combine apparent height measurement with STS if the adatom or molecule shows spectroscopic features at accessible tunneling biases. We show in this thesis the characteristic STS spectra of Fe, TiH_B and TiH_O in chapter 4 and of Tb^{br} in chapter 6. The other adatoms in table 3.2 are deduced and identified exclusively with apparent height measurements.

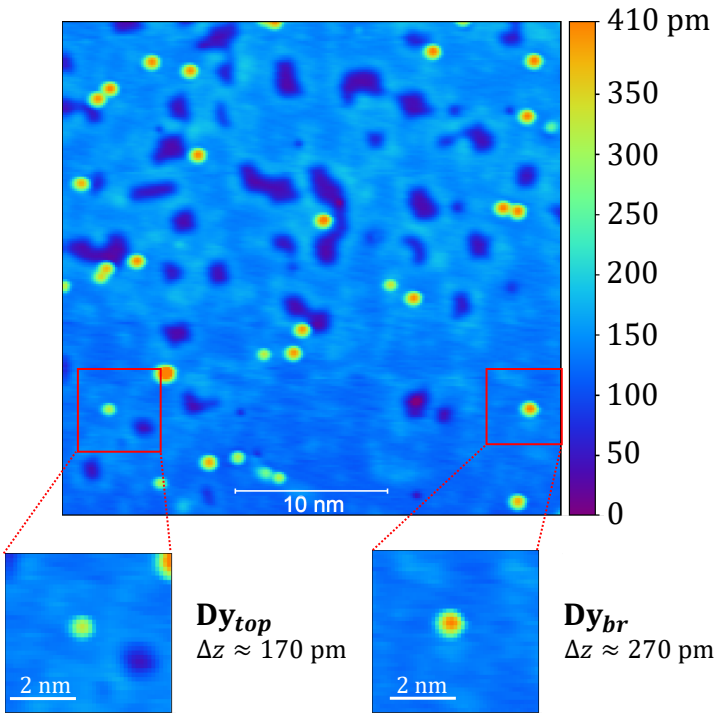

Figure 3.20: STM image of Dy adatoms adsorbed on 2 ML-thick MgO. The tunneling parameters are $V_t = 50$ mV, $I_t = 10$ pA.

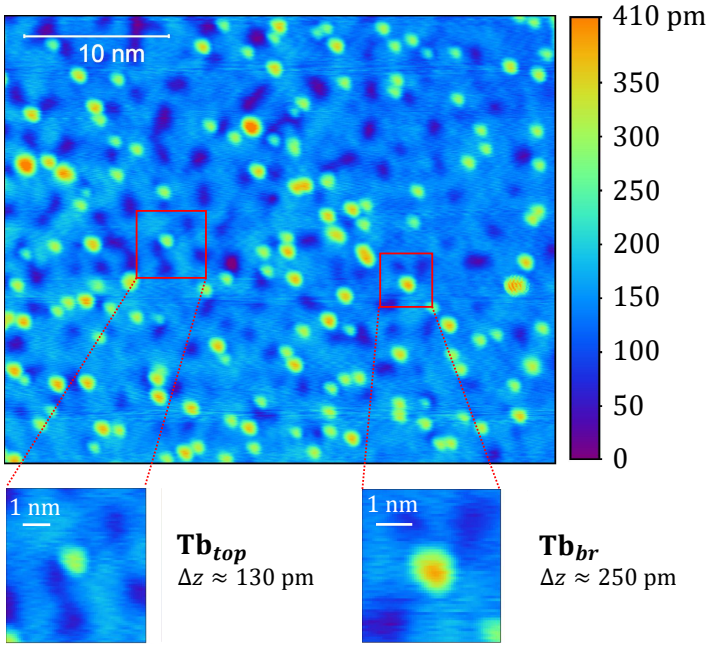

Figure 3.21: STM image of Tb adatoms adsorbed on 2 ML-thick MgO. The tunneling parameters are $V_t = 50$ mV, $I_t = 20$ pA.

4 ESR-STM on TiH Molecules Adsorbed on MgO

To characterize our RF cabling after the changes described in section 3.1.5, we investigate the well-known system TiH/MgO/Ag(100) and measure the corresponding g-factor and magnetic moment. This system is preferred to Fe/MgO/Ag(100) since the ESR amplitude reported for TiH is about twice as large as for Fe, at equivalent experimental parameters [45]. The expected resonance condition of TiH on MgO is around 25 GHz/T [117]. It is accessible at relatively low RF frequencies, where the RF transmission is high, and at sufficiently large magnetic fields to polarize our tip. This offers a large RF power range in the tunneling junction to maximize our chance to detect an ESR signal. As described in section 2.4.1, our SP tip has to be atomically built to induce and sense coherent transitions between Zeeman-split states. However, we observe that only few SP tips can resolve an ESR contrast above our noise level. A first part of this chapter is thus dedicated to the preparation of an ESR tip. We then present and discuss our ESR results on TiH molecules at $T_{\mathrm{STM}} = 0.4$ K and $T_{\mathrm{STM}} = 4.2$ K.

4.1 Preparation of an ESR Tip

Our STM tip is made by electro-chemical etching from a 0.25 mm diameter wire of Platinum-Iridium Pt(90%)/Ir(10%). The non-magnetic bulk tip is spin-polarized *in situ* by picking up several magnetic Fe atoms adsorbed on the MgO surface. A magnetic cluster is formed at the tip apex that acts as a spin valve through the TMR effect.

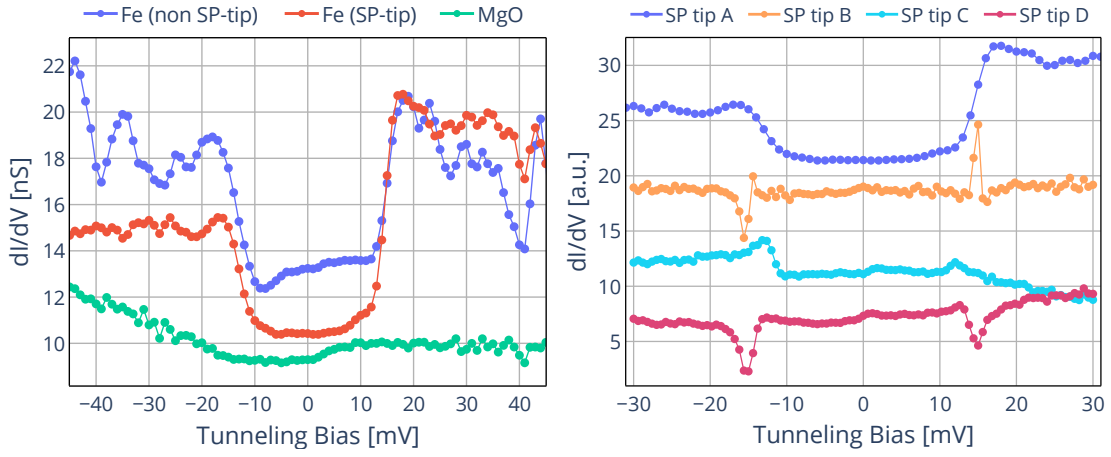

Figure 4.1: Left: different STS traces measured on Fe and MgO, with a non-SP tip (blue, green) and SP tip (red). The tunneling parameters are $V_t = 100$ mV, $I_t = 5$ pA and a lock-in modulation amplitude of 1 mV is applied. Traces are measured at $T_{\mathrm{STM}} = 4.2$ K and $B_z = 0.6$ T. Right: different STS traces measured with different SP tips on Fe. Offsets are applied for clarity.

On figure 4.1 (left), STS are performed on Fe before (red trace) and after (blue trace) picking up 3 Fe atoms in a magnetic field of $B_z = 0.6$ T. As a result, a spin polarization of approximately 26% is acquired. The steps at ±14 mV are identified as spin excitations from $|S_z = \pm 2\rangle$ to $|S_z = \pm 1\rangle$ induced by inelastic tunneling electrons. If we assume that the tip is polarized along the external magnetic field direction, a higher step at positive tip bias (red

trace in figure 4.1) imposes transitions $|S_z = -2\rangle \rightarrow |S_z = -1\rangle$ as the dominant contribution to the asymmetric signal. Figure 4.1 (right) shows how the different SP tips can lead to different spectra on Fe. We use STS on adsorbed atoms to identify the signature of a given SP tip, as not all tip configurations are producing ESR signals. Similarly to Fe, Oxygen-bridge TiH_B and top-Oxygen TiH_O reveal characteristic features in STS. Figures 4.2 and 4.3 show the spectra of the two adsorption sites TiH molecules on MgO for an SP tip (blue) and a non-SP tip (red). For both molecules, the step at 0 mV indicates the spin polarization of our tips and can change for different tip terminations.

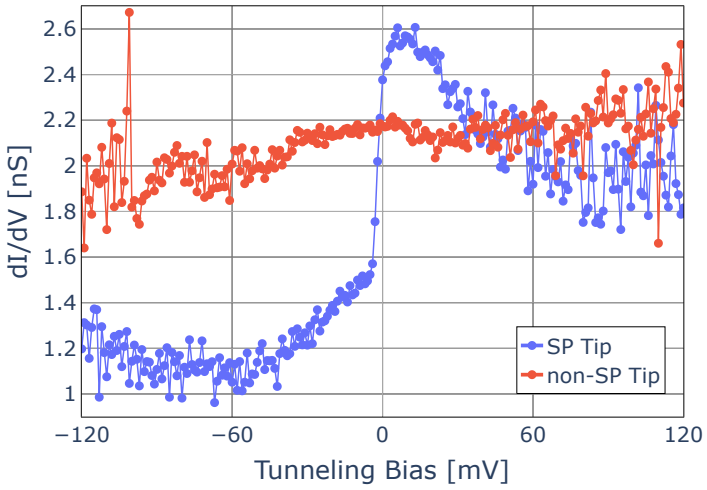

Figure 4.2: STS traces measured on TiH_B at $T_{STM} = 4.2$ K with an SP and non-SP tip.

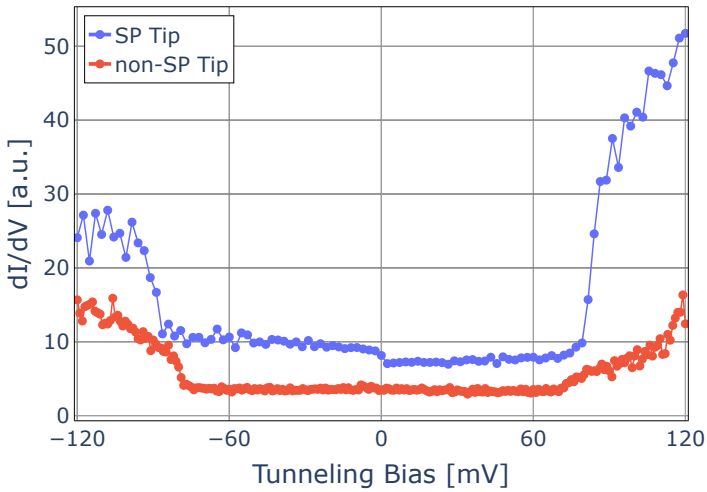

Figure 4.3: STS traces measured on TiH_O at $T_{STM} = 0.4$ K with an SP and non-SP tip.

As the process of building an ESR tip is time-consuming, we need to verify fast if a given SP tip can reveal ESR contrast. The fastest method is to perform tip-field sweeps (see section 2.4.1). In contrast, frequency sweeps are more time-consuming, since they require to characterize the TF, that can change up to 2 dB at a given frequency and on a period of measurement (~ 14 hours). Figure 4.4 shows tip-field sweeps measured on TiH_B for different RF frequencies. For each data point, the lock-in signal is divided by the tunneling current such that, in the absence of a resonance, a flat background signal is obtained.

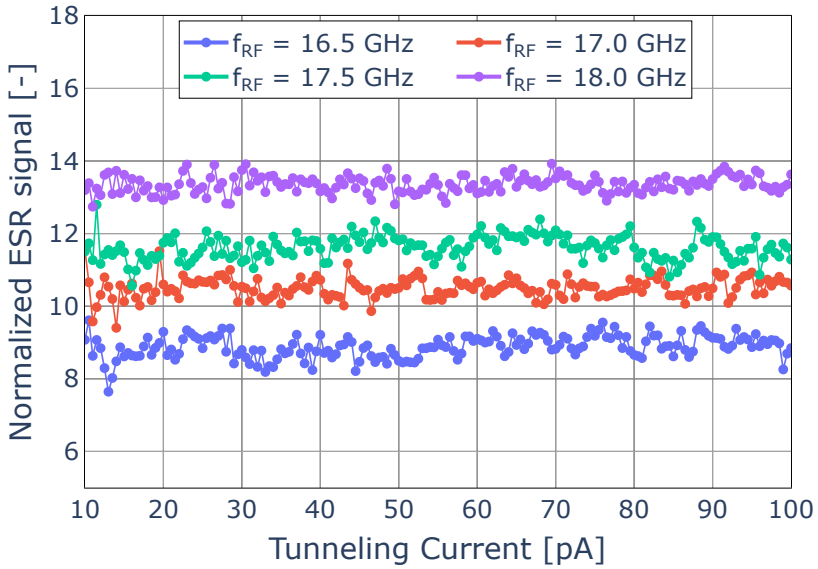

Figure 4.4: Tip-field sweep measurement at $T_{\mathrm{STM}} = 0.4$ K on TiH_B, showing no ESR signals in an external magnetic field of $B_{\mathrm{xy}} = 600$ mT and at $V_{\mathrm{RF}}^{\mathrm{jun}} = 28$ mV. Offsets are applied for clarity.

This SP tip, used to measure the STS spectrum in figure 4.2, does not show ESR contrast above our noise level and within this tunneling current range. As introduced in chapter 3, we recall that $V_{\mathrm{RF}}^{\mathrm{src}}$ and $V_{\mathrm{RF}}^{\mathrm{jun}}$ are the zero-to-peak amplitudes of the RF bias modulation applied from the generator and in the tunneling junction respectively. The choice of RF frequencies and magnetic field used in figure 4.4 is motivated by the existing ESR measurements on TiH_B [118]. In our case, most of the tips did not show ESR contrast, as in figure 4.4. In figure 4.5, we report STS spectra measured on Fe and TiH_B with an SP tip showing ESR contrast. A spin polarization of 50 % can be estimated from the IETS on Fe. This SP tip is able to detect ESR signals, measured on TiH_B and presented in section 4.3.

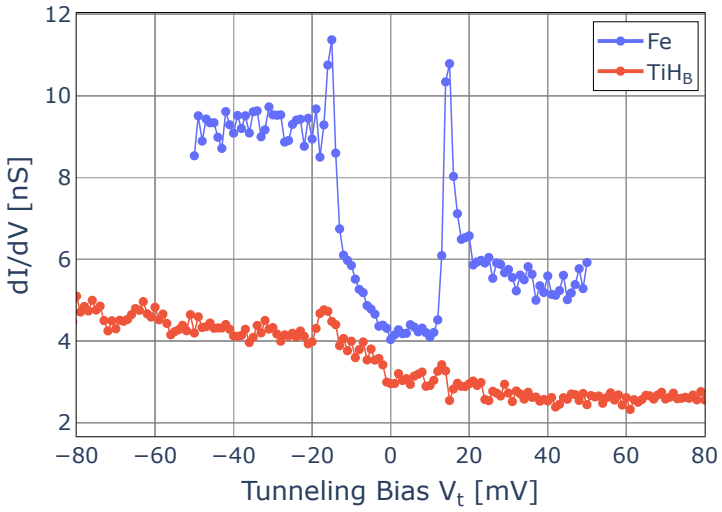

Figure 4.5: STS traces recorded with the same SP tip on Fe and TiH_B at $T_{STM} = 0.4$ K. This tip reveals ESR signals on TiH_B.

4.2 Fitting ESR Lineshapes

Given the complex expression of the ESR lineshape derived in equation 2.37, we use a Fano function with a lower number of parameters to fit our ESR signals measured with the frequency sweep method [15]:

$$\Delta I(f) = I_0 + A \cdot \frac{\left(\frac{q\Gamma}{2} + (f - f_0)\right)^2}{\left(\frac{\Gamma}{2}\right)^2 + (f - f_0)^2} \tag{4.1}$$

where A is the amplitude of the peak, q the Fano factor, Γ the FWHM, I_0 an offset and f_0 is the resonance frequency. q is equivalent to α in equation 2.38 with $\alpha = 2q/(q^2-1)$. Note that f_0 does not always correspond to the Fano function maximum and shows a strong dependency on the Fano factor q [149]. This parameter describes the asymmetry of the lineshape, similarly to β in equation 2.38, where $q = 0$ corresponds to a pure Lorentzian function. The Fano factor scales linearly with the RF amplitude and current [46]. Consequently, ESR signals measured at the same RF amplitude and tunneling current in frequency sweeps are fitted using the same Fano factor. We employ a least square method to find the optimal q_{opt} that minimizes the residuals' sum of the Fano functions fitting a data set. Finally, all error bars shown in this chapter are computed from the diagonalized covariance matrix, output by the Python *curvefit* function, and calculated from the differences between Fano fits and data.

4.3 Results at 0.4 K

We present here the results as well as the analysis of tip-field and frequency sweeps measured on TiH_B at $T_{STM} = 0.4$ K.

4.3.1 Tip-Field Sweeps

Using the tip characterized in figure 4.5, tip-field sweeps revealing ESR contrast are shown in figure 4.6 for different RF frequencies. Each ESR peak is measured as an increase of the tunneling current ΔI, and shifts linearly with the RF frequency, in a fixed external magnetic field of B_{xy} = 600 mT. The RF junction amplitude is approximately 55 mV given the average transfer function of −32 dB between 16.5 GHz and 18.0 GHz. We fit the data using the Fano function defined in equation 4.1 and replacing $(f - f_0)$ by $(I - I_0)$, where I_0 is the resonance current.

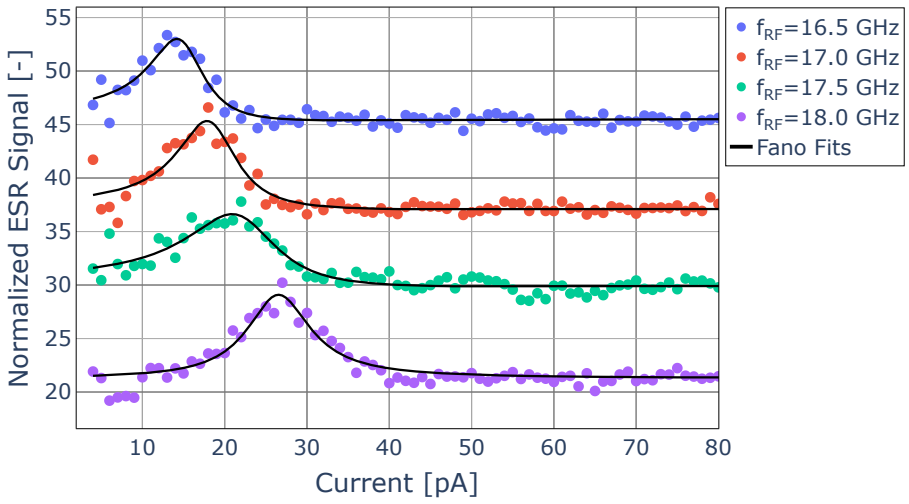

Figure 4.6: Tip-field sweeps on TiH_B at T_{STM} = 0.4 K, in an external magnetic field of B_{xy} = 600 mT and at a constant RF source amplitude of V_{RF}^{src} = 2.26 V. The tunneling bias is set to V_t = 100 meV. Offsets are applied for clarity.

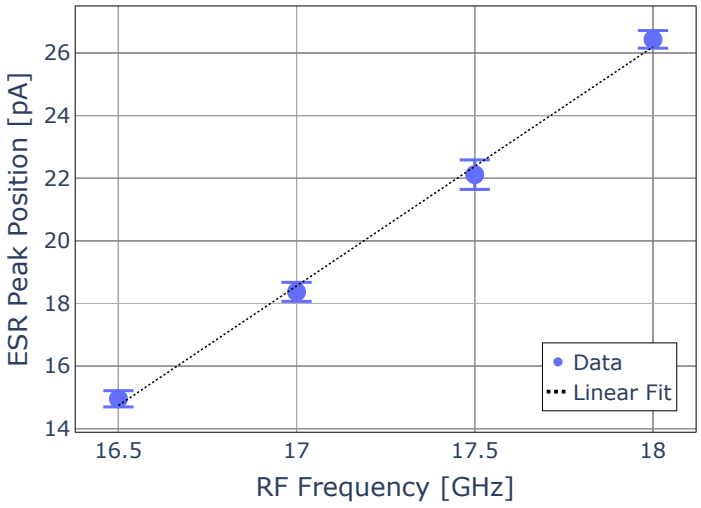

Figure 4.7: ESR peak positions in tunneling current, obtained from the Fano fits in figure 4.6.

In figure 4.7, we report the resonance tunneling current as a function of the RF frequency. A linear shift of the resonance current is observed in figure 4.7 and suggests a linear behavior of the tip magnetic field with the tunneling current, according to equation 2.29. This motivates the realization of frequency sweeps on this molecule, to measure the g-factor and the magnetic moment along the external magnetic field direction.

4.3.2 Frequency Sweeps

Frequency sweeps are performed on TiH_B at four external magnetic fields and are presented in figure 4.8.

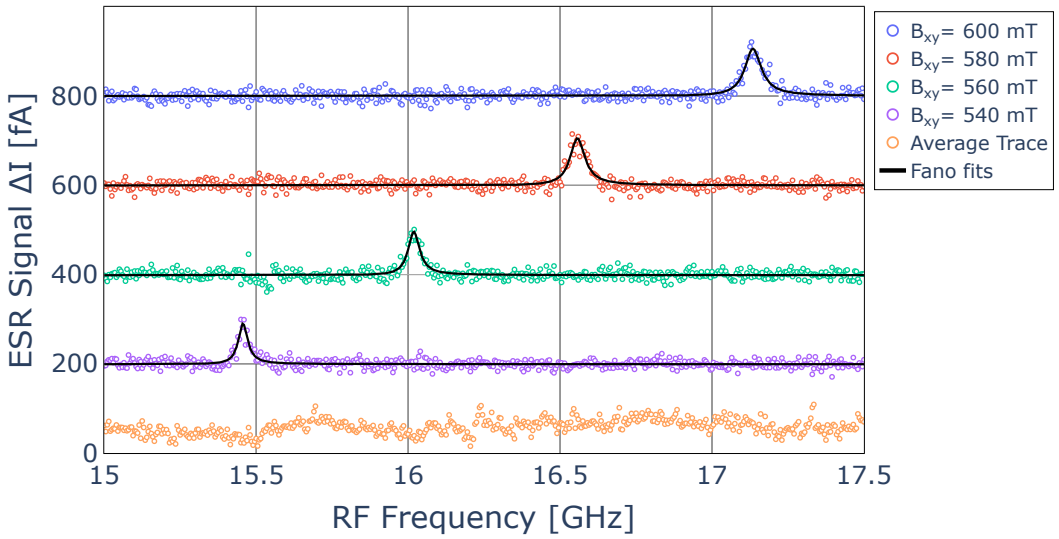

Figure 4.8: Frequency sweeps measured on TiH_B at T_{STM} = 0.4 K. The tunneling parameters are V_t = 60 mV and I_t = 15 pA with a junction amplitude V_{RF}^{jun} = 28 mV. An average trace, plotted with orange symbols, is substracted to the four sweeps and offsets are applied for clarity.

In figure 4.8, the orange trace corresponds to an average of the four sweeps, calculated outside of their respective resonance regions. This average trace is substracted to all four sweeps, for an improved signal-to-noise ratio. The optimal Fano factor fitting the traces is $q_{opt} = -0.027$, obtained by minimizing the residuals' sum of all four Fano fits with respect to the data, as shown in figure 4.9. This value is close to zero and is consistent with the Lorentzian lineshapes in figure 4.8.

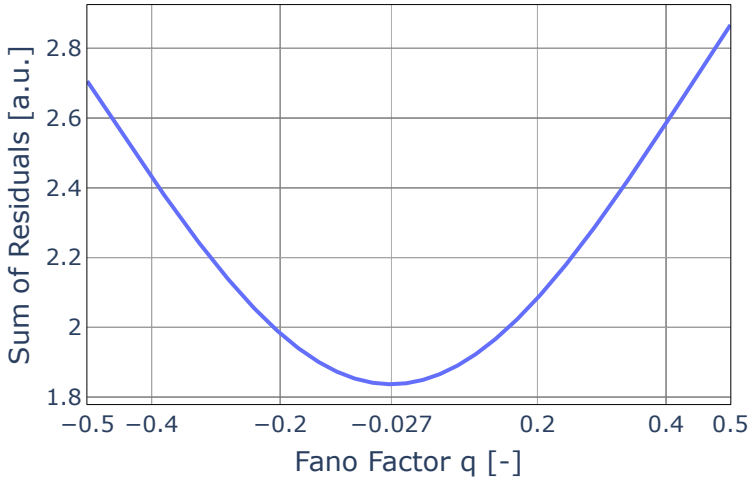

Figure 4.9: Optimal Fano Factor found for the four frequency sweep traces shown in figure 4.8.

We plot in figure 4.10 the resonance frequencies, extracted from the Fano fits of figure 4.8, as a function of B_{xy}. Error bars are not visible as the standard deviation is on the order of $10^{-4} \cdot f_{\text{RF}}$.

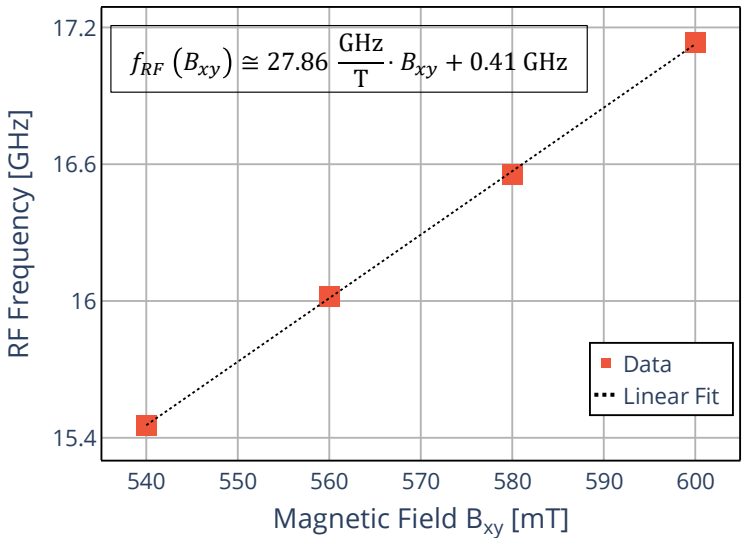

Figure 4.10: Resonance frequencies extracted from the Fano fits in figure 4.8, as a function of the external magnetic field.

A slope of approximately 27.86 GHz/T is obtained from the linear fit and is used to derive the g-factor of the TiH_B molecule. One has:

$$f_{\text{RF}} \approx (27.86 \pm 0.26) \cdot B_{\text{ext, xy}} + (0.41 \pm 0.15) \quad \text{with} \quad f_{\text{RF}} = \frac{\mu_B}{h} g_{\text{xy}} \Delta S_{\text{xy}} (B_{\text{ext, xy}} + B_{\text{tip, xy}}) \tag{4.2}$$

In equation 4.2, there are two unknowns g_{xy} and B_{tip}, for one equation. To solve it, we

assume that B_{tip} is constant and independent of $B_{\text{ext,xy}}$ in the interval [540 mT, 600 mT]. This allows the following identification:

$$\begin{cases} (27.86 \pm 0.26) \cdot 10^9 = \frac{\mu_B}{h} g_{\text{xy}} \Delta S_{\text{xy}} \rightarrow g_{\text{xy}} = (1.99 \pm 0.02) \\ (0.41 \pm 0.15) \cdot 10^9 = \frac{\mu_B}{h} g_{\text{xy}}^{\text{eff}} \Delta S_{\text{xy}} B_{\text{tip, xy}} \rightarrow B_{\text{tip, xy}} = (14.7 \pm 4.0) \text{ mT} \end{cases} \tag{4.3}$$

where $B_{\text{tip, xy}}$ is the residual resonance field when extrapolating the linear fit in figure 4.10 to $B_{\text{ext,xy}} = 0$. The g-factor is obtained while neglecting a possible variation of $B_{\text{tip, xy}}$ with the applied external field. We find $g_{\text{xy}} = (1.99 \pm 0.02)$, in good agreement with (1.953 ± 0.003), reported in reference [150] for one of the Oxygen-bridge site TiH. The molecule's magnetic moment can be derived according to equation 4.4, neglecting the tip magnetic field [122]:

$$|\mathbf{m}_{\text{TiH}_B}| \approx \left| \frac{h f_{\text{RF}}}{2\mathbf{e}_{\text{spin}} \cdot (\mathbf{B}_{\text{ext}})} \right| \approx (0.99 \pm 0.01)\mu_B \tag{4.4}$$

where $\mathbf{e}_{\text{spin}}$ corresponds to the axis along which molecule's magnetic moment lies. Given the small anisotropy of TiH on MgO, we assume that $\mathbf{e}_{\text{spin}}$ coincides with the external field orientation, along $\hat{x}\hat{y}$. The magnetic moment is therefore simply the g-factor multiplied by $0.5\mu_B$. A more precise measurement of the g-factor and of the magnetic moment requires a precise measurement of the tip magnetic field. One can characterize it by the sum of an exchange and dipolar fields as in references [45, 122]. However, quantifying the contribution of each field requires the measurement of many ESR signals, taken at different tip-sample distances. We could not perform such an experiment, given the time-consuming process of building an ESR tip with respect to our hold time of 14 hours at $T_{\text{STM}} = 0.4$ K. Also, we were not able to keep an ESR tip during the filling process of our cryostat, despite retracting the tip sufficiently away from the sample to avoid a change of the atomic termination.

In table 4.1, the fitting parameters of the ESR traces shown in figure 4.8 are listed and discussed below.

	$\mathbf{B}_{\text{xy}} = 540$ **mT**	$\mathbf{B}_{\text{xy}} = 560$ **mT**	$\mathbf{B}_{\text{xy}} = 580$ **mT**	$\mathbf{B}_{\text{xy}} = 600$ **mT**
$\lvert A \rvert$ [fA]	91.4 ± 5.2	97.6 ± 5.2	105 ± 5	106 ± 4
Γ [MHz]	37.16 ± 3.06	45.40 ± 3.52	58.55 ± 3.73	65.40 ± 3.93
q_{opt} [-]	-0.027			

Table 4.1: Parameters fitting the ESR traces in figure 4.8.

The ESR amplitudes correspond, on average, to 0.65 % of the tunneling current $I_t = 15$ pA. This value is quite low compared to what has been achieved in literature at a similar temperature and RF amplitudes. Furthermore, we observe, that ESR amplitudes increase for increasing external magnetic fields. This can be explained by a stronger tip spin polarization and a larger energy difference E_{01} with respect to $k_B T$ as $B_{\text{ext,xy}}$ increases. FWHM are reported in table 4.1 with linewidths as narrow as 37 MHz. We will discuss the importance of narrow ESR linewidths Γ and what limits a further decrease of Γ in section 4.5.

4.4 Results at 4.2 K

To study the effect of temperature on the ESR lineshape, we measure ESR signals on TiH_O at a higher temperature T_{STM} = 4.2 K. Similarly to the previous section, we use an in-plane magnetic field of $B_{ext,xy}$ = 600 mT and we identify an ESR-active tip in tip-field sweeps followed by frequency sweep measurements. A more detailed analysis is provided in this section, including a measurement of the ESR lineshape as a function of the RF amplitude.

4.4.1 Tip-Field Sweeps

Tip-field sweeps on TiH_O are shown in figure 4.11. The resonance tunneling current is plotted as a function of the RF frequency in figure 4.12: a linear behavior confirms that the tip magnetic field scales linearly with the tunneling current. Compared to figure 4.6, the ESR signals in figure 4.11 are spread out over a wider current range. This implies a weaker effect of $B_{tip,\,xy}$ sensed by the adsorbed molecule in figure 4.11. The ESR linewidth increases and the amplitude decreases as the resonance condition moves to higher currents. This is mainly due to the decrease of T_2 at higher currents, suggesting that each tunneling electron from the tip interacts with the TiH spin and induces a loss of phase information [45, 46]. Moreover, ESR signals shift towards higher currents with decreasing RF frequencies. This can be understood as follow: as the tunneling current increases, the tip magnetic field, sensed by the molecule, reduces linearly the effect of the external magnetic field on the resonance condition. This implies that $\mathbf{B}_{tip,\,xy}$ is anti-aligned with $\mathbf{B}_{ext,xy}$. This behavior is opposite to what is shown in figure 4.6, at T_{STM} = 0.4 K. We provide a simplified model in figure 4.13 to explain these two opposite behaviors. In this model, we consider only the dipolar field from the SP tip, and neglect the influence of the exchange interaction field.

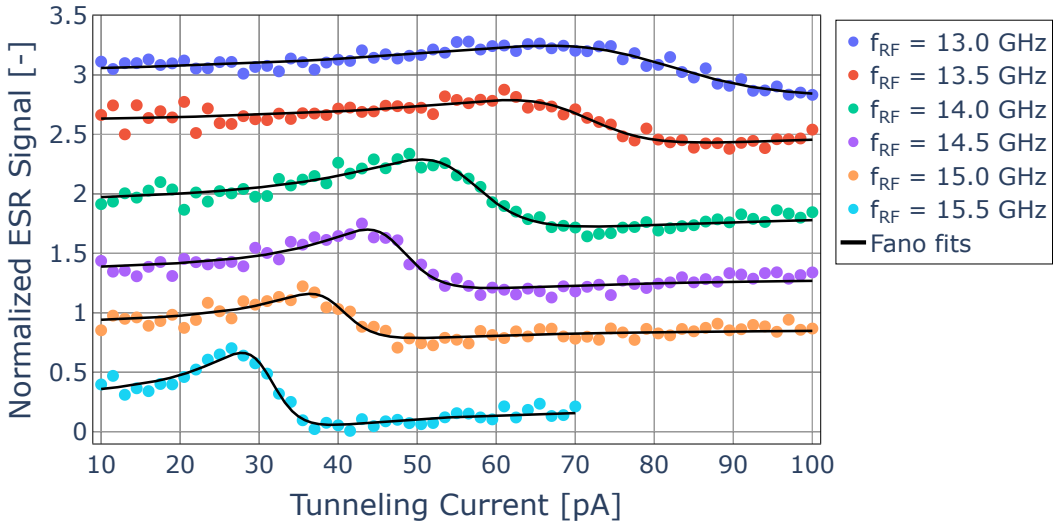

Figure 4.11: Tip-field sweeps measured on TiH_O revealing a shift of the ESR condition for different f_{RF} frequencies. Sweeps are performed at B_{xy} = 600 mT and V_t = 100 mV, for a source amplitude V_{RF}^{src} varying between 2.26 V and 2.40 V.

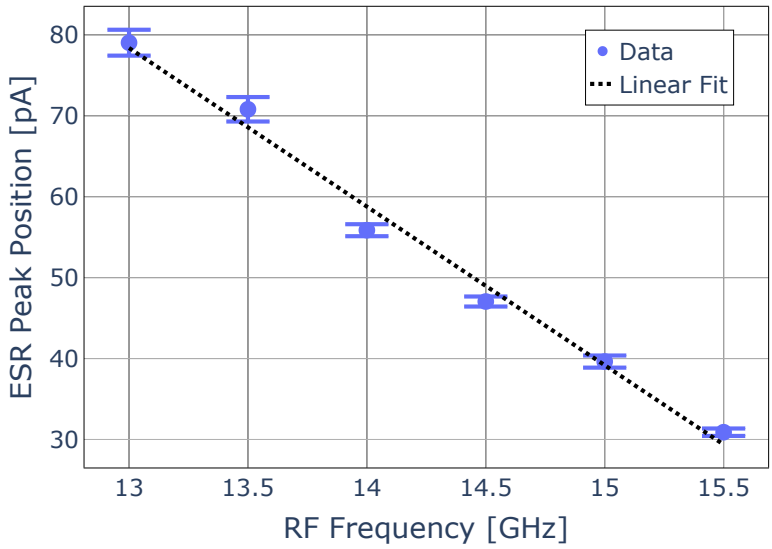

Figure 4.12: ESR peak positions in tunneling current extracted from the Fano fits of figure 4.11, as a function of the RF frequency used.

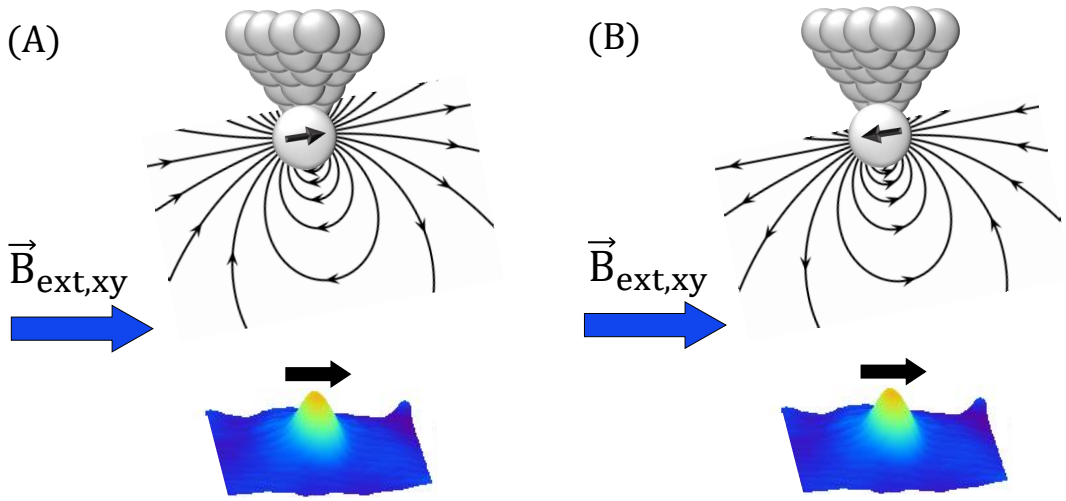

Figure 4.13: Dipolar magnetic field generated by an SP tip for a ferromagnetic (A) and antiferromagnetic alignment (B) between the tip's and molecule's magnetic moments. An STM image of TiH_B is shown, and the black arrow indicates the molecule's magnetic moment, aligned with the external field.

In figure 4.13, the direction of the dipolar field lines, closed to the molecule, determines the relative orientation of $\mathbf{B}_{\text{tip}}$ with respect to $\mathbf{B}_{\text{ext}}$. Panel (A) explains the behavior of the resonance condition in figure 4.11, where the total field sensed by the molecule along $\hat{x}\hat{y}$ is $B_{\text{ext,xy}} - B_{\text{tip,xy}}(I_t)$. In panel (A), the tip's and molecule's magnetic moments are ferromagnetically aligned. In contrast, panel (B) explains figure 4.6, where the total field sensed by the molecule along $\hat{x}\hat{y}$ is $B_{\text{ext,xy}} + B_{\text{tip,xy}}(I_t)$. In this case, the tip's and molecule's magnetic moments are anti-ferromagnetically aligned.

Controlling the lineshape of ESR-STM signals is an essential step for probing precise and reliable information on a magnetic adsorbed species and for sensing magnetic interactions from its local surface environment. For example, the ESR lineshape can be controlled with the RF amplitude applied in the tunneling junction. We present in figure 4.14 the effect of V_{RF} on ESR signals measured on a TiH_O molecule. Experimentally, the source amplitude $V_{\text{RF}}^{\text{jun}}$ is controlled from the RF generator and can be converted into the junction amplitude $V_{\text{RF}}^{\text{jun}}$ using our TF. The amplitudes in figure 4.14 are extracted from the fits and shown as a function of V_{RF} in figure 4.15.

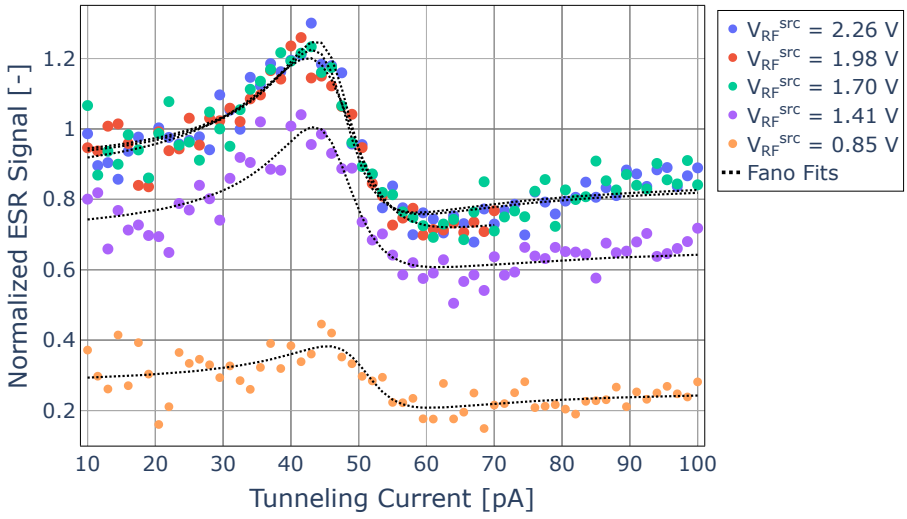

Figure 4.14: RF amplitude dependency of the ESR lineshape, measured at $f_{\text{RF}} = 14.5$ GHz, $B_{\text{xy}} = 600$ mT and $V_t = 100$ mV on TiH_O.

In figure 4.15, the amplitude increases with increasing V_{RF}, up to a saturation value for which the RF voltage is strong enough to equalize the population of states $|0\rangle$ and $|1\rangle$ [14, 46]. This behavior confirms that $V_{\text{RF}}^{\text{jun}}$ is proportional to the Rabi rate Ω, and that its effect on the molecule drives the ESR transitions. The FWHM of signals in figure 4.14 are relatively constant with respect to $V_{\text{RF}}^{\text{jun}}$, whereas a linear increase is expected considering equation 2.39 and is reported in references [14, 46]. We can explain our results by the presence of strong decoherence sources that reduce the coherence time T_2, beyond the broadening effect of $V_{\text{RF}}^{\text{jun}}$ on the FWHM. Strong variations in the tip-sample distance and the corresponding variation of B_{tip} on a short timescale could lead to such a broadening.

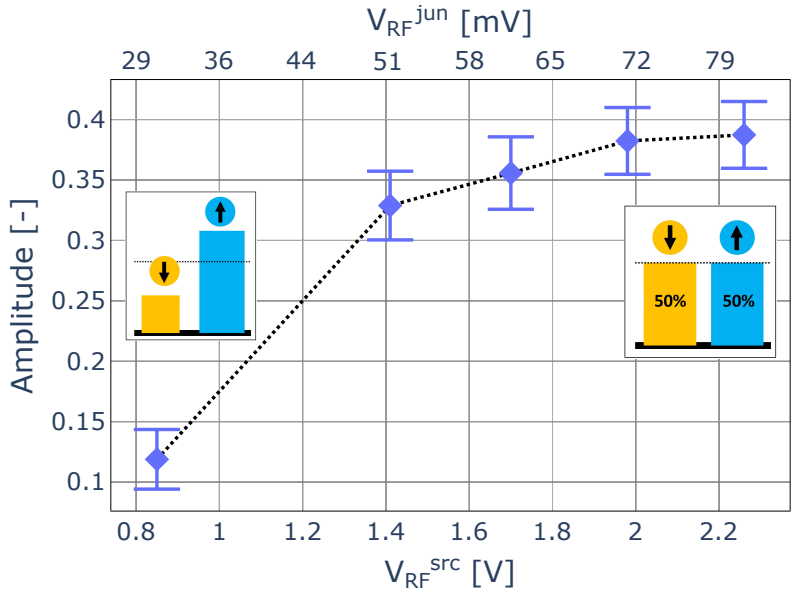

Figure 4.15: ESR signal amplitudes as a function of V_{RF}. The molecule's magnetic ground and excited state populations are illustrated in blue and yellow respectively, changing under the application of V_{RF}.

The data presented so far, at T_{STM} = 4.2 K, were acquired on the same TiH_O molecule. But does the ESR lineshape change when other molecules, adsorbed on the same site, are addressed with the same ESR tip? To answer this question, we show in figure 4.16 different tip-field sweeps measured with the same tip on TiH_O molecules, labeled from A to D.

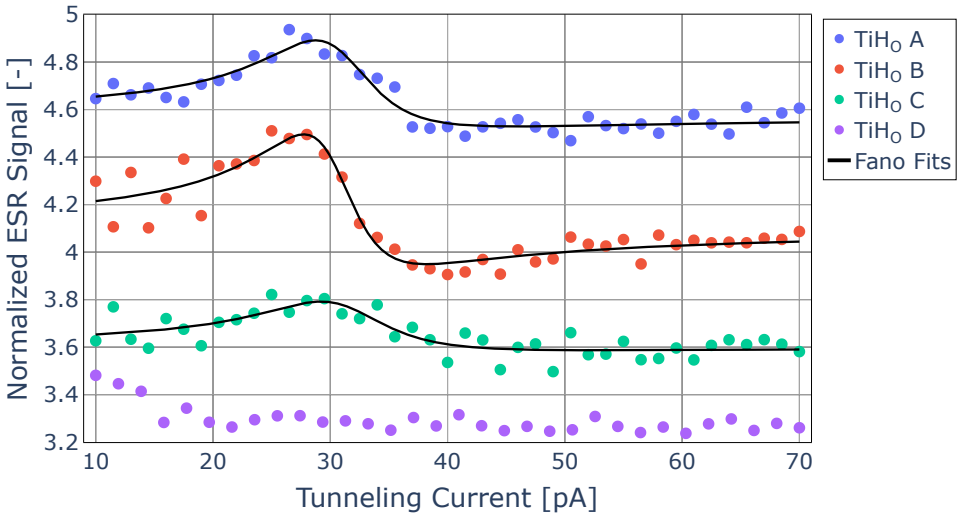

Figure 4.16: Tip-field sweeps measured on TiH_O molecules at T_{STM} = 4.2 K, B_{xy} = 580 mT, f_{RF} = 15 GHz and V_{RF}^{src} = 2 V. A DC tunneling voltage of V_t = 100 mV is applied.

All molecules are isolated on the surface, with no other magnetic species in a radius of

$r \approx 3$ nm. This prevents the influence of magnetic stray fields from nearby adatoms on the resonance condition. For example, the static dipolar magnetic field sensed by a TiH molecule and generated by an Fe adatom at a distance $r \approx 3$ nm is around $B_{\mathrm{Fe}} \approx \frac{\mu_0 m_{\mathrm{Fe}}}{4\pi r^3} \approx 0.2$ mT, using the dipolar field approximation. We use $m_{\mathrm{Fe}} = 5.2\ \mu_B$ taken from reference [38] and assume that the magnetic moment of Fe is stable in the out-of-plane direction. This field is 3 orders of magnitude lower compared to $B_{\mathrm{ext,xy}}$ and the influence of nearby adatoms outside this radius on molecules A, B and C can be neglected. Tip-field sweeps for four TiH_O molecules A, B, C and D are plotted in figure 4.16 and we find similar resonance tunneling currents for molecules A, B and C with (30.90 ± 0.72) pA, (30.59 ± 0.61) pA and (31.27 ± 1.80) pA, respectively. The asymmetry and amplitude strongly depend on the investigated molecule. This result is unexpected as the relaxation time, coherence time and Rabi rate, that determine the lineshape, should be similar at a fixed V_{RF} and a fixed tunneling conductance. For molecule D, we do not observe an ESR signal, above our noise level. A change of the tip apex can be excluded since we were able to reproduce the ESR signal on TiH_O A after the measurements on B-D. We explain the different lineshapes by different tip-molecules interactions. In conclusion, the data shown in figure 4.16 suggests that only some molecules, adsorbed on the same MgO site, show an ESR contrast for a given ESR tip and highlights the difficulty of probing these signals efficiently.

In the next section, we introduce and discuss the frequency sweep results performed at $T_{\mathrm{STM}} = 4.2$ K. We measure the g-factor of molecules A, B and C, along the external magnetic field direction $\hat{x}\hat{y}$. We neglect the possible variation of $B_{\mathrm{tip,xy}}$ with the applied external field to derive g.

4.4.2 Frequency Sweeps

Figure 4.17 shows frequency sweep ESR measured on molecule A. An average trace is substracted to the data, as in figure 4.8. An optimized Fano factor of $q_{\mathrm{opt}} = 0.384$ is found. The ESR amplitude increases with increasing external magnetic field (see section 4.3.2 for the interpretation). The resonance frequency scales linearly with the external magnetic field and is shown in figure 4.18.

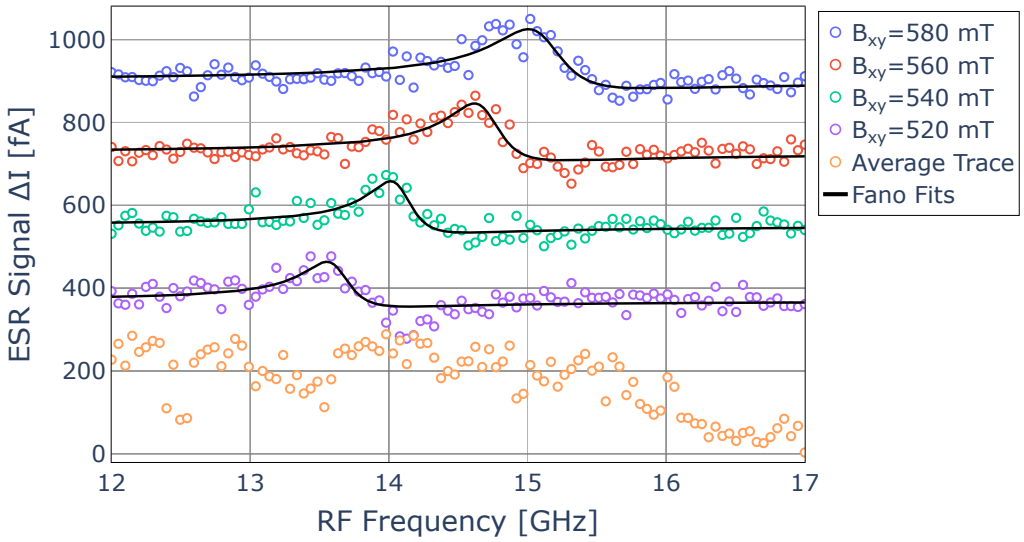

Figure 4.17: Frequency sweeps measured on TiH_O A at $T_{STM} = 4.2$ K. The tunneling parameters are $V_t = 100$ mV, $I_t = 27$ pA and $V_{RF}^{jun} = 28$ mV. Offsets are applied for clarity.

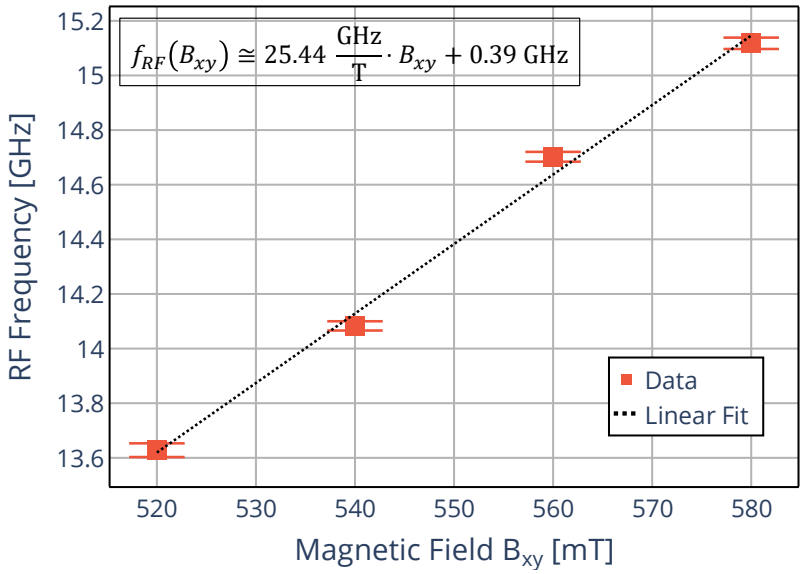

Figure 4.18: Resonance frequencies obtained from the Fano fits in figure 4.17, as a function of the external magnetic field.

From figure 4.18, the experimental g-factor and tip magnetic field are determined:

$$\begin{cases} g_{\text{xy}} = (1.82 \pm 0.09) \\ B_{\text{tip, xy}} = (15.33 \pm 28.95) \end{cases} \tag{4.5}$$

Our value for g_{xy} is consistent with (1.67 ± 0.16), measured for TiH_O in reference [151]. The

measurement of the tip magnetic field is, however, imprecise due to the deviation of the data from the linear fit in figure 4.18. Our method to determine B_{tip} is therefore too sensitive and unreliable, even for small deviations of the resonance frequency with respect to the linear fit. However, it should not alter significantly the g-factor that we measure, as $B_{\text{tip}} << B_{\text{ext}}$ for a low tunneling current of $I_t = 27$ pA. We present in table 4.2 the parameters used for fitting the data in figure 4.17.

	$\mathbf{B_{xy} = 520\ mT}$	$\mathbf{B_{xy} = 540\ mT}$	$\mathbf{B_{xy} = 560\ mT}$	$\mathbf{B_{xy} = 580\ mT}$
$\lvert A \rvert$ [fA]	77.7 ± 10.8	115 ± 11	121 ± 10	131 ± 9
Γ [MHz]	387.71 ± 60.71	368.13 ± 51.64	450.63 ± 58.17	617.00 ± 74.86
q_{opt} [-]	0.384			

Table 4.2: Fit parameters of the ESR traces at $T_{\text{STM}} = 4.2$ K on TiH_O A.

We show the ESR results on molecules B and C in figures 4.19 to 4.22. The data treatment and analysis are identical to what has been presented so far. Table 4.3 summarizes the experimental parameters determined on molecules TiH_O A, B and C. In section 4.5, we discuss in details the lineshapes of ESR signals at $T_{\text{STM}} = 4.2$ K, and a comparison with signals measured at $T_{\text{STM}} = 0.4$ K is given.

	ESR Data on TiH_O A	**ESR Data on TiH_O B**	**ESR Data on TiH_O C**
q_{opt} [-]	0.384	0.221	0.411
g_{xy} [-]	(1.82 ± 0.09)	(1.73 ± 0.09)	(2.04 ± 0.06)
$B_{\text{tip, xy}}$ [mT]	(15.33 ± 28.95)	(51.74 ± 27.65)	(-43.36 ± 15.08)

Table 4.3: Fano factors, g-factors and tip-induced magnetic fields extracted from the ESR signals on TiH_O A, B and C.

In table 4.3, the g-factors of molecules A and B are similar. A higher value is found for molecule C. This deviation is consistent with the ESR lineshapes observed on the three molecules in figure 4.16 and can be explained by different tip-molecule interactions. A tip-molecule distance-dependent measurement of the g-factor of a given molecule would give further insights into the nature of the interaction. Characterizing and controlling the effect of the magnetic tip is therefore crucial for the reproducibility and reliability in ESR-STM experiments [45, 122].

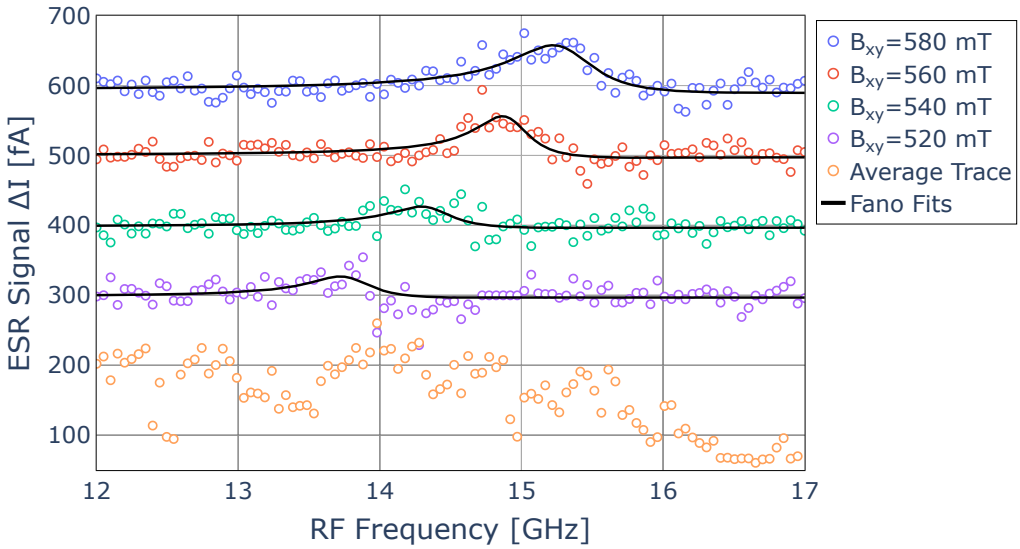

Figure 4.19: Frequency sweeps measured on TiH_O B at T_{STM} = 4.2 K with V_t = 100 mV, I_t = 27 pA and V_{RF}^{jun} = 28 mV. Offsets are applied for clarity.

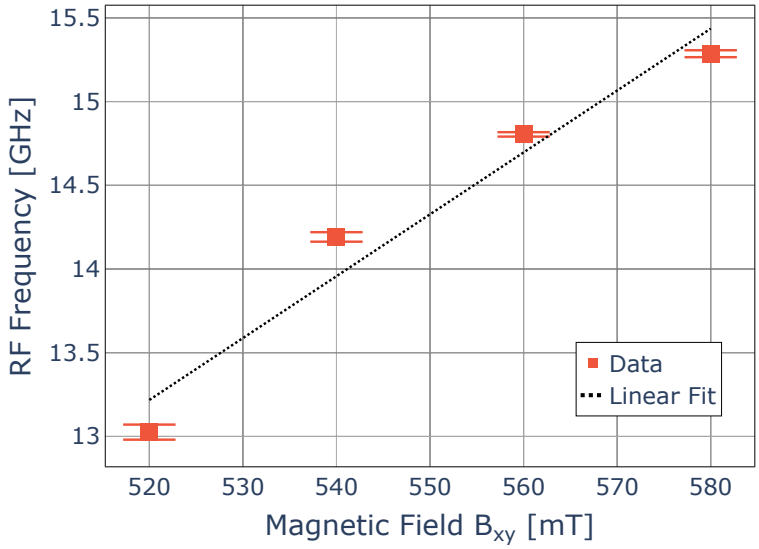

Figure 4.20: Resonance frequencies of TiH_O B, obtained from the Fano fits in figure 4.19, as a function of the external magnetic field.

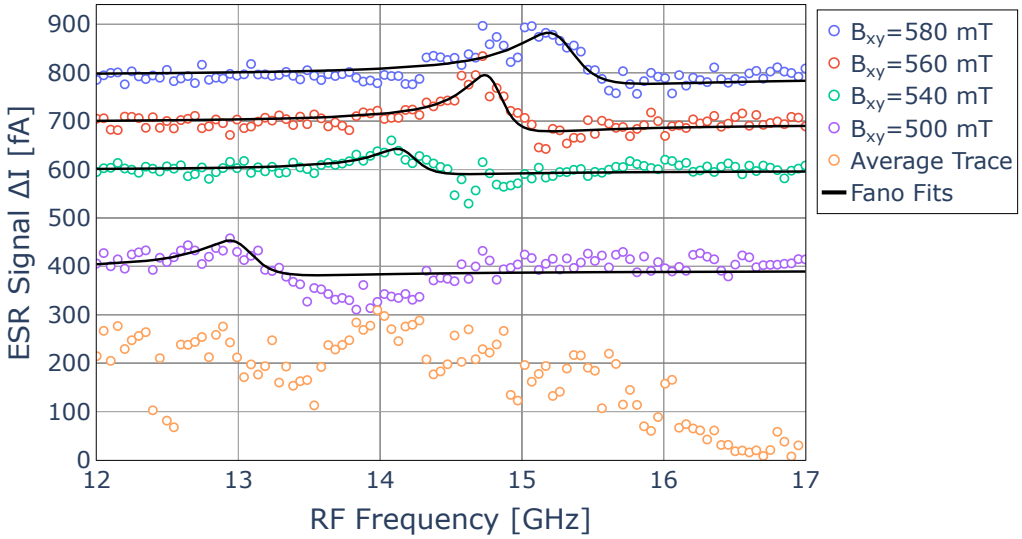

Figure 4.21: Frequency sweeps measured on TiH_O C at T_{STM} = 4.2 K. The tunneling parameters are V_t = 100 mV, I_t = 27 pA for an RF amplitude of V_{RF}^{jun} = 28 mV. Offsets are applied for clarity.

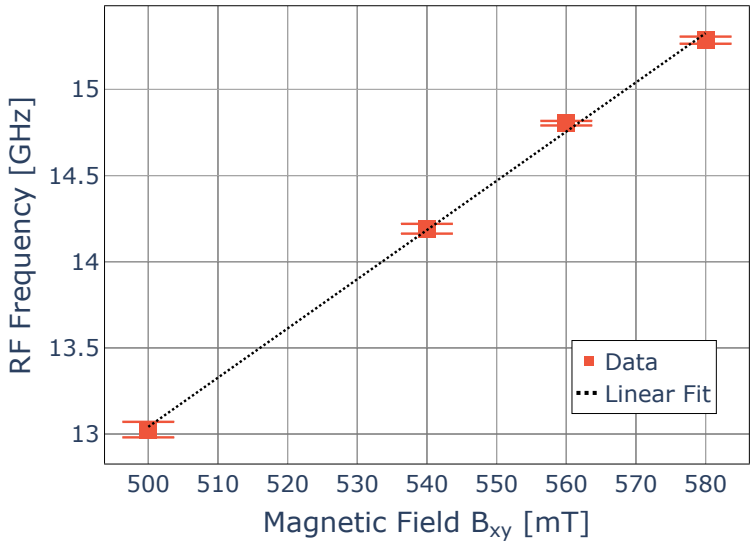

Figure 4.22: Resonance frequencies of TiH_O C, obtained from the Fano fits in figure 4.21, as a function of the external magnetic field.

4.5 Discussion and Conclusion

A comparison of the ESR signals at different temperatures is shown in figure 4.23.

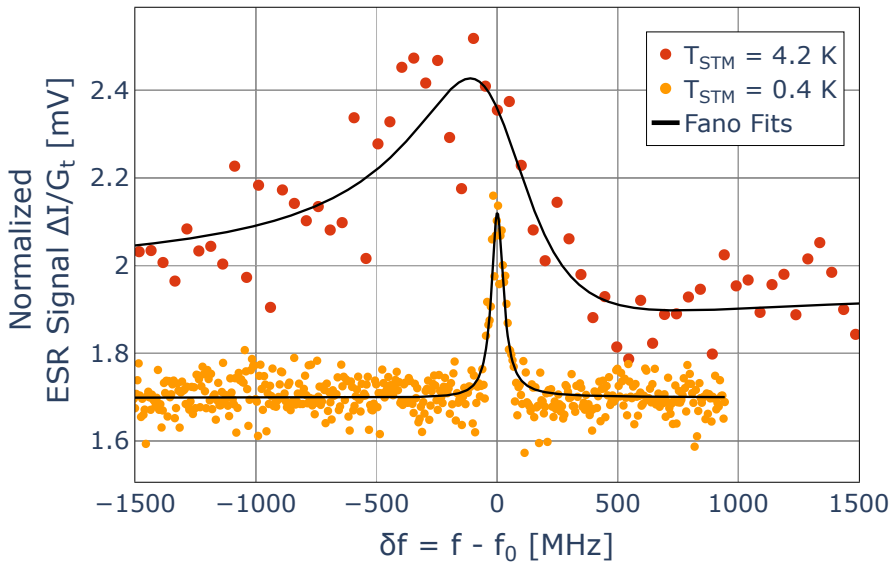

Figure 4.23: ESR signals normalized to the tunneling conductance, centered around the resonance frequencies. Both traces are acquired at B_{xy} = 580 mT and V_{RF} = 28 mV. The trace at 4.2 K is measured with a tunneling current I_t = 27 pA, as the one at 0.4 K with I_t = 15 pA. Offsets are applied for clarity.

The two signals in figure 4.23 have similar amplitudes which, in principle, would contradict the expected decrease in amplitude with increasing temperature [46]. However, a direct comparison is not possible, since these measurements are obtained with different tips, each characterized by distinct spin polarization. Consequently, the integrated signal amplitudes are not only temperature-dependent.

In figure 4.23, the FWHM changes by one order of magnitude from 0.4 K (Γ = 58 MHz) to 4.2 K (Γ = 617 MHz), suggesting a higher decoherence rate at higher temperature. This can be explained by a higher tunneling current, by nearly a factor of 2, used for the trace at 4.2 K (I_t = 27 pA) with respect to the one at 0.4 K (I_t = 15 pA). This leads to broader ESR linewidths, independently of the temperature, as tunneling electrons induce a loss of phase information and contribute in shortening T_2.

The broadening of 58 MHz in figure 4.23 can originate from different sources such as the atom-tracking scheme, that produces a circular motion of the tip with respect to the molecule to compensate piezo actuator creep and drift. Even for small tracking radii (here r = 10 pm), a tip-field gradient can be experienced by the adatom and broadens the ESR peak [45]. Other broadening mechanisms can contribute to the finite linewidth, such as variations in the tip-adatom distance z, external magnetic field imprecision, scattering of tunneling electrons and

substrate phonons, thermal noise, etc.

We now discuss the different lineshape profiles in figure 4.23. The asymmetric lineshape at 4.2 K can be explained by the higher tunneling current with respect to the almost purely symmetric lineshape measured at 0.4 K. An increase of the homodyne contribution is expected at a larger I_t [46]. It is, however, not clear how the temperature influences the asymmetry of the ESR signal and further investigations on the temperature-dependent lineshape are required.

In this chapter, we have demonstrated the feasibility to measure ESR signals at different temperatures with our ESR-STM, after the changes described in section 3.1. This demonstration opens the way for probing new systems with ESR-STM, such as rare-earth adatoms on thin decoupling layers.

4.6 Magnetic Field-Sensing Experiment with ESR-STM

The search for narrow linewidths in ESR-STM experiments is motivated by the measurement of small dipolar and exchange fields generated by surrounding adatoms and sensed by an ESR-active sensor [16, 50, 94, 113]. For the frequency sweeps in figure 4.23, the linewidth ranges from 37 MHz (B_{xy} = 540 mT) to 65 MHz (B_{xy} = 600 mT) for a temperature of 0.4 K which is equivalent to a magnetic field of 1.3 mT and 2.3 mT respectively using the g-factor obtained experimentally. A field of 2.3 mT corresponds to the static dipolar field of a top-Oxygen site Dy atom sensed by a TiH molecule at a distance of $d \approx 1.59$ nm. We derive this distance using a magnetic moment of $m_{Dy} = 10\ \mu_B$ for Dy^{top} [50] and using the magnetic dipole approximation $B_{Dy^{top}} \approx \frac{\mu_0 m_{Dy}}{4\pi d^3}$, with $B_{Dy^{top}} = 2.3$ mT and where μ_0 is the vacuum permeability. Based on this calculation, we propose an experiment at 0.4 K that benefits from narrow ESR linewidths and that measures the magnetic moment of Dy^{top}.

First, a frequency sweep ESR is measured on an isolated TiH molecule at a resonance frequency f_0 and in an external magnetic field B_{ext}. We then manipulate a Dy^{top} adatom and place it next to the molecule at a distance d. This can be achieved by lateral or vertical atomic manipulation schemes of the tip and adatom along the surface [152] and is typically performed in similar ESR-STM experiments [50]. We measure another frequency sweep ESR on TiH with the nearby Dy adatom and with the same experimental parameters as before. We expect the resonance to shift to a new resonance frequency $f_0'(d)$. We repeat this step for many TiH-Dy distances and determine the magnetic moment m_{Dy} by fitting the resonance frequencies to the distance-dependent function f_{fit}:

$$f_{fit}(d) = \frac{g\mu_B}{h} \cdot \left(B_0 + \frac{\mu_0 m_{Dy}}{4\pi d^3}\right) \quad \text{with} \quad B_0 = \left(B_{ext} + B_{tip}\right) \tag{4.6}$$

where the magnetic field of Dy^{top} is described by a static dipolar field. m_{Dy} can be extracted from the fit in equation 4.6, assuming that B_0 is independent of d as in reference [50]. One can also add to equation 4.6 the short-range exchange interaction field, for a more complete

description of B_{Dy}, if necessary:

$$B_{\mathrm{exc}}(d) = Ae^{-d/\lambda_{\mathrm{exc}}} \tag{4.7}$$

where A is the exchange field parameter and λ_{exc} the exchange decay length [45]. This experiment can be extended to any other adatom with a stable magnetic moment. For example, we tried to measure the possible magnetic stray field of an Oxygen-bridge site Dy atom placed next to a TiH molecule. However, and as described in section 5.4, we were not able to build an ESR-active tip in these conditions and therefore could not conduct such an experiment.

4.7 Outlook

Despite the successful measurement of ESR signals demonstrated on TiH molecules, some questions remain open, especially regarding the reproducibility of these signals. In figure 4.16 and in the frequency sweeps presented in section 4.4.2, we show that different TiH molecules, adsorbed on the same MgO site, do not have the same ESR lineshape. We discuss, in this section, three possible origins of this result and propose further experiments to better understand what influences the lineshape of ESR signals.

First, the different lineshapes in figure 4.16 could be explained by different mechanical noise levels in the tip-adatom distance, leading to a variable broadening of the ESR peaks, from one molecule to another. This would imply that a significantly higher noise level is found for molecule D, as we do not measure any signal on it. To verify this hypothesis experimentally, we would need to perform multiple tip-field sweeps on a given TiH molecule to see if we observe any change caused by mechanical noise variations.

Second, a more realistic explanation for the lineshape variation would come from different magnetic properties of molecules A to D. If the molecules are adsorbed on the same site (top-Oxygen), they could be made of different Ti isotopes, with different nuclear spins and hyperfine interactions. We show in table 4.4 the five stable isotopes of Ti, with different mass numbers M, nuclear spins I and natural abundances.

$^{\mathbf{M}}$**Ti**	**I**	**Abundance [%]**
^{46}Ti	0	8.0
^{47}Ti	5/2	7.3
^{48}Ti	0	73.8
^{49}Ti	7/2	5.5
^{50}Ti	0	5.4

Table 4.4: List of stable isotopes of Ti [153, 154]

From table 4.4, the probability that at least one of the four molecules has a non-zero nuclear spin is close to 52%. This implies that we probably investigated molecules with

different hyperfine structures, leading to different ESR lineshapes in figure 4.16. However, resolving the hyperfine splitting of an adatom has only been done at temperatures below 1.5 K [114, 120, 155, 156], with a characteristic frequency spacing on the order of 50 MHz between adjacent peaks, for ^{47}Ti and ^{49}Ti at $V_{RF} \leq 50$ mV and $T_{STM} = 0.6$ K [156]. In our case, at $T_{STM} = 4.2$ K, a higher decoherence rate from scattering electrons and phonons might broaden the ESR peaks, preventing the resolution of individual nuclear spin states for ^{47}Ti and ^{49}Ti. This hypothesis partially explains how the ESR lineshape can be broadened differently by an additional hyperfine contribution, depending on the isotope of Ti. However, and as for the first hypothesis, it does not explain why we do not measure an ESR signal on molecule D, in figure 4.16.

Finally, variations in ESR signals can be attributed to different interactions between the molecules and the substrate. Specifically, if the CF remains uniform for all top-Oxygen TiH molecules, we suspect the nuclear spins from the substrate to interact inhomogeneously with the adsorbed molecules, causing different ESR lineshapes. For MgO, the main contribution of nuclear spins comes from the Magnesium atoms, whose stable isotopes are ^{24}Mg, ^{25}Mg, ^{26}Mg and where ^{25}Mg is the only isotope with a non-zero nuclear spin $I = 5/2$, abundant by 10% [154]. Stable isotopes of Oxygen with $I \neq 0$, however, are negligible with an abundance below 0.04% [157]. If this hypothesis explains the lack of reproducibility of these signals, other substrates with a low amount of nuclear spins should generate less variations in the ESR lineshape. As an outlook, we could measure ESR-STM signals on rare earth atoms adsorbed on graphene. The choice of this substrate is justified by the low density of nuclear spins, as stable Carbon atoms with $I \neq 0$ are abundant by only 1% [154]. Also, rare earth adatoms are attractive for ESR-STM, given the existing studies of Dy and Ho on graphene, showing long relaxation times T_1 [158, 159]. As described in section 2.4.3, systems showing long T_1 are susceptible to reveal a long T_2.

5 Magnetism of Single Dy Atoms on MgO with SP-STM

Rare-earth adatoms on decoupling layers can retain a stable magnetic moment in absence of an external magnetic field. The shielded nature of 4f electrons presents magnetic stability advantages compared to other elements such as 3d transition metals. By providing a symmetry-protected magnetic ground state, some rare-earth atoms could be used to store information in single atom magnets. The first study of single lanthanide adatoms that showed magnetic remanence was on Ho on MgO, that revealed a long lifetime up to 1500 s at $T = 10$ K [158]. A coercive field of at least 8 T was demonstrated with a first excited state lifetime of at least 1000 s at $T = 35$ K [94].

Regarding single Dy atoms adsorbed on MgO, we introduce in this chapter the electronic and magnetic properties of this system characterized in references [50, 97]. We show that these works focus mainly on the top-Oxygen adsorption site Dy^{top} in the $4f^9$ configuration, revealing the largest MAE barrier observed for any magnetic adsorbed single atom [97]. However, the Oxygen-bridge site Dy^{br} has not been studied with STM. By presenting the energy level scheme of Dy^{br}, obtained from multiplet calculations, we show that this system has a predicted in-plane easy axis of the magnetization. Therefore, these calculations motivate the investigation of Dy^{br} with SP-STM. To do so, we first characterize our SP tip by recording two-state noise on Dy^{top} and compare our results with reference [50]. Then, we show how the tip's magnetization can be oriented along the sample plane to address the magnetism of Dy^{br} adatoms. We finally present the attempts in measuring two-state noise on Dy^{br} at different tunneling voltages and tunneling currents.

5.1 Electronic and Magnetic Properties of Single Dy Atoms on MgO

Single Dy atoms on MgO have been addressed with XAS, XMCD and STM in references [50, 97]. From STM images, apparent heights of 230 pm and 310 pm have been attributed to Dy^{top} and Dy^{br} respectively, at $T_{STM} = 2$ K, $V_t = 100$ mV and $I_t = 20$ pA [50]. Our STM image shown in figure 5.1 also reveals a higher apparent height for Dy^{br} ($\Delta z \approx 270$ pm) with respect to Dy^{top} ($\Delta z \approx 170$ pm). Δz values are, however, lower than the ones of reference [50] due to the different tunneling parameters and to different tip terminations. Nonetheless, the difference of ~ 100 pm between Dy^{top} and Dy^{br} allows us to identify the Dy adsorption site on the MgO surface by an apparent height measurement. Figure 5.1 also shows a higher number of Dy^{br} atoms with respect to Dy^{top} which is consistent with the relative coverage of Dy calculated in reference [97]: for 2 ML-thick MgO, Dy^{br} are more abundant (79%) than Dy^{top} (21%). For 3 and 4 ML-thick MgO, Dy^{top} becomes more favorable with a relative abundance of 75%.

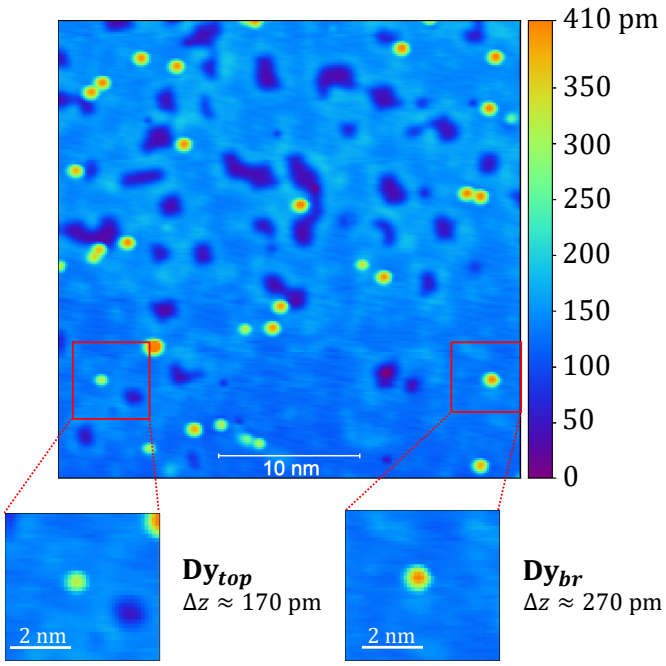

Figure 5.1: STM image of Dy adatoms adsorbed on 2 ML-thick MgO. The scanning tunneling parameters are $V_t = 50$ mV, $I_t = 10$ pA.

The electronic configuration of the 4f shell goes from $4f^9$ to $4f^{10}$ with increasing MgO thickness as shown in figure 5.2. Note that the MgO thicknesses reported in figure 5.2 and in reference [97] are 1 ML lower than our definition (cf. section 3.3).

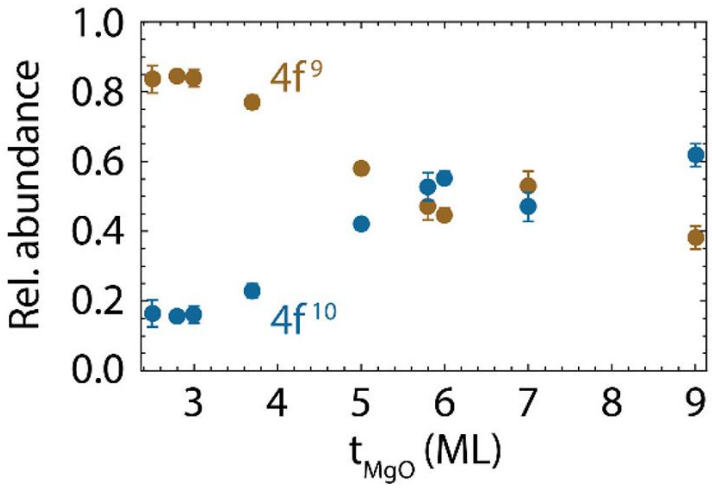

Figure 5.2: Relative abundance of the electronic configurations of Dy on MgO. Data are obtained by fitting the experimental XAS spectra with simulated spectra obtained from multiplet calculations using the *MultiX* code [97, 160].

A total of 4 species can thus be found on the MgO surface: $Dy^{top}(4f^9)$, $Dy^{br}(4f^9)$, $Dy^{top}(4f^{10})$ and $Dy^{br}(4f^{10})$. In our case, we investigate Dy adatoms on up to 3 ML MgO with STM. Con-

sequently, the Dy adatoms that we address are mostly in the $4f^9$ configuration. In a two-state noise trace, we would expect a higher switching rate for $Dy^{top}(4f^{10})$ as the MAE is significantly reduced compared to $Dy^{top}(4f^9)$ [50]. The switching rate that we measure on Dy^{top}, shown in section 5.2, is consistent with the one predicted from multiplet calculations for the $4f^9$ configuration. Therefore, we addressed the adatom $Dy^{top}(4f^9)$ and we consider exclusively this electronic configuration from now on and for both sites Dy^{top} and Dy^{br}.

The magnetic properties of Dy adatoms are now discussed. Multiplet calculations, using a point charge electrostatic model (PCEM) for estimating the CF, reveal an out-of-plane easy axis magnetic anisotropy for Dy^{top} in the $4f^96s^2$ configuration [50]. The quantum numbers obtained from these calculations are $S_z = 5/2$, $L_z = 5$, and a ground state doublet of $< J_z >= \pm 15/2$. The g-factor calculated from these quantum numbers is $g \approx 1.33$, yielding a magnetic moment of 9.9 μ_B in the ground state. The corresponding energy level scheme from reference [50] is shown in figure 5.3, revealing a MAE barrier of ~ 235 meV for the modified PCEM, that will be explained below.

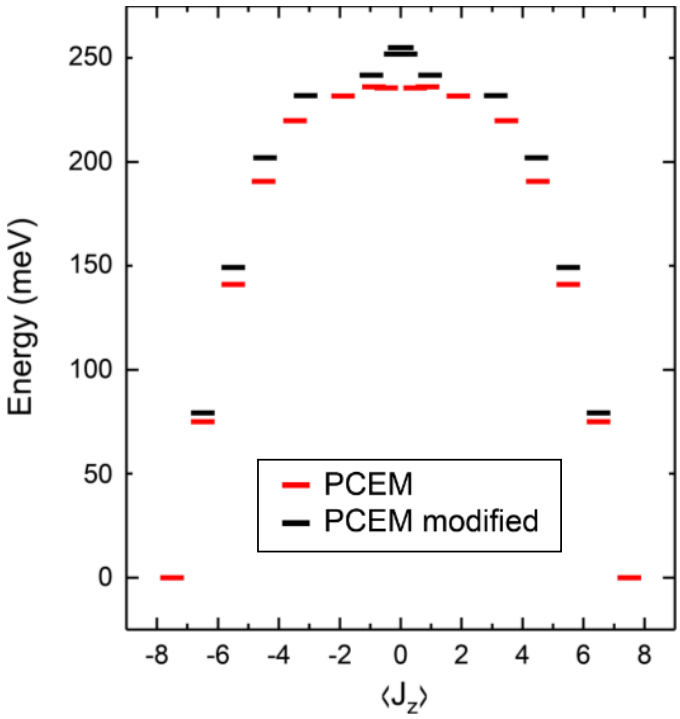

Figure 5.3: Energy level scheme of Dy^{top} in the $4f^9$ configuration calculated from the *Quanty* multiplet calculation code [161]. A PCEM model is used to estimate the CF contribution [50].

Given the C_{4v} CF environment, the ground state doublet is protected from QTM, leading to a long magnetic ground state lifetime. When addressing this system with SP-STM, the magnetic moment is found stable in the ground state over days at low tunneling voltages, with T_{STM} = 1 K and B_{ext} = 0 T [50]. When applying tunneling voltages above 146 meV, rever-

sals of the magnetization are measured as a two-state noise and correspond to the two orientations of the magnetic moment $< J_z >= \pm 15/2$. To match the switching rates obtained from multiplet calculations and the ones measured experimentally in reference [50], the PCEM model is re-scaled (black markers in figure 5.3) by increasing the transverse term E_4^4 in the CF Hamiltonian [50]. A higher transverse term can be explained by the hybridization of the 6s electrons with the Mg orbitals, creating a 4-fold deformation, not included in the *Quanty* multiplet calculation model. Finally, ESR signals have been measured with a magnetic bistable tip on an Fe atom, sensing the magnetic dipolar field of a Dy^{top} atom placed at various distances from the Fe sensor [50]. Two ESR signals are observed in a given tip-field sweep and correspond to the two resonance conditions generated by the two orientations of the tip's magnetic moment along the external magnetic field. The spacing between the two peaks is a direct measurement of the magnetic dipolar field generated by Dy^{top} that fits well the magnetic dipole approximation with the Fe-Dy^{top} distance. A value of $m_{Dy^{top}} = 10.1 \pm 0.3\ \mu_B$ is found and is in good agreement with the multiplet calculations [50].

The magnetic properties of Dy^{br} have not been deeply investigated in both references [50, 97]. The main reason lies in the lower CF symmetry C_{2v}, predicting a weaker magnetic stability for Dy^{br}. Indeed, multiplet calculations from reference [97] show a non-magnetic ground state along the $\hat{z}$ axis. In the $\hat{x}$-direction, however, the same calculations predict a ground state doublet with $< J_x >= \pm 15/2$ and a high MAE. Both projections along $\hat{z}$ and $\hat{x}$ are shown in figure 5.4. The axis $\hat{x}$ is defined along the O-Dy^{br}-O direction of a given Oxygen-bridge adatom. The $\hat{x}$ axis of Oxygen-bridge site 1 is therefore orthogonal to the $\hat{x}$ axis of Oxygen bridge site 2, as illustrated in figure 3.18. The positive $\hat{z}$ axis is defined along the tip-sample distance and points from the sample toward the STM tip.

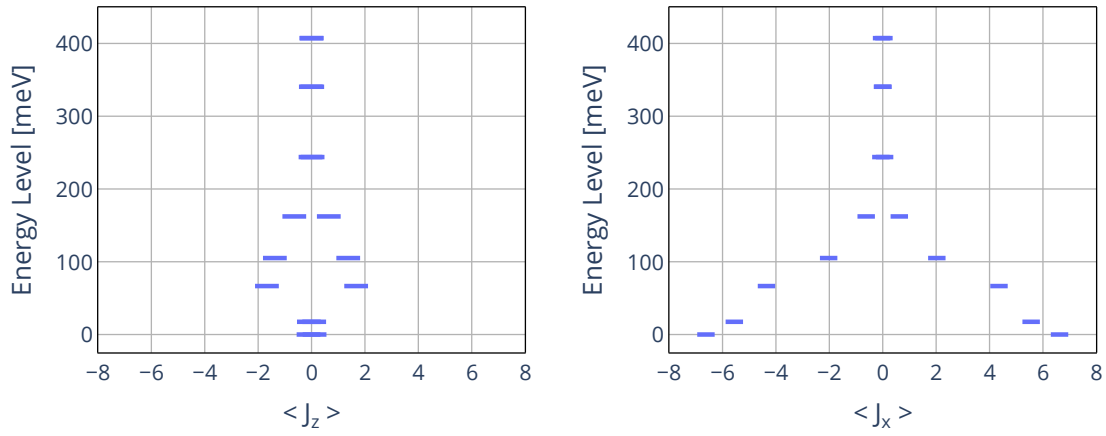

Figure 5.4: Energy level schemes of Dy^{br} in the $4f^9$ configuration, projected along $\hat{z}$ (left) and $\hat{x}$ (right). Both graphs are computed with the *MultiX* multiplet calculation code, using the same parameters as in reference [97]. The positions and charges of the nearest ions are provided by DFT calculations [97, 162].

The ground state wave function compositions are also obtained from the multiplet cal-

culations and are expressed in the $|J_x\rangle$ basis in equation 5.1.

$$\begin{aligned} |\pm\Psi_{\mathrm{Dy^{br}}}\rangle : &+0.797\,|\pm 15/2\rangle \\ &-0.533\,|\pm 11/2\rangle \\ &+0.229\,|\pm 7/2\rangle \\ &-0.081\,|\pm 3/2\rangle \\ &+0.029\,|\mp 1/2\rangle \\ &-0.011\,|\mp 5/2\rangle \\ &+0.007\,|\mp 9/2\rangle \\ &-0.006\,|\mp 13/2\rangle \end{aligned} \tag{5.1}$$

As shown in figure 5.4 (right) and in equation 5.1, the predicted magnetic ground state doublet along $\hat{x}$ motivates the study of Dy^{br} with SP-STM, similarly to what has been done on Dy^{top} along $\hat{z}$ [50]. The method employed here, consists of measuring the energy-dependent switching rate from two-state noise experiments on Dy^{top} that can be compared to the rates reported in reference [50]. The same SP tip is then placed over a Dy^{br} adatom (site 1 or 2) to check if magnetization switching can also be observed along the $\hat{x}$ easy axis for a wide range of parameters V_t and I_t. To conduct two-state noise experiments along two orthogonal easy axis of the magnetization ($\hat{z}$ and $\hat{x}$), a control of the tip's magnetic moment's orientation is necessary and is presented in section 5.3.

5.2 Two-state Noise on Top-Oxygen Site Dy

Figure 5.5 shows a two-state noise measured on Dy^{top} as time-dependent changes in the apparent height Δz at a constant tunneling current, with the two possible out-of-plane magnetic orientations in red and blue.

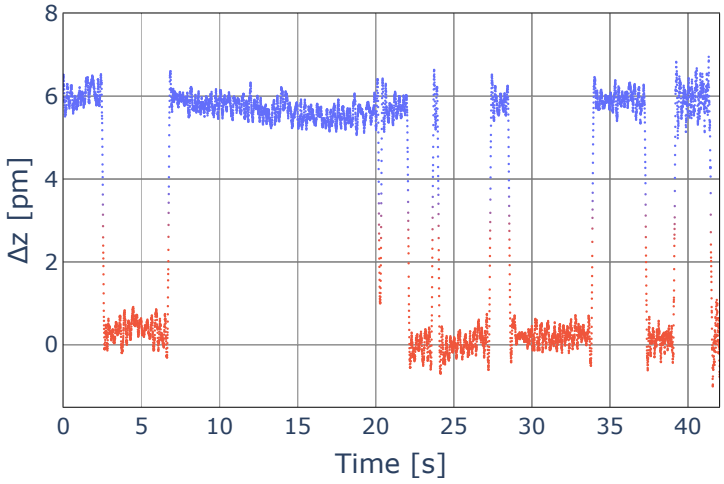

Figure 5.5: Two-state noise on Dy^{top}, measured at $T_{STM} = 4.2$ K, $V_t = 240$ mV and $I_t = 30$ pA, with $B_z = 600$ mT. A Gaussian filter is applied with $\sigma = 5$ and a sampling rate of 200 Hz.

A contrast of $\Delta z = 6$ pm is observed between the two magnetic orientations. From one SP tip to another, Δz varies from 4 to 8 pm for the same tunneling conductance. This difference can be explained by the different spin polarizations of the tips and the different projections of the tip's and adatom's magnetic moments. To characterize the two-state noise recorded with a given SP tip, and to verify if a single-electron process governs the magnetization switching, we perform a current-dependent measurement of the switching rate. We show the corresponding rates for 2 SP tips in figure 5.6. Error bars are defined as the rates corresponding to the square root of the total number of switching counts.

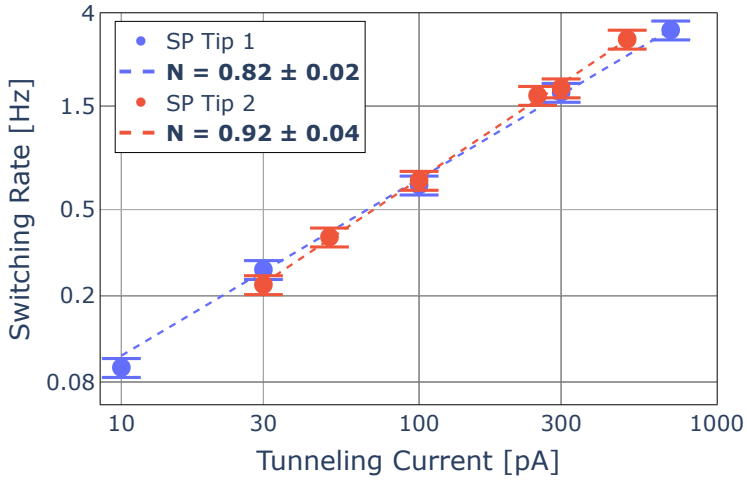

Figure 5.6: Switching rate of Dy^{top} as a function of tunneling current, shown in a log-log plot. Data are acquired at $T_{STM} = 4.2$ K, in an external magnetic field of $B_z = 600$ mT. Tunneling biases of $V_t = 240$ mV and $V_t = 250$ mV are used for SP Tip 1 and 2 respectively.

The switching rate is defined as the number of transitions from one magnetic orientation to another over a given measurement time. In figure 5.6, the dashed lines represent the fits using the model described in section 2.3.7, with the following function:

$$\Gamma = a \cdot \left(\frac{I}{I_0}\right)^N \tag{5.2}$$

where Γ is the switching rate, a the switching coefficient and N the fitting exponent, indicated for each fit in the legend box of figure 5.6. We report in table 5.1 the parameters obtained from the fits, using $I_0 = 1$ pA.

	SP Tip 1 $V_t = 240$ mV	**SP Tip 2** $V_t = 250$ mV
a [Hz]	(7.38 ± 0.94)	(1.54 ± 0.28)
N [-]	(0.82 ± 0.02)	(0.92 ± 0.04)

Table 5.1: Fitting parameters from figure 5.6.

The parameter a reported in table 5.1 changes by a factor of 5 from SP Tip 1 to SP Tip 2. We think that this coefficient can vary depending on the magnetic interactions between the

tip and the adatom and, therefore, strongly depends on the SP tip. Table 5.1 reports fitting exponents closed to 1, confirming that a single-electron process governs the magnetization switching. This allows a direct comparison with the data and point charge model from reference [50] that finds $N \approx 1.08$ for $V_t = 230$ mV, $B_z = 5$ T and $T_{\mathrm{STM}} = 1.8$ K.

To identify the energy onsets of the system, we measure the switching rate as a function of tunneling voltage. The energy onsets correspond to the opening of magnetization reversal paths induced by scattering electrons. We show this measurement in figure 5.7. Our data are compared to the modified PCEM model from reference [50], shown as a red line in figure 5.7. We define the rate Γ_{PCEM} from this model as:

$$\Gamma_{\mathrm{PCEM}}(V) = \sum_{i=1}^{7} H(V - V_i) \cdot c_i \cdot \frac{(V - V_i)}{V_i} \quad \text{with} \quad c_i = c_0 \cdot (I/e) \cdot P(i) \tag{5.3}$$

Seven onsets are found from multiplet calculations and are incorporated in equation 5.3 via the Heaviside function $H(V - V_i)$, where $|e|V_i$ is the energy onset associated to a coefficient c_i, a transition probability $P(j)$ and an SP tip-dependent pre-factor c_0. We find $c_0 = 0.026$, obtained by fitting our data to the switching rate of equation 5.3. In comparison, reference [50] finds $c_0 = 0.045$. The coefficient c_0 can be seen as the fraction of tunneling electrons that interact with the adatom's magnetic states and that participate in the spin-excitation process [50]. Its value is tip-dependent, which explains the difference found with reference [50].

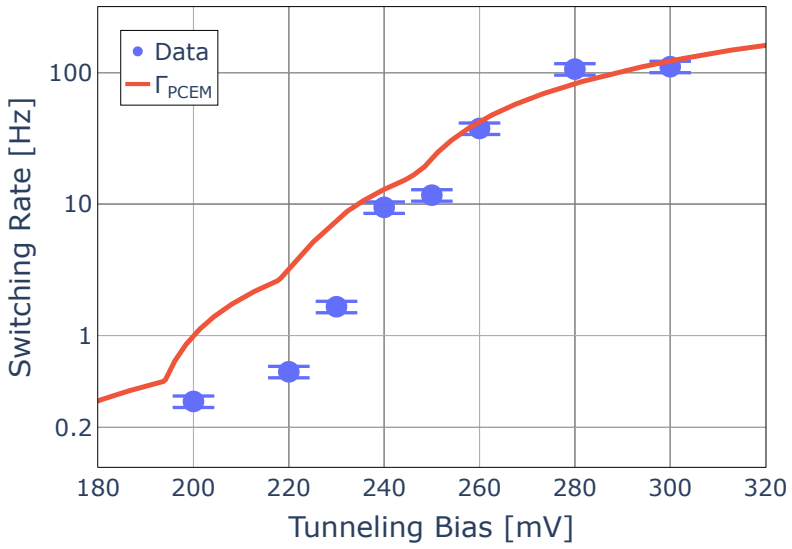

Figure 5.7: Switching rate of Dy^{top} as a function of tunneling voltage, shown in a semi-log plot and acquired at $T_{\mathrm{STM}} = 4.2$ K, $B_z = 600$ mT. Data are scaled to $I_t = 1.5$ nA, using equation 5.2 with $N = 1$. The red curve corresponds to equation 5.3, where $c_0 = 0.026$ is an optimized parameter fitting our data.

The probabilities $P(i)$ and energies $|e|V_i$, used for plotting the red curve in figure 5.7, are

reported in table 5.2 and are adapted from reference [50].

$\|e\|V_i$ [meV]	P(i)	c_i [Hz]
146	$5.62 \cdot 10^{-9}$	1.4
194	$6.61 \cdot 10^{-8}$	15.9
218	$1.64 \cdot 10^{-7}$	39.6
220	$1.01 \cdot 10^{-7}$	24.2
226	$1.40 \cdot 10^{-7}$	33.7
245	$3.73 \cdot 10^{-7}$	89.7
248	$1.14 \cdot 10^{-6}$	275.3

Table 5.2: Values of energy thresholds $|e|V_i$, transition probabilities $P(i)$ and switching rates c_i obtained from multiplet calculations [50]. The rates c_i are calculated for $c_0 = 0.026$.

The data shown in figure 5.7 are not measured at the same tunneling current: I_t is adjusted for a given V_t such that the resulting two-state noise trace can be resolved with our sampling rate and within the I/V converter bandwidth. All switching rates are then scaled to the same tunneling current of $I_t = 1.5$ nA, using equation 5.2 and an exponent of $N = 1$. In principle, one should use an experimental exponent N, obtained by fitting the current-dependent switching rate for a given SP tip, using equation 5.2. Unfortunately, this has not been done for the tip that measured the voltage-dependent rates in figure 5.7, due to a change of the tip apex. We thus have to assume an ideal one-electron process with $N = 1$, as in reference [50]. Our data shown in figure 5.7 are in good agreement with the modified PCEM model, especially for tunneling voltages above 240 mV. Two onsets can be identified at around 220 meV and 250 meV. They are matching the onsets found with the modified PCEM model at 218 meV, 245 meV and 248 meV. However, we measure lower switching rates from 200 mV to 230 mV compared to the ones predicted by the PCEM model. A similar deviation is found in reference [50] at these voltages and suggests that the model overestimates the electron scattering probabilities in this energy interval. Finally, we did not observe any magnetization switching at 140 mV and below, confirming the first threshold value found at 146 meV.

5.3 Investigation of Oxygen-bridge Site Dy Magnetic Properties

To attempt the measurement of a two-state noise on Dy^{br}, it is necessary to orient the tip's magnetic moment $\mathbf{m}_{tip}$ along the $\hat{x}$ axis, i.e. along the predicted easy axis of the magnetization. To do so, we measure the change of magnetic contrast Δz from the two-state noise on Dy^{top} for different orientations of the magnetic field. The amplitude of the field is kept to a constant value of $|\vec{B}_{ext}| = 600$ mT. In figure 5.8, the magnetic field is set along $\hat{z}$ (top graph) and a contrast of $\Delta z \approx 4$ pm is recorded. When the field is flipped and oriented in the $\hat{x}\hat{y}$-plane (middle graph), magnetization switchings are still probed along the $\hat{z}$ easy axis with a reduced contrast $\Delta z \approx 2$ pm. The field is then oriented back along $\hat{z}$ (bottom graph) and a contrast of 4 pm is retrieved, indicating that the atomic structure of the tip apex remained stable during the changes of magnetic field directions. We conclude from the reduced contrast

shown in the middle graph that the tip's magnetic moment is projected along the sample's surface $\hat{x}\hat{y}$ when applying a fully in-plane external magnetic field. From our STM images, we cannot say which Dy^{br} atom is on which of the two non-equivalent bridge sites, having their easy axes along two orthogonal directions. We thus investigate many Dy^{br} atoms in order to maximize the chance of having sufficient projection between the tip's and adatom's magnetic moments.

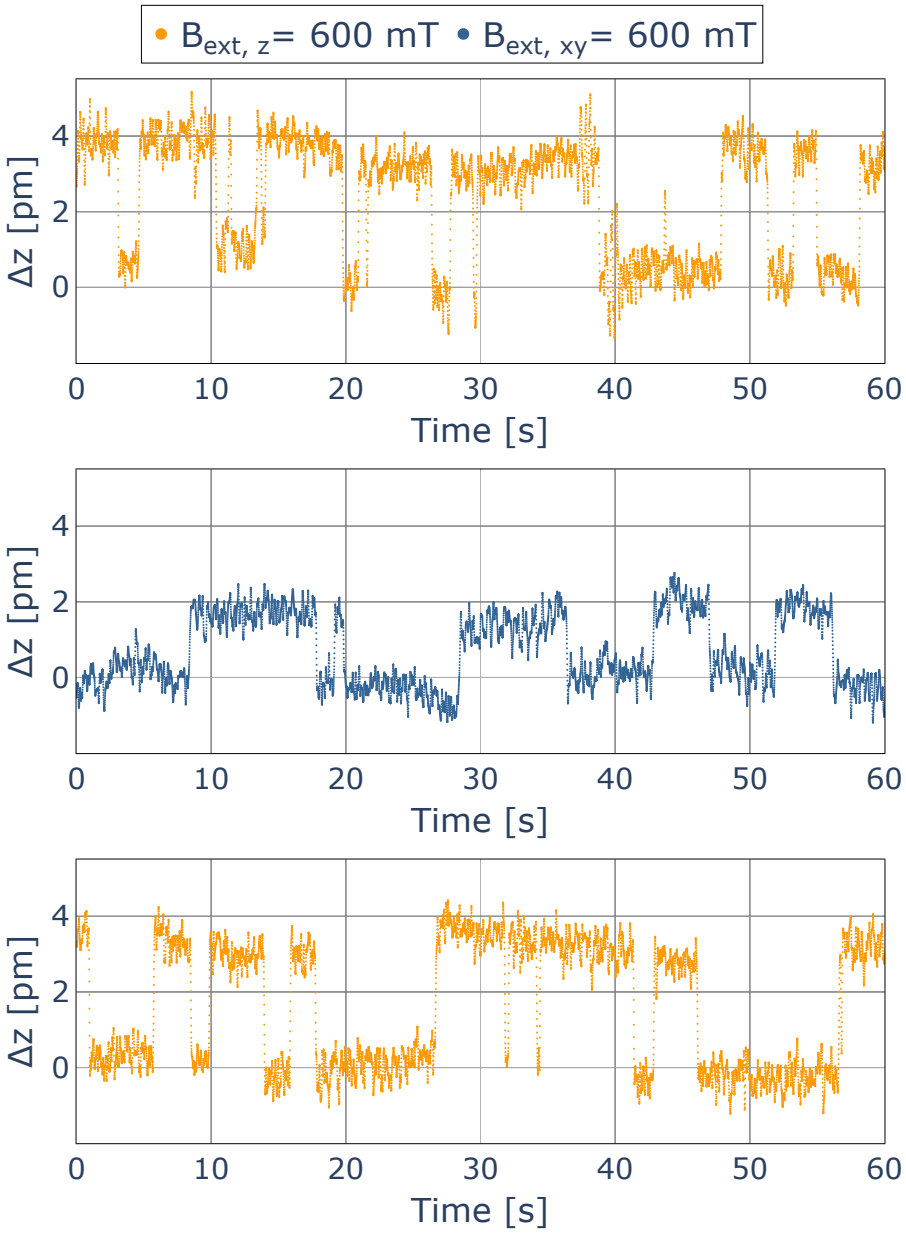

Figure 5.8: Two-state noise on Dy^{top}, performed at T_{STM} = 4.2 K, V_t = 280 mV, I_t = 5 pA, and $\mathbf{B}_{ext} \cdot \hat{n}$ = 600 mT, for different external magnetic field orientations $\hat{n}$. Top: $\hat{n} \equiv \hat{z}$, middle: $\hat{n} \equiv \hat{x}\hat{y}$, bottom: $\hat{n} \equiv \hat{z}$. Gaussian filters with $\sigma = 5$ are applied to the data for a sampling rate of 200 Hz.

The STM image in figure 5.9 shows Dy and Fe atoms deposited on MgO. The z color scale helps to distinguish the different adsorbed species on the surface, as defined in figure 3.20.

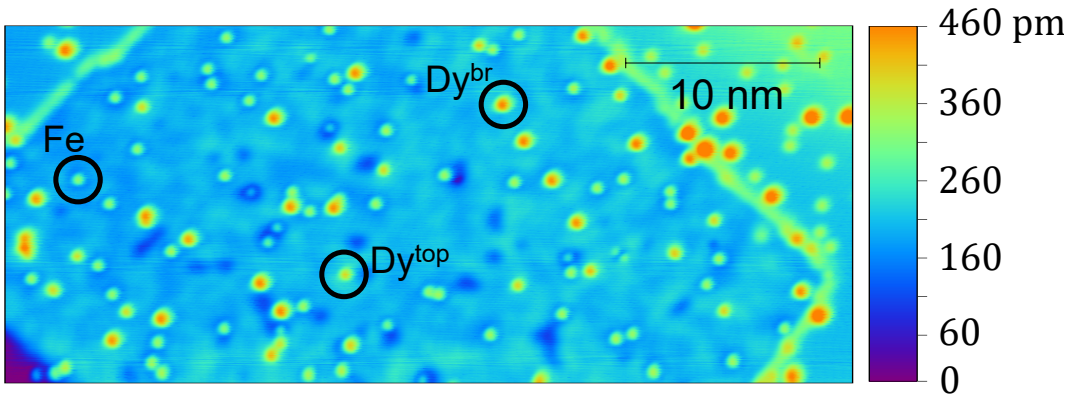

Figure 5.9: STM image showing Fe and Dy adatoms adsorbed on 2 ML-thick MgO. The tunneling parameters are V_t = 100 mV and I_t = 10 pA. The image is taken at T_{STM}=4.2 K.

On this MgO patch, an SP tip is prepared and reveals two-state on Dy^{top} for an out-of plane external magnetic field $B_{\mathrm{ext,z}}$ = 600 mT. The tip is then polarized along the sample's surface, by rotating the field in the $\hat{x}\hat{y}$ direction, and reveals a reduced magnetic contrast on Dy^{top}, as shown in figure 5.8. We place the in-plane SP tip over six different Dy^{br} adatoms shown in figure 5.9. No magnetization switchings that exceed our noise level are observed for a tunneling bias ranging from 40 mV to 440 mV. Table 5.3 shows the values taken by the tunneling parameters during this experiment. These measurements were reproduced with different SP tips, confirming the absence of a two-state noise on many Oxygen-bridge adatoms.

$\mathbf{V_t}$ [mV]	$\mathbf{I_t}$ [pA]
40	5, 50, 500
80	5, 50
120	5
160	5
200	5
240	5
280	5
320	5
360	5
400	5
440	5, 50, 250, 500

Table 5.3: Parameters used on Dy^{br} adatoms with an in-plane SP tip revealing two-state noise on Dy^{top} at B_{xy} = 600 mT.

Figure 5.10 shows different feature-less apparent height traces measured on one of the Dy^{br} adatoms of figure 5.9.

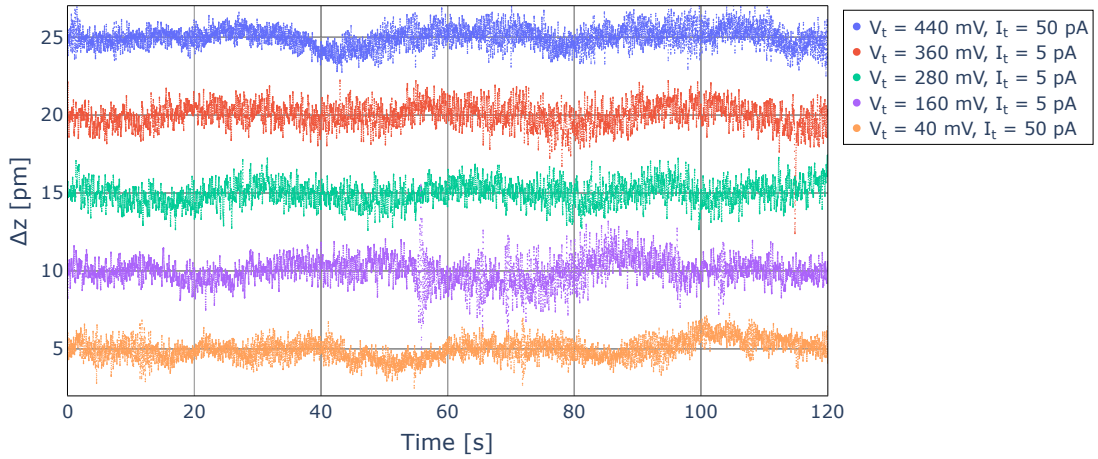

Figure 5.10: z traces measured on Dy^{br} with an in-plane SP tip for different pairs of tunneling parameters, in a field of $B_{ext,xy}$ = 600 mT, at T_{STM} = 4.2 K. Logarithmic fits are done and substracted to each trace, removing the creep induced by the piezoelectric actuators. Gaussian filters are applied with $\sigma = 5$ for a sampling rate of 200 Hz.

5.4 Conclusion

In this chapter, we measured the magnetization switching rate from a two-state noise experiment on Dy^{top} as a function of the tunneling voltage and current. The data are in good agreement with the ones reported in reference [50], confirming a first energy onset at 140 meV, and a linear behavior of the switching rate with the tunneling current. Moreover, we developped a method to characterize the orientation of the tip's magnetic moment, deduced from the apparent height change Δz in a two-state noise experiment on Dy^{top} for a given orientation of the external vector magnetic field. Based on the calculations presented in reference [97], Dy^{br} is predicted to have a magnetic ground state doublet along $\hat{x}$, corresponding to the O-Dy^{br}-O direction. Despite the low coordination environment, the high MAE of 400 meV motivated the attempts of probing the in-plane magnetization of this single-atom. However, we did not observe a two-state noise signal on Dy^{br} for a wide range of tunneling parameters and SP tips with in-plane magnetic moment projections. We provide below different explanations of this result.

First, the projection of the tip's magnetic moment along the presumed adatom's easy axis is not large enough to probe reversals of the magnetization, above our noise level. We minimized the probability of having a low projection by measuring many Dy^{br} atoms with different in-plane SP tips.

Second, the reduced contrast of 2 pm shown in figure 5.8 (middle graph) is exclusively caused by a change of the tunneling properties when applying an in-plane external magnetic field. Consequently, we do not gain in-plane magnetic contrast as the orientation of the tip's

magnetic moment does not necessarily change with respect to the out-of-plane moment of Dy^{top}.

Third, Dy^{br} has a stable magnetic moment along $\hat{x}$ but tunneling biases higher than 440 mV are required to induce a reversal of the magnetization. As reported in table 5.3, we did not exceed 440 mV as higher bias values led to a change of the adatom's adsorption site or to a change of the tip apex.

Fourth, Dy^{br} does not have a net magnetic moment along the $\hat{x}$ axis. The energy diagram calculated and shown in figure 5.4 might not be accurate as small changes in the point charge model lead to large differences in the calculated eigenvalues.

Fifth, the magnetic ground state of the adatom is too unstable, at time scales beyond the current amplifier bandwidth. Therefore no real-time readout of the magnetization reversal can be measured.

Attempts in measuring the magnetic moment of Dy^{br} were made by trying to detect ESR signals on a nearby TiH molecule, as described by the proposed experiment in section 4.7. Unfortunately, no ESR-compatible tips were achieved and no signals have been measured in these conditions. This is partially explained by the long process of preparing an SP tip capable of giving ESR contrast, especially with the limited operational time of our STM at 0.4 K. After our present hold-time of 14 h, the insert of the cryostat has to be refilled with liquid helium. This operation requires to retract the tip far away from the sample surface and generally changes its atomic termination when a new approach is made. As a consequence, one has to built an ESR tip and perform all necessary measurements over one hold time, which is very hard, respectively, unrealistic.

6 Magnetism of Single Tb Atoms on MgO with SP-STM

Some rare-earth single atoms adsorbed on MgO/Ag(100) remain unexplored with SP-STM. Their magnetic stability advantage motivates the research in finding new rare-earth systems that show long magnetic lifetimes on surfaces. The magnetic properties of single Tb atoms on MgO/Ag(100) have been investigated with XAS and XMCD and the results are summarized in a manuscript in preparation [163]. This system reveals a long magnetic ground state lifetime, above 800 s at $T = 6$ K. A dynamic CF multiplet model also predicts a long intrinsic lifetime at low temperatures. Finally, Tb on MgO shows a high temperature stability with an hysteresis observed in the magnetization curve up to 30 K. These findings motivate the study of this system with SP-STM at $T_{\mathrm{STM}} = 0.4$ K. In this chapter, we introduce first the results from reference [163]. We then present and discuss two-state noise and IETS measurements on adsorption sites $\mathrm{Tb}^{\mathrm{top}}$ and $\mathrm{Tb}^{\mathrm{br}}$, respectively.

6.1 Electronic and Magnetic Properties of Single Tb Atoms on MgO

In the gas phase, the electronic configuration of Tb is $4f^9 6s^2$. When adsorbed on 6 ML MgO, XAS and XMCD experiments, performed at the $M_{4,5}$ adsorption edges, reveal a configuration of $4f^8$ with $J = 6$. The XMCD peak at 1240 eV exhibits a twofold increase in intensity under normal incidence compared to a grazing incidence of 60°, suggesting an out-of-plane easy axis of the magnetization. These measurements do not differentiate the adsorption sites of Tb. According to the statistical analysis in reference [163], 83 % of the Tb adatoms reside on top-Oxygen sites ($\mathrm{Tb}^{\mathrm{top}}$) for 2 ML MgO and the 17 % left are adsorbed on Oxygen-bridge sites ($\mathrm{Tb}^{\mathrm{br}}$). The presence of different adsorbed atoms prevents a direct measurement of the individual ground state compositions of $\mathrm{Tb}^{\mathrm{top}}$ and $\mathrm{Tb}^{\mathrm{br}}$, from XAS spectra. For this reason, quantum chemical calculations are performed on a Tb-MgO cluster to determine the crystal field parameters and deduce the ground state composition for each adsorbed species.

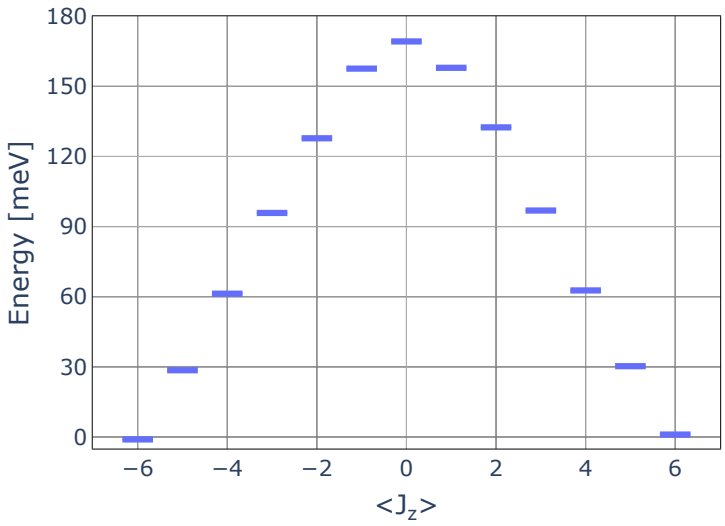

Figure 6.1: Energy level scheme at $B_z = 1.5$ T for $\mathrm{Tb}^{\mathrm{top}}$ in the $4f^8$ configuration [163].

Figure 6.1 shows the resulting energy level scheme of Tb^{top} on MgO, plotted in the $|J_z\rangle$ basis. The positive $\hat{z}$ axis is defined along the tip-sample distance and points from the sample toward the STM tip. The first excited quasi-doublet is found around 30 meV and the MAE is close to 170 meV, 28% lower than the one of Dy^{top}. The calculations are in good agreements with the experimental XAS spectra and predict a nearly pure $< J_z > \approx \pm 6$ ground state for Tb^{top}. In contrast, the magnetic ground state of Tb^{br} is strongly mixed in the $|J_z\rangle$-basis and is expected to have a zero net magnetic moment.

6.2 Two-state Noise on Top-Oxygen Site Tb

To confirm the presence of a stable magnetic moment along an out-of-plane easy axis of the magnetization, we study Tb^{top} with SP-STM in an out-of-plane external magnetic field. The two magnetic orientations of Tb^{top} are successfully probed with a SP tip in a two-state noise experiment at $T_{STM} = 0.4$ K and $B_z = 1.5$ T. A contrast of $\Delta z = 5$ pm is observed at a current setpoint of 20 pA and a junction bias of 190 mV.

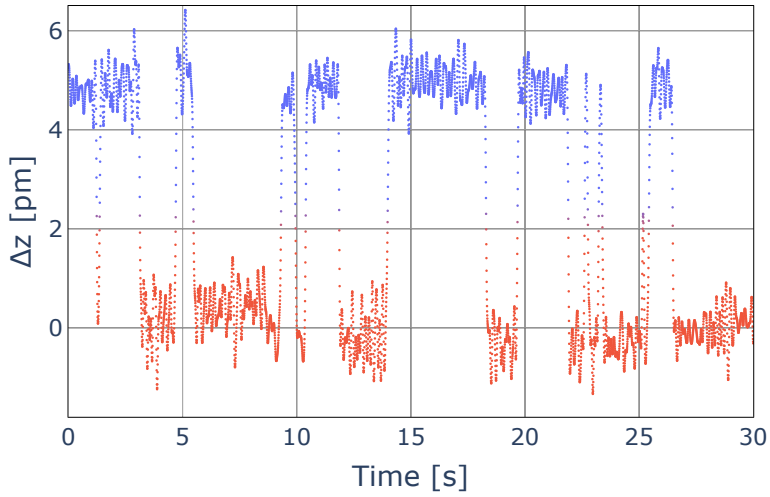

Figure 6.2: Two-state noise on Tb^{top}, performed at $T_{STM} = 0.4$ K, $V_t = 190$ mV and $I_t = 20$ pA, in an external magnetic field of $B_z = 1.5$ T. A Gaussian filter is applied with $\sigma = 6.5$ for a sampling rate of 200 Hz.

We assume that the tip's magnetic moment is pointing upwards, aligned with the external magnetic field applied out-of-plane. The blue points in figure 6.2 correspond to the higher conductance state and, therefore, to the magnetic ground state $< J_z > \approx -6$. The ground state is found stable for more than 500 s at $B_z = 1.5$ T and $T_{STM} = 0.4$ K for tunneling parameters of $V_t = 70$ mV and $I_t = 400$ pA. Under these conditions, the excited state, that is fully anti-parallel to the external field, shows a similar stability. Therefore, the lower limit of the magnetic lifetime is 500 s.

Similarly to Dy^{top}, we verify if the magnetization switching is governed by a single-electron process by measuring the switching rate as a function of tunneling current. We show this

measurement for three different tips in figure 6.3. The data are fitted with the function defined in equation 5.2. The exponents N, from the fits, are provided in the figure for each data and show values close to 1, confirming that magnetization reversal pathways are induced by single-electron processes. The error bars in figure 6.3 are the rates corresponding to the square root of the total number of switching counts. Traces "SP Tip 1" and "2" are measured at a fixed tunneling voltage of $V_t = 170$ meV but differ up to a factor of 3 in the switching rate at 150 pA. This difference can be explained by the different tip-adatom interactions, induced, for example, by different tip magnetic stray fields. Additionally, spin-pumping can also affect the probability of the magnetization reversal, from one data set to another. The data "SP Tip 3" in figure 6.3 is measured at a lower voltage $V_t = 120$ mV and shows, consequently, a lower switching rate.

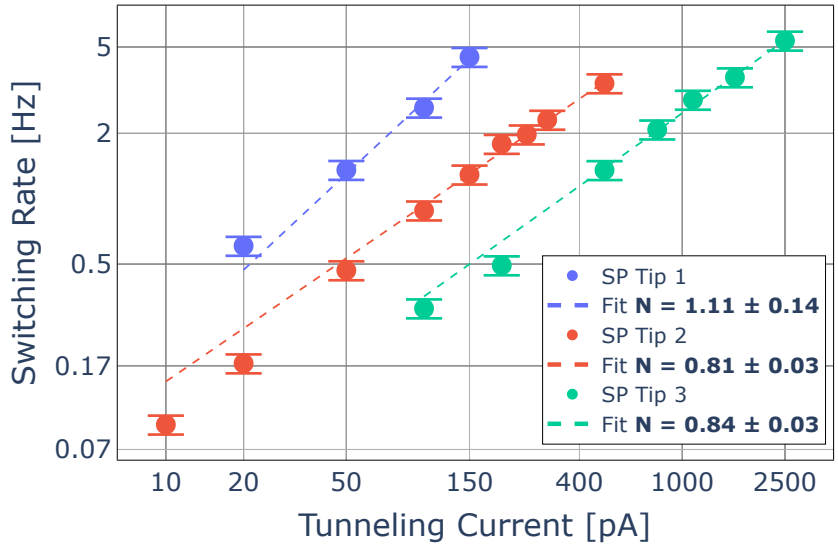

Figure 6.3: Switching rate of Tb^{top} as a function of tunneling current, and shown in a log-log plot. The data are measured at $T_{STM} = 0.4$ K, in an external magnetic field of $B_z = 1.5$ T.

To identify the energy onsets for different magnetization reversal paths, and to gain further insights into the low-energy levels of Tb^{top} along $\hat{z}$, we measure the switching rate as a function of tunneling voltage. We show the results for three different tips in figure 6.4. The data in this figure are scaled to a tunneling current of $I_0 = 1.5$ nA, according to the following equation:

$$\Gamma_{1.5\,\mathrm{nA}}(V_t) = \Gamma(V_t, I_1) \cdot \left(\frac{I_0}{I_1}\right)^N \tag{6.1}$$

where $\Gamma_{1.5\,\mathrm{nA}}(V_t)$ is the switching rate shown in figure 6.4, $\Gamma(V_t, I_1)$ the switching rate measured initially with a tunneling current I_1 and N obtained from equation 5.2. The trace "SP Tip 4" of figure 6.4 is scaled with an exponent of 1, assuming an ideal single-electron process, since no current-dependent measurement has been realized with this tip. The two other traces are scaled using the fitting exponents provided in figure 6.3. The error bars in figure 6.4 are the rates corresponding to the square root of the total number of switching counts.

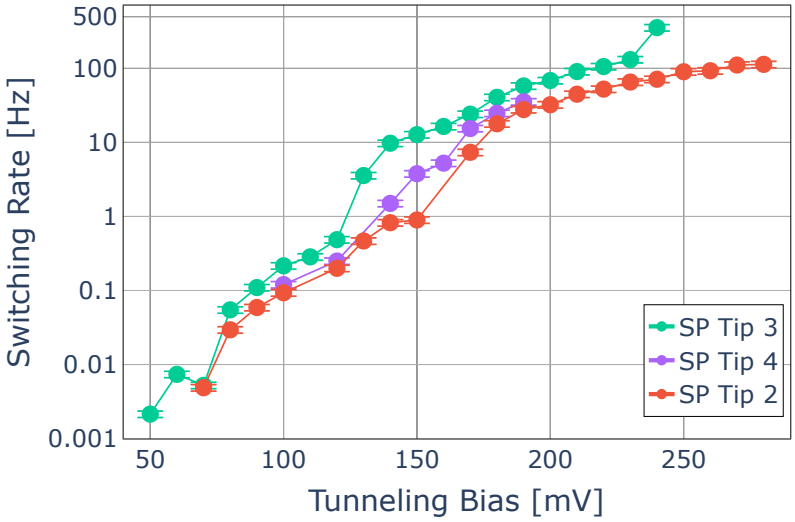

Figure 6.4: Switching rate of Tb^{top} as a function of the tunneling voltage, shown in a semi-log plot. The data are acquired at T_{STM} = 0.4 K and B_z = 1.5 T. SP tip 2 and SP tip 3 are the same tips used for the measurements shown in figure 5.6.

The switching rates in figure 6.4 are consistent for different tips at voltages below 120 mV. At 50 mV, a current of 2.5 nA is applied and 3 magnetization switchings are recorded over 15 minutes. A reliable measurement of the switching rate, below 50 mV, implies recording traces for hours at a high tunneling current. In addition to the risk of changing the atomic tip termination, such a high current can lead to strong spin-pumping effects and low tip-adatom distances can modify the CF parameters and the magnetic system itself. For these reasons, we did not conduct two-state noise experiments below 50 mV and we were not able to compare our results with the quantum chemical calculations below 50 meV. Above 120 mV, the switching rates differ for the different tips by up to one order of magnitude at 150 mV. As for the current-dependent measurements, this difference can originate from spin-pumping effects and different tip-adatom interactions, such as Heisenberg exchange and dipolar field interactions.

To quantify the role of each SP tip in figure 6.4, we plot the evolution of the corresponding ground state population with the tunneling voltage in figure 6.5. At this external magnetic field, the magnetic populations are expected to be close to 50% in a two-state noise experiment and in absence of spin-pumping effects from the SP tip. In figure 6.5, the ground state population is converging towards 50% for "SP Tip 2" and "3" at high biases since the switching rate increases with the tunneling voltage. The time spent in the ground and excited state before a reversal of the magnetization is thus likely to be the same at high energies. Below 100 mV, strong deviations from 50% are observed for the three tips and can be explained by the low number of magnetization switchings. One would need to measure longer at these low tunneling voltages to estimate accurately the ground state population. Between 120 mV and 170 mV, differences in ground state populations are observed, especially for "SP Tip 3" with respect to the others. From this graph, we conclude that the three tips have different spin-

pumping contributions and magnetic fields sensed by the adatom, seen as different ground state populations, that could explain the different switching rates shown in figure 6.4 between 120 mV and 170 mV.

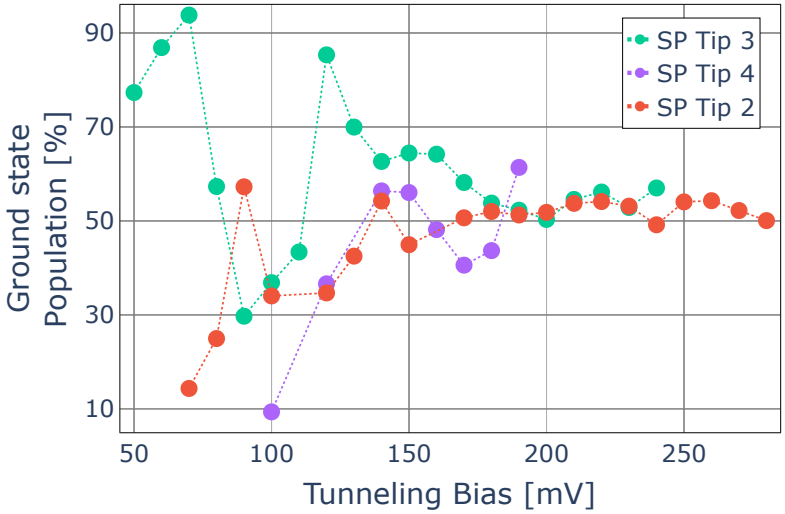

Figure 6.5: Evolution of the ground state population corresponding to the data and SP tips shown in figure 6.4.

Despite different tip-adatom interactions, we show below that the three tips reveal similar energy onsets around 70 meV, 120 meV and 160 meV. To extract these energies, we use the same function as in equation 5.3 to fit the traces of figure 6.4:

$$\Gamma_{1.5\,\mathrm{nA}} = \sum_{i=1}^{3} H(V - V_i) \cdot c_i \cdot \frac{(V - V_i)}{V_i} \tag{6.2}$$

where $H(V - V_i)$ is the Heaviside function and $|e|V_i$ the energy onset associated to a coefficient c_i. Figures 6.6 to 6.8 show each data set with the individual onset contributions extracted from the fit. In figure 6.8, only the two onsets at high energy are fitted, given the narrower bias range. Table 6.1 summarizes the energy onsets obtained from the fits.

	SP Tip 2	**SP Tip 3**	**SP Tip 4**	**Average**
$\|e\|V_1$ [meV]	(69.57 ± 0.02)	(74.13 ± 0.04)	-	(71.85 ± 3.22)
$\|e\|V_2$ [meV]	(119.40 ± 0.75)	(120.12 ± 0.11)	(130.25 ± 0.03)	(123.26 ± 4.29)
$\|e\|V_3$ [meV]	(162.43 ± 0.05)	(168.36 ± 0.05)	(160.0 ± 0.01)	(163.60 ± 3.04)

Table 6.1: Energy onsets found for the data sets presented in figure 6.4, using equation 6.2.

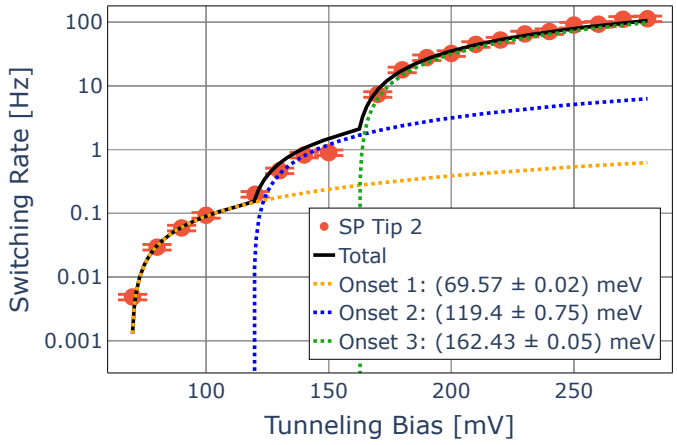

Figure 6.6: Energy onsets fitted to the "SP Tip 2" trace using equation 6.2.

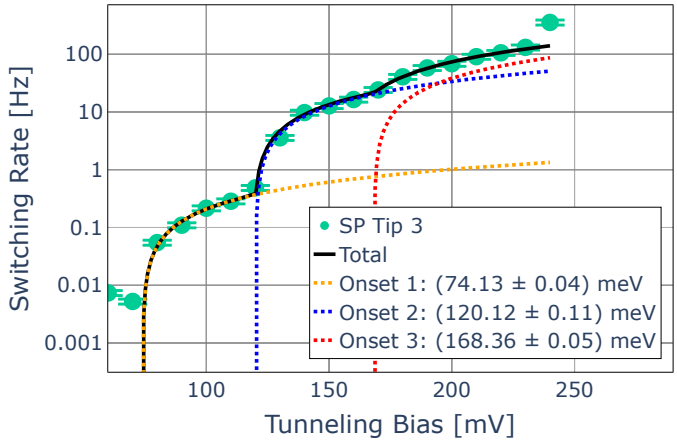

Figure 6.7: Energy onsets fitted to the "SP Tip 3" trace using equation 6.2.

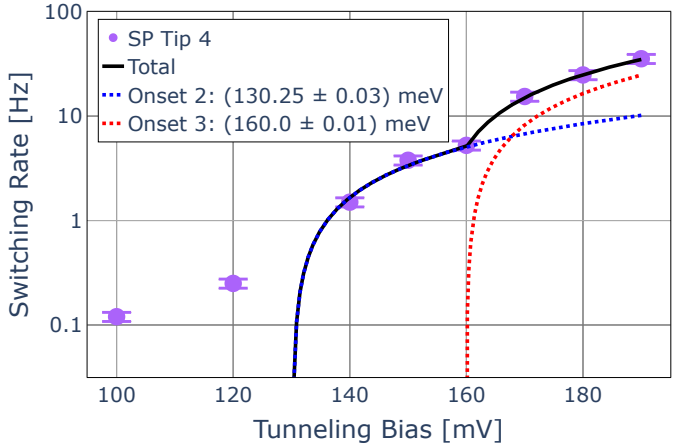

Figure 6.8: Energy onsets fitted to the "SP Tip 4" trace using equation 6.2.

6.2.1 Discussion

The onsets found in the energy-dependent measurements of the switching rate can be attributed to the opening of reversal paths of the 4f magnetization, according to the scheme shown in figure 6.1. The magnetization's reversal of the 4f electrons cannot directly be observed as spin contrast in SP-STM. As discussed in section 2.3.7, we therefore assume an exchange coupling between the 6s5d electrons, accessible with SP-STM, and the confined 4f electrons. In the case of lanthanides, this exchange coupling has to be larger than the splitting of the magnetic states caused by the CF field. Based on this assumption, we attribute the onsets to the following 4f transitions, from state $|\pm 6\rangle$ to state $|\mp 6\rangle$, assuming that the system can be approximately described by pure states in the $|J_z\rangle$ basis:

$$\begin{cases} \text{Onset 1 } (\sim 72 \text{ meV}): & |\pm 6\rangle \rightarrow |\pm 4\rangle \rightarrow \ldots \rightarrow |\mp 6\rangle \quad (\Delta m_J = \mp 2) \\ \text{Onset 2 } (\sim 123 \text{ meV}): & |\pm 6\rangle \rightarrow |\pm 2\rangle \rightarrow \ldots \rightarrow |\mp 6\rangle \quad (\Delta m_J = 0) \\ \text{Onset 3 } (\sim 164 \text{meV}): & |\pm 6\rangle \rightarrow |\pm 1\rangle \rightarrow \ldots \rightarrow |\mp 6\rangle \quad (\Delta m_J = \mp 1) \end{cases} \tag{6.3}$$

We use the selection rules for single-electron inelastic scattering $\Delta m_J = 0, \pm 1$ as we showed in figure 6.3 that a single-electron process governs the magnetization switching for SP Tips 2 and 3. In figures 6.9 to 6.11, we illustrate the possible excitations from the ground state $|J_z = -6\rangle$, corresponding to the magnetization reversal paths introduced in equation 6.3. We use, in these figures, the energy level scheme predicted by quantum chemical calculations in an out-of-plane magnetic field of 1.5 T. States drawn with the same color are mixed by the predicted C_{4v} CF.

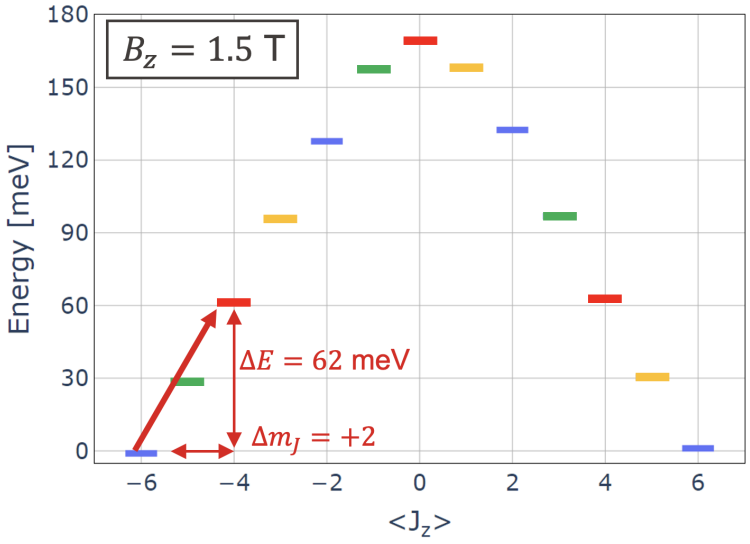

Figure 6.9: Excitation path for Onset 1 (72 meV), according to equation 6.3, corresponding to the transition $|-6\rangle \rightarrow |-4\rangle$ with a predicted energy difference of $\Delta E = 62$ meV. Once the system is in the excited state, the adatom's spin can tunnel through the anisotropy barrier and relax to $J_z = 6$ due to sufficient state mixing caused by the C_{4v} CF.

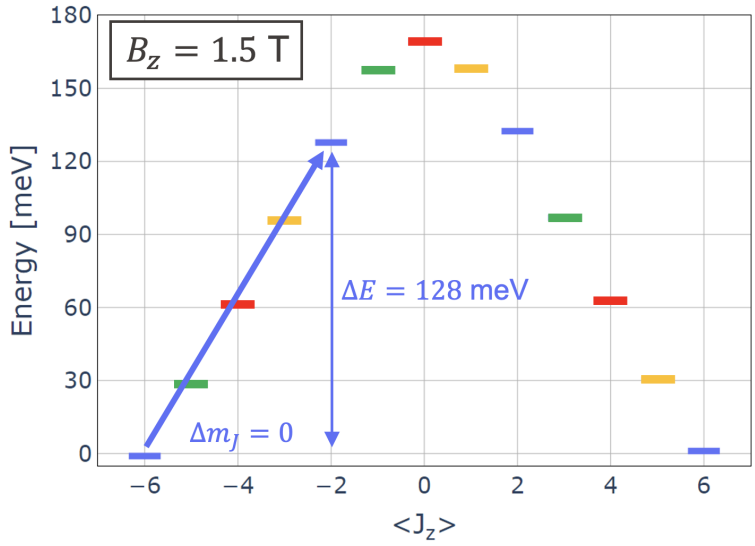

Figure 6.10: Excitation path for Onset 2 (123 meV), according to equation 6.3, corresponding to the transition $|-6\rangle \rightarrow |-2\rangle$ with a predicted energy difference of ΔE = 128 meV. Once the system is in the excited state, the adatom's spin can tunnel through the anisotropy barrier and relax to $J_z = 6$ due to sufficient state mixing caused by the C_{4v} CF.

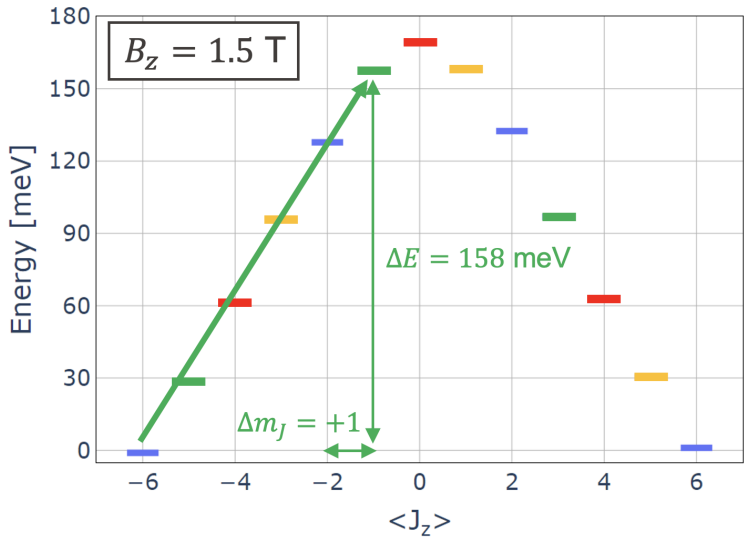

Figure 6.11: Excitation path for Onset 3 (164 meV), according to equation 6.3, corresponding to the transition $|-6\rangle \rightarrow |-1\rangle$ with a predicted energy difference of ΔE = 158 meV. Once the system is in the excited state, the adatom's spin can tunnel through the anisotropy barrier and relax to $J_z = 6$ due to sufficient state mixing caused by the C_{4v} CF.

As shown in figure 6.9, the energy found for Onset 1 corresponds most closely to the transition $|-6\rangle \rightarrow |-4\rangle$ in the energy level scheme, with $\Delta m_J = +2$. This requires the inelastic scattering of a phonon, which should not appear in the bias-dependent switching rate. We provide different explanations to this apparent contradiction. First, there can be a coupling

mechanism between tunneling electrons and phonons, explaining the observed onset indirectly caused by phonon scattering. This hypothesis is unlikely as the predicted vibrational modes of Tb^{top} on MgO are one order of magnitude lower in energy [163]. Second, the onset value we identify at 72 meV is inaccurate, given the low switching statistics at low biases. We could imagine that the system possesses a lower onset energy, accessible at higher tunneling currents and closer to 30 meV. In this case, this energy would be consistent with a predicted magnetization reversal path $|-6\rangle \rightarrow |-5\rangle \rightarrow |+6\rangle$ ($\Delta E \sim 30$ meV) and could be explained by inelastic electron scattering. Third, the energy level scheme predicted by quantum chemical calculations is imprecise, rendering the comparison to our experimental onsets obsolete. Nevertheless, on figures 6.10 and 6.11, the experimental onsets match relatively well the predicted energy splittings, corresponding to excitations allowed by inelastic electron scattering. As the states $|-6\rangle$ and $|-2\rangle$ are mixed by the C_{4v} CF, no spin exchange is required between tunneling electrons and the adatom's spin for the transition $|-6\rangle \rightarrow |-4\rangle$. This explains the difference $\Delta m_J = 0$ in figure 6.10, and $\Delta m_J = +1$ in figure 6.11.

6.2.2 Outlook

To verify the validity of the magnetization reversal paths, introduced in equation 6.3, we could measure the switching rates from the ground and first excited states separately, across a given rate onset, as a function of the out-of-plane magnetic field. We could then identify E_0 and E_1, defined as the energy onsets from the ground state and from the first excited state respectively, splitted by the Zeeman interaction such that $E_0 \neq E_1$ for $B_z \neq 0$. This allows the determination of the slope $\mathrm{d}\big(E_0 - E_1\big)/\mathrm{d}B_z$ that gives information about the magnetic transition induced. Such measurement has already been done on Ho adatoms on MgO in reference [94]. We show, here, how it could be conducted using the onset measured at 164 meV (Onset 3), identified as the transition $|\pm 6\rangle \rightarrow |\pm 1\rangle \rightarrow \ldots \rightarrow |\mp 6\rangle$, written in the $|J_z\rangle$ basis.

Figure 6.12 (A) shows the predicted excitations associated to Onset 3, separating the excitations from the ground state $|J_z = -6\rangle$ (green arrows) with the ones from the first excited state $|J_z = +6\rangle$ (blue arrows). In figure 6.12 (B), we show how the energies E_0 and E_1 change with the applied out-of-plane magnetic field, assuming that the system can be approximately described by pure states in the $|J_z\rangle$ basis. The difference $E_0 - E_1$ can be written as:

$$E_0 - E_1 = g\mu_B B_z \Delta m_J \tag{6.4}$$

where $\Delta m_J = (12 - 2) = 10$ if one assumes that the excitation $|\pm 6\rangle \rightarrow |\pm 1\rangle$ correctly describes the rate Onset 3. As XAS experiments reveal $J = 6$, $L = 3$ and $S = 3$ for Tb^{top} in reference [163], the g-factor in equation 6.4 can be replaced by 1.5. This leads to the following expected slope:

$$\mathrm{d}(E_0 - E_1)/\mathrm{d}B_z = 15\mu_B \approx 0.87 \text{ meV/T} \tag{6.5}$$

Figure 6.13 shows the expected behavior of $(E_0 - E_1)$ as a function of B_z for Onset 3 considering the expected difference $\Delta m_J = 10$ (red). At 8 T (the maximum out-of-plane magnetic

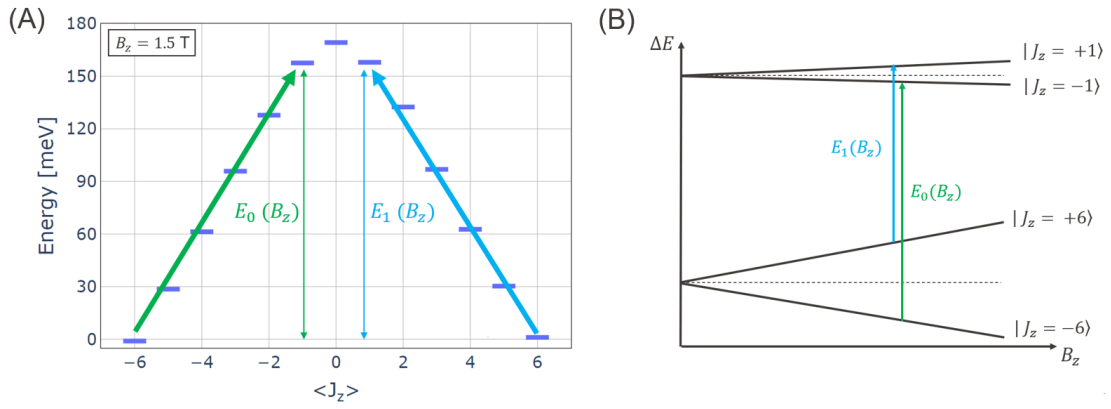

Figure 6.12: Predicted excitations from the ground and first excited states for Onset 3 (164 meV) according to equation 6.3. In (A), we use the energy level scheme at B_z = 1.5 T from quantum chemical calculations to illustrate the different energies E_0 and E_1. In (B), we show the Zeeman splitting of the magnetic states to show how the difference $E_0 - E_1$ grows linearly with the out-of-plane magnetic field.

field we can apply with our coil), an energy difference of ~ 7 meV is expected and would confirm that a transition $\Delta m_J = 10$ is associated to Onset 3. As a comparison, an energy of 5.6 meV at 8 T would correspond to a transition $\Delta m_J = 8$ (blue line in figure 6.13) and would contradict the predictions from the level scheme. As a conclusion, measuring the state-resolve switching rate across a given onset, as a function of B_z, allows to gain insights into the real energy level scheme of Tb^{top}. Also, measuring the slope $d(E_0 - E_1)/dB_z$ provides a comparison with the calculated energy level scheme from quantum chemical calculations, presented in reference [163]. This experiment would have to be done with the same SP tip to prevent variations in the experimental onsets caused by different tip magnetic stray fields, interacting with the adatom.

6.3 STS on Oxygen-Bridge Site Tb

Similarly to Dy^{br}, we do not observe two-state noise on the Oxygen-bridge Tb. However, STS measured with an SP tip in a perpendicular external magnetic field shows steps at around ±23 mV. Figure 6.14 shows STS spectra measured with the same SP tip on Tb^{br}, Fe and MgO.

The conductance of Tb^{br} is asymmetric with a higher step amplitude at negative tip bias. Assuming that these steps correspond to spin excitations and that the tip magnetic moment is aligned with the external magnetic field, the asymmetry can be explained by the combination of elastic and inelastic scattering events as illustrated in figure 2.15. Under these assumptions, a larger step at negative bias corresponds to the inelastic electron scattering with $\Delta m = -1$. STS spectra of Tb^{br} are shown in figure 6.15 for different tips and reproduce the asymmetry and the presence of the steps, at ±23 mV. Surprisingly, spectra with non-SP tips did not show these conductance steps. It is possible that an SP tip enhances the signal-to-noise ratio of the steps through spin-pumping as a non-SP is still capable of probing them but not above our noise level. On each trace of figure 6.15, the conductance experiences a

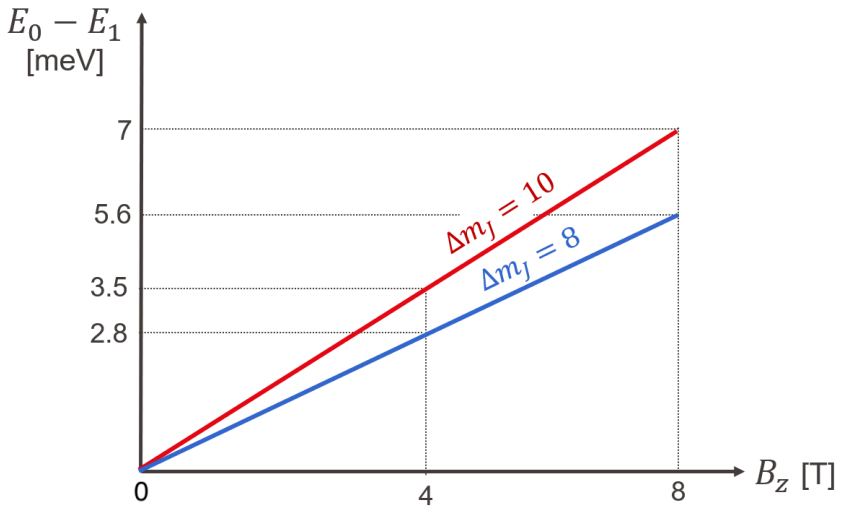

Figure 6.13: Idealistic behavior of $(E_0 - E_1)$ as a function of B_z with $\Delta m_J = 10$ (red line) compared to $\Delta m_J = 8$ (blue line).

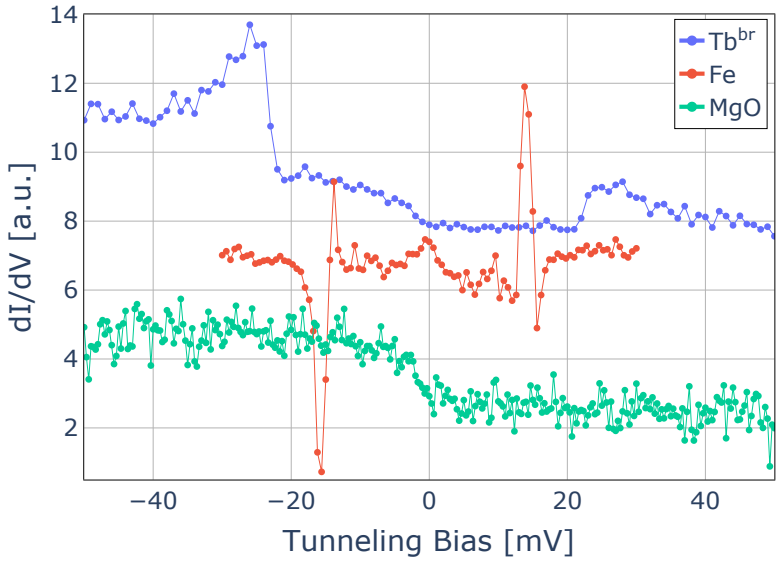

Figure 6.14: STS spectra measured with the same SP tip on Tb^{br}, Fe and MgO. Traces are measured at $T_{STM} = 0.4$ K and $B_z = 1.5$ T. Offsets are applied for clarity.

decay after the step, suggesting transitions mediated by spin-pumping [92].

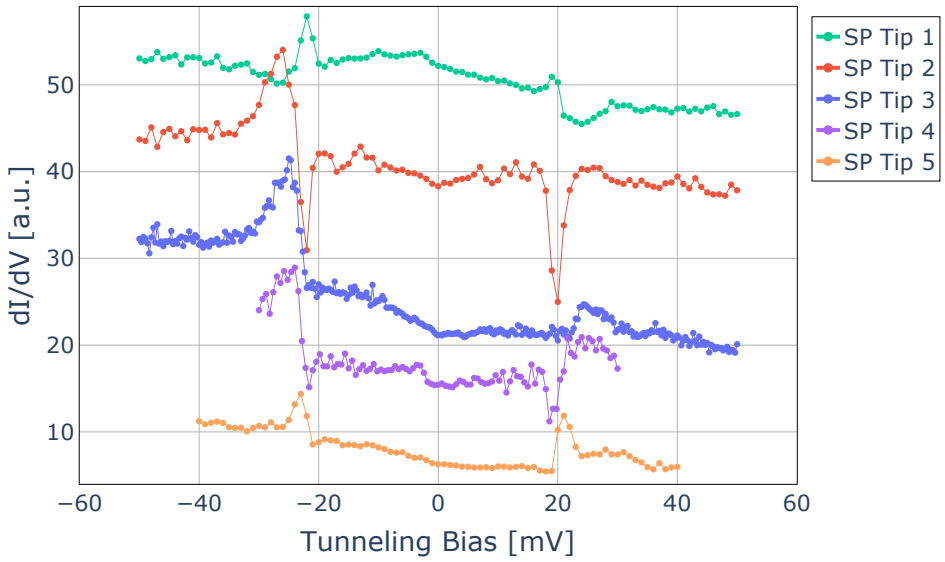

Figure 6.15: STS spectra acquired on Tb^{br} with different SP tips at $T_{STM} = 0.4$ K and $B_z = 1.5$ T.

dI/dV traces are normalized to the tunneling conductance and shown in figure 6.16. Top and bottom graphs of figure 6.16 show the full range and a zoom in the negative-bias step of STS traces, respectively. The decaying behavior of the signal becomes clear above 50 pA and saturates to a maximum amplitude above 500 pA. A possible explanation of the decay is the excitation to higher spin states of Tb^{br} leading to changes in the tip-adatom conductance, as described in reference [92]. Based on this assumption, and at low currents, only the first excited state is accessed and leads to a single step, visible at 10 pA and 20 pA in figure 6.16. At high currents, a decay of the signal above 23 meV corresponds to the access of higher conductance-dependent spin states, each separated by $\Delta m_J = \pm 1$ according to selection rules. This explanation suggests the presence of higher spin states for Tb^{br} and can be verified by determining the electronic configuration of this adatom. Although XAS data determine 8 electrons in the 4f shell, the complete electronic configuration, including the valence electrons, of Tb on MgO is not known. Accessing the electronic configuration of rare-earth adatoms is essential to address and control the magnetic states of the 4f electrons, readily available with STM through their magnetically coupled valence electrons [164]. The step at 23 meV in figure 6.16 can be compared to the energy level splitting of a Tb ion in the gas phase, using the *NIST* spectroscopic database. When the adatom's and ion's electronic configurations are similar, the first energy level splitting of the ion is typically in good agreement with the IETS step energy of the adatom. An example of how this database can be used is given in table 6.2, where rare-earth adatoms on gr/Cu with $4f^n(6s5d)^1$ are compared to their corresponding ion with a similar configuration $4f^n 6s^1$ (positively charged).

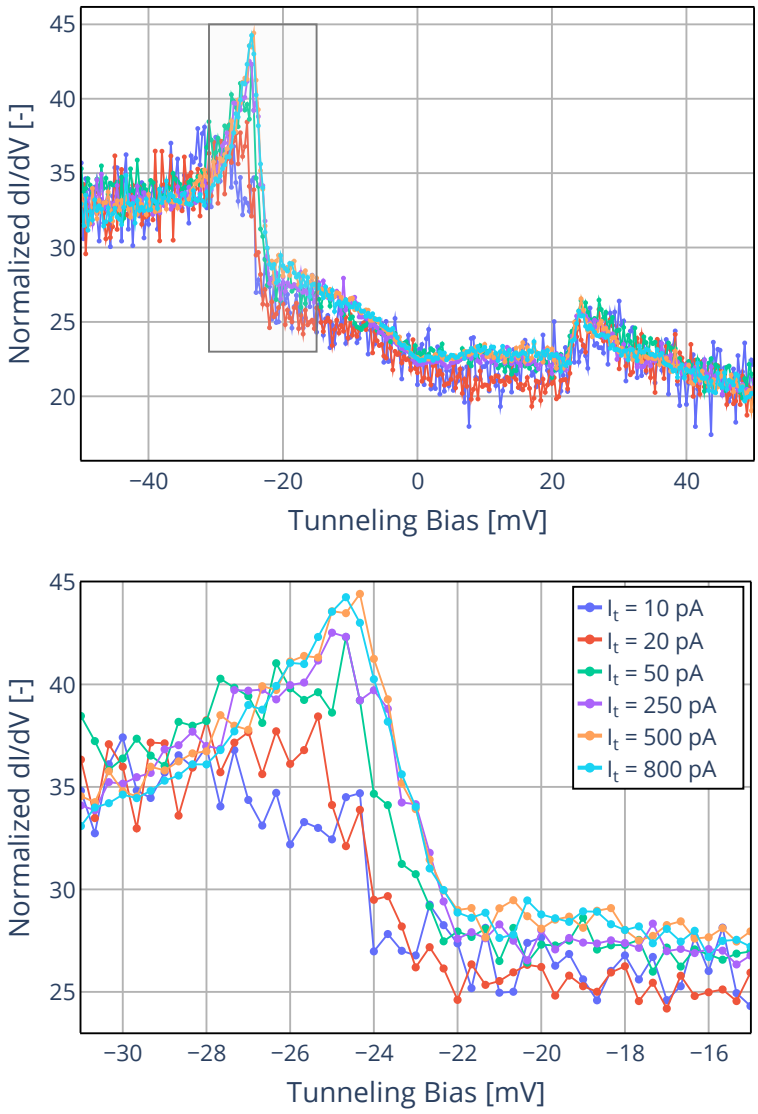

Figure 6.16: STS spectra on Tb^{br} with an SP tip, normalized to the tunneling conductance. Traces are acquired at $T_{STM} = 0.4$ K, in a magnetic field of $B_z = 1.5$ T.

System	Energy from IETS [87] for the adatom on gr/Cu [meV]	Energy from database [165] for the positively charged atom [meV]
Dy	97	103
Ho	74	79
Er	54	55
Tm	32	29

Table 6.2: Comparison of the energies found with IETS in reference [87] and the ones found with the *NIST* database for positively charged ions [165].

The left column of table 6.2 reports the exchange energies between $4f^n$ and $(6s5d)^1$ electrons measured with IETS in reference [87]. The right column shows the energy difference between $S_{6s} = +1/2$ and $S_{6s} = -1/2$ for the positively charged atom using the *NIST* database. Table 6.2 shows that similar energies are found for a similar electronic configuration between the ion and the adatom. Using this method, we can estimate the most probable electronic configuration of Tb^{br} by comparing the step energy of 23 meV found in IETS with the energy level splittings of different ionic states. Table 6.3 shows the low-energy levels of different Tb ions in the gas phase, taken from the *NIST* database. Only the most relevant configurations are shown for our comparison, with a maximum spacing of 38 meV between levels. The energies are given relative to the lowest energy state, for each configuration. Both $4f^8$ and $4f^9$ configurations are considered in table 6.3 since XAS results, predicting $4f^8$, apply mostly to Tb^{top}, with a relative abundance of 83% on the surface [163]. Table 6.3 shows only the first levels for each configuration as higher levels are well above 50 meV. In the gas phase, there are no high spin states that are consecutively separated by $\Delta m_J = 1$ and available from 23 meV to 50 meV. The decay, found with STS, is therefore not explained based on the existence of higher spin states and using this table. For Tb ($4f^9 \rightarrow 4f^8$) and Tb^{++}, the first accessible energies are probably too high to match our experimental value of 23 meV. For Tb ($4f^8$) and Tb^+, the first transitions at 22 meV and 23 meV are in good agreement with the energy we find in IETS. These transitions correspond to a change of $\Delta m_J = -1$ which is consistent with the asymmetry of our IETS spectra, according to figure 2.15.

Ionic State	**Electronic Configuration**	$\mathbf{m_J}$	**ΔE [meV]**
Tb ($4f^9 \rightarrow 4f^8$)	$4f^9 6s^2$	−15/2	0
	$4f^8 5d^1 6s^2$	−13/2	35
Tb ($4f^8$)	$4f^8 5d^1 6s^2$	−13/2	0
		−15/2	22
		−11/2	28
Tb^+	$4f^8 5d^1 6s^1$	−7	0
		−8	23
		−6	25
Tb^{++}	$4f^8 5d^1$	−13/2	0
		−11/2	31
		−15/2	38

Table 6.3: Low-energy levels for different electronic configurations of Tb in the gas phase [165]. The negative value of the quantum number m_J arises from the projection to the quantization axis $\hat{z}$, where the external magnetic field is applied with our STM.

From the experimental IETS results and the gas phase comparison, the best candidates for the complete electronic configuration of Tb^{br} are Tb ($4f^8$) with $4f^8 5d^1 6s^2$ and Tb^+ with $4f^8 5d^1 6s^1$.

6.4 Conclusion

XAS and XMCD data on Tb atoms adsorbed on MgO reveal a stable and out-of-plane magnetic moment for the top-Oxygen adatoms. We confirm with SP-STM the magnetic bistability of the system, that takes two possible magnetization orientations in two-state noise experiments for different SP tips. Current-dependent measurements of the switching rate are realized and confirm the single-electron nature of the magnetization switching process. Voltage-dependent measurements revealed three energy onsets, found at 72 meV, 123 meV and 164 meV. These energies can be attributed to magnetization's reversal pathways, obtained from quantum chemical calculations.

STS spectra on Oxygen-bridge Tb revealed, with an SP tip, inelastic steps at ±23 meV. We think that these steps correspond to the change of total angular momentum of Tb^{br} induced by inelastic electron scattering. A comparison with energy levels in the gas phase allows to speculate on the electronic configuration of this adatom. We find a good agreement in the level spacings for the $4f^{8}5d^{1}6s^{2}$ and $4f^{8}5d^{1}6s^{1}$ configurations. However, this comparison provides only an estimation as an adatom is typically described by different interactions, hybridization effects and charge transfer with the substrate compared to an atom in the gas phase.

7 Quantum Stochastic Resonance Applied to Single Fe Atoms on MgO

ESR-STM is not the only technique that requires an RF bias modulation in the tunneling junction. Recently, QSR has been applied to magnetic bi-stable Fe atoms adsorbed on Cu_2N/Cu(100) [89]. It shows that the RF modulation can efficiently couple to the magnetization dynamics of the system. In this chapter, we apply QSR to the magnetism of single Fe adatoms on MgO/Ag(100). The main goal is to gain a better understanding of this technique and to explore its potential applications in the context of single atom magnetism at low temperature. The study of Fe on MgO is motivated by the system's short relaxation time, on the order of 1 ms [49]. This characteristic enables the probing and control of the spin dynamics beyond the I/V converter bandwidth, referred to as high-frequency QSR.

In this chapter, we first introduce the magnetic properties of single Fe atoms on MgO. We then present the current- and magnetic field-dependent measurements of the ground state population in RF frequency sweeps. We compare the time τ^*, defined in equation 2.28 and obtained from these measurements, to the relaxation time of the system T_1 reported in reference [49] and shown in figure 2.17.

7.1 Magnetic Properties of Single Fe Atoms on MgO

The magnetic properties of single Fe atoms adsorbed on the top-Oxygen site of MgO have already been investigated with XAS and STM [38, 57]. Multiplet calculations of XMCD spectra reveal a $3d^6$ electronic configuration and a total magnetic moment of 5.2 μ_B in reference [38] and 5.4 μ_B in reference [57]. Both results are consistent with the moments measured with ESR-STM in references [113] and [115], reporting values of $(5.44 \pm 0.03)\mu_B$ and $(5.35 \pm 0.14)\mu_B$ respectively. The energy level scheme, written in the $|S_z\rangle$ basis, is shown in figure 7.1.

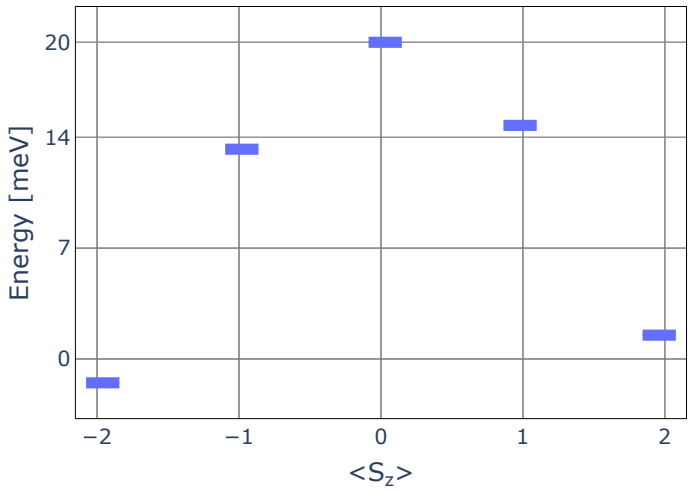

Figure 7.1: Low-energy level scheme of Fe on MgO, for an external magnetic field of $B_z = 2.5$ T. The scheme is obtained using a full point charge model and multiplet calculations [36].

The scheme is obtained from multiplet calculations, based on a full point charge model and on DFT calculations to estimate the CF field contribution [36]. Figure 7.1 shows an out-of-plane easy axis of the magnetization, with a MAE barrier of 20 meV. A ZFS splitting of 14 meV is found and is consistent with the steps observed at ±14 mV in STS spectra, presented in figure 4.1. The Zeeman splitting is included in the energy level scheme, with $B_z = 2.5$ T. We use an effective g-factor of $g^{\text{eff}} = 2.57 \pm 0.06$, deduced from STS spectra measured in different externally applied magnetic fields [38]. Given the C_{4v} CF symmetry, the ground and first excited states are mixed with $|S_z = \pm 2\rangle$ (cf. equation 2.22). A short lifetime of the first excited state is reported and can be controlled up to ~ 3 ms on 2 ML MgO and at low tunneling conductance, as shown in figure 2.17 [49]. We present in figure 7.2 two-state noise measured on Fe at $T_{\text{STM}} = 0.4$ K. The magnetic contrast of $\Delta z \approx 1.15$ pm is much lower than the one found for Dy^{top} and Tb^{top}. Compared to reference [49], the switching rate is lower at these tunneling parameters. The ground and first excited states in figure 7.2 are more stables, with lifetimes on the order of seconds. This difference can be attributed to strong spin-pumping effects from this SP tip, favoring the higher-apparent height state at $I_t = 400$ pA.

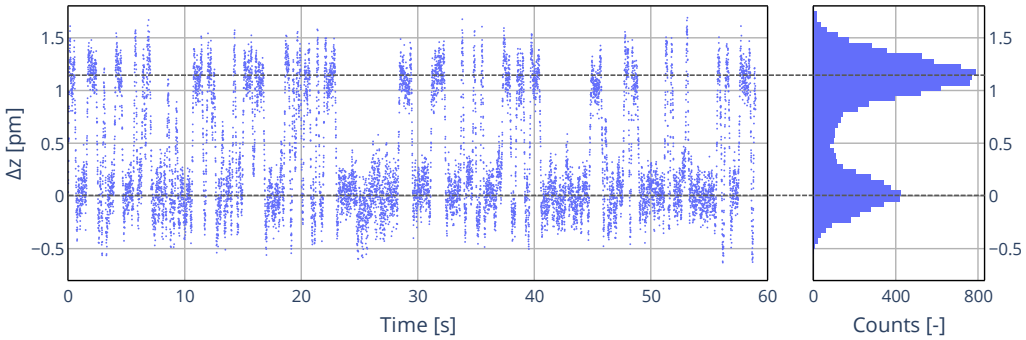

Figure 7.2: Two-state noise on a single Fe atom adsorbed on MgO, measured at $T_{\text{STM}} = 0.4$ K with an external magnetic field of $B_{xy} = 250$ mT, $B_z = 1.0$ T. The tunneling parameters are $V_t = 14$ mV and $I_t = 400$ pA. A Savitzky-Golay filter is applied to the data with a window of 181 points for a sampling rate of 200 Hz. A histogram of Δz is provided and shows uneven magnetic state populations.

Unfortunately, we were not able to record two-state noise with milliseconds timescale and within the I/V converter bandwidth, despite the use of a high sampling rate. We conclude that the low contrast of $\Delta z \approx 1$ pm cannot be probed with an SP tip at these timescales, above our noise level. We assume that this low magnetic contrast can be resolved beyond the I/V converter bandwidth, using a lock-in amplifier and an RF modulation, as described in section 2.3.8. This assumption motivates the conduction of high-frequency QSR experiments on Fe.

7.2 High-frequency QSR Applied to Single Fe Atoms on MgO

We introduce our results in figure 7.3 where lock-in signals are reported for an SP and a non-SP tip, placed over an Fe atom adsorbed on 2 ML-thick MgO. We apply a zero-to-peak

RF amplitude of 10 mV in the tunneling junction for both sweeps and the TF, presented in figure 3.11, is used to compensate the frequency-dependent losses of the RF cabling. The lock-in amplifier is synchronized with the RF chopping scheme shown in figure 2.24. Consequently, the demodulated current recorded with the SP tip in figure 7.3 is proportional to the integrated conductance difference betweeen the ground and first excited state of the system. As introduced in figure 2.21, this signal also provides a measurement of the relative magnetic state occupation. A Lorentzian function fits well the SP tip trace and a decrease of the signal corresponds to a decrease of the magnetic ground state population.

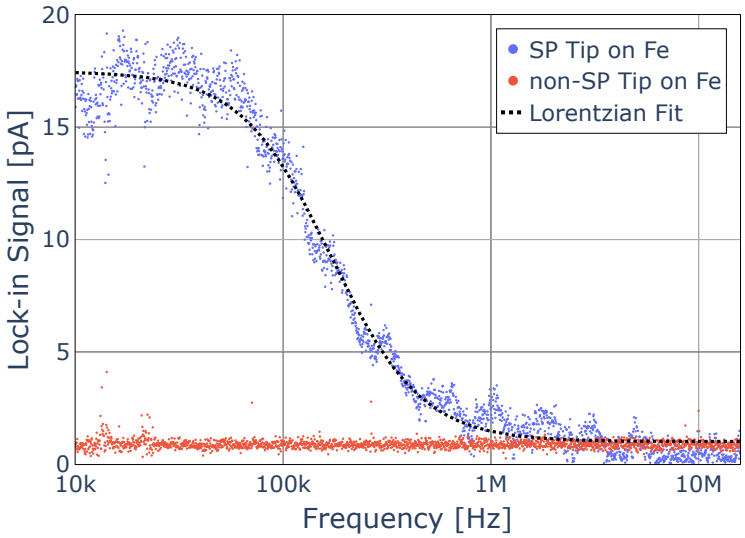

Figure 7.3: Lock-in signals over an RF frequency sweep on Fe adsorbed on 2 ML MgO, measured at $T_{STM} = 0.4$ K and $B_z = 2.5$ T. An RF modulation amplitude of 10 mV is applied, with the following tunneling parameters: $V_t = -10$ mV, $I_t = 400$ pA.

In figure 7.3, we extract the HWHM from the Lorentzian and find (169.65 ± 1.23) kHz. The corresponding time, defined in equation 2.28, is $\tau^* = (5.89 \pm 0.04)$ μs. In comparison, the non-SP tip of figure 7.3 does not show magnetic contrast and results in a feature-less demodulated current, as expected.

To estimate if $\tau^*/2$ could provide a measurement of the relaxation time T_1 of the non-driven system, we conduct current- and magnetic field-dependent measurements of $\tau^*/2$ and compare its behavior with T_1, taken from reference [49].

7.2.1 Current-dependent Measurements

Figures 7.4 to 7.6 show the current-dependent measurements of the change in magnetic state population of Fe at $B_z = 1.5$ T and $T_{STM} = 0.4$ K. Each graph corresponds to a different SP tip and each data point is normalized by the tunneling current, adjusted between 0 and 1. A Savitzky-Golay filter is applied to the traces of figure 7.6 with a window of 24 points and a polynomial order of 7 for a sampling rate of 200 Hz. These operations do not affect the value

of the HWHM, the only fitting parameter of the Lorentzian function.

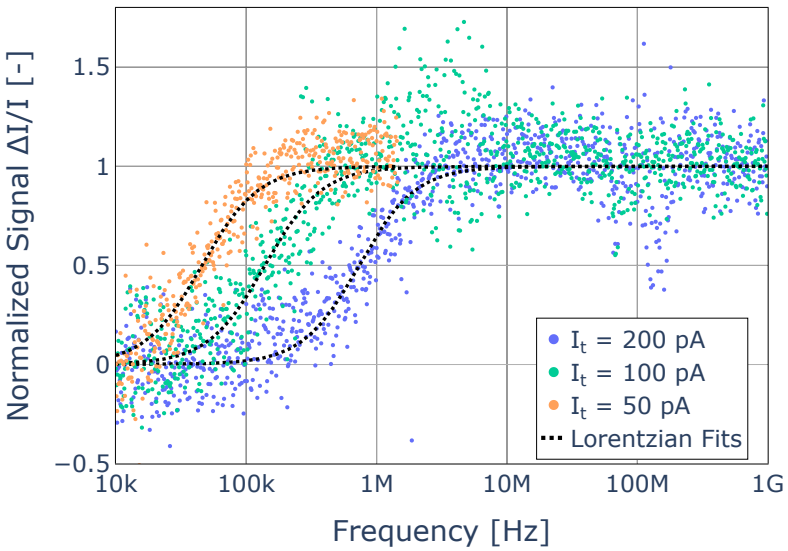

Figure 7.4: SP Tip 1. Relative change in the magnetic state population of Fe on 3 ML MgO. A tunneling voltage of $V_t = -10$ mV is used in addition to an RF modulation amplitude of $V_{\mathrm{RF}} = 10$ mV.

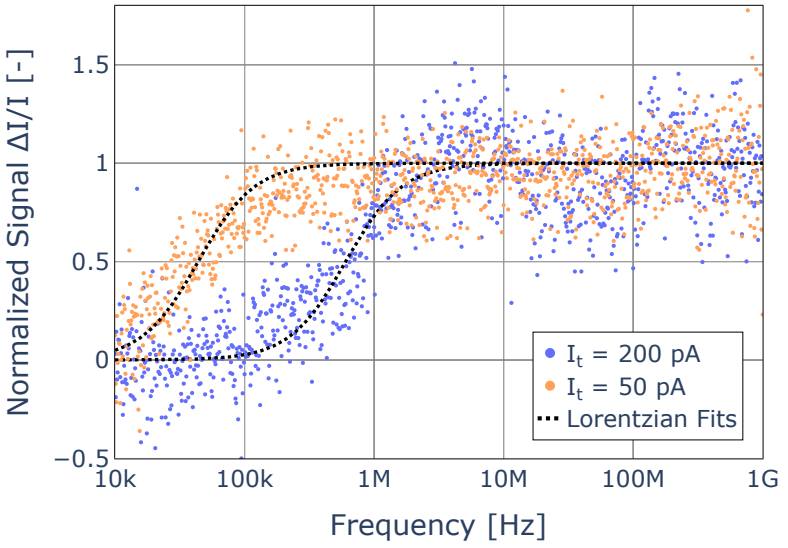

Figure 7.5: SP Tip 2. Relative change in the magnetic state population of Fe on 3 ML MgO. A tunneling voltage of $V_t = -10$ mV is used in addition to an RF modulation amplitude of $V_{\mathrm{RF}} = 10$ mV.

Compared to figure 7.3, the Lorentzian amplitudes are inverted, fitting a demodulated current increasing with increasing RF frequency, and is explained by opposite tip's and adatom's magnetic ground states. This can be explained by a strong antiferromagnetic exchange coupling between the tip and the adatom, favoring an anti-parallel configuration.

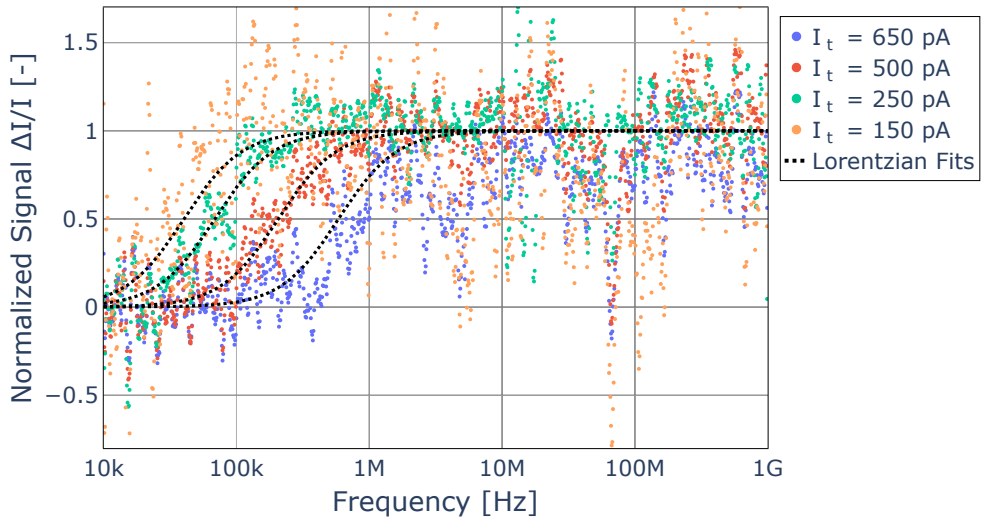

Figure 7.6: SP Tip 3. Relative change in the magnetic state population of Fe on 2 ML MgO. A tunneling voltage of $V_t = -10$ mV is used in addition to an RF modulation amplitude of $V_{\mathrm{RF}} = 10$ mV.

We report the time $\tau^*/2$ in figure 7.7, where τ^* is the drive period extracted from the Lorentzian fits at the HWHM. Tip 1 and 2 show consistent values, measured on 3 ML MgO. The data acquired on 2 ML MgO differ by a factor of 3 in current for the same time. This can be explained by a higher conductance on thinner MgO films measured at a fixed tip-adatom distance.

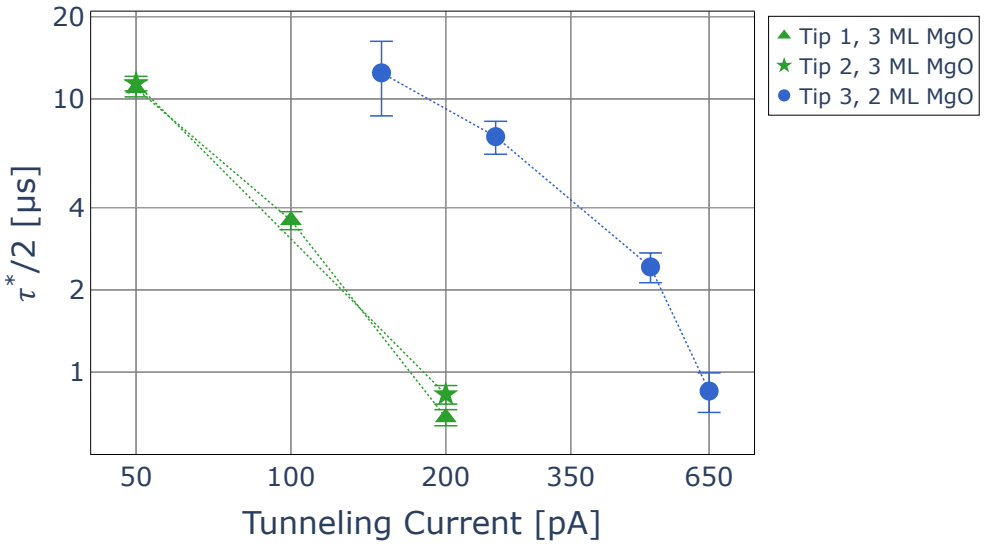

Figure 7.7: Log-log plot of the time $\tau^*/2$ found for all traces shown from figures 7.4 to 7.6. The data are measured in a magnetic field of $B_z = 1.5$ T at $T_{\mathrm{STM}} = 0.4$ K.

In figure 7.8, we show the relaxation time T_1, measured with pump-probe spectroscopy at $T = 1.2$ K and $B_z = 5$ T, taken from reference [49]. During the delay time, separating the pump and probe pulses, no bias is applied, leading to a lower contribution of tunneling electron scattering compared to the case $V_t \neq 0$. Given the different experimental parameters, a

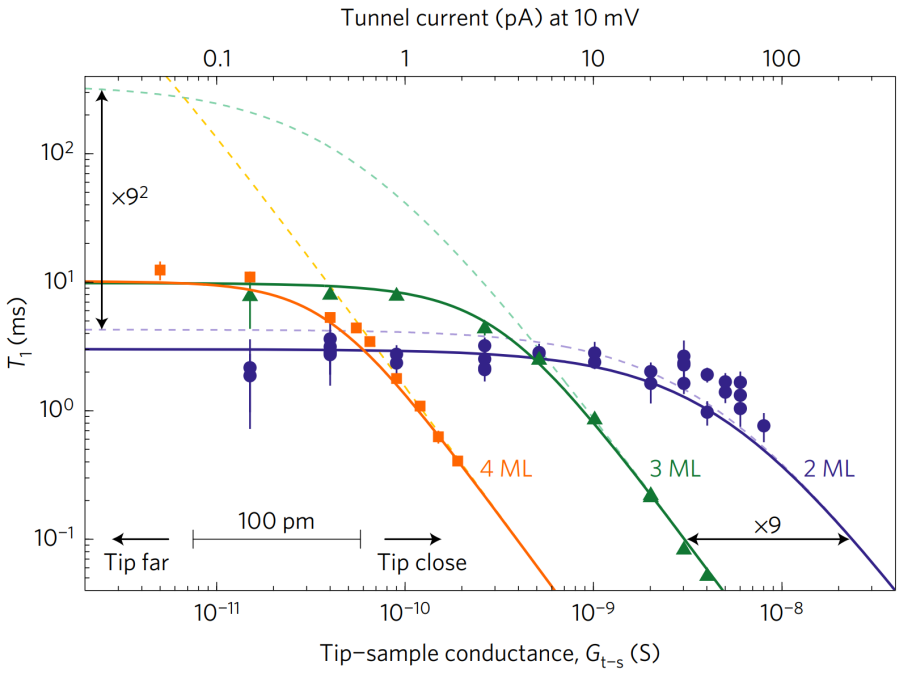

Figure 7.8: T_1 measured with pump-probe spectroscopy (data points). The solid lines represent the rate equation model $1/T_1 = r_e + r_{ne}$, described in section 2.3.6. The rate r_{ne} is a fitting parameter, taken as a constant and independent of the MgO thickness. The measurement conditions are $B_z = 5$ T and $T_{STM} = 1.2$ K [49].

quantitative comparison of our time with T_1 of figure 7.8 is not possible. We can, however, compare the variation of both times to estimate if $\tau^*/2$ is limited by the same scattering processes as T_1. We show in the same plot our time $\tau^*/2$ and T_1 from reference [49] in figure 7.9, where the $\hat{x}$ axis has been extended as well as the solid lines to higher tunneling current. Our data appear at the bottom right corner of figure 7.9 and show a similar asymptotic behavior than T_1, suggesting that our time is also limited by the tip-tip electron scattering at high tunneling currents. The value of $\tau^*/2$ is, however, lower than the rate equation fit at the same tunneling current, by a factor of 3 and 20 for 3 and 2 ML MgO respectively. Further experiments are therefore required to see if both times show similar values at the same experimental conditions.

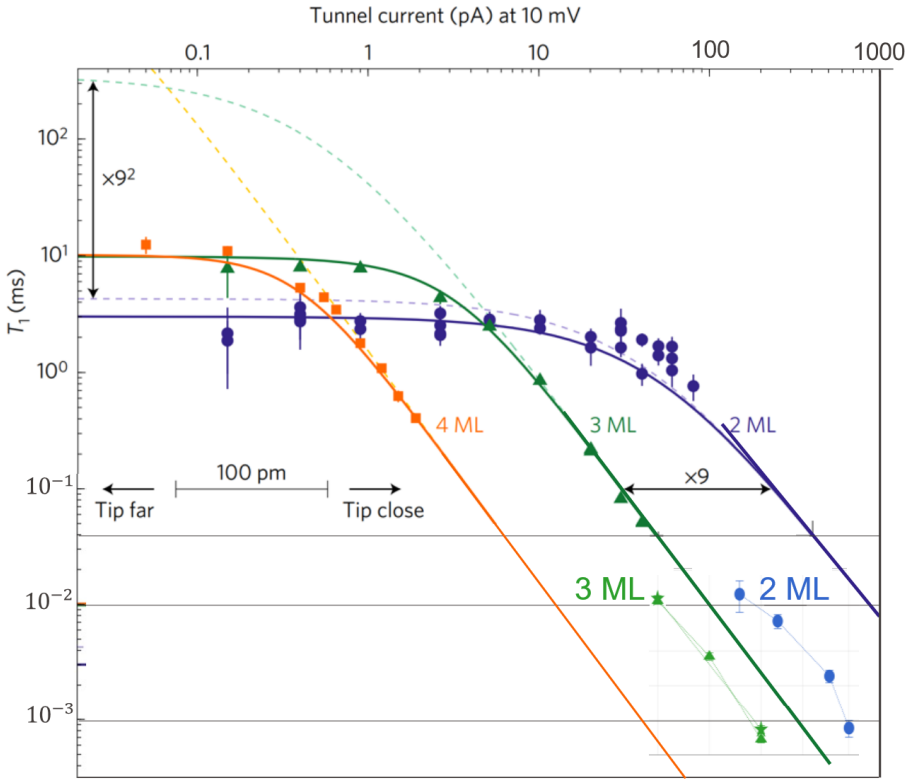

Figure 7.9: T_1 from reference [49] plotted with our time $\tau^*/2$ from figure 7.7.

7.2.2 Magnetic field-dependent Measurements

We present in figure 7.10 the relaxation time as a function of out-of-plane magnetic field, measured with pump-probe spectroscopy at $T = 1.2$ K and taken from reference [49]. A relatively large tip-adatom distance is used for this measurement, defined by a tunneling conductance below 150 pS. Consequently, the dominant process shortening T_1, here, is the scattering from substrate electrons and phonons. Using the spin Hamiltonian in equation 2.21 with $E_4 = 1.4$ neV, a linear increase of T_1 is expected with increasing B_z (dashed line). The data points are in good agreement with the model up to a field of 2 T. Beyond this value, the relaxation time deviates from the prediction and saturates around ~ 3 ms. This plateau is not completely understood and could originate from additional non-electronic processes such as the spontaneous emission of a phonon [49]. In comparison, we show in figure 7.11 the magnetic field-dependent measurement of the relative change in the magnetic state population of Fe. The measurements are performed at $T_{STM} = 0.4$ K on an Fe atom sitting on a 3 ML-thick MgO layer. A much shorter tip-adatom distance is used compared to the conditions in figure 7.10, as a tunneling current of 200 pA is applied. The corresponding times $\tau^*/2$ are plotted in figure 7.12.

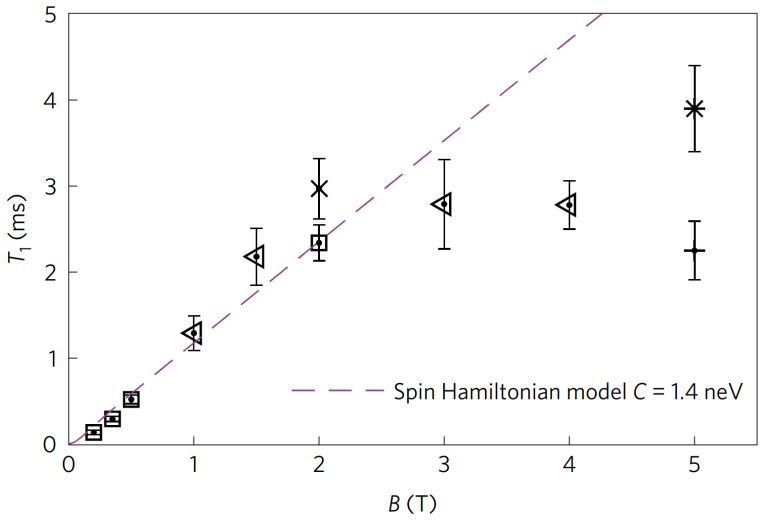

Figure 7.10: T_1 measured on Fe adsorbed on 2 ML MgO as a function of out-of-plane magnetic field. The data points are obtained at a large tip-adatom distance defined by a tunneling conductance below $1.5 \cdot 10^{-10}$ S and at $T_{\mathrm{STM}} = 1.2$ K. The dashed line indicates the predicted T_1 from the spin Hamiltonian model [49].

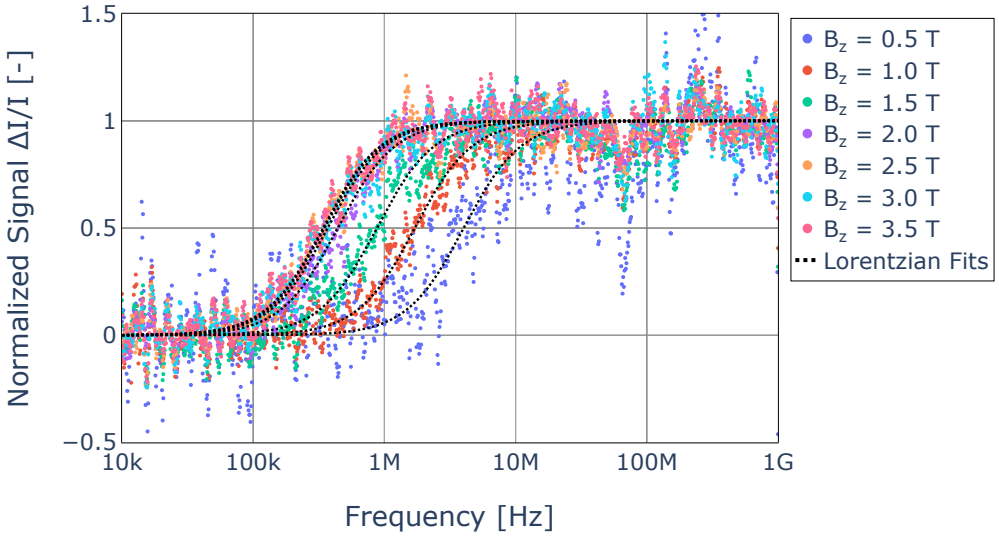

Figure 7.11: Relative change in the magnetic state population of Fe on 3 ML MgO as a function of out-of-plane magnetic field. The tunneling parameters are $V_t = -10$ mV, $I_t = 200$ pA and an RF modulation amplitude of 10 mV is used.

In figure 7.12, the time $\tau^*/2$ increases linearly up to 2.5 T, after which it plateaus around 3 μs. This behavior is identical to the one of figure 7.10. Despite the different tip-adatom distances used, $\tau^*/2$ follows the same trend as T_1, which corroborates the current-dependent measurements. Further experiments are required to compare T_1 from a pump-probe experiment with $\tau^*/2$ at identical experimental conditions.

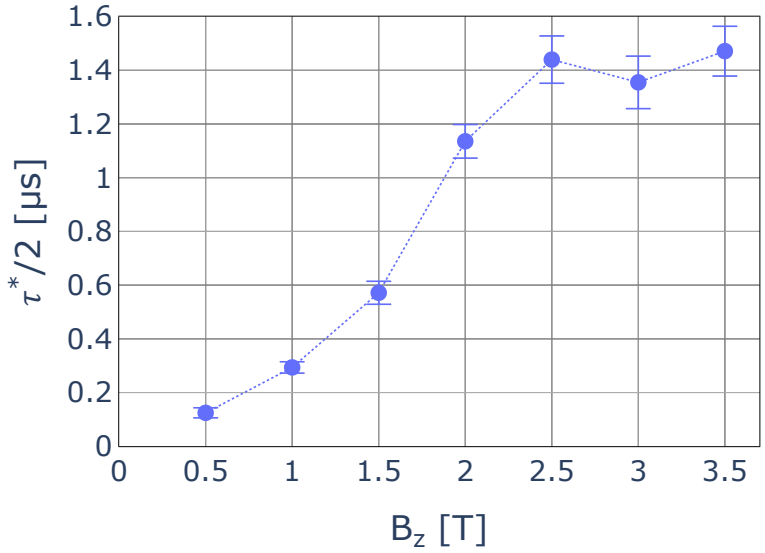

Figure 7.12: Time $\tau^*/2$ found for all traces shown in figure 7.11. The data are measured at $T_{\mathrm{STM}} = 0.4$ K.

7.3 Conclusion and Outlook

Based on the work presented in reference [89], we apply the high-frequency QSR technique to single Fe adatoms on MgO, at switching rates beyond the current amplifier bandwidth. We observe magnetic contrast on Fe atoms in RF frequency sweeps, when applying a constant RF modulation amplitude. We attribute this contrast to the relative change of the magnetic state population, as introduced in section 2.3.8. The traces acquired with an SP tip are well fitted by a Lorentzian lineshape. We report the values of $\tau^*/2$, found from the fits at the Lorentzian HWHM, as a function of MgO thickness, tunneling current, and out-of-plane magnetic field. The variations of $\tau^*/2$ are identical to the one of T_1 from reference [49], suggesting that $\tau^*/2$ is limited by the same scattering processes as the relaxation time of the system. We conclude, conservatively, that $\tau^*/2 \propto T_1$. Unfortunately, we were not able to compare the value of both times at the same experimental conditions. To do so, we could think of measuring T_1 with pump-probe spectroscopy, applying a 10 mV bias during the delay time, and compare it with $\tau^*/2$ measured at $V_t = 10$ mV, $V_{\mathrm{RF}} = 10$ mV and at the same tip-adatom distance, magnetic field and temperature. We expect the two times to be similar, as described in section 2.3.8. However, it remains questionable whether the application of an RF bias modulation in the QSR technique could generate additional relaxation rates compared to a pump-probe measurement. We list, here, different processes, proper to the QSR technique, that could shorten the adatom's spin lifetime: 1) the time-varying tunneling current induced by the RF bias modulation, 2) spin-photon interaction, 3) small variations of the CF caused by the piezoelectric response of the adatom to the time-varying electric field. To overcome these driven mechanisms, one could extrapolate the time $\tau^*/2$ to zero tunneling current and see whether it can provide a measurement of the intrinsic relaxation time of the system.

Beyond the comparison between $\tau^*/2$ and T_1, high-frequency QSR can be extended to other magnetic systems, showing fast spin dynamics. For example, TiH molecules on MgO should reveal a magnetic contrast at high RF frequencies. This technique can also be applied to Dy^{br} and could reveal whether there is an unstable magnetic moment in the ground state, along the $\hat{x}$ axis, or whether the Dy^{br} magnetic moment is so stable that we simply couldn't excite it with the tunnel voltages used in section 5.3.

8 Conclusion and Outlook

In this thesis, the magnetism of single surface adsorbed atoms and molecules has been addressed with a 0.4 K ESR-STM. The upgrades brought to the RF cabling leads to an improved RF transmission down to the tunneling junction, up to 40 GHz. This allows the conducting of frequency sweeps in ESR and QSR experiments, while applying a constant RF junction amplitude.

To characterize our instrument after the technical upgrades implemented on the system, and to test the ability of conducting ESR experiments on new single surface adsorbed atoms, we have addressed the system TiH/MgO/Ag(100) with ESR-STM, as a benchmarked system for our microscope. We have successfully measured ESR signals on TiH_B and TiH_O at 0.4 K and 4.2 K respectively. The g-factor and molecule's magnetic moment have been determined from frequency sweep experiments and are consistent with the values found in literature. We could, however, improve the precision and accuracy of such measurements by quantifying the influence of the magnetic tip on the resonance condition. A tip-sample distance-dependent measurement of the ESR signal would enable a better understanding of a given ESR tip contribution, described by the sum of an exchange and dipolar magnetic fields. Additionally, we have resolved narrow ESR linewidths below 40 MHz at 0.4 K. This allows the conducting of other ESR-STM experiments such as the sensing of small magnetic fields on an ESR-active sensor. In this case, we could determine the magnetic moment of a nearby top-Oxygen Tb adatom, and compare the result with XAS experiments and quantum chemical calculations. Overall, our results on TiH molecules show that our instrument is capable of probing ESR signals up to 4.2 K above our noise level and motivate the investigation of new ESR-active systems that could reveal long coherence times. Besides looking for new ESR-active elements, another option is to investigate different substrates than MgO. Graphene is prospective since many rare-earth adatoms have open valence shell electronic configurations on it [87, 166]. The open valence shell gives rise to spin-contrast in a spin-polarized tunneling junction which is the prerequisites to measure ESR contrast. In addition, many rare-earth atoms are stable single atom magnets on graphene. As a result, it is very promising to perform ESR-STM on rare-earth adatoms on graphene.

Dy and Tb adatoms on MgO have been studied with SP-STM. For both top-Oxygen adsorption sites, the objective was to investigate the stability of their magnetic moments along an out-of-plane easy axis of the magnetization, predicted by multiplet (Dy^{top}) and quantum chemical (Tb^{top}) calculations and demonstrated in XAS experiments. To achieve this goal, two-state noise experiments have been realized at 0.4 K (Tb^{top}) and 4.2 K (Dy^{top}) to study the reversal of the magnetization for each system, and the magnetization switching rate has been measured as a function of tunneling current and voltage. As tunneling electrons can induce QTM at a certain energy, onsets in the voltage-dependent switching rate provide information about the low-energy level scheme of each system, and can be identified to the possible reversal paths, predicted by calculations. For Dy^{top}, our results are in good agree-

ment with the experimental data and PCEM model of reference [50], where we find a first energy threshold at 140 meV. We report the first two-state noise study on Tb^{top} adatoms and we find three energy onsets at 72 meV, 123 meV and 164 meV. The low-energy level scheme obtained from quantum chemical calculations is compatible with these onsets as they can be identified to magnetization reversal paths predicted at comparable energies. We have thus gained insights into the magnetic stability of the system and report a magnetic ground state lifetime of at least 500 s, in an external magnetic field of B_z = 1.5 T and for a junction bias of 70 mV. We have not observed any magnetization switching at 50 mV, over a time of 15 minutes. As an outlook, we could extend this measurement time significantly, on the order of hours, to measure the intrinsic magnetic lifetime of Tb^{top} in these conditions. This would provide a more complete description of the system and allow a comparison with the magnetic stability of Dy or Ho on MgO.

The Oxygen-bridge adsorption sites Dy and Tb have also been investigated. Multiplet calculations predict an in-plane easy axis of the magnetization for Dy^{br} which motivates the study of this adatom with SP-STM. The objective was to record two-state noise with a tip spin-polarized along the sample's surface. However, we have not achieved this goal with an in-plane SP tip, for voltages up to 440 mV, and we propose different explanations in section 5.4. One of them is that the magnetic moment is too unstable along the in-plane easy axis to detect the magnetization switching within the real-time limit of our instrument. Nonetheless, we have shown that the tip's magnetic moment can be projected along the sample's surface, by applying an in-plane external magnetic field. This method can be used in the future to address single surface adsorbed atoms with a stable in-plane magnetic moment with SP-STM. For Tb^{br}, reference [163] does not indicate if an in-plane easy axis of the magnetization is predicted from calculations. However, we have measured at 0.4 K spin excitation features in SP-IETS at ±23 mV that allow to speculate on the complete electronic configuration of this adatom, including the number of valence electrons. Knowing the complete electronic structure of any rare-earth adatom is essential for controlling the magnetic states of the 4f electrons, accessible with STM via their magnetically coupled valence electrons [164]. To estimate the electronic structure of Tb^{br}, we have compared our SP-IETS data with the *NIST* spectroscopic database for atoms in the gas phase. From this comparison, we identify two possible configurations that are consistent with the step asymmetry measured with SP-IETS: $4f^{8}5d^{1}6s^{2}$ and $4f^{8}5d^{1}6s^{1}$. However, this method constitutes only an estimation of the electronic configuration, as an adatom is subject to different interactions, hybridization effects or charge transfer with the substrate compared to an ion in the gas phase.

Finally, we have investigated the fast spin dynamics of Fe adatoms on MgO/Ag(100) with the QSR technique, beyond the I/V converter bandwidth. The main objective was to gain a better understanding of this recent technique and characterize a system that has not been addressed with it. We find, as reported in reference [89], that the relative magnetic ground state occupation follows a Lorentzian lineshape in frequency sweeps, as the RF modulation drives efficiently the magnetic moment's dynamics. To characterize the spin dynamics of the

system, we have defined the time τ^* related to the drive period at which the ground and first excited state populations are identical. We find in current- and magnetic field-dependent measurements that $\tau^*/2$ scales linearly with the relaxation time T_1, obtained in reference [49]. Therefore, we have successfully gained insights into this technique, that could be used to quantify the influence of external parameters on the system's magnetic lifetime. It could also be promising to estimate the influence of a nearby magnetic adatom on the time τ^*, measured for a given system.

References

[1] F. Hund, Zur Deutung der Molekelspektren. I. Zeitschrift für Physik **40** (1927), p. 742–764.

[2] F. Hund, Zur Deutung der Molekelspektren. II. Zeitschrift für Physik **42** (1927), p. 93–120.

[3] F. Hund, Zur Deutung der Molekelspektren. III. Zeitschrift für Physik **43** (1927), p. 805–826.

[4] J. Frenkel, On the electrical Resistance of Contacts between solid conductors. Physical Review **36** (1930), p. 1604.

[5] H. Iwai, End of the scaling theory and Moore's law. 16th International Workshop on Junction Technology (IWJT) (2016).

[6] M. N. Baibich, J. M. Broto, A. Fert, et al., Giant Magnetoresistance of (001)Fe/(001)Cr Magnetic Superlattices. Physical Review Letters **61** (1988), p. 2472.

[7] Gil Press. 6 Predictions About Data In 2020 And The Coming Decade. Accessed 07/06/2023 at https://www.forbes.com/sites/gilpress/2020/01/06/6-predictions-about-data-in-2020-and-the-coming-decade/, 2020.

[8] R. P. Feynman. *Miniaturization.* 1961.

[9] Fujifilm Group. Fujifilm develops technology to deliver the world's highest 580TB storage capacity for magnetic tapes using strontium ferrite (SrFe) magnetic particles. Accessed 31/07/2023 at https://www.fujifilm.com/fr/en/news/Fujifilm-develops-technology-to-deliver-the-worlds-highest-580TB-storage-capacity-for-magnetic-tapes, 2020.

[10] G. Binnig, H. Rohrer, C. Gerber, E. Weibel, 7x7 Reconstruction on Si(111) Resolved in Real Space. Physical Review Letters **50** (1982), p. 120.

[11] R. Wiesendanger, H. J. Guntherodt, G. Giintherodt, et al., Observation of vacuum tunneling of spin-polarized electrons with the scanning tunneling microscope. Physical Review Letters **65** (1990), p. 247.

[12] D.M. Eigler and E. K. Schweizer, Positioning single atoms with a scanning tunnelling microscope. Nature **344** (1990), p. 524–526.

[13] S. Loth, C. P. Lutz, A. J. Heinrich, Spin-polarized spin excitation spectroscopy. New Journal of Physics **12** (2010), p. 125021.

[14] S. Baumann, W. Paul, T. Choi, et al., Electron paramagnetic resonance of individual atoms on a surface. Science **350** (2015), p. 417–420.

[15] T. S. Seifert, S. Kovarik, C. Nistor, et al., Single-atom electron paramagnetic resonance in a scanning tunneling microscope driven by a radio-frequency antenna at 4 K. Physical Review Research **2** (2020), p. 013032.

[16] K. Yang, Y. Bae, W. Paul, et al., Engineering the eigenstates of coupled spin-1/2 atoms on a surface. Physical Review Letters **119** (2017), p. 227206.

[17] X. Zhang, C. Wolf, Y. Wang, et al., Electron spin resonance of single iron phthalocyanine molecules and role of their non-localized spins in magnetic interactions. Nature Chemistry **14** (2022), p. 59–65.

[18] S. Kovarik, R. Robles, R. Schlitz, et al., Electron Paramagnetic Resonance of Alkali Metal Atoms and Dimers on Ultrathin MgO. Nano Letters **22** (2022), p. 4176–4181.

[19] R. Kawaguchi, K. Hashimoto, T. Kakudate, et al., Spatially Resolving Electron Spin Resonance of π-Radical in Single-molecule Magnet. Nano Letters **23** (2023), p. 213–219.

[20] G. Czap, J. Jr. Valesco, R. M. Macfarlane, et al., Electrically Accessing Electron and Nuclear Spins of Individual Surface Adsorbed Rare-Earth Atoms. Article in Preparation (2023).

[21] O. Stern and W. Gerlach, Der experimentelle Nachweis des magnetischen Moments des Silberatoms. Zeitschrift für Physik **8** (1922), p. 110–111.

[22] O. Stern and W. Gerlach, Der experimentelle Nachweis der Richtungsquantelung im Magnetfeld. Zeitschrift für Physik **9** (1922), p. 349–352.

[23] J. Stöhr and H. C. Siegmann, Magnetism From Fundamentals to Nanoscale Dynamics. Solid-State Sciences **152** (2006), p. 236.

[24] G. E. Uhlenbeck and S. Goudsmit, Ersetzung der Hypothese vom unmechanischen Zwang durch eine Forderung bezüglich des inneren Verhaltens jedes einzelnen Elektrons. Naturwissenschaften **13** (1925), p. 953–954.

[25] I. M. L. Billas, W. A. de Heer, A. Chatelin, Magnetic properties of small iron systems: from ferromagnetic resonance of precipitated particles in silica to Stern-Gerlach deflections in molecular beam. Journal of Non-Crystalline Solids **179** (1994), p. 316–323.

[26] I. M. Billas, A. Châtelain, W. A. de Heer, Magnetism of Fe, Co and Ni clusters in molecular beams. Journal of Magnetism and Magnetic Materials **168** (1997), p. 64–84.

[27] J. Meyer, M. Tombers, C. Van Wüllen, et al., The spin and orbital contributions to the total magnetic moments of free Fe, Co, and Ni clusters. Journal of Chemical Physics **143** (2015).

[28] C. Kittel. *Introduction to solid state physics.* John Wiley & Sons, 2005.

[29] C. Anderson, B. Sanyal, O. Eriksson, et al., Influence of Ligand States on the Relationship between Orbital Moment and Magnetocrystalline Anisotropy. Physical Review Letters **99** (2007), p. 177207.

[30] J. Zubáč. *Anisotropic magnetic properties and magnetic phase diagram of NdPd*. PhD thesis, Charles University, Prague, 2016.

[31] M. Phillips. *Classical Electrodynamics*, volume 2. 1962.

[32] E. Bauer and M. Rotter. *Properties And Applications Of Complex Intermetallics*, volume 2. 2009.

[33] C. Hübner, B. Baxevanis, A. A. Khajetoorians, D. Pfannkuche, Symmetry effects on the spin switching of adatoms. Physical Review B - Condensed Matter and Materials Physics **90** (2014), p. 155134.

[34] T. Miyamachi, T. Schuh, T. Märkl, et al., Stabilizing the magnetic moment of single holmium atoms by symmetry. Nature **503** (2013), p. 242–246.

[35] S. A. Altshuler and B. M. Kozyrev. *Electron Paramagnetic Resonance in Compounds of Transition Elements*. 2nd edition, 1974.

[36] S. Baumann. *Investigation of the unusual magnetic properties of Fe and Co on MgO with high spatial, energy and temporal resolution*. PhD thesis, Basel University, 2015.

[37] C. F. Hirjibehedin, C. Y. Lin, A. F. Otte, et al., Large Magnetic Anisotropy of a Single Atomic Spin Embedded in a Surface Molecular Network. Science **317** (2007), p. 1199–1203.

[38] S. Baumann, F. Donati, S. Stepanow, et al., Origin of Perpendicular Magnetic Anisotropy and Large Orbital Moment in Fe Atoms on MgO. Physical Review Letters **115** (2015), p. 237202.

[39] M. Marciani, C. Hübner, B. Baxevanis, General scheme for stable single and multiatom nanomagnets according to symmetry selection rules. Physical Review B **95** (2017), p. 125433.

[40] A. F. Otte. *Magnetism of a single atom*. PhD thesis, Leiden University, 2008.

[41] M. Steinbrecher. *Tuning Single Atom Magnetism and Non-Collinear Magnetic Interactions in Nanostructures by STM*. PhD thesis, Universität Hamburg, 2017.

[42] H. A. Kramer, Théorie générale de la rotation paramagnétique dans les cristaux. Proc. R. Acad. Sci. Amsterdam **33** (1930).

[43] G. Christou, D. Gatteschi, D. Hendrickson, R. Sessoli, Single-molecule Magnets. MRS Bulletin **25** (2000), p. 66–71.

[44] F. D. Natterer, K. Yang, W. Paul, et al., Reading and writing single-atom magnets. Nature **543** (2017), p. 226–228.

[45] T. S. Seifert, S. Kovarik, D. M. Juraschek, et al., Longitudinal and transverse electron paramagnetic resonance in a scanning tunneling microscope. Science Advances **6** (2020).

[46] P. Willke, W. Paul, F. D. Natterer, et al., Probing quantum coherence in single-atom electron spin resonance. Science Advances **4** (2018), p. 1543.

[47] P. Willke, K. Yang, Y. Bae, et al., Magnetic resonance imaging of single atoms on a surface. Nature Physics **15** (2019), p. 1005–1010.

[48] F. D. Natterer, F. Patthey, T. Bilgeri, et al., Upgrade of a low-temperature scanning tunneling microscope for electron-spin resonance. Review of Scientific Instruments **90** (2019).

[49] W. Paul, K. Yang, S. Baumann, et al., Control of the millisecond spin lifetime of an electrically probed atom. Nature Physics **13** (2017), p. 403–407.

[50] A. Singha, P. Willke, X. Zhang, et al., Engineering atomic-scale magnetic fields by dysprosium single atom magnets. Nature Communication **12** (2021), p. 4179.

[51] J. Pal, M. Smerieri, E. Celasco, et al., Morphology of monolayer MgO films on Ag(100): Switching from corrugated islands to extended flat terraces. Physical Review Letters **112** (2013), p. 126102.

[52] B. Sorokin. *Long Spin Lifetime in Rare-Earth Single-Atom Magnets at Surfaces*. PhD thesis, Ecole Polytechnique Fédérale de Lausanne, 2022.

[53] E. Bartolome, A. Arauzo, J. Luzon, et al. *Handbook of Magnetic Materials: Magnetic Relaxation of Lanthanide-Based Molecular Magnets*, volume 26. Elsevier B.V, 2017.

[54] A. Abragam and B. Bleaney. *Electron Paramagnetic Resonance of Transition Ions*. Dover, dover edition, 1986.

[55] R. Orbach, Spin-lattice relaxation in rare-earth salt. The Royal Society **264** (1961), p. 458–484.

[56] D. Gatteschi, R. Sessoli, J. Villain. *Molecular Nanomagnets*, volume 5. 2006.

[57] I. G. Rau, S. Baumann, S. Rusponi, et al., Reaching the magnetic anisotropy limit of a 3d metal atom. Science **344** (2014), p. 988–992.

[58] C. Wolf, F. Delgado, J. Reina, N. Lorente, Efficient Ab Initio Multiplet Calculations for Magnetic Adatoms on MgO. Journal of Physical Chemistry A **124** (2020), p. 2318–2327.

[59] J. Sievers, Asphericity of 4f-Shells in Their Hund's Rule Ground States. Condensed Matter **45** (1982), p. 289–296.

[60] J. D. Rinehart and J. R. Long, Exploiting single-ion anisotropy in the design of f-element single-molecule magnets. Chemical Science **2** (2011), p. 2078–2085.

[61] R. Skomski and D. J. Sellmyer, Anisotropy of rare-earth magnets. Journal of Rare Earths **27** (2009), p. 675–679.

[62] F. Donati, A. Singha, S. Stepanow, et al., Magnetism of Ho and Er atoms on close-packed metal surfaces. Physical Review Letters **113** (2014), p. 237201.

[63] C. J. Chen. *Introduction to Scanning Tunneling Microscopy*. Oxford University Press, second edition, 1993.

[64] E. Fernandes. *Adsorption Sites of Metal Atoms on MgO Thin Films and Rotational Quantum State Spectroscopy of Adsorbed H2*. PhD thesis, Ecole Polytechnique Fédérale de Lausanne, 2017.

[65] E. Meyer, R. Bennewitz, H. J. Hug. *Scanning Probe Microscopy, The Lab on a Tip*, volume 4. Second edition, 2021.

[66] R. Young, J. Ward, F. Scire, Observation of Metal-Vacuum-Metal Tunneling, Field Emission, and the Transition Region. Physical Review Letters **27** (1971), p. 922.

[67] R. Young, J. Ward, F. Scire, The Topografiner: An Instrument for Measuring Surface Microtopography. Review of Scientific Instruments **43** (1972), p. 999–1011.

[68] G. Binnig, H. Rohrer, C. Gerber, E. Weibel, Tunneling through a controllable vacuum gap. Applied Physics Letters **40** (1982), p. 178–180.

[69] E. L. Wolf. *Principles of electron tunneling spectroscopy*, volume 152. Second edition, 2011.

[70] B. Voigtländer. *Scanning Probe Microscopy: Atomic Force Microscopy and Scanning Tunneling Microscopy*. Springer, 2015.

[71] J. Tersoff and D. R. Hamann, Theory and application for the scanning tunneling microscope. Physical Review Letters **50** (1983), p. 1998.

[72] J. Tersoff and D. R. Hamann, Theory of the scanning tunneling microscope. Physical Review B **31** (1985), p. 805.

[73] J. Bardeen, Tunnelling from a many-particle point of view. Physical Review Letters **6** (1961), p. 57.

[74] T. E. Feuchtwang and P. H. Cutler, Tunneling and Scanning Tunnel Microscopy: a Critical Review. Physica Scripta **35** (1987), p. 132.

[75] W. Wulfhekel and J. Kirschner, Spin-Polarized Scanning Tunneling Microscopy of Magnetic Structures and Antiferromagnetic Thin Films. Annual Review of Materials Research **37** (2007), p. 69–91.

[76] M. Bode, Spin-polarized scanning tunnelling microscopy. Reports on Progress in Physics **66** (2003), p. 523.

[77] M. Julliere, Tunneling between ferromagnetic films. Physics Letters A **54** (1975), p. 225–226.

[78] J. C. Slonczewski, Exchange through a tunneling barrier. Le Journal de Physique Colloques **49** (1988), p. 1629.

[79] H. Prüser. *Scanning Tunneling Spectroscopy of Magnetic Bulk Impurities: From a Single Kondo Atom Towards a Coupled System.* Springer, 2014.

[80] B. C. Stipe, M. A. Rezaei, W. Ho, Single-molecule vibrational spectroscopy and microscopy. Science **280** (1998), p. 1732–1735.

[81] S. Li, A. Yu, F. Toledo, et al., Rotational and Vibrational Excitations of a Hydrogen Molecule Trapped within a Nanocavity of Tunable Dimension. Physical Review Letters **111** (2013), p. 146102.

[82] F. D. Natterer, F. Patthey, H. Brune, Distinction of Nuclear Spin States with the Scanning Tunneling Microscope. Physical Review Letters **111** (2013), p. 175303.

[83] A. J. Heinrich, J. A. Gupta, C. P. Lutz, D. M. Eigler, Single-atom spin-flip spectroscopy. Science **306** (2004), p. 466–469.

[84] T. Choi, C. D. Ruggiero, J. A. Gupta, Tunneling spectroscopy of ultrathin insulating films, and single Co adatoms. Journal of Vacuum Science & Technology B **27** (2009), p. 887–890.

[85] S. Loth, M. Etzkorn, C. P. Lutz, et al., Measurement of Fast Electron Spin Relaxation Times with Atomic Resolution. Science **329** (2010), p. 1628–1630.

[86] B. Bryant, A. Spinelli, J. J. T. Wagenaar, et al., Local Control of Single Atom Magnetocrystalline Anisotropy. Physical Review Letters **111** (2013), p. 127203.

[87] M. Pivetta, F. Patthey, I. Di Marco, et al., Measuring the Intra-Atomic Exchange Energy in Rare-Earth Adatoms. Physical Review X **10** (2020), p. 031054.

[88] A. Curcella, D. Sblendorio, S. Rusponi, et al., Valence Orbitals Driving the Spin Dynamics in a Rare-Earth Single-Atom Magnet. Physical Review Letters **130** (2023), p. 106702.

[89] M. Hänze, G. McMurtrie, S. Baumann, et al., Quantum stochastic resonance of individual Fe atoms. Science Advances **7** (2021), p. 2616.

[90] A. A. Khajetoorians, B. Baxevanis, C. Hübner, et al., Current-Driven Spin Dynamics of Artificially Constructed Quantum Magnets. Science **339** (2013), p. 55–59.

[91] A. A. Khajetoorians, S. Lounis, B. Chilian, et al., Itinerant nature of atom-magnetization excitation by tunneling electrons. Physical Review Letters **106** (2011), p. 037205.

[92] S. Loth, K. von Bergmann, M. Ternes, et al., Controlling the state of quantum spins with electric currents. Nature Physics **6** (2010), p. 340–344.

[93] B. W. Heinrich, L. Braun, J. I. Pascual, K. J. Franke, Protection of excited spin states by a superconducting energy gap. Nature Physics **9** (2013), p. 765–768.

[94] F. Natterer, F. Donati, F. Patthey, H. Brune, Thermal and Magnetic-Field Stability of Holmium Single-Atom Magnets. Physical Review Letters **121** (2018), p. 027201.

[95] P. R. Forrester, T. Bilgeri, F. Patthey, et al., Antiferromagnetic MnNi tips for spin-polarized scanning probe microscopy. Review of Scientific Instruments **89** (2018).

[96] P. R. Forrester, F. Patthey, E. Fernandes, et al., Quantum state manipulation of single atom magnets using the hyperfine interaction. Physical Review B **100** (2019), p. 180405.

[97] F. Donati, M. Pivetta, C. Wolf, et al., Correlation between Electronic Configuration and Magnetic Stability in Dysprosium Single Atom Magnets. Nano Letters **21** (2021), p. 8266–8273.

[98] S. Loth, S. Baumann, C. P. Lutz, et al., Bistability in Atomic-Scale Antiferromagnets. Science **335** (2012), p. 196–199.

[99] L. M. Ward, S. Desai, D. Rootman, et al., Noise can help as well as hinder seeing and hearing. Bulletin of the American Physical Society **46** (2001), p. 002.

[100] F. Moss, L. M. Ward, W. G. Sannita, Stochastic resonance and sensory information processing: a tutorial and review of application. Clinical Neurophysiology **115** (2004), p. 267–281.

[101] R. Benzi, G. Parisi, A. Sutera, A. Vulpiani, Stochastic resonance in climatic change. Tellus **34** (1982), p. 10–16.

[102] G. Matteucci, A study of the climatic regimes of the Pleistocene using a stochastic resonance model. Climate Dynamics **6** (1991), p. 67–81.

[103] I. Y. Lee, X. Liu, B. Kosko, C. Zhou, Nanosignal processing: Stochastic resonance in carbon nanotubes that detect subthreshold signals. Nano Letters **3** (2003), p. 1683–1686.

[104] T. Wagner, P. Talkner, J. C. Bayer, et al., Quantum stochastic resonance in an a.c.-driven single-electron quantum dot. Nature Physics **15** (2019), p. 330–334.

[105] R. Löfstedt and S. N. Coppersmith, Quantum stochastic resonance. Physical Review Letters **72** (1994), p. 1947.

[106] R. Löfstedt and S. N. Coppersmith, Stochastic resonance: Nonperturbative calculation of power spectra and residence-time distributions. Physical Review E **49** (1994), p. 4821.

[107] M. Albert, C. Flindt, M. Büttiker, Distributions of waiting times of dynamic single-electron emitters. Physical Review Letters **107** (2011).

[108] Y. Zavoisky, Paramagnetic relaxation of liquid solutions for perpendicular fields. Journal of Physics **9** (1945), p. 211.

[109] J. L. Lado, A. Ferron, J. Fernandez-Rossier, Exchange mechanism for electron paramagnetic resonance of individual atoms. Physical Review B **96** (2017), p. 205420.

[110] A. Blank, C. R. Dunnam, P. P. Borbat, J. H. Free, High resolution electron spin resonance microscopy. Journal of Magnetic Resonance **165** (2003), p. 116–127.

[111] J. Lambe and R. C. Jaklevic, Molecular Vibration Spectra by Inelastic Electron Tunneling. Physical Review **165** (1968), p. 821.

[112] R. C. Jaklevic and J. Lambe, Molecular Vibration Spectra by Electron Tunneling. Physical Review Letters **17** (1966), p. 1139.

[113] T. Choi, W. Paul, S. Rolf-Pissarczyk, et al., Atomic-scale sensing of the magnetic dipolar field from single atoms. Nature Nanotechnology **12** (2017), p. 420–424.

[114] P. Willke, Y. Bae, K. Yang, et al., Hyperfine interaction of individual atoms on a surface. Science **362** (2018), p. 336–339.

[115] P. Willke, A. Singha, X. Zhang, et al., Tuning Single-Atom Electron Spin Resonance in a Vector Magnetic Field. Nano Letters **19** (2019), p. 8201–8206.

[116] K. Yang, W. Paul, F. D. Natterer, et al., Tuning the Exchange Bias on a Single Atom from 1 mT to 10 T. Physical Review Letters **122** (2019), p. 227203.

[117] K. Yang, W. Paul, S. H. Phark, et al., Coherent spin manipulation of individual atoms on a surface. Science **366** (2019), p. 509–512.

[118] Y. Bae, K. Yang, P. Willke, et al., Enhanced quantum coherence in exchange coupled spins via singlet-triplet transitions. Science Advances **4** (2018), p. 4159.

[119] W. M. J. Van Weerdenburg, M. Steinbrecher, N. P. E. Van Mullekom, et al., A scanning tunneling microscope capable of electron spin resonance and pump-probe spectroscopy at mK temperature and in vector magnetic field. Review of Scientific Instruments **92** (2021), p. 033906.

[120] K. Yang, P. Willke, Y. Bae, et al., Electrically controlled nuclear polarization of individual atoms. Nature Nanotechnology **13** (2018), p. 1120–1125.

[121] F. Delgado and N. Lorente, A theoretical review on the single-impurity electron spin resonance on surfaces. Progress in Surface Science **96** (2021), p. 100625.

[122] T. S. Seifert, S. Kovarik, P. Gambardella, S. Stepanow, Accurate measurement of atomic magnetic moments by minimizing the tip magnetic field in STM-based electron paramagnetic resonance. Physical Review Research **3** (2021), p. 043185.

[123] S. Yan, D. J. Choi, J. A.J. Burgess, et al., Control of quantum magnets by atomic exchange bias. Nature Nanotechnology **10** (2015), p. 40–45.

[124] W. Paul, S. Baumann, C. P. Lutz, A. J. Heinrich, Generation of constant-amplitude radio-frequency sweeps at a tunnel junction for spin resonance STM. Review of Scientific Instruments **87** (2016).

[125] M. A. Nielsen and I. L. Chuang. *Quantum computation and quantum information*. Cambridge university press, 2010.

[126] M. Peter. *Towards magnetic resonance in scanning tunneling microscopy using heterodyne detection*, volume 18. KIT Scientific Publishing, 2015.

[127] F. Delgado and J. Fernández-Rossier, Spin decoherence of magnetic atoms on surfaces. Progress in Surface Science **92** (2017), p. 40–82.

[128] C. Cohen-Tannoudji, G. Grynberg, J. J. Dupont-Roc, Atom–Photon Interactions. Wiley and Sons, Inc., New York (1998).

[129] G. R. Eaton, S. S. Eaton, D. P. Barr, R. T. Weber. *Quantitative EPR*. Springer Science & Business Media, 2010.

[130] P. Anderson, Localized magnetic states in metals. Physical Review **124** (1961), p. 41.

[131] F. Delgado and J. Fernandez-Rossier, Cotunneling theory of atomic spin inelastic electron tunneling spectroscopy. Physical Review B **84** (2011), p. 045439.

[132] J. Reina-Galvez, C. Wolf, F. Delgado, N. Lorente, Cotunneling mechanism for all-electrical electron spin resonance of single adsorbed atoms. Physical Review B **100** (2019), p. 035411.

[133] Property of SPECTRA. Acoustic Chamber. , drawings realized in March, 2021.

[134] L. Claude. *Construction d'un microscope à effet tunnel à basse température et études d'impuretés magnétiques en surface*. PhD thesis, LNS - EPFL, 2005.

[135] Q. Dubout. *Magnetism of Single Adatoms and Small Adsorbed Clusters Investigated by Means of Low-Temperature STM*. PhD thesis, LNS - EPFL, 2013.

[136] C. Soulard, PhD Research Plan. LNS - EPFL (2020).

[137] Nanonis - Specs Group. Accessed 31/07/2023 at https://www.specs-group.com/nanonis/philosophy/, 7 2023.

[138] Cable provided by elSpec, Duratest150-21481 .

[139] retrieved from Coax Co. LTD. Product data sheet SC-119/50-SSS-SS, Accessed 31/07/2023 at http://www.coax.co.jp/en/product/sc/119-50-sss-ss.html .

[140] retrieved from Coax Co. LTD. Product data sheet SC-119/50-NbTi-NbTi, Accessed 31/07/2023 at http://www.coax.co.jp/en/product/sc/119-50-nbti-nbti.html .

[141] Dynawave Inc. Confidential document, DWG. NO. DX086 (2012) .

[142] J. Li, W.-D. Schneider, S. Crampin, R. Berndt, Tunnelling spectroscopy of surface state scattering and confinement. Surface Science **422** (1999), p. 95–106.

[143] O. Jeandupeux, L. Bü, A. Hirstein, et al., Thermal damping of quantum interference patterns of surface-state electrons. Physical Review B **59** (1999), p. 15926.

[144] S. Schintke, S. Messerli, M. Pivetta, et al., Insulator at the Ultrathin Limit: MgO on Ag(001). Physical Review Letters **87** (2001), p. 276801.

[145] E. Fernandes, F. Donati, F. Patthey, et al., Adsorption sites of individual metal atoms on ultrathin MgO(100) films. Physical Review B **96** (2017), p. 045419.

[146] S. Baumann, I. G. Rau, S. Loth, et al., Measuring the three dimensional structure of ultrathin insulating films at the atomic scale. ACS Nano **8** (2014), p. 1739–1744.

[147] H-C. Ploigt, C. Brun, M. Pivetta, et al., Local work function changes determined by field emission resonances: NaCl/Ag(100). Physical Review B **76** (2007), p. 195404.

[148] F. Natterer, F. Patthey, H. Brune, Quantifying residual hydrogen adsorption in low-temperature STMs. Surface Science **615** (2013), p. 80–87.

[149] U. Fano, Sullo spettro di assorbimento dei gas nobili presso il limite dello spettro d'arco. Il Nuovo Cimento **12** (1935), p. 154–161.

[150] L. M. Veldman, L. Farinacci, R. Rejali, et al., Free coherent evolution of a coupled atomic spin system initialized by electron scattering. Science **372** (2021), p. 964–968.

[151] M. Steinbrecher, W. M.J. Van Weerdenburg, E. F. Walraven, et al., Quantifying the interplay between fine structure and geometry of an individual molecule on a surface. Physical Review B **103** (2021), p. 155405.

[152] J. Stroscio and D. M. Eigler, Atomic and molecular manipulation with the scanning tunneling microscope. Science **254** (1991), p. 1319–1326.

[153] K. Barbalace. Periodic Table of Elements - Ti - Titanium. Accessed 12/12/2023 at https://EnvironmentalChemistry.com/yogi/periodic/Ti-pg2.html, 1995.

[154] F. G. Kondev, M. Wang, W. J. Huang, et al., The NUBASE2020 evaluation of nuclear physics properties. Chinese Physics C **45** (2021), p. 030001.

[155] L. M. Veldman, E. W. Stolte, M. P. Canavan, et al., Coherent spin dynamics between electron and nucleus within a single atom. Article in Preparation (2023).

[156] J. Kim, K. Noh, Y. Chen, et al., Anisotropic Hyperfine Interaction of Surface-Adsorbed Single Atoms. Nano Letters **22** (2022), p. 9766–9772.

[157] K. Barbalace. Periodic Table of Elements - O - Oxygen. Accessed 12/12/2023 at https://environmentalchemistry.com/yogi/periodic/O-pg2.html, 1995.

[158] F. Donati, S. Rusponi, S. Stepanow, et al., Magnetic remanence in single atoms. Science **352** (2016), p. 312–318.

[159] R. Baltic, M. Pivetta, F. Donati, et al., Superlattice of Single Atom Magnets on Graphene. Nano Letters **16** (2016), p. 7610–7615.

[160] A. Uldry, F. Vernay, B. Delley, Systematic computation of crystal-field multiplets for x-ray core spectroscopies. Physical Review B **85** (2012), p. 125133.

[161] M. W. Haverkort, Quanty for core level spectroscopy - excitons, resonances and band excitations in time and frequency domain. Journal of Physics: Conference Series **712** (2016), p. 012001.

[162] Data obtained from private communication with Dr. S. Rusponi.

[163] L. Persichetti, S. Stepanow, S. Rusponi, et al., Initial-state dependent spin relaxation time of the long-lived magnetic states of Tb single-atom magnets on MgO. Article in Preparation (2023).

[164] A. Singha, D. Sostina, C. Wolf, et al., Mapping Orbital-Resolved Magnetism in Single Lanthanide Atoms. ACS Nano **15** (2021), p. 16162–16171.

[165] A. Kramida, Y. Ralchenko, J. Reader, NIST ASD Team, NIST Atomic Spectra Database (ver. 5.10, accessed 04/09/2023 at https://physics.nist.gov/asd). National Institute of Standards and Technology, Gaithersburg (2022).

[166] M. Pivetta, S. Rusponi, H. Brune, Direct capture and electrostatic repulsion in the self-assembly of rare-earth atom superlattices on graphene. Physical Review B **98** (2018), p. 115417.

CLÉMENT SOULARD

PhD Candidate in Physics

clementmsoulard@gmail.com | +33(0)640273103 | 27/05/1995

Morges, Switzerland | clément-soulard-aba89a170

PROGRAMMING

- Python
- Matlab
- C++ (basics)
- Microsoft Office
- Latex

LANGUAGES

French: Mother tongue

English: C1

German: A2

Levels:
A2: Basic user.
C1 : Proficient user.

REFERENCE

Prof. Harald Brune
LNS, EPFL
harald.brune@epfl.ch

PUBLICATION

A high bandwidth STM bias line for ESR and stochastic resonance measurements at 400 mK., J. Schwenk, C. Soulard, S. Shan, F. Patthey, H. Brune (in preparation)

Magnetic properties of Tb adatoms on MgO/Ag(100) studied with SP-STM, C. Soulard, J. Schwenk, S. Shan, J. Dolezal, H. Brune (in preparation)

EXPERIENCE

PhD Candidate | Laboratory of Nanostructures at Surface, Ecole Polytechnique Fédérale de Lausanne (EPFL)

Dec 2019 – Nov 2023 | Lausanne, Switzerland

I have worked on a scanning tunneling microscope, capable of probing and manipulating the quantum magnetic properties of single atoms adsorbed on surfaces, in a ultra-high vacuum environment at low temperatures. I have developped experimental (mechanical, acoustic insulation of the machine, RF cabling, micro-electronics, cryogenics, etc.), numerical (automatized measurement routine and data analysis) and communication skills (conferences attended) during my PhD thesis.

Intern | Saint-Gobain Research Provence

Feb 2019 – Aug 2019 | Cavaillon, France

- Worked with multiple techniques: mechanical tests (rupture, elasticity), scanning electron microscopy, numerical simulations.
- Quantified value proposition for new kiln furniture materials with a business team.
- Worked in production for the fabrication of high-performance ceramics (slurry preparation, slip-casting, firing steps).

Intern | Paul Scherrer Institute

Sep 2018 – Nov 2018 | Villigen, Switzerland

- Synchrotron beam-times realized for the investigation of Tm ions quantum properties in a $LiYF_4$ crystal with frequency-domain spectroscopy.

EDUCATION

Master in Physics | EPFL

Sep 2016 – Sep 2019 | Lausanne, Switzerland

Bachelor in Physics | EPFL

Sep 2013 – Sep 2016 | Lausanne, Switzerland

HOBBIES AND INTERESTS

Sports

- Regular participation in triathlons and marathons since 2016
- Competitive tennis for 17 years, winner of the East -Asian Youth Championship (2011, 2012, 2013)
- Captain of the rugby high-school team (2011-2013)

Music

- Member and co-Founder of *The Riot Experience*.
- Choirboy at the Paris Opera (2003-2008)

Volunteering

- Volunteer for the *Scientastic* Festival (2017-2019)
- Coach at *Coaching EPFL* (2014-2015)
- Volunteer for *Habitat for Humanity* in China: rebuilding houses after natural disaster (2012)